PATTERN FORMATION AND PHASE TRANSITIONS IN BENT-CORE LIQUID CRYSTALS

A dissertation submitted to
Kent State University in partial
fulfillment of the requirements for the
degree of Doctor of Philosophy

by

David Wiant

February, 2007

Dissertation written by

David Wiant

B.A., Kenyon College, 2002

Ph.D., Kent State University, 2007

Approved by

_____ , Chair, Doctoral Dissertation Committee

Dr. James Gleeson

_____ , Members, Doctoral Dissertation Committee

Dr. Samuel Sprunt

_____ ,

Dr. Antal Jákli

_____ ,

Dr. John Portman

Accepted by

_____ , Chair, Department of Physics

Dr. Makis Petratos

_____ , Dean, College of Arts and Sciences

Dr. Jerry Feezel

TABLE OF CONTENTS

LIST OF FIGURES

LIST OF TABLES

ACKNOWLEDGEMENTS

There are so many wonderful people that I have met over the last five years that have helped me to get to this point, where I am both ready and well prepared to graduate and move on to something new. I sincerely thank all of you, I will do my best to remember as many of you as I can in the next page or so, and to anyone that I inadvertantly leave out I apologize in advance.

I would like to start by thanking my advisor Dr. James Gleeson for his support and careful guidance, and most of all for his patience with me over the past few years. I never would have been able to finish my dissertation without him. Next, I would like to thank Dr. Sam Sprunt and Dr. Antal Jákli for the countless times they answered my questions and shared advice with me. Gyanu Acharya for the discussions and ideas we shared in Dr. Gleeson's lab. Krishna Neupane and Sunil Sharma for their help with the light scattering measurements. Dr. Nandor Eber for inviting me into his lab and showing me around Budapest. Wade Aldhizer for putting up with my terrible drawings, and machining several pieces that allowed me to do my experiments. All the office staff, who were an immeasurable help the entire time I was here. Also, the staff at the NHMFL for your assistance while I was there.

I would like to acknowledge financial support from NSF Grant Nos. DMR-0606160, DMS-0456221 and DMR-9988614. And NSF cooperative agreement No. DMR-0084173, the state of Florida, and the DOE, which supported work at the National High Magnetic Field Laboratory. And also, NSF Grant No. OISE-0225963 , which allowed me to visit the Institute for Solid State Physics and Optics in Budapest,

Hungary.

Finally, and most importantly, I would like to thank my family for their love and support. Without them none of this would have been possible.

David Wiant, 24 January, 2007.

CHAPTER 1

INTRODUCTION

1.1 A BRIEF HISTORY OF LIQUID CRYSTALS

The history of liquid crystals (LCs) dates back to the mid-nineteenth century, when several European scientists observed unusual behavior while passing polarized light through liquid-like biological materials. Rudolph Virchow, C. Mettenheimer, and G. Valentin were among the first to observe LC behavior in biological systems, but none of them realized that they were actually observing a "new" state of matter [1]. In its earliest years, the field of LC science was led by Otto Lehmann and W. Heintz. Although neither received credit as being the first to discover LCs, both men made key contributions to the field in its infancy. Lehmann was the first to use a microscope that incorporated polarizers and a hot stage [1], while Heintz observed two melting points in natural fats [1].

In 1888, Austrian botanist Friedrich Reinitzer, working with cholesteryl benzoate, observed two melting points and some of the same behavior with regard to polarized light that had been previously observed [1]. Reinitzer's work and subsequent reports of his findings raised a great deal of interest among other scientists in the materials that would come to be known as LCs, and subsequently earned him the title as the "discoverer" of LCs.

Following Reinitzer's work, Lehmann became an important figure in the field through the use of his new polarizing microscope. In fact, Lehmann was the first to use the term liquid crystal to describe these new materials [1]. In 1922, Georges Freidel

established a great deal of the modern nomenclature used to describe LCs; using the words nematic, smectic, and cholesteric in a paper published that year [1]. Following World War II, interest in LC research declined for several years, but was revived in the late 1950's by Glenn Brown, a chemist at Kent State University. Brown was at the fore front of LC research until the 1980's, helping to bring LCs and technology together. Among his numerous achievements were the founding of the Liquid Crystal Institute at Kent State University and the International Liquid Crystal Conference. In subsequent years, the development of industrial applications for LCs promoted an explosion in LC research that has continued into the twenty-first century. This growth was primarily based on the success of LCs in electro-optical information displays. Early displays used polarizers and twisted nematic configurations of rod-like liquid crystals to produce black and white images. Later displays used ferroelectric liquid crystals and smectic phases to produce images, and now the race is on to identify new materials and set-ups that can be used to produce greater contrast and wider viewing angles than their predecessors.

1.2 REVIEW OF THERMOTROPIC CALAMITC LIQUID CRYSTALS AND THEIR PHASES

The basic unit of interaction in a LC system is called a mesogen, which can be a molecule or complex of molecules. The mesogens of many thermotropic LC systems consist of anisotropic organic molecules composed of a rigid aromatic core of benzene rings with attached end groups. This core may be either straight or bent. Molecules with a straight core are often referred to as rod-like, or calamitic, LCs. Through the twentieth century rod-like LCs have been far more prevalent in science and industry

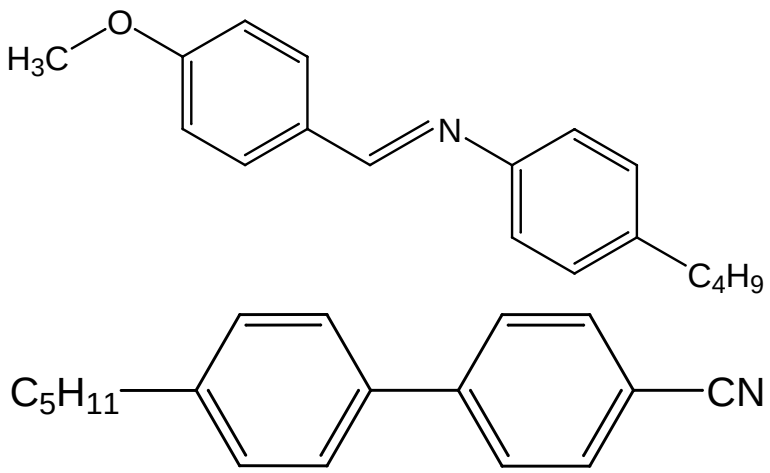

Figure 1.1: Examples of common calamitic LCs. (top) n-4'-methoxybenzylidene-n-butylaniline, MBBA. One of the first room temperature nematics and the first LC to be fully characterized. (bottom) 4-pentyl-4'-cyanobiphenyl, 5CB. A common LC used in electro-optic displays.

than the bent-core LCs. Examples of rod-like molecules are shown in Fig. 1.1. Rod-like LCs generally have dimensions on the order of $\sim 20\mathring{A}$ long and $\sim 5\mathring{A}$ wide.

Calamitic thermotropic LCs experience changes in molecular order as the temperature is changed, which leads to phase transitions as the temperature is varied. The different phases of these LCs can be described by three types of order. The first type of order is orientational order, which describes a preferred direction of an axis (a direction with which a certain axis, usually the long axis, of the molecules are roughly parallel) of a LC by means of a unit vector $\hat{n}$ called the director. The director is defined such that the physical properties of the LC system are left unchanged under a rotation that takes $\hat{n}$ to -$\hat{n}$. The next type of order is positional order, which describes the spatial organization of the system in terms of lattice vectors. The final type of order is bond orientational order. In this case a bond is a imaginary line joining the centers of two molecules (not to be confused with a chemical bond). If two of these bonds are parallel they are said to be oriented in the same direction.

I will briefly describe the most common LC phases found in calamitic LCs starting from high temperatures and moving to lower temperatures (see Fig. 1.2). The least ordered and completely symmetric phase, which exists at higher temperatures than the other states, is the isotropic I phase. In the I phase the system possesses no orientational, positional, or bond order. LCs in this phase will be purely liquid and will flow like more conventional liquids, such as water.

The uniaxial nematic N phase, which is slightly more ordered than the I phase, may be seen on cooling from the I phase. The N state has orientational order denoted by the director and short range bond order, but it lacks positional order. The system possesses $D_{\infty h}$ symmetry, i.e. the system is invariant to arbitrary rotations about $\hat{n}$ and to inversions of $\hat{n}$. The N phase may be described by an order parameter, $S = \frac{1}{2} < 3cos^2\theta - 1 >$. This order parameter gives the average alignment of the long axes of the molecules with respect to the director [2], with θ being the angle the long axis of a molecule makes with respect to the director. In the I phase, where the molecules are randomly oriented with respect to the director, $S = 0$. When the long axes of the molecules are perfectly aligned with the director $S = 1$. When the long axes of the molecules are all oriented perpendicular to the director $S = -1/2$.

The temperature dependent transition between the I and N phase is a first order transition. First order transitions possess latent heat and show a discontinuity in physical properties related to orientational order. The discontinuity in order parameter has been experimentally measured for many different calamitic LCs using nuclear magnetic resonance. These experiments show that S generally goes from 0 in I to ~ 0.4 at the N-I transition in calamitic LCs.

The N state described above is achiral (having mirror symmetry). If a chiral

molecule is inserted into an achiral nematic system the system will undergo a helical distortion. This same helical distortion is also found in cholesterol esters, hence this phase is also known as the cholesteric phase. In the cholesteric phase the local director rotates about an axis periodically in space. The period of this rotation is called the pitch. The pitch is typically much longer than the molecular length, and can be on the order of optical wavelengths.

The smectic Sm phases are more ordered than the N phase. The SmA phase usually appears at temperatures below the I and N phases. The SmA phase has D_∞ symmetry. It consists of a layered structure with 1D positional order between the layers. The layers are made up of molecules oriented roughly parallel to the layer normal with only short-range bond order within the layers. For the direction perpendicular to the layers, $\hat{z}$, the structure is invariant under transformations that take $\hat{z} \rightarrow$ -$\hat{z}$. The SmA phase is optically uniaxial, such that two distinct indices of refraction may be defined in this system. One axis is parallel to $\hat{z}$, the other is defined perpendicular to $\hat{z}$.

The SmC phase is similar to the SmA phase except that the long axes of the molecules within the layers are tilted at an angle with respect to $\hat{z}$. The tilting of the layers breaks the $\hat{z} = -\hat{z}$ symmetry seen in the SmA phase, which leaves the SmC structure optically, magnetically, and electrically biaxial. The SmC phase is described by C_{2h} symmetry. There is also a chiral SmC phase, which is denoted by SmC^*. (Chiral phases are denoted by a star.) SmC^* has a helical deformation about $\hat{z}$ with a pitch greater than the interlayer spacing, similar to the deformation seen in the cholesteric phase. The SmC^* phase generally has a net polarization along the two-fold rotation axis, which makes this phase ferroelectric within the space of one

pitch.

More ordered than the SmC phase are the hexatic smectic phases; B_{HEX}, SmF, SmI, and SmL. The hexatic smectics are 2-D fluids, similar to the SmA and SmC phases, but they possess long-range bond orientational order within their fluid layers (though they still only have short range positional order within their layers). Further ordering leads to the crystal states. Namely, the SmB_{cry} and SmE, or $crystalB$ and $crystalE$ respectively, which have a 3D crystalline structure with the molecules oriented perpendicular to the layers, and long range bond and positional order. Their tilted analogs SmG, SmJ, SmH, and SmK (also known as $crystalG$, $crystalJ$, $crystalH$, $crystalK$ respectively) also have long range bond and positional order, but with the molecules tilted within each plane.

1.3 BENT-CORE LIQUID CRYSTALS

The first published report of the synthesis of a bent LC molecule was by Vorländer and Apel in 1932 [3]. There was little interest in bent-core systems from Vorländer's time until 1996 when Niori *et al.* reported the observation of ferroelectricity in a LC phase of an achiral bent-core molecule (again, an achiral molecule is one in which a molecule and its mirror image are equivalent) [4]. The existence of ferroelectricity in systems of achiral molecules, and later the possibility of biaxial nematic phases, generated a tremendous amount of interest in the topic.

Bent-core (also known as banana, boomerang, or v-shaped) LCs are generally formed from achiral molecules composed of five aromatic rings with a meta-substituted central ring, linking groups, and terminal chains. An example of this general formula is shown in Fig. 1.3. The properties of a bent-core mesogen; such as bend-angle, polarity, transition temperatures, etc; can be altered by substitutions to the general

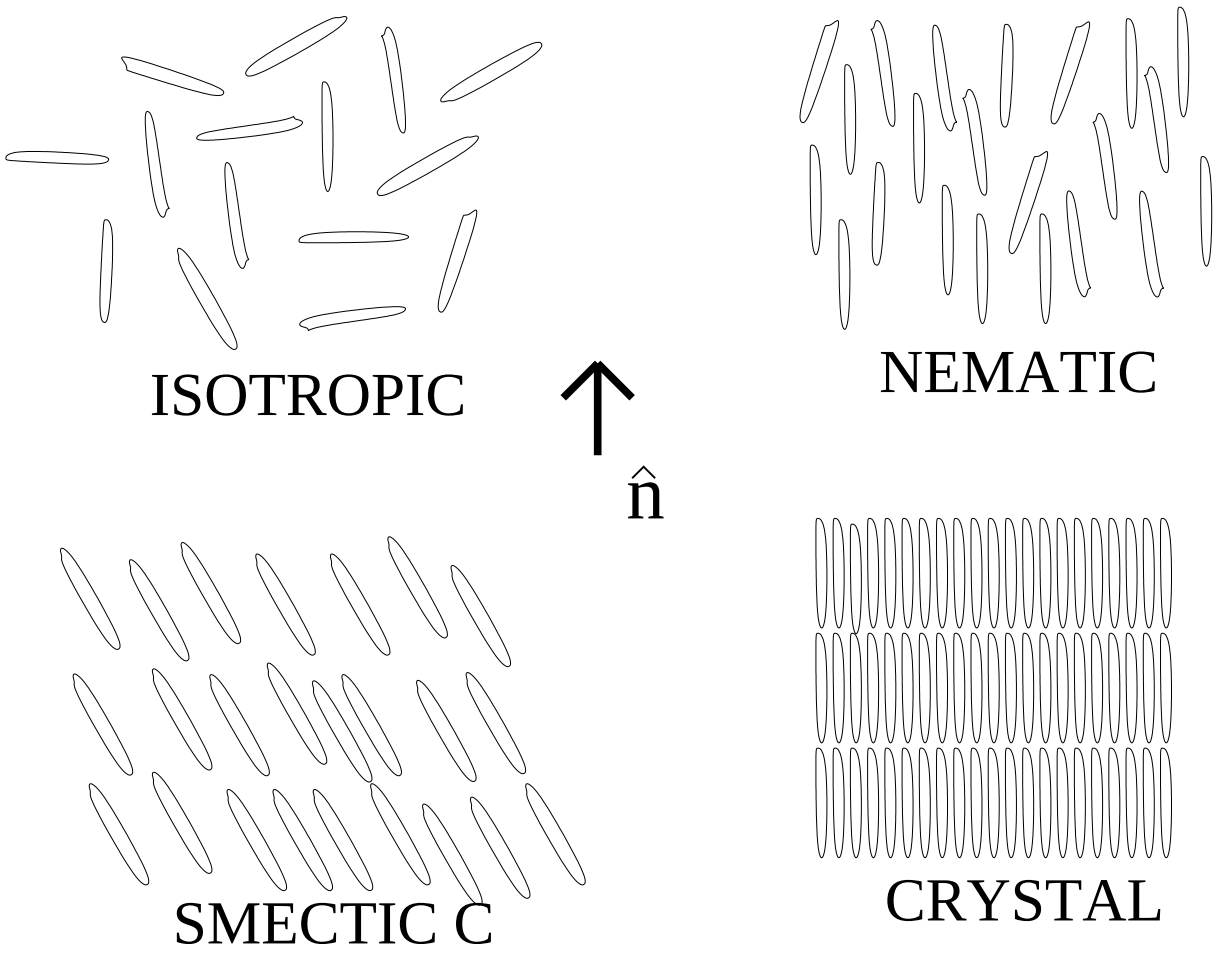

Figure 1.2: Schematic representation of common LC phases.

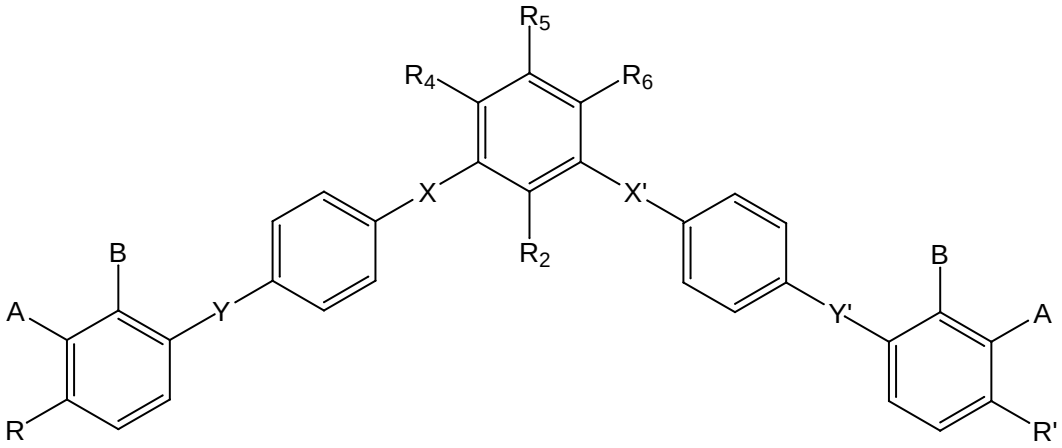

Figure 1.3: Schematic diagram of bent-core LC with five benzene rings. X, X', Y', and Y' represent the linkage groups between the rings. R and R' represent the terminal chains. R_2, R_4, R_5, R_6, A, and B represent lateral substituents.

formula described in Fig. 1.3 [5–7]. Although not nearly as common as the five-ring variety, bent-core molecules with six or seven rings, and appropriate substitutions, have also been synthesized (see [5] and Refs. within).

The shape of the bent-core, or banana, molecules allows for packing of the molecules in such a way that LC phases with no calamitic analogue are created [5, 8]. The most celebrated of these "new" phases are the B phases, which are phases that exhibit smectic and polar ordering. In addition to the smectic phases, a rich variety of orientationally ordered but spatially homogeneous phases, or *liquid* phases, with exotic symmetries have also been predicted [9], although not yet experimentally observed. Much of the following work I will present focuses on the identification of several of these predicted *liquid* phases in two bent-core materials. In the remainder of this chapter, I will briefly introduce some of the liquid phases, then for completeness I will discuss the bent-core smectic phases.

1.3.1 LIQUID PHASES IN BENT-CORE LIQUID CRYSTALS

Bent-core systems can exhibit a "classic" uniaxial nematic phase, in addition to the exotic phases mentioned earlier, which is indeed a *liquid* phase using the definition provided above. To date the nematic phase in bent-core LCs has received far less attention then its smectic counterparts. This is because the shape of bent-core molecules sterically inhibits translational motion parallel to the director and rotation about the director, which tends to prevent bent-core molecules from developing nematic phases. Subsequently there are not many bent-core LCs with nematic phases available to study. But as the field of bent-core LC research matures and more lines of bent-core mesogens are being synthesized some optically uniaxial nematic materials are beginning to become available [7, 10–19], and with an increased supply the interest in nematic phases is increasing.

Now, on to the more interesting *liquid* phases. As mentioned previously, rod-like molecules are invariant to rotations and inversions about their long axes. The $D_\infty h$ symmetry of this system can be described by a second rank traceless symmetric tensor. The bend in the core of the bent-core molecules leaves them with a lower symmetry, $C_{2\nu}$, than the rod-like molecules. They have a two-fold rotation axis perpendicular to the long axis of the molecule and a mirror plane parallel to the two-fold rotation axis. For the bent-core molecules, odd rank tensor order parameters, along with the even rank nematic order parameter, must be used to describe the experimentally observed orientational ordering. The ordering of a third rank traceless symmetric tensor order parameter T^{ijk} and its interactions with the nematic Q^{ij} and vector p^i order parameters leads to the prediction of the unique *liquid* phases and many transitions among these phases in bent-core liquid crystals (see Fig. 1.4).

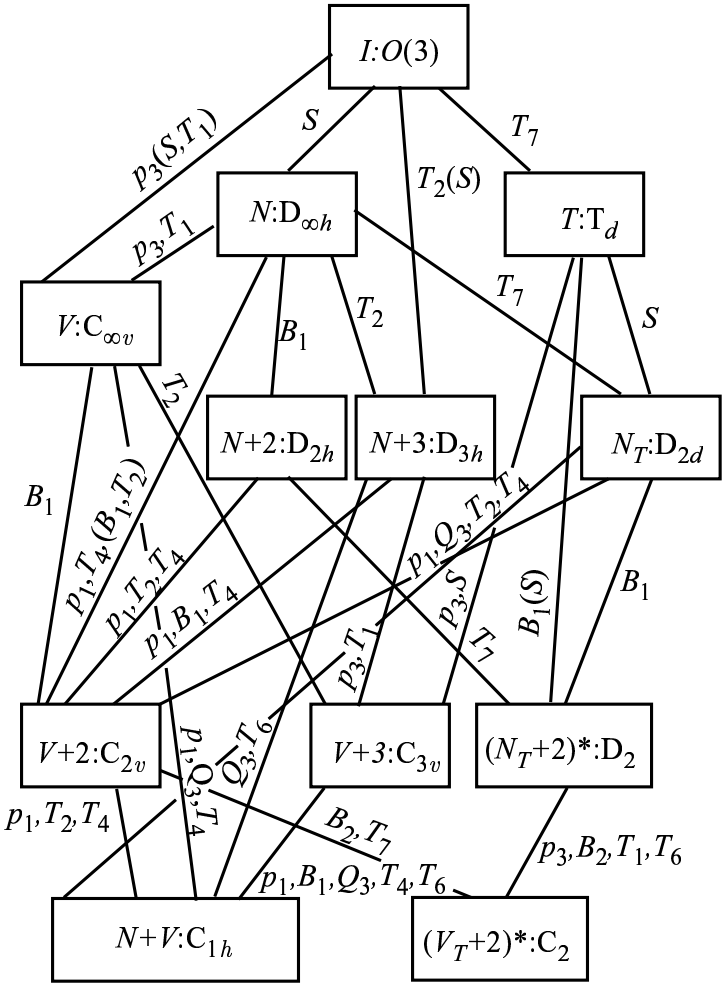

Figure 1.4: A chart of the LC transitions in bent-core LCs. The symmetry groups are listed in each box following the phase. The order parameters that become non-zero at a transition are listed on the lines connecting the phases [9].

Starting from the I phase and moving toward lower symmetry phases, Lubensky and Radzihovsky [9] theorize that there are two distinct phase sequences that will occur. One sequence consists of phases in which a single bent-core molecule is the active mesogenic unit, and the other transition line is made up of phases in which a complex of two or more molecules acts as the primary mesogenic unit. In the former case, symmetry reducing transitions from the I phase yield optically uniaxial or biaxial phases, with unique global symmetries, formed from single molecule complexes. In the latter case, the tetrahedratic T phase is observed on cooling from the I phase. (The symbol T will be used to denote both temperature and the tetrahedratic phase. However, the surrounding text should make the meaning of the symbol clear.) In the T phase groups of molecules arrange themselves in units with shapes approximating that of a tetrahedron. The system has T_d symmetry, which leaves it with local orientational order, yet optically isotropic. Other phases with interesting properties along this line are the N_T phase, which a nematic phase consisting of complexes of molecules that is non-polar and is neither uniaxial or biaxial; the $(N_T + 2)^*$, which is spontaneously chiral and optically biaxial; and the chiral polar $(V_T + 2)^*$ phase (I will come back to these phases later in this work).

1.3.2 SMECTIC PHASES IN BENT-CORE LIQUID CRYSTALS

The shape of the bent-core molecules, which allows for packing not seen in calamitic LCs, produces unique smectic phases along with the fore mentioned *liquid* phases. Figure 1.5 shows the four basic possibilities for packing bent-core molecules within a smectic layer to create these new phases. Interest generated by these new phases and their electric properties is what led to the establishment of bent-core LCs as a separate sub field of LC research. Following the suggestion of the Workshop on

Banana-Shaped Liquid Crystals: Chirality by Achiral Molecules, held in Berlin in 1997, the new phases have been labeled 'B_n' (where n represents the order in which they were discovered). This naming system is intended to be temporary. It is probable that the B_n labels will eventually be replaced by labels that take into account the structure and symmetry of the phases.

Thus far eight distinct banana phases have been identified, B_{1-8} [8, 20]. The B_2 phase was the one which was first seen by Niori *et al.* [4], and has been the most frequently studied banana phase since that time. The B_2 is a smectic phase where the molecules are uniformly packed and tilted at an angle between 35° and 40° [8] in the bend direction within each layer. This structure possesses C_{2v} symmetry which should yield a spontaneous polarization in the direction of the two-fold symmetry axis. Due to this configuration the B_2 phase shows antiferroelectric switching under the change of sign of an applied electric field. In this case, antiferroelectric switching is used to describe a situation where the molecular dipoles are aligned within each layer, with the alignment direction inverted in alternating layers with no electric field applied. (Ferroelectric switching describes a situation where the molecular dipoles are oriented in the same direction in all layers with no field.) When an electric field is applied, the dipoles will align above a critical field (see Fig. 1.6). Although antiferroelectric behavior is more common, a few cases of B_2 like systems with ferroelectric ground states have also been reported [21, 22]. Link *et al.* [23] postulated that two equally probable ground states exist that will exhibit antiferroelectric switching. These two state are shown in Fig. 1.6. The first is the racemic structure, in which the polar axis of the molecule (along the direction of the molecular kink) alternates from layer to layer, but the tilt direction is the same in each layer. The handedness alternates in

each layer as well. The other state is the homogenously chiral structure. Where the tilt and the polar direction each alternate from layer to layer, but the handedness is the same in each layer.

The B_7 phase is noted for its rich variety of textures not seen in other B phases. Patterns of twisted helical fibers, high- and low-birefringence focal conic stripes, banana leaf-shaped domains, and checkerboards all appear in the B_7 phase. The structure of this phase is not completely understood at this time. Jákli *et al.* [24] suggested that the B_7 phase is identical to the SmC_G phase predicted by de Gennes [2]. In this case the structure of the phase can be described by a tilt of the molecular normal with respect to the layer normal, called the "clinic" tilt, and a tilt of the layer polarization with respect to the layer normal, called the "lean" tilt (see Fig. 1.7). The Boulder group theorized that the B_7 structure consists of stacked smectic layers periodically modulated on a microscopic scale, where the undulation wavelength varies from $\sim$4 to $\sim$70 nm [25]. It is possible that the Boulder model might correspond to the SmC_G phase when viewed on a macroscopic scale, but further work is needed to verify this conjecture [26].

Differential scanning calorimetry, X-ray diffraction, NMR, dielectric, electro-optical, and optical studies have been used to identify the other banana phases. A clear understanding of the structures of these other B phases has not yet been achieved, so instead I will briefly discuss the key attributes of each phase. First is the B_5 phase, which is similar to the B_2 in most regards. The main differences between the two are the greater viscosity of B_5 and an additional short-range order in the layers [27]. The B_1 phases possess some 2D ordering, which is evidenced by X-ray patterns with two or more reflections in the small angle regions [8]. The B_6 phase appears to have

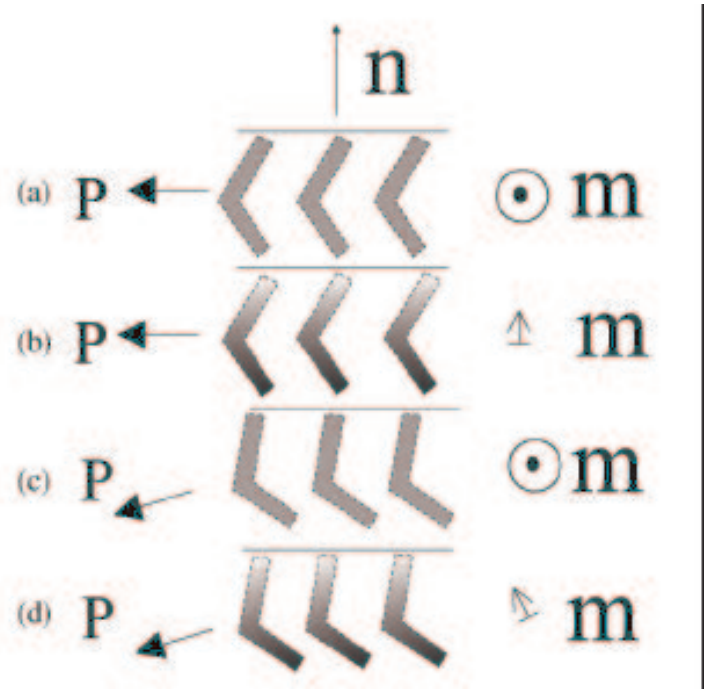

Figure 1.5: Possibilities for packing bent-core molecules into layers. Shading indicates tilt of the molecules out of the page, with the brighter areas being closer to the observer. The packing structure is described by three vectors: the smectic layer normal **m**, the molecular plane normal **n**, and the direction of the molecular kink **P** (which determines the direction of the polarization). (a) $\mathbf{n}\perp\mathbf{m}$ and $\mathbf{n}\perp\mathbf{P}$. (b) $\mathbf{n}\perp\mathbf{P}$ but $\mathbf{n}\not\perp\mathbf{m}$. (c) $\mathbf{n}\perp\mathbf{m}$ but $\mathbf{n}\not\perp\mathbf{P}$. (d) $\mathbf{n}\not\perp\mathbf{P}$ or $\mathbf{n}\not\perp\mathbf{m}$. [24]

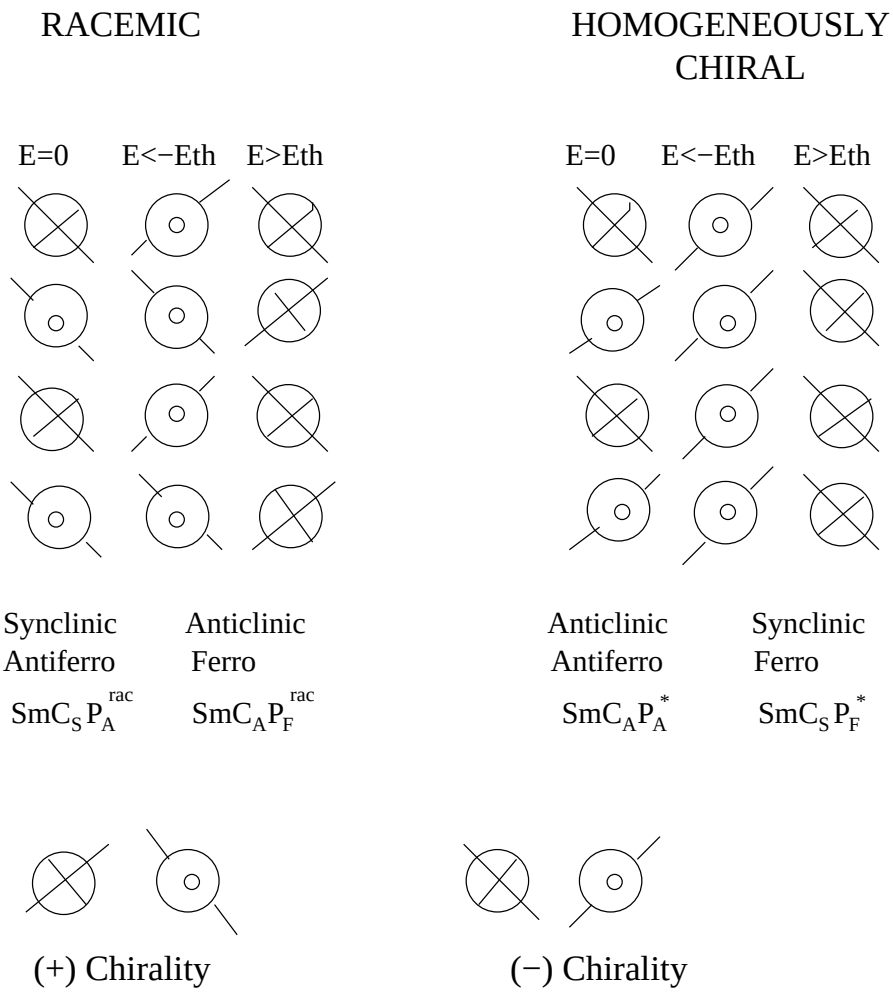

Figure 1.6: The Boulder group's model for antiferroelectric switching of the B_2 phase [23]. The E values at the top of the figure refer to the applied electric field. The long lines going through the circles represent the orientation of the molecules' long axes. The crosses and dots inside the circles represent the direction of the molecular dipole, either into or out of the page. The three columns represent the layer structure at 0 field, below the negative switching threshold, and above the positive switching threshold; from left to right respectively. Below the threshold the structure is antiferroelectric, above the threshold the structure becomes ferroelectric.

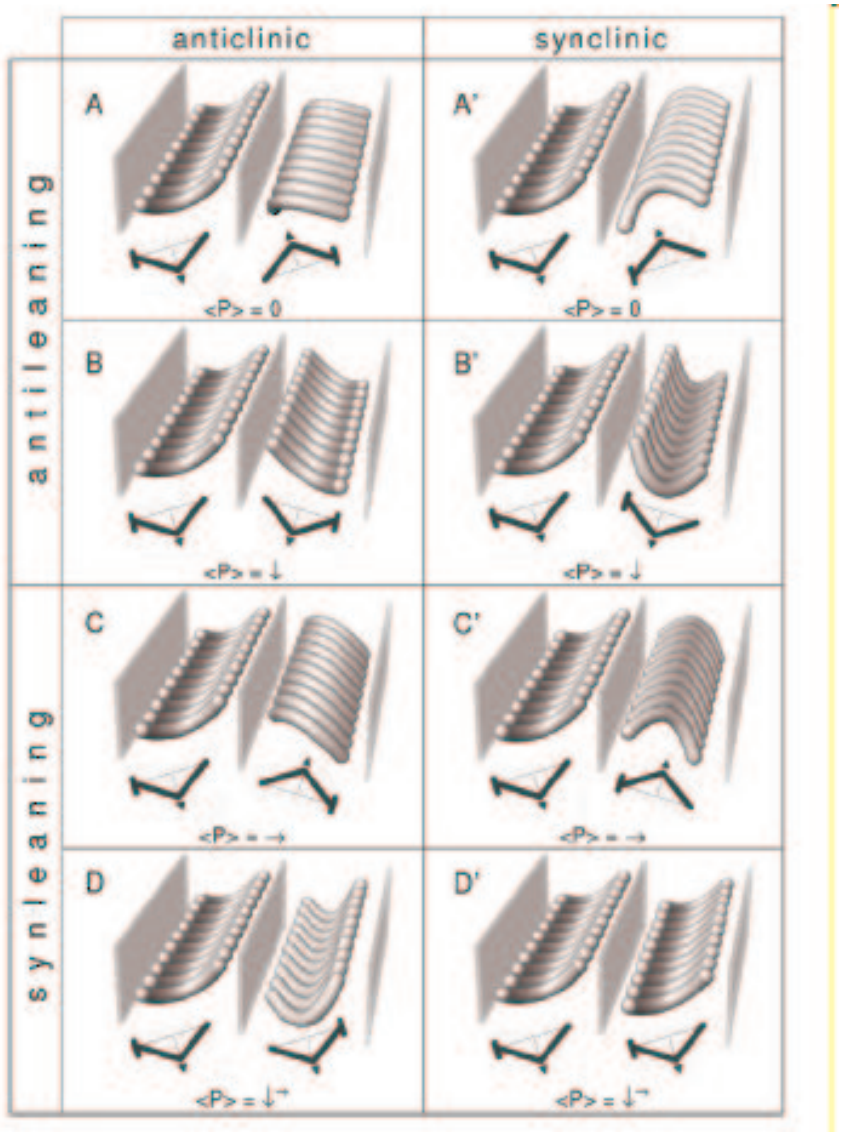

Figure 1.7: Possible SmC_G structures allowing different configurations in two layers, where $< P >$ is the resulting polarization vector. A and A' are antiferroelectric with $< P > = 0$. B and B' are have in-layer polarization, which is similar to the ferroelectric B_2 phase. C and C' have out-of-layer polarization. D and D' have both in-layer and out-of-later polarization [24].

a tilted, intercalated structure with layer spacing less than half the length of the molecule [8]. The B_3 and B_4 phases have long range order, not present in the other B phases, and might be classified as crystals [8]. Also, the B_4 phase is noted for its intense blue color (see [8] and refs. within). B_8 is the only B phase to possess a bilayer structure [20]. Along with these is the $SmAP$ (or SmC_{PA}) phase, which is the orthogonal analogue to the B_2 phase [12, 19, 28]. The $SmAP$ phase shows uniform packing and spontaneous polarization in the bend direction, but no molecular tilt (with respect to the layer normal) in its layers.

Bent-core mesogens which exhibit the B_n phases typically have a bending angle between 105° and 140° [6]. Bent-core molecules with angles near the extremes of this range tend to show the "classic" SmA and SmC phases observed in calamitic LCs. In the SmA phase, the long axes of the molecules are normal to layer, but lack in layer positional or polar order. This phase is discernible by its fan shaped or homeotropic texture, its x-ray diffraction pattern, and the absence of ferroelectric switching [6, 17, 28–30]. The SmC phase has in layer molecular tilt, but it also lacks any in layer positional or polar order. The SmC phase is identified by its broken fan shaped or Schlieren texture and its x-ray diffraction pattern [6, 29, 30].

The field of bent-core LCs only promises to flourish in the future. Recently there have been several reports citing the observation of thermotropic biaxial nematic phases in bent-core LCs [31–34] and bent-core LCs with gigantic flexoelectric coefficients [35]. These reports have created a great deal of excitement in the field as these findings help to validate earlier theoretical predictions and could lead to extraordinary advances in the field of LC technology.

BIBLIOGRAPHY

[1] P. J. Collings. *Liquid Crystals: Nature's Delicate State of Matter.* Princeton University Press, 1990.

[2] P. G. de Gennes and J. Prost. *The Physics of Liquid Crystals.* Oxford Science Publications, 1993.

[3] D. Vorländer and A. Apel. *Ber.*, 65:1101, 1932.

[4] T. Niori, F. Sekine, J. Watanabe, T. Furukawa, and H. Takezoe. *J. Mater. Chem.*, 6:1231, 1996.

[5] W. Weissflog, H. Nadasi, U. Dunemann, G. Pelzl, S. Diele, A. Eremin, and H. Kresse. *J. Mater. Chem.*, 11:2748, 2001.

[6] I. Wirth, S. Diele, A. Eremin, G. Pelzl, S. Grande, L. Kovalenko, N. Pancenko, and W. Weissflog. *J. Mater. Chem.*, 11:1642, 2001.

[7] T. J. Dingemans adnd E. T. Samulski. *Liq. Cryst.*, 27:131, 2000.

[8] G. Pelzl, S. Diele, and W. Weissflog. *Adv. Mater.*, 11:707, 1999.

[9] T. C. Lubensky and L. Radzihovsky. *Phys. Rev. E*, 66:031704–1–27, 2002.

[10] T. Niori, J. Yamamoto, and H. Yokoyama. *Mol. Cryst. Liq. Cryst.*, 409:475, 2004.

[11] J. Matraszek, J. Mieczkowski, J. Szydlowska, and E. Gorecka. *Liq. Cryst.*, 27:429, 2000.

[12] W. Weissflog, H. Nadasi, U. Dunemann, G. Pelzl, S. Diele, A. Eremin, and H. Kresse. *J. Mater. Chem.*, 11:2748, 2001.

[13] W. Weissflog, S. Sokolowski, H. Dehne, B. Das, S. Grande, M. Schroder, A. Eremin, S. Diele, G. Pelzl, and H. Kresse. *Liq. Cryst.*, 31:923, 2004.

[14] K. Fodor-Csorba, A. Vajda, G. Galli, A. Jakli, D. Demus, S. Holly, and E. Gacs-Baitz. *Macromol. Chem. Phys.*, 203:1556, 2002.

[15] D. Shen, S. Diele, G. Pelzl, I. Wirth, and C. Tschierske. *J. Mater. Chem.*, 9:261, 1999.

[16] W. Weissflog, C. Lischka andS. Diele, G. Pelzl, I. Wirth, S. Grande, H. Kresse, H. Schmalfuss, H. Hartung, and A. Stettler. *Mol. Cryst. Liq. Cryst.*, 333:203, 1999.

[17] H. Matzunaki and Y. Matsunaga. *Liq. Cryst.*, 14:105, 1993.

[18] S. Stojadinovic, A. Adorjan amd S. Sprunt, H. Sawade, and A. Jakli. *Phys. Rev. E.*, 66:060701, 2002.

[19] M. W. Scroder, S. Diele, G. Pelzl, U. Dunemann, H. Kresse, and W. Weissflog. *J. Mat. Chem.*, 13:1877, 2003.

[20] J. P. Bedel, J. C. Rouillon, J. P. Marcerou, M. Laguerre, H. T. Nguyen, and M. F. Achard. *Liq. Cryst.*, 28:1285, 2001.

[21] D. M. Walba, E. Korblova, R. Shao, J. E. Maclennan, D. R. Link, M. A. Glaser, and N. A. Clark. *Science*, 288:2181, 2000.

[22] E. Gorecka, D. Pociecha, F. Araoka, D. R. Link, M. Nakata, J. Thisayukta, K. Ishikawa, J. Watanabe, and H. Takezoe. *Phys. Rev. E*, 66:031704–1–27, 2002.

[23] D. R. Link, G. Natale, R. Shao, J. E. Maclennan, N. A. Clark, E. Korblova, and D. M. Walba. *Science*, 278:1924, 1997.

[24] A. Jakli, D. Kruerke, H. Sawade, and G. Heppke. *Phys. Rev. Lett.*, 86:5715, 2001.

[25] D. A. Coleman, J. Fernsler, N. Chattham, M. Nakata, Y. Takanishi, E. Korblova, D. R. Link, R. F. Shao, W. G. Yang, J. E. Maclennan, O. Mondainn-Monoval, C. Boyer, W. Weissflog, G. Pelzl, L. C. Chien, J. Zasadzinski, J. Watanabe, D. M. Walba, H. Takezo, and N. A. Clark. *Science*, 301:1204, 2003.

[26] S. Stojadinovic. *Light Scattering Studies of Dynamics of Bent-Core Liquid Crystals.* PhD thesis, Kent State University, 2005.

[27] S. Diele, S. Grande, H. Kruth, C. Lischka, G. Pelzl, W. Weissflog, and I. Wirth. *Ferroelectrics*, 212:169, 1998.

[28] A. Eremin, S. Diele, G. Pelzl, H. Nadasi, W. Weissflog, J. Salfetnikova, and H. Kresse. *Phys. Rev. E*, 64:051707, 2001.

[29] W. Weissflog, L. Kovalenko, I. Wirth, S. Diele, G. Pelzl, H. Schmalfuss, and H. Kresse. *Liq. Cryst.*, 27:677, 2000.

[30] H. Kresse, H. Schlacken, U. Dunemann, M. W. Schroder, G. Pelzl, and W. Weissflog. *Liq. Cryst.*, 29:1509, 2002.

[31] J. A. Oliveras, S. Stojadinovic, T. J. Dingemans, S. Sprunt, and A. Jakli. *Phys. Rev. E*, 68:041704–1–6, 2003.

[32] B. R. Acharya, A. Primak, T. J. Dingemans, E. T. Samulski, and S. Kumar. *Pramana*, 61:231, 2003.

[33] L. A. Madsen, T. J. Dingemans, M. Nakata, and E. T. Samulski. *Phys. Rev. Lett.*, 92(14):145505, 2004.

[34] B. R. Acharya, A. Primak, and S. Kumar. *Phys. Rev. Lett.*, 92(14):145506, 2004.

[35] J. Harden, B. Mbanga, N. Eber, K. Fodor-Csorba, S. Sprunt, J. T. Gleeson, and A. Jakli. *Phys. Rev. Lett.*, 97:157802, 2006.

CHAPTER 2

MAGNETIC FIELD INDUCED BIREFRINGENCE

The locally ordered, optically isotropic, tetrahedratic phase was theoretically predicted several years ago [1], but until now had not been experimentally observed. One reason for this is the difficulty is recognizing the tetrahedratic phase. Most of the methods used to characterize a LC phase, such as the observation of textures through polarizing microscopy, x-ray diffraction, NMR, and AFM for example cannot differentiate between a truly isotropic phase and a tetrahedratic phase. One powerful way to identify the T phase is by looking for the signatures of a T-I transition. A tool that has been successfully used to examine phase transitions in calamitic LCs is magnetic field induced birefringence (MB).

I performed MB measurements on two bent-core LCs. The MB measurements gave evidence of a transition between a nematic phase and an optically isotropic phase, as well as a transition between two optically isotropic phases at temperatures above the clearing point, in both materials. In the remainder of this chapter, I will discuss the MB experimental set-up, the transition at the clearing point, and finally the transition between the two optically isotropic phases.

2.1 EXPERIMENTAL SET-UP

The MB experiment was first performed at Kent State University (KSU) using a relatively low magnetic field at temperatures just above the clearing point. Later, the experiment was repeated in Cell 4 at the National High Magnetic Field Laboratory

at Florida State University (NHMFL) using larger, varying fields, at temperatures well above the clearing point. I will, first, describe the experiment as performed at the NHMFL, and then note the changes in the experiment used at KSU. I will end the section with a description of the sample preparation.

2.1.1 NHMFL SET-UP

Figure 2.1 shows the set-up used at the NHMFL. The optical components were fixed to 2×8 ft. Vere aluminum breadboard. The breadboard sat on four uncharged Newport low profile isolators, which had their steel screws replaced by non-magnetic stainless steel screws. The laser radiation was provided by a polarized Melles Griot laser that gave a 30 mW maximum output at $\lambda = 632.8$ nm. The polarization of the laser was aligned parallel to the first polarizer. The beam first traveled to a piece of glass that acted as a beam splitter. One branch of the beam went to a film polarizer (used to attenuate the signal) then to a Thorlabs det 110 photovoltaic detector. The signal from the detector was sent to a Hewlett-Packard 34401A multimeter with the resolution set at "slow 6 digit" because the meter acts as a low-pass DC filter in this mode. This branch was used as a reference to monitored any changes in the intensity of the laser.

The other branch of the beam went to a 0.5 neutral density filter (in order to prevent the lock-in amplifier from overloading). The beam then went through a Glan-laser polarizer oriented at 45° to the vertical. Next, was a Hinds Instruments PEM-90 photoelastic modulator. The PEM-90 consists of a piece of quartz bonded to a piezoelectric transducer, with its optic axis oriented in the x-direction in Fig. 2.1. When driven the PEM produces an oscillating birefringence with a variable amplitude at a frequency of 50 kHz. The amplitude of the PEM birefringence was set at 2.405

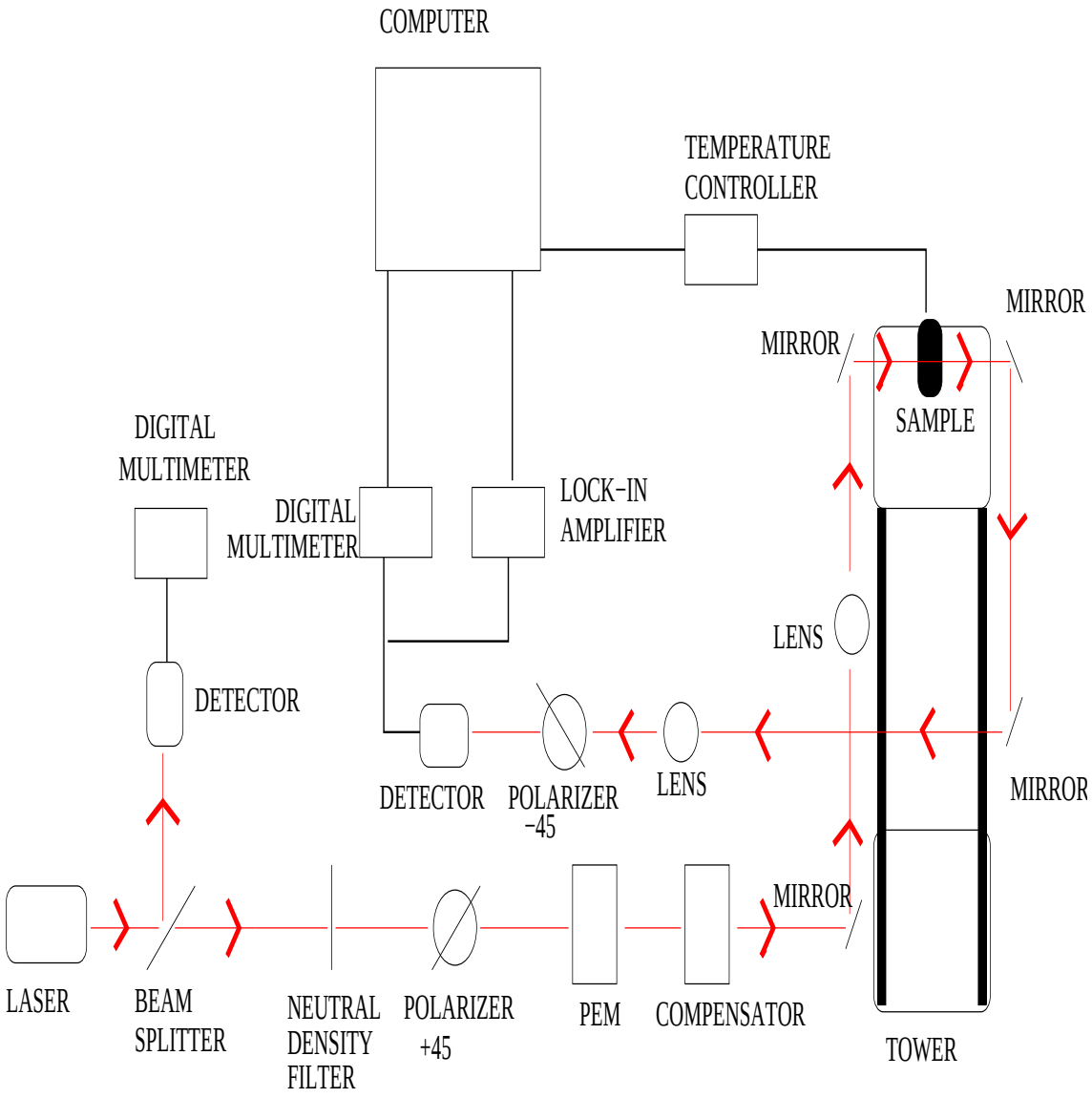

Figure 2.1: A schematic diagram of the set-up used at the NHMFL. The red lines and arrows represent the laser beam and its direction. The black lines represent connections between instrumentation. The magnet in not shown. The magnet would surround the tower starting above the two lower mirrors and would produce a field in the vertical direction in the diagram. In this figure $\hat{x}$ is in the vertical direction, $\hat{z}$ is in the horizontal direction, and $\hat{y}$ is out of the page.

radians for all MB experiments.

The amplitude setting of the PEM controller was calibrated in two different ways, using the fact that the zeroth order Bessel function is zero at 2.405 radians and at this value the V_{DC} signal should remain constant as the measured birefringence changes. First, the method outlined in the Hinds Instruments PEM-90 User manual was used. This method consisted of measuring the V_{DC} component at several different amplitude settings for different angular orientations of the second polarizer (with no sample or compensator present). V_{DC} was then plotted as a function of controller setting for each angular position of the second polarizer. The intersection of the curves should be the amplitude setting were the zeroth Bessel function is zero. This method was limited by the number of sample points taken at each angular setting, so after the general location of the zero was found another technique was used. The second polarizer was again crossed with the first polarizer and the compensator was returned to the beam path. Then the V_{DC} component was recorded for several different compensator settings at a fixed controller amplitude. This was repeated for several different controller settings close to the zero value determined by the first method. The controller setting that produced the smallest change in V_{DC} was assumed to be the setting which produced an amplitude of 2.405 radians.

After the PEM was a Special Instruments Soleil-Babinet compensator. This compensator consists of two quartz wedges, which are able to produce varying birefringence by moving one of the wedges across the other to change the path length for the light inside the quartz. The compensator was used to set the birefringence of the system to zero with the sample in the isotropic phase and no magnetic field applied. (Any birefringence in this case was due to the glass faces of the sample cell, or to the

polarizers not being exactly crossed.)

Now, the beam entered the magnet. The magnet used for this experiment was a resistive magnet, with vertical optical access, which provided fields up to 200 kG. The magnet had a circular bore with a 195.6 mm diameter. The center of the magnet was 1295.9 mm above the floor. There was access to the bore from above and below the magnet (see Fig. 2.4). The sample needed to be raised to the center of the bore to ensure that it encountered the most homogeneous field possible. This was accomplished by constructing a "tower," to support the oven that housed the sample (see Fig. 2.3), out of non-magnetic materials.

The base of the tower was aluminum, and was fixed to the breadboard. The legs were brass tubes, which were supported by nylon braces. The cross braces between the legs were made from aluminum. All screws used in the tower were brass, stainless steel, or nylon. The top plate was constructed from a glass ceramic that was an excellent thermal and electrical insulator. The oven sat on a base made of electrical grade phenolic, which was also a very good thermal and electrical insulator (see Fig. 2.5), which was fixed to the top plate by rubber bands. The oven was fixed to the base by setscrews, which allowed for the oven to be rotated in the base. The base had a sapphire ball mounted in one corner and brass screws in the other corners, which allowed the oven and base to be rotated about the y and z axes (which were set in Fig. 2.1).

The oven consisted of a rectangular $12.5 \times 12.5 \times 40$mm piece of aluminum with a 5 mm slit through the center to hold the sample. This sat in 25 mm diameter, 70 mm tall copper cylinder wrapped in two flexible Minco Kapton heaters (24.1 Ω) secured with Minco #20 thermal stretch tape. The copper cylinder was surrounded by a 45

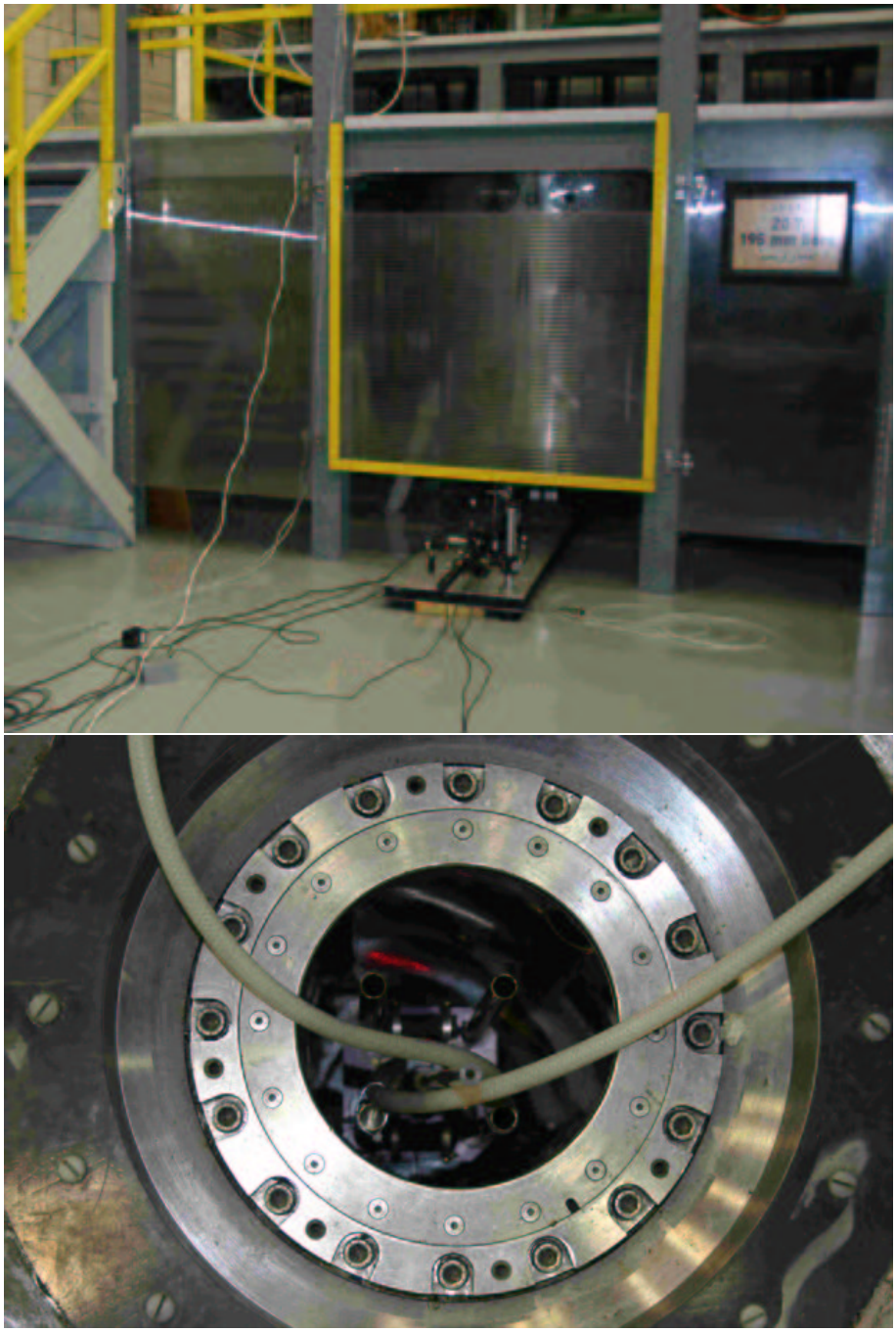

Figure 2.2: The top picture shows the magnet at NHMFL with the breadboard underneath. The bottom picture shows a view looking down from the top of the bore at the oven inside the magnet.

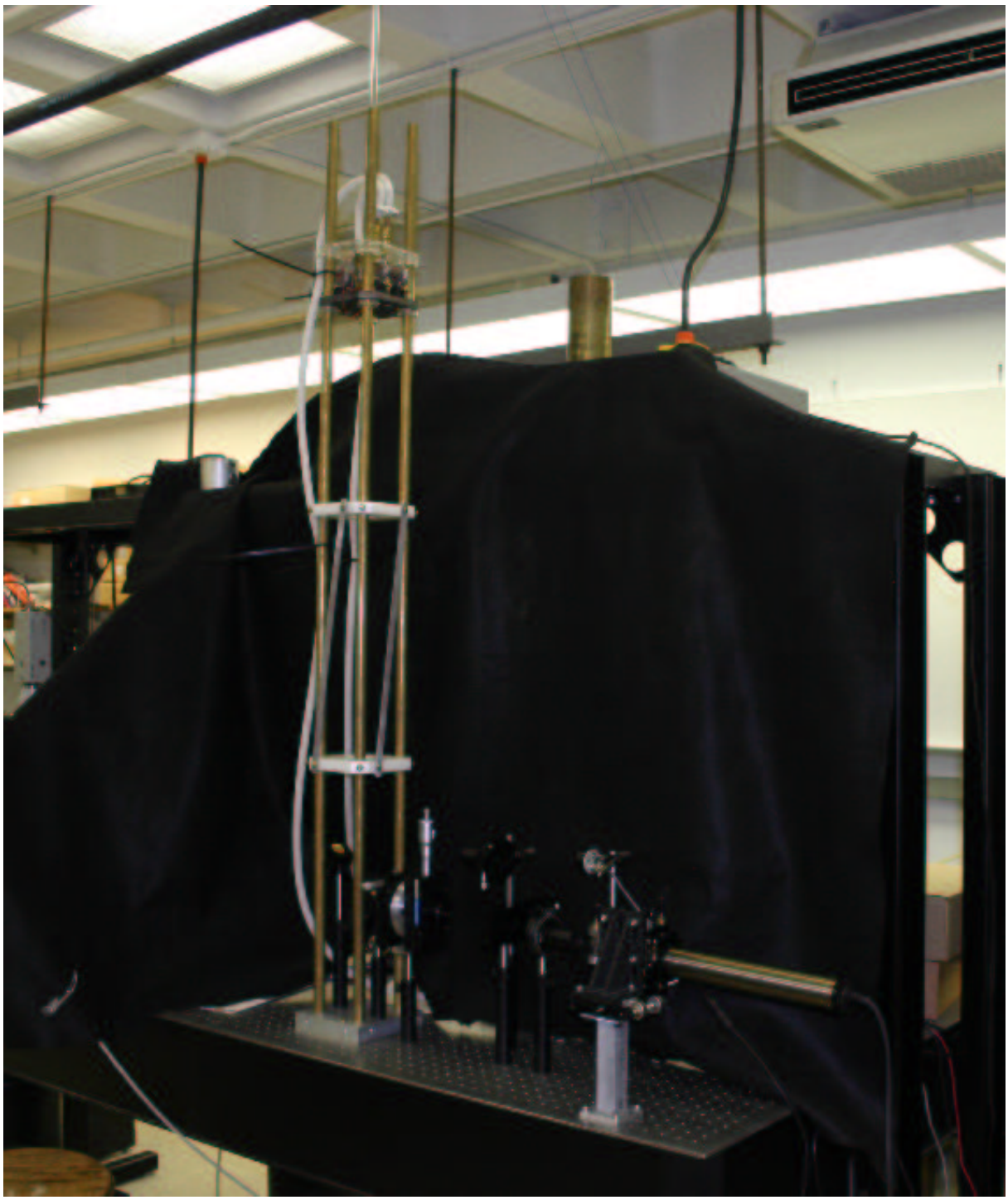

Figure 2.3: The tower used to lift the sample to the center of the NHMFL magnet.

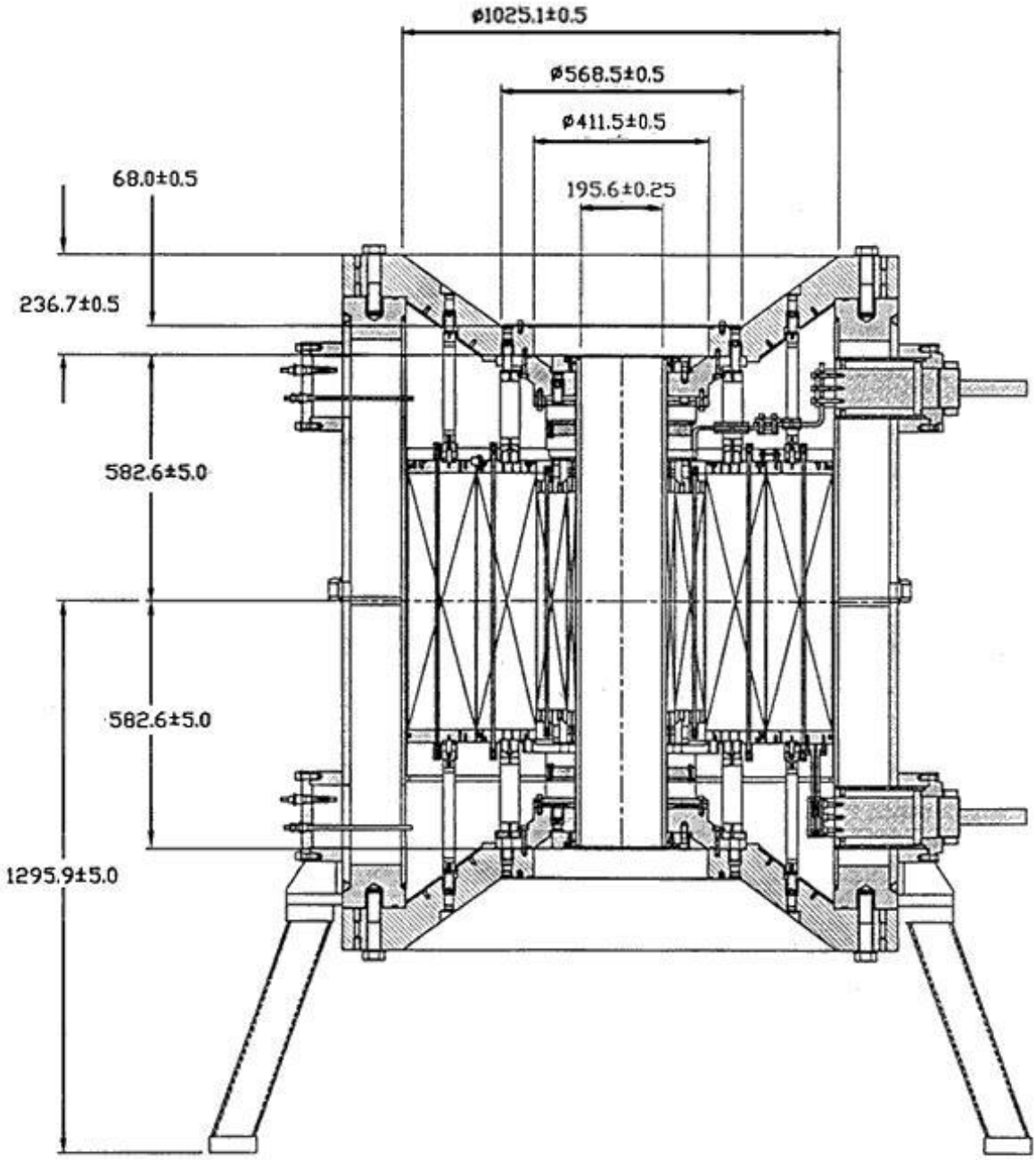

Figure 2.4: A schematic diagram of the 20 T magnet located in cell 4 at the NHMFL, which was used to make the reported MB measurements. [2]

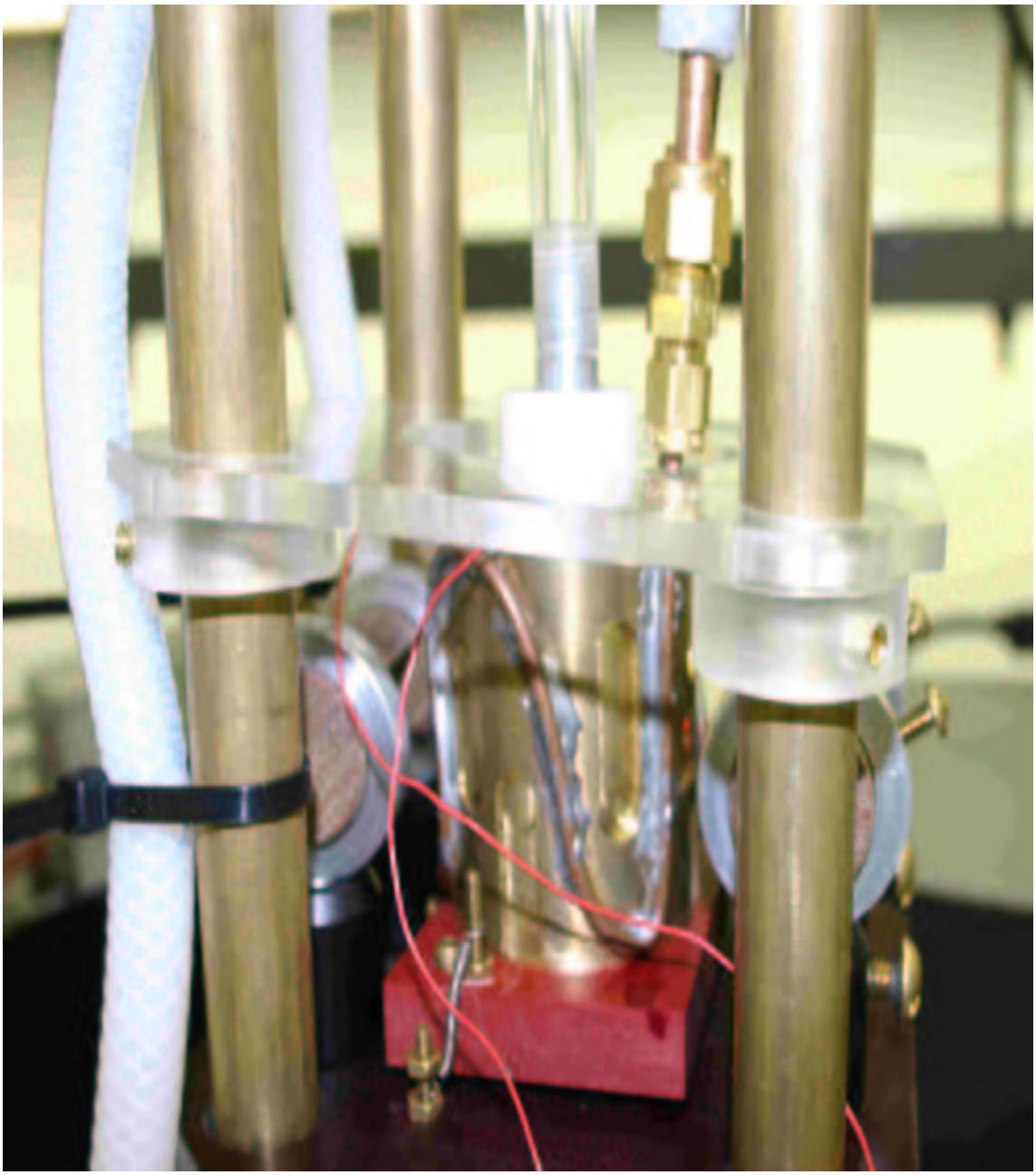

Figure 2.5: An image of the glass ceramic top plate and the oven resting on a phenolic base. The removable insert can be seen coming out of the top of the oven. The movable mirror mounts are visible to the left and right of the oven.

mm teflon cylinder, which was housed inside a 50 mm cylindrical brass water jacket. The oven had a teflon lid, which screwed into the aluminum insert. A 2 ft. long lucite rod was attached to the other side of the teflon lid, to allow the samples to be switched without removing the oven from magnet bore (see Fig. 2.6). The temperature was regulated to < 0.01°C by a Lakeshore 340 temperature controller using a Lakeshore silicon diode to monitor the temperature. (Water was not circulated through the jacket in this experiment due to time constraints at the NHMFL, which prevented us from getting the set-up aligned with the water hoses connected.)

At the base of the tower the beam hit the first mirror and went up the tower. The mirror was a 25.4 mm protected silver mirror, which was mounted on non-magnetic kinematic mount that was mounted at 45° to the vertical. About 300 mm in front of the second mirror the beam passed through a 25.4 mm plano-convex lens mounted on the leg of the tower, which focused the beam on the sample. The beam then hits the second mirror and goes through the sample. This is a 12.7 mm protected silver mirror in a custom mount that gives translational motion in the $\hat{x}$ and $\hat{y}$ and rotation about the $\hat{y}$-axis. The beam then passed through the sample and hit the third mirror, which was identical to the second mirror. This mirror directed the beam down the tower, where the beam then hit the fourth mirror, that sent the beam out of the magnet. The beam then passed through another 300 mm plano-convex lens. Finally, the beam went through a second Glan-laser polarizer, crossed with the first, and then to a Thorlabs PDA-50 photovoltaic detector. The two polarizers were set at 45° and -45° to the vertical by first setting the polarizers at 0° and 90° to the vertical and then rotating each by 45° using the scale on the rotation stage. (The polarizers were set at 0° and 90° by changing the polarization until the situation was reached that

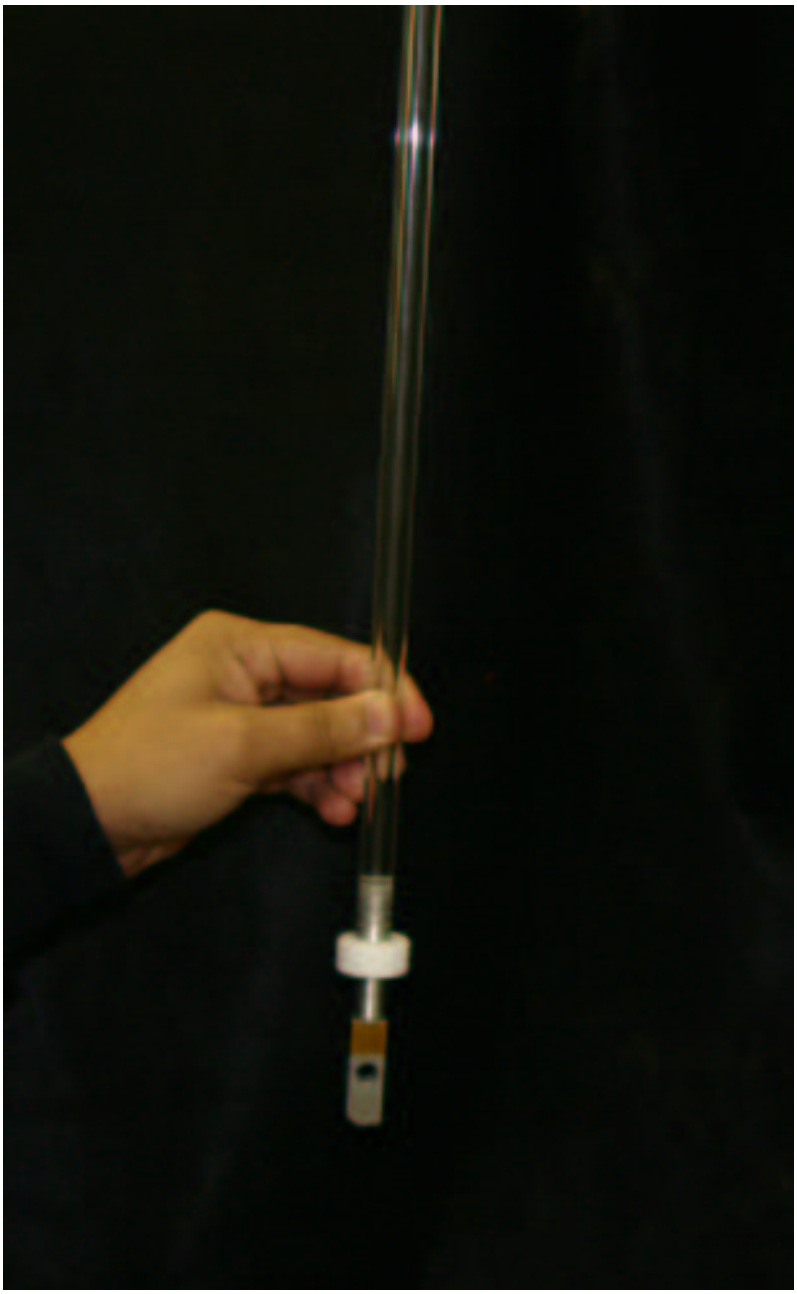

Figure 2.6: The aluminum insert with attached lucite rod and teflon lid. This insert was easily removed from the oven, while inside the magnet, which allowed for easy switching of samples.

the second polarizer could be turned backwards with respect to the first and still be crossed. This only occurs when the polarizers are parallel and perpendicular to the ground.) The signal from the detector went to a Stanford Research Systems SR 830 lock-in amplifier and another 34401A multimeter. This multimeter was configured in the same manner as the multimeter used for the reference signal. The lock-in had a time constant set to 300 ms and a sensitivity of 1 V. The reference for the lock-in was provided by the PEM.

2.1.2 KSU SET-UP

The set-up at KSU consisted of the same basic components as the NHMFL set-up described in the previous section. The main difference between the two was the type of magnet used in the experiment. The magnet at KSU was a 13.5 kG split coil electromagnet with 7 cm of separation between the pole faces. This magnet allowed horizontal optical access, and thus alleviated the need for the tower and mirrors used at the NHMFL.

At KSU the MB experiment was set-up on a triangular optical rail which ran between the pole faces of the electromagnet. The rail was supported by an aluminum frame that rested on Newport low profile isolators. Here a polarized 4.5 mW intensity stabilized Spectra Physics laser at $\lambda = 632.8$ nm, with the polarization fixed in the direction of the initial polarizer, was used. The intensity stabilization allowed the experiment to be run without a reference signal. The next component was a Glan-Thompson polarizer set at 45° to the vertical. Then there was a Hinds Instruments PEM-90 photoelastic modulator set at 2.405 radians (it was calibrated in the same manner as mentioned above). Next, was a Special Instruments Soleil-Babinet compensator, which was used to zero the birefringence in the isotropic phase.

After the compensator was a 25.4 mm plano-convex lens, with a 300 mm focal length, which focused the laser beam on the sample. The sample was housed in the same oven used at the NHMFL. This time water was circulated through the water jacket by a Neslab RTE-111 circulator, at a temperature about 20°C below the temperature region being investigated. With the water circulating the temperature inside the oven was regulated to < 0.003°C by means of Conductus LTC-10 temperature controller using a platinum RTD to monitor the temperature.

A second Glan-Thompson polarizer at -45° followed sample. This was followed by a second lens, identical to the first lens, which focused the beam on the face of a Thorlabs PDA-55 photovoltaic detector with a lens tube attached (the gain was set at zero). The signal from the detector was connected to a Hewlett-Packard 34401A digital multimeter and a Stanford Research Systems SR830 lock-in amplifier. The multimeter was configured in the same manner as the ones used at the NHMFL. The lock-in amplifier had its time constant set to 100 ms and its sensitivity to 200 mV.

2.1.3 THEORY GOVERNING THE MB EXPERIMENT

The MB experiment is designed to measure small birefringence values through the use of photoelastic optical phase modulation and lock-in detection. This is done by monitoring changes in polarization of the laser beam in the set-up described above. The situation can best be understood in terms of normalized Jones matrices. Consider the situation shown in Fig. 2.1 with $\hat{x}$ set in the direction of the magnetic field, $\hat{z}$ the initial direction of propagation, and $\hat{y}$ perpendicular to $\hat{x}$ and $\hat{z}$.

The initial beam is polarized at the laser at an angle of 45° to the vertical (in the

x-y plane), which can be described by

$$\vec{E_1} = \frac{1}{\sqrt{2}} \begin{pmatrix} 1 \\ 1 \end{pmatrix}. \tag{2.1}$$

The polarization of the light wave is unchanged by the first polarizer

$$\vec{E_2} = \frac{1}{2\sqrt{2}} \begin{pmatrix} 1 & 1 \\ 1 & 1 \end{pmatrix} \begin{pmatrix} 1 \\ 1 \end{pmatrix} = \frac{1}{\sqrt{2}} \begin{pmatrix} 1 \\ 1 \end{pmatrix}. \tag{2.2}$$

The function of the modulator is to introduce a phase difference ϕ between the $\vec{x}$ and $\vec{y}$ components of the light wave, where

$$\phi = A_0 \sin \omega t \tag{2.3}$$

with A_0 describing the amplitude of the phase difference. After passing through the modulator the polarization of the light is

$$\vec{E_3} = \frac{1}{\sqrt{2}} \begin{pmatrix} 1 & 0 \\ 0 & e^{i\phi} \end{pmatrix} \begin{pmatrix} 1 \\ 1 \end{pmatrix} = \frac{1}{\sqrt{2}} \begin{pmatrix} 1 \\ e^{i\phi} \end{pmatrix}. \tag{2.4}$$

Next, the light encounters two mirrors, each at an incident angle of 45°. Each mirror retards the component of the light in the reflection plane, i.e. the $\vec{x}$ part of the light, by a factor of π with respect to the $\vec{y}$ part of the signal

$$\vec{E_4} = \frac{1}{\sqrt{2}} \begin{pmatrix} e^{i\pi} & 0 \\ 0 & 1 \end{pmatrix} \begin{pmatrix} e^{i\pi} & 0 \\ 0 & 1 \end{pmatrix} \begin{pmatrix} 1 \\ e^{i\phi} \end{pmatrix} = \frac{1}{\sqrt{2}} \begin{pmatrix} e^{i2\pi} \\ e^{i\phi} \end{pmatrix} = \frac{1}{\sqrt{2}} \begin{pmatrix} 1 \\ e^{i\phi} \end{pmatrix}, \tag{2.5}$$

where $e^{i2\pi} = 1$. Then the light passes through the sample, which is oriented so that the faces of its cell are perpendicular to the incoming beam. This introduces another phase shift between the ordinary and extraordinary axes of the sample. This phase shift will be referred to as β

$$\beta = k\Delta n d, \tag{2.6}$$

where $k = 2\pi/\lambda$ is the wave vector, $\Delta n = n_e - n_o$ (the sample induced birefringence), and d is the optical path length of the sample. So following the sample the polarization of the light is

$$\vec{E_5} = \frac{1}{\sqrt{2}} \begin{pmatrix} 1 & 0 \\ 0 & e^{i\beta} \end{pmatrix} \begin{pmatrix} 1 \\ e^{i\phi} \end{pmatrix} = \frac{1}{\sqrt{2}} \begin{pmatrix} 1 \\ e^{i(\phi+\beta)} \end{pmatrix}. \tag{2.7}$$

The signal will now pass another set of mirrors at 45°, which will each introduce a π phase shift. Again, this will give a total phase shift of 2π, which will not change the polarization of the signal. Finally, after the second polarizer, which is set at $-45°$ to the x-axis, the polarization is

$$\vec{E_6} = \frac{1}{2\sqrt{2}} \begin{pmatrix} 1 & -1 \\ -1 & 1 \end{pmatrix} \begin{pmatrix} 1 \\ e^{i(\phi+\beta)} \end{pmatrix} = \frac{1}{2\sqrt{2}} \begin{pmatrix} 1 - e^{i(\phi+\beta)} \\ e^{i(\phi+\beta)} - 1 \end{pmatrix}. \tag{2.8}$$

The transmitted intensity is then given by

$$|E_7|^2 = \frac{1}{2}(1 - \cos\phi\cos\beta + \sin\beta\sin\phi) \tag{2.9}$$

The $\cos\phi$ and $\sin\phi$ terms can be expanded as series of Bessel functions

$$\cos(A_0 sin\omega t) = J_0(A_0) + 2\sum_{k=1}^{\infty} J_{2k}(A_0)\cos 2k\omega t \tag{2.10}$$

$$\sin(A_0 sin\omega t) = 2\sum_{k=0}^{\infty} J_{2k+1}(A_0)\sin(2k+1)\omega t. \tag{2.11}$$

Equations 2.10 and 2.11 can be substituted into Eq. 2.9 to give

$$|E_8|^2 = \frac{1}{2} - \cos\beta J_0(A_0) + J_1(A_0)\sin\beta\sin\omega t + J_2(A_0)\cos\beta\cos 2\omega t + \cdots \tag{2.12}$$

The transmitted intensity in this form can be used to calculate the birefringence of the sample. If A_0 is chosen such that $J_0(A_0) = 0$ (which occurs when $A_0 = 2.405$ radians) then the transmitted DC component is

$$V_{DC} = K/2, \tag{2.13}$$

where K is a proportionality constant due to any amplification of the signal at the detector and the signal transmitted at the frequency ω is

$$V_{1f} = KJ_1(A_0)\sin\beta, \tag{2.14}$$

where V_{1f} is in peak-peak voltage. V_{1f} can be divided by V_{DC} to eliminate the proportionality constant, and then one can solve for β

$$\beta = k\Delta nd = \sin^{-1}\frac{V_{1f(RMS)}}{\sqrt{2}V_{DC}J_1(A_0)} \tag{2.15}$$

where Δn is the magnetic field induced birefringence, $k = 2\pi/\lambda$ is the wavevector of the probing laser, d is the path length, and V_{1f} was divided by $\sqrt{2}$ to give RMS voltage. The magnetic field induced birefringence Δn is the term that will be used in the following discussions. It is determined by dividing the experimentally calculated β by kd.

2.1.4 SAMPLE PREPARATION

The MB measurements were made on two bent-core liquid crystals. The first being 4-chloro-1,3-phenylenebis[4-(4-9-decenyloxy) benzoyloxy benzoate] (ClPbis10BB) and the second 4-chlororesorcinol bis[4-(4-n-dodecyloxybenzoyloxy)benzoate] (ClPbis10BBs), which is structurally identical to ClPbis10BB except for two additional hydrogen in its terminal methyl group (see Fig. 2.7). However, even though the two molecules are structurally similar they have very different phase transition temperatures and phase sequences. The ClPbis10BB sample used for the KSU measurements was synthesized in Hungary, while the ClPbis10BB and ClPbis10BBs used for the NHMFL measurements were made by J. Kim at the Liquid Crystal Institute, Kent State University. Both materials exhibit monotropic LC phases, so they must be heated to melt the crystal and then cooled to observe the LC phases.

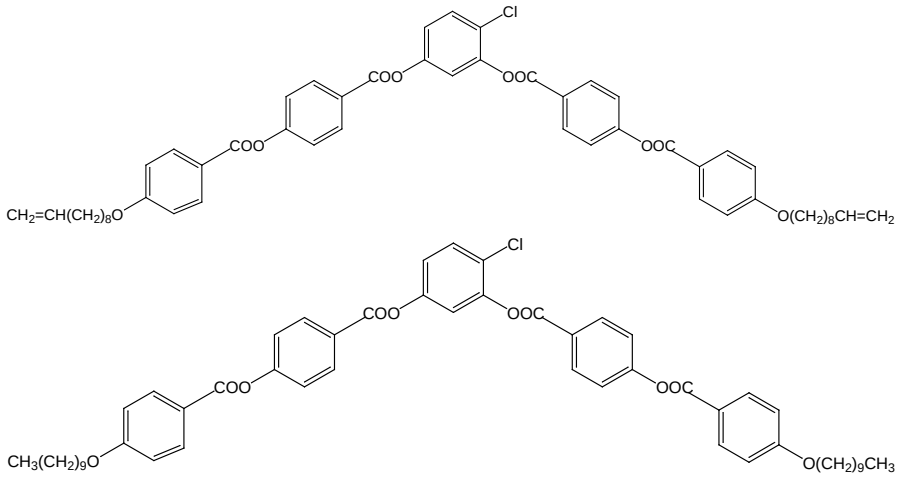

Figure 2.7: (top)Schematic chemical structure of 4-chloro-1,3-phenylene bis4-[4'-(9-decenyloxy)benzoyloxy]benzoate (ClPbis10BB). (bottom) Schematic chemical structure of 4-chlororesorcinol bis[4-(4-n-dodecyloxybenzoyloxy)benzoate](ClPbis10BBs).

The samples were housed in rectangular borosilicate tubes with nominal inner dimensions of 2 × 4 mm. The tubes were purchased from Friedrich and Dimmock, Inc. in 12 in. lengths. First, one end of the tube was sealed over a flame then the tube was scored and broke off ∼2 cm above the sealed end. This was repeated for the length of the tube. After the glass was cut, the individual pieces were soaked in a isopropanol bath for twelve hours, then flushed with deionized water ten times, and finally baked at 200°C for 2 hours at dry them.

The tubes were loaded by placing the sample, in its crystal state, into a sealed piece of glass. The glass was then placed in a cylindrical phenolic block, which was cut to fit into a Will Scientific centrifuge (with a matching block used to balance the weight). The block, with sample, was heated to ∼5°C above the clearing point of the sample then placed in the centrifuge set at level 5 (about 1800 rpms) for ∼30 s. This was done to pull the sample to the bottom of the cell so that a minimum amount of liquid crystal would be used. This step was repeated, with sample being added as

needed, until the column of sample was ∼5 mm tall (this would completely cover the opening in the oven).

After the cell was filled to an appropriate level with sample the liquid crystal was allowed to crystallize. The cell was then placed in a vice grip with the long side of the cell horizontal to the ground. The open end of the cell was covered with a two-part epoxy using the tip of a syringe. The cell was then turned and the epoxy was allowed to cure with the open end of the cell facing the ground, so that no epoxy mixed with the sample. (Several different manufactures of two-part epoxy were used with equal success.) This process was performed in a laminar flow work station to prevent contamination of the samples.

2.2 THE TRANSITION AT THE CLEARING POINT

The transition at the clearing point was probed at KSU at temperatures near the clearing point using a constant 13.5 kG magnetic field. The MB measurements were made by heating ClPbis10BB to melt the crystal, then cooling to several degrees below the clearing point, then heating to $\sim$ 3 above the clearing point and then cooling. At temperatures below the clearing point the sample became very turbid, with no coherent beam passing through the sample. This increase in turbidity was used to measure the clearing point as $T_{CL} = 75.43 \pm 0.02$°C. The temperature was then decreased in 0.05-0.2°C intervals with a 12 minute pause after each change to allow the temperature to equilibrate. At each temperature 200 values of V_{DC} and V_{1f} were recorded with the magnetic field at zero and with the field at 13.5 kG. This process was automated using GPIB interfaces between the components and software written in the Yorick programming language for a Linux operating system (see Appendix A). The average of these readings were used to calculate Δn for zero field and for

the higher field. The Δn values at zero were generally very small compared to the high field values, but not insignificant at higher temperatures. They were caused by inability to tune the compensator to exactly cancel out any residual birefringence. The Δn values at zero were subtracted from the high field Δn to get the final Δn for a temperature. The standard deviation of the averages of V_{DC} and V_{1f} were used to establish uncertainty in the measurements.

MB results in liquid crystals are generally reported in terms of the inverse Cotton-Mouton coefficient as a function of temperature, with the Cotton-Mouton coefficient defined as

$$CM = \Delta n/H^2, \tag{2.16}$$

and the inverse Cotton-Mouton coefficient as

$$CM^{-1} = 1/CM = H^2/\Delta n, \tag{2.17}$$

where H^2 is the applied magnetic field and Δn is the field induced birefringence. The MB results for ClPbis10BB are shown in Fig. 2.8. The clearing point is $T_{CL} = 75.43 \pm 0.02$°C.

2.2.1 DISCUSSION OF RESULTS

The phase below the clearing point in ClPbis10BB was previously shown to possess uniaxial nematic ordering [3]. Therefore, one may attempt to understand these results using the Landau-de Gennes mean field model, which has been shown to well describe MB at the N-I transition in uniaxial calamitic LCs.

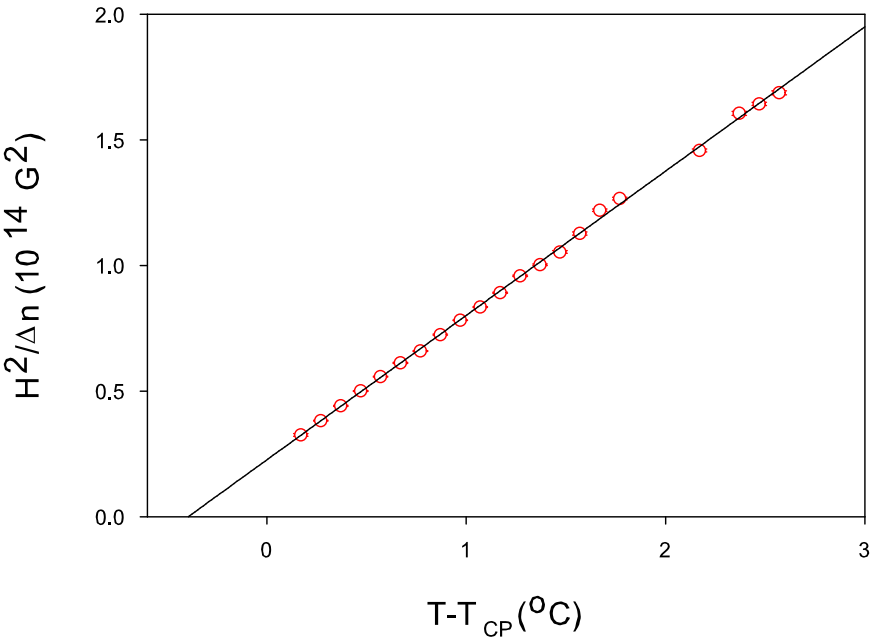

Figure 2.8: CM^{-1} as a function of temperature for ClPbis10BB on cooling from above the clearing point ($T_{CP} = 75.43 \pm 0.02$°C), measured at KSU. The straight line represents a linear fit to the data. The error bars are about the same size as the data symbols in this figure.

LANDAU-DE GENNES MEAN FIELD MODEL

The order of a uniaxial nematic LC may be specified by the symmetric, traceless tensor

$$Q_{ij} = \frac{1}{2}S(3n_i n_j - \delta_{ij}) \tag{2.18}$$

where $n_{i,j}$ are components of the director and the scalar order parameter, S, is given by

$$S = \frac{1}{2} < 3cos^2\theta - 1 > \tag{2.19}$$

with θ being the angle between the molecular long axis and the director. The rotational invariance if the system allows for the anisotropies of the molecules to be defined as a scalar multiple of Q_{ij}. Therefore the magnetic susceptibility and the dielectric constant tensors may be written as

$$\chi_{ij} = \bar{\chi}\delta_{ij} + \frac{2\Delta\chi}{3}Q_{ij} \tag{2.20}$$

and

$$\epsilon_{ij} = \bar{\epsilon}\delta_{ij} + \frac{2\Delta\epsilon}{3}Q_{ij} \tag{2.21}$$

respectively. Here, $\Delta\chi$ and $\Delta\epsilon$ are the anisotropies in χ_{ij} and ϵ_{ij} for a fully ordered system, i.e. a system where all the molecules are completely aligned with the director or $S = 1$. $\bar{\chi} = \frac{1}{3}(2\chi_\perp + \chi_\parallel)$ and $\bar{\epsilon} = \frac{1}{3}(2\epsilon_\perp + \epsilon_\parallel)$ are the average magnetic susceptibility and dielectric constant, or the values of these parameters in the I phase.

In the LdG model the free energy per unit volume in the vicinity of the phase transition in a magnetic field can be expanded in a power series in the order parameter [4]

$$F = F_0(\rho, T) + \frac{A}{2}Q_{ij}Q_{ji} - \frac{B}{3}Q_{ij}Q_{jk}Q_{ki} + \frac{C}{4}(Q_{ij}Q_{ji})^2 - \frac{1}{2}\chi_{ij}H_iH_j + \cdots \tag{2.22}$$

where F_0 is the free energy density of the isotropic phase, $A = a(T - T^*_{NI})$, and H is the applied magnetic field. Here, T^*_{NI} represents the supercooling limit, or the virtual second order transition temperature, for the N-I transition.

Summing over the indices in Eq. 2.22 allows us to rewrite the equation in terms of the scalar order parameter, S,

$$F = F_0(\rho, T) + \frac{3A}{4}S^2 - \frac{B}{4}S^3 + \frac{9C}{16}S^4 - \frac{\bar{\chi}}{2} + \frac{\Delta\chi}{3}H^2S + \cdots. \tag{2.23}$$

Minimizing Eq. 2.23 with respect to S and keeping only the lowest order terms gives

$$\frac{\partial F}{\partial S} = \frac{3}{2}AS - \frac{1}{3}\Delta\chi H^2 = 0. \tag{2.24}$$

Only the lowest order terms in S need to be considered because any pretransitional ordering above the N-I transition in the isotropic phase will be very small, and will yield a small S value ($\ll 1$), that will be negligible at higher orders of S .

Then solving for S and putting it into Eq. 2.18 for Q_{ij} gives

$$Q_{ij} = \frac{\Delta\chi}{9A}(3H_iH_j - H^2\delta_{ij}). \tag{2.25}$$

If H is defined to be in the $\hat{z}$ direction the field induced birefringence can be calculated by inserting Eq. 2.25 into Eq. 2.21 and expanding the square root of the resulting equation in a Taylor series, retaining only up to the quadratic terms.

$$\Delta n = \sqrt{\epsilon_{zz}} - \sqrt{\epsilon_{xx}} = \frac{\Delta\epsilon\Delta\chi H^2}{9a\sqrt{\bar{\epsilon}}(T - T^*_{NI})}, \tag{2.26}$$

where Δn is the magnetic field induced birefringence. Equation 2.26 can be rearranged to describe the Cotton-Mouton coefficient as a function of temperature,

$$CM = \frac{\Delta n}{H^2} = \frac{\Delta\epsilon\Delta\chi}{9a\sqrt{\bar{\epsilon}}(T - T^*_{NI})}. \tag{2.27}$$

Material	$T_{NI} - T^*_{NI}$(°C)	$a(erg/cm^3K)$
MBBA	1.0 [5–7]	6×10^5 [6]
5CB	1.4 - 2.55 [8, 9]	1.3×10^6 [10]
6CB	1.1 - 32.12 [8, 9, 11, 12]	1.5×10^6 [10]
7CB	1.3 - 1.58 [8, 9, 11]	2.1×10^6 [10]
8CB	1.0 - 3.30 [8, 9, 11]	1.8×10^6 [10]
9CB	1.5 [8]	2.6×10^6 [13]
3OCB	1.45 [14]	-
5OCB	1.82 [9]	-
6OCB	2.12 [9]	-
7OCB	3.8 [9]	-
8OCB	0.65 [9]	-
9OCB	2.13 [9]	-
PCH-5	1.2 -1.5 [15–17]	-
PCH-6	2.6 [15]	-
PCH-7	1.8 [15]	-
PCH-8	2.8 [15]	-
PCH-9	1.7 [15]	-

Table 2.1: Virtual second order transition temperatures and leading Landau coefficients for several common calamitic LCs.

The predictions of the LdG theory have been well borne out in uniaxial calamitic liquid crystals. Figure 2.9 represents a typical plot of the inverse Cotton-Mouton coefficient as a function of temperature for the common calamitic compound p-methoxy benzylidene p-n-butylanilene (MBBA). The measurement was made using the KSU set-up. In this case, the sample was housed in a rectangular glass cuvette with a 10 mm path length. The clearing point was found to be 36.2±0.1°C by observing an abrupt increase in Δn at this point. This plot clearly shows that $CM^{-1} \propto T - T^*_{NI}$ for at least 10°C above the clearing point and that $T_{NI} - T^*_{NI} \approx 1.0$°C. Table 2.1 provides examples of the values for parameters that come about in the LdG model for several common calamitic compounds.

The values for the LdG parameters, described above, can be calculated for ClP-bis10BB using the MB data from the KSU measurements. $T_{CL} - T^*_{CL} = 0.38 \pm 0.02$°C

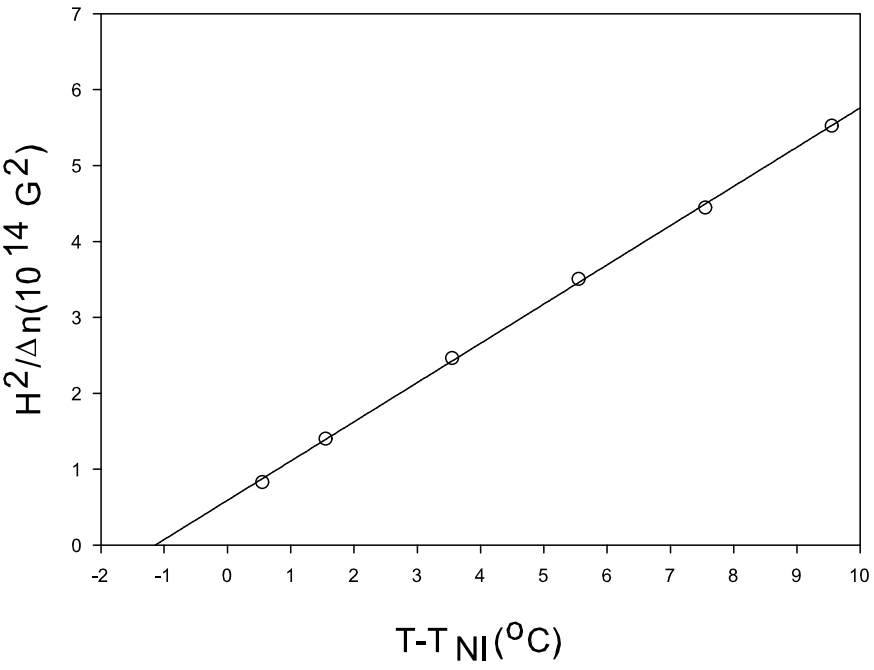

Figure 2.9: CM^{-1} as a function of temperature for MBBA on cooling from above the clearing point, $T_{NI} = 36.2 \pm 0.1°C$. The straight line represents a linear fit to the data. The error bars are about the same size as the data symbols in this figure.

for ClPbis10BB. Independent measurements of the magnetic and dielectric anisotropy (these measurements are described in Chap. 5) can be used to estimate the saturated values for χ_a and ϵ_a, which can then be used to calculate the leading Landau coefficient a. It was mentioned in the introduction that the scalar order parameter S is $\sim$0.4 at the N-I transition in uniaxial calamitic LCs. A reasonable guess is that $S \sim$0.4 just below the clearing point in ClPbis10BB. Then, using this theory one can take measurements of χ_a and ϵ_a near the clearing point and assume that $S \sim$0.4 at this point. Since the anisotropies are proportional to the order parameter they may be multiplied by 2.5 to give values for anisotropies when S=1. This method gives estimated saturated values of χ_a and ϵ_a

$$\Delta\chi = 3.0 \pm 0.6 \times 10^{-8} (cgs) \tag{2.28}$$

and

$$\Delta\epsilon = 0.40 \pm 0.08. \tag{2.29}$$

Using these values and the isotropic part of the dielectric tensor, which was measured by Jakli [18] as

$$\sqrt{\bar{\epsilon}} = 1.56 \pm 0.01, \tag{2.30}$$

the leading Landau coefficient can be determined from the slope of Fig. 2.8 using Eq. 2.27. The slope of the plot in Fig. 2.8 is $a\sqrt{\bar{\epsilon}}/\Delta\epsilon\Delta\chi = 5.746 \pm 0.006 \times 10^{13}$ erg-cm$^{-3\circ}$C^{-1}. Solving for a yields $a = 5 \pm 1 \times 10^4$ erg cm$^{-3\circ}$C^{-1}.

The values of a and $T_{CL} - T^*_{CL}$ calculated for ClPbis10BB using the LdG model for calamitics are both significantly lower than the values for the N-I transition in common calamitic liquid crystals shown Table 2.1. These results show that the transition at the clearing point in ClPbis10BB at low magnetic fields can be qualitatively

understood using the LdG model for calamitics, but significant differences in the experimental parameters entering the LdG model, exist between calamitics and ClP-bis10BB. These results provided motivation to repeat the MB experiment at higher fields, which would increase the signal strength, allowing access to higher temperatures, and would allow for Δn to be measured as a function of magnetic field at a given temperature.

2.3 ISOTROPIC-ISOTROPIC TRANSITION

The MB measurements were repeated at the NHMFL using the set-up described earlier, using fields up to 180 kG. Here, the induced birefringence was measured as a function of temperature and magnetic field for ClPbis10BB and ClPbis10BBs. ClPbis10BB was heated until it melted, then was cooled to several degrees below the clearing point (again the clearing point was found by an increase in turbidity, $T_{CL} = 76.9° \pm 0.1$C), then heated to 96°C. ClPbis10BB was then cooled in 0.5-2.5°C intervals. After each step the temperature was given 5 min. to equilibrate, then the magnetic field was increased in 10 kG intervals from 10 kG to 150 kG in 10 s time steps (it took $\sim$ 7 s for the field to increase by 10 kG) with the reference signal, V_{DC}, and V_{1f} being recorded at each point. The field was then ramped back down to 10 kG at a rate of 180 kG / min.. This process was fully automated using GPIB interfacing and software written in Labview. Once the sample was cooled below the clearing point in this manner, the process was repeated on heating. Here the temperature was increased in 0.5-1°C intervals up to 96°C.

The measurements were made on ClPbis10BBs in the same manner as described above. The material was initially heated until the crystal melted, then cooled below the clearing point ($T_{CL} = 90.2° \pm 0.1$C), then heated to 135°C. From this point it

was cooled in 0.5-3°C intervals through the clearing point with the reference signal, V_{DC}, and V_{1f} being recorded at each point. The magnetic field was ramped up in the same manner as above, but here the initial field was set to 30 kG and the final field was 180 kG. The process was then repeated on heating. For each sample the compensator was used to set the birefringence as close to zero as possible with the sample in the isotropic phase and no field applied. This value was not reset at each individual temperature because any small changes in the birefringence of the glass tube holding the sample with temperature were insignificant compared to the changes induced by the magnet field at each temperature.

The large birefringence changes produced by the high magnetic fields produced a response in the lock-in amplifier that was not present in the KSU experiment. This response must be discussed to understand how to interpret the raw data collected at the NHMFL. Equation 2.15 shows that Δn is a function of arcsine, which has an argument that cannot exceed one. As the magnetic field is increased the V_{1f} signal will increase with a fixed V_{DC} until the argument of the arcsine equals one. At this point the V_{1f} signal will decrease back to zero, this process will repeat itself as Δn increases. When analyzing the results one must be careful to account for this behavior, which I will call the "roll-over" of the V_{1f} signal. This can be corrected in the following manner: the value of Δn should be set equal to $\pi/2kd$ at the first maximum that V_{1f} reaches. Then from this point until V_{1f} reaches zero again, Δn can be found by adding (π/kd) - (Δn found using V_{1f} measured by the lock-in) to $\pi/2kd$. Then from zero to the next maximum, (π/kd) is added to the (Δn found using the V_{1f} measured by-the lock-in). This method is then repeated for each cycle of V_{1f}.

The induced birefringence for both samples was plotted as a function of the square of magnetic field for different temperatures on heating and cooling between the nematic phase and the isotropic phase. Figures 2.10 and 2.11 are representative sets of data for ClPbis10BB and ClPbis10BBs, respectively (the plots for all temperatures can be seen in Appendix B). These plots show all the qualitative features observed as the temperature was changed. The typical uncertainty for Δn in these measurements was on the order of $\pm 5 \times 10^{-7}$. The uncertainty was determined by recording 500 values for V_{1f} and V_{DC} at a fixed temperature and field, and then finding the standard deviation for each of these sets. The uncertainties in V_{1f} and V_{DC} were used to establish an uncertainty for Δn. (The plots of Δn vs. H^2 do not always go through the (0,0) point due to changes in the zero-field birefringence with temperature, mentioned above. These changes do not affect the slope, or shape of the plot, and thus are not considered in the following explanations.)

2.3.1 DISCUSSION OF RESULTS

The LdG model for the N-I transition in calamitic liquid crystals predicts a proportional relation between H^2 and Δn. At temperatures well above the clearing point both materials seem to exhibit this behavior, but at temperatures near the clearing point the rate at which Δn changes with respect to field, significantly decreases with increasing field, in both materials. Thus, both ClPbis10BB and ClPbis10BBs show a marked deviation from LdG behavior in this temperature region.

The unusual LdG values produced when trying to explain the transition at the clearing point by the LdG model for calamitics and the behavior of $\Delta n(H)$ show that the behavior of the bent-core materials is fundamentally different from that of the calamitics. Furthermore, the behavior of ClPbis10BB and ClPbis10BBs cannot be

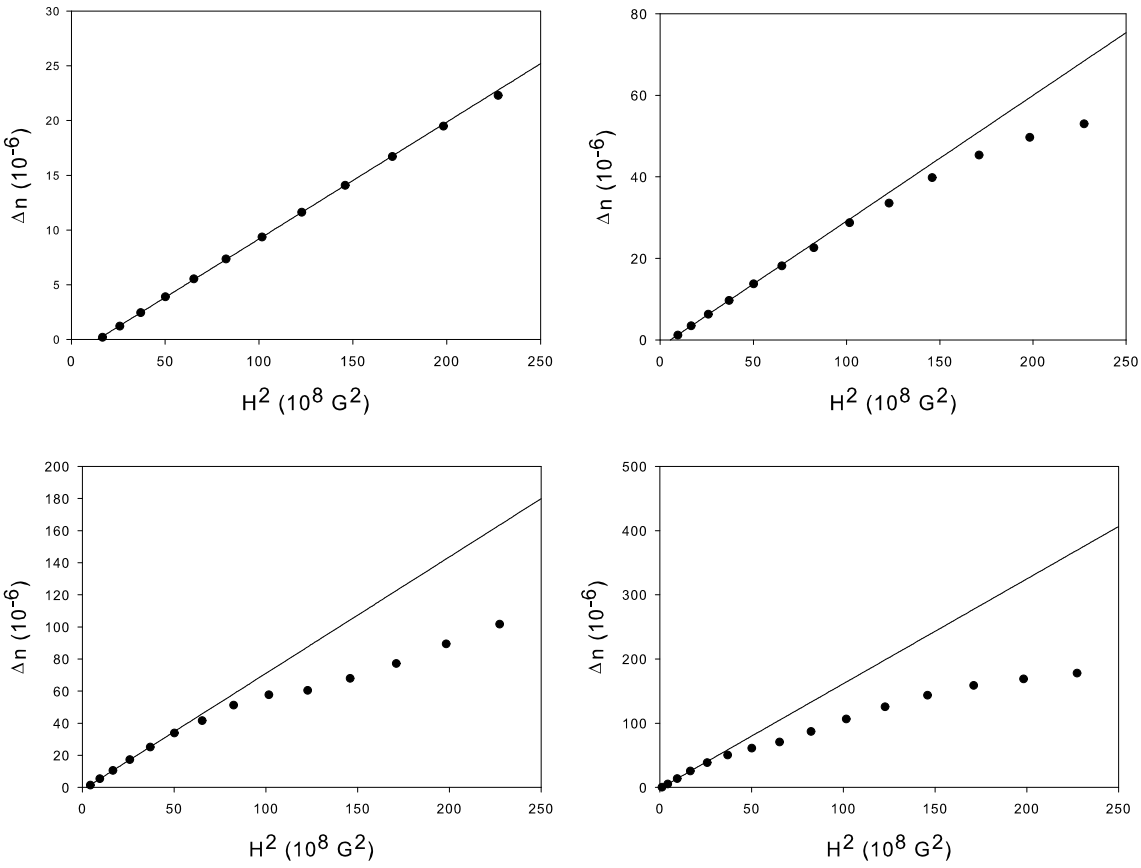

Figure 2.10: Induced birefringence as a function of the square of the magnetic field for ClPbis10BB on cooling from the isotropic. The clearing point on cooling was 76.9°C. The straight line is a linear fit to the low field data points. Clockwise from upper left: $T - T_{CP} = 18.1$, 6.1, 2.1, and 0.6°C.

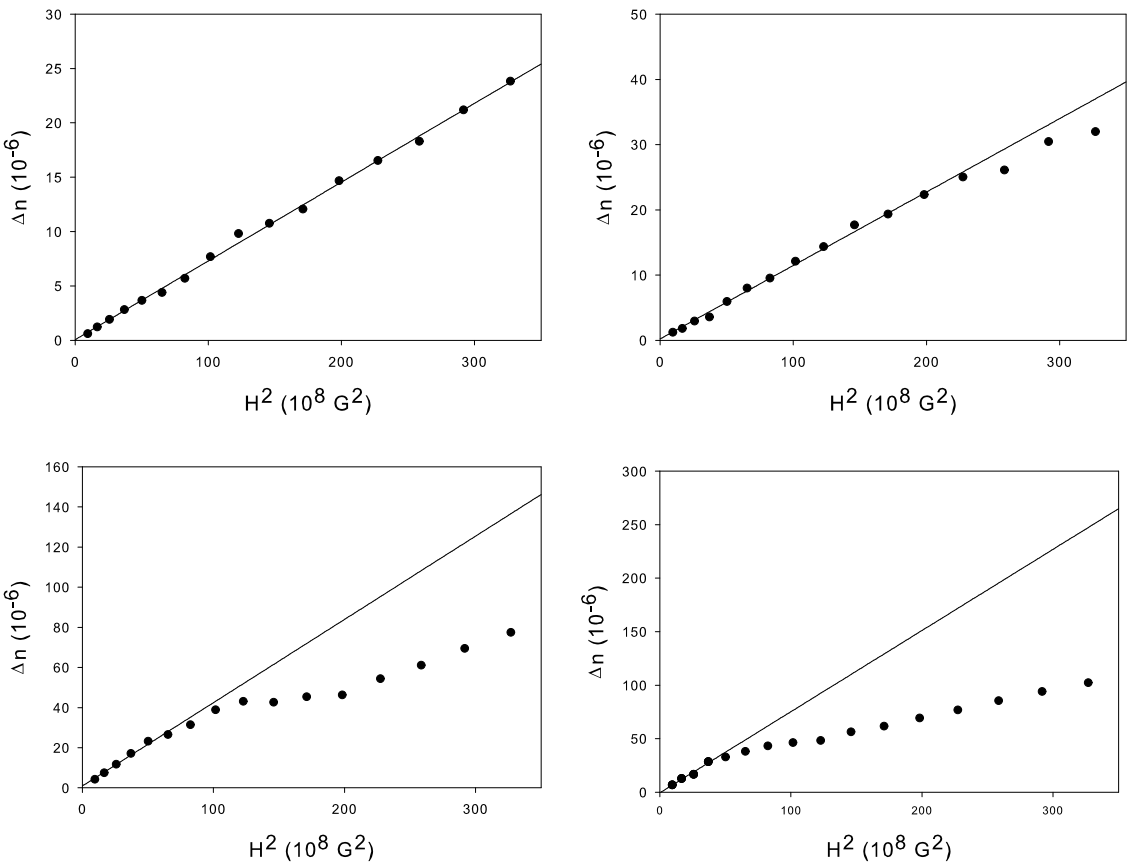

Figure 2.11: Induced birefringence as a function of the square of the magnetic field for ClPbis10BBs on cooling from the isotropic. The clearing point on cooling was 90.2°C. The straight line is a linear fit to the low field data points. Clockwise from upper left: $T - T_{CP} = 14.8$, 8.8, 1.3, and 0.8°C.

explained by any theory developed to explain the N-I transition in calamitics. The standard LdG model, the LdG model including higher order terms in S and H, the LdG model with nematic fluctuations included [19], and a saturation model developed from molecular Maier-Saupe theory [20–22] fail to explain the experimental results (see Appendix C for explanation of these models). However, the behavior of the these bent-core materials can be completely qualitatively explained by assuming that a optically isotropic state, that consists of "complexes" or "clusters" of molecules, exists between a clustered nematic and neat isotropic phase.

The tetrahedratic T phase, predicted by Lubensky *et al.* [1], is the only theoretically predicted optically isotropic phase in which the mesogenic units are clusters of molecules. (The symbol T will be used to denote both temperature and the tetrahedratic phase. However, the surrounding text should make the meaning of the symbol clear.) As mentioned in the introduction, the T phase consists of clusters of locally ordered molecules that as groups (mesogenic units) possess tetrahedral T_d symmetry (see Fig. 2.13). The order of the phase can be described by a third-rank traceless symmetric tensor order parameter T_{ijk}. The T phase appears on cooling from the isotropic phase, and on cooling from the T phase Lubensky *et al.* [1] show that there is only one symmetry reducing transition, T-N_T, that leads to a phase that exhibits uniaxial nematic type behavior. The N_T phase consists of clusters of molecules (tetrahedrons) that are uniaxially distorted along one axis (see Fig. 2.13), which induces nematic ordering in the system. (Above I used the phrase "uniaxial nematic type behavior" as the N_T phase is technically neither uniaxial or biaxial as it possesses tetrahedral order in the plane transverse to the distorted axis.)

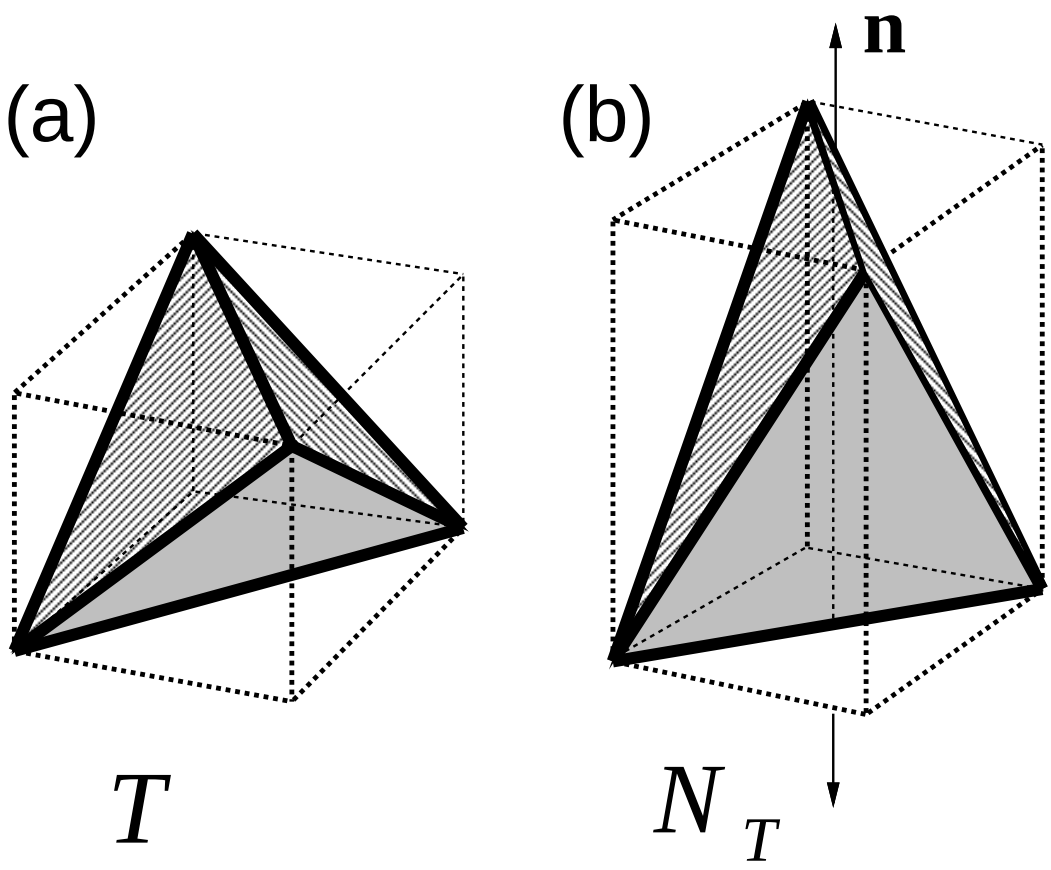

Figure 2.12: (a) In the T phase the mesogenic units can be viewed as tetrahedral complexes with bent-core molecules decorating the axes of the randomly distributed tetrahedrons, such that all three axes of the cube are equivalent. (b) In the N_T phase the tetrahedrons are uniaxially distorted along one axis of the cube inducing S order. The tetrahedron is distorted along the n direction in this figure [1].

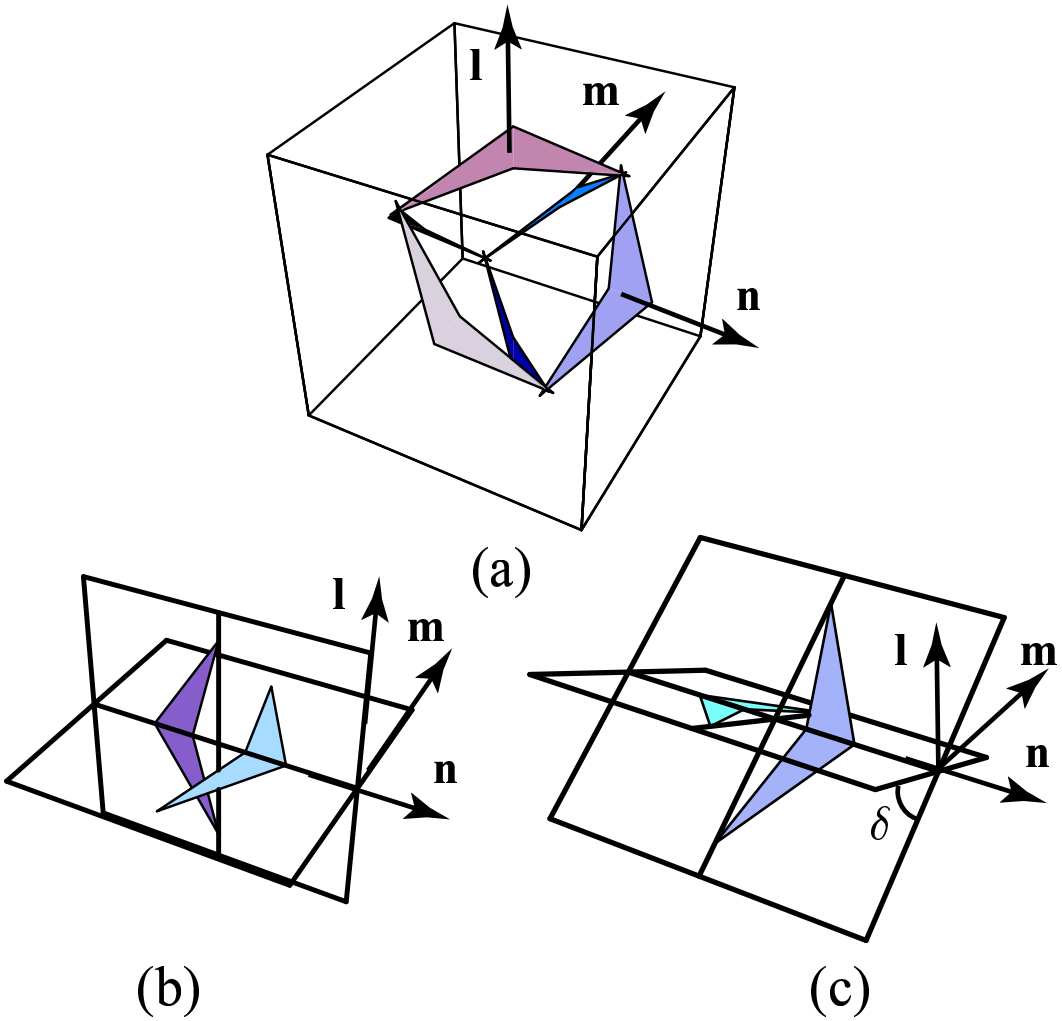

Figure 2.13: (a) A schematic representation of the T, (b) the N_T phase, and (c) the $(N_T{+}2)^*$ using bent-core molecules. The N_T phase is formed by a uniaxial distortion along one axis, which favors one pair of crossed molecules [shown in (b)]. The $(N_T{+}2)^*$ phase is formed by creating a uniaxial distortion along one axis and then rotating the planes containing the two crossed bent-core molecules [1].

The presence of a tetrahedratic phase dictates that the phase found at temperatures below the clearing point is actually the N_T phase, and that a T-I transition occurs at a temperature above that of the N_T-T transition (the clearing point). So, the phase sequence that we are dealing with is I-T-N_T on cooling from the I phase. The inclusion of the T_{ijk} term in a LdG mean field model for the bent-core liquid crystals explains their unique behavior in a magnetic field. The birefringence in the T and I phases is described by induced nematic ordering in those phases, not by T ordering, as this induces optical isotropy.

MB IN THE T PHASE

The beginning point is to write the free energy in the T phase as a power series of irreducible tensor relations. In the T phase the tetrahedratic order parameter is non-zero, which forces a fourth order term in the tetrahedratic order parameter to appear in order to stabilize T order. Also, in the T phase the nematic order parameter is zero in the absence of orienting fields, so only lowest order terms in Q_{ij} were kept in the free energy, as the induced nematic order parameter is expected to be small in the T (see Appendix C for argument).

$$F_T = \frac{1}{2}A_Q Q_{ij}Q_{ij} + \frac{1}{2}A_T T_{ijk}T_{ijk} + u_T(T_{ijk}T_{ijk})^2 - w_1 Q_{ij}T_{ikl}T_{jkl} \qquad (2.31)$$
$$-\frac{\chi_{ij}}{2}H_iH_j - w_2 H_iH_jQ_{kl}T_{ikm}T_{jlm} - w_3 H_iH_jT_{ikl}T_{jkl},$$

where $A_Q = a_Q(T - T_Q^*)$, $A_T = a_T(T - T_T^*)$, and $\chi_{ij} = \bar{\chi}\delta ij + (2\Delta\chi/3)Q_{ij}$ [$\Delta\chi$ is the saturated magnetic susceptibility anisotropy in the N_T phase and $\bar{\chi} = 1/3(2\chi_\perp + \chi_\parallel)$]. The u and w terms are coupling constants, the T_Q^* and T_T^* represent the supercooling limits for the N_T-T and T-I transitions, respectively.

In Ref. [1] the tensor order parameters were derived from mass moments fixed

relative to a coordinate system oriented on the body of each molecule, these tensors can be described relative to a space fixed coordinate system, such that

$$Q^{ij}(\mathbf{x},\mathbf{y},\mathbf{z}) = \sum_{\alpha} Q^{\alpha} J_{\alpha}^{ij}(\mathbf{m},\mathbf{l},\mathbf{n}) \tag{2.32}$$

$$T^{ijk}(\mathbf{x},\mathbf{y},\mathbf{z}) = \sum_{\alpha} T^{\alpha} I_{\alpha}^{ijk}(\mathbf{m},\mathbf{l},\mathbf{n}) \tag{2.33}$$

where

$$\begin{aligned} J_1^{ij} &= \sqrt{3/2}(n^i n^j - \frac{1}{3}\delta^{ij}), \\ J_2^{ij} &= \sqrt{1/2}(m^i m^j - l^i l^j), \\ J_3^{ij} &= \sqrt{1/2}(n^i m^j + m^i n^j), \\ J_4^{ij} &= \sqrt{1/2}(n^i l^j + l^i n^j), \\ J_5^{ij} &= \sqrt{1/2}(m^i l^j + l^i m^j), \end{aligned} \tag{2.34}$$

and

$$\begin{aligned} I_1^{ijk} &= \sqrt{5/2}[n^i n^j n^k - \frac{1}{5}(\delta^{ij} n^k + \delta^{jk} n^i + \delta^{ki} n^j)], \\ I_2^{ijk} &= \frac{1}{2}(m^i m^j m^k - m^i l^j l^k - m^j l^k l^i - m^k l^i l^j), \\ I_3^{ijk} &= \frac{1}{2}(l^i l^j l^k - l^i m^j m^k - l^j m^k m^i - l^k m^i m^j), \\ I_4^{ijk} &= \sqrt{5/2}[m^i n^j n^k + m^j n^k n^i + m^k n^i n^j - \frac{1}{5}(m^i \delta^{jk} + m^j \delta^{ik} + m^k \delta^{ij})], \\ I_5^{ijk} &= \sqrt{5/2}[l^i n^j n^k + l^j n^k n^i + l^k n^i n^j - \frac{1}{5}(l^i \delta^{jk} + l^j \delta^{ik} + l^k \delta^{ij})], \\ I_6^{ijk} &= \frac{1}{\sqrt{6}}[n^i (m^j m^k - l^j l^k) + n^j (m^i m^k - l^i l^k) + n^k (m^i m^j - l^i l^j)], \\ I_7^{ijk} &= \frac{1}{\sqrt{6}}(n^i m^j l^k + n^i l^j m^k + m^i l^j n^k + m^i n^j l^k + l^i n^j m^k + l^i m^j n^k) \end{aligned} \tag{2.35}$$

with **m,l,n** being a space-fixed orthonormal basis where $\mathbf{m} \times \mathbf{l} = \mathbf{n}$. These tensors are normalized such that

$$\sum_{ij} J_{\alpha}^{ij} J_{\alpha'}^{ij} = \delta_{\alpha,\alpha'}, \tag{2.36}$$

and

$$\sum_{ijk} I_{\alpha}^{ijk} I_{\alpha'}^{ijk} = \delta_{\alpha,\alpha'}. \tag{2.37}$$

The orientation of the **m,l,n**-axes can be chosen so that the N_T phase is described by development of the Q^1 order parameter and the tetrahedratic order in the T and N_T phases can be described by T^7 ordering. Equation 2.31 can then be written in terms of scalar order parameters from Eqs. 2.32 and 2.33. Note, the terms that have a H-T coupling are only non-zero when H is non-zero. For these terms the order parameters were summed over an arbitrary direction of H, and the indices were left with H to show that these terms are only non-zero in the direction of H. To simplify the algebra the constants derived from summing over the terms in Eq. 2.31 will be absorbed into the previous coefficients, which will now be denoted with primes (all primed terms will retain the same sign as the original terms, except for the HQT coupling in which the prime term changes sign). Also, to be consistent with the previous sections the nematic scalar order parameter will be denoted by S instead of Q, while the tetrahedratic scalar order parameter will be denoted by T

$$\begin{aligned} F_T = \frac{1}{2}A'_Q S^2 + \frac{1}{2}A'_T T^2 + u'_T T^4 - w'_1 S T^2 - \frac{\bar{\chi}}{2}H^2 \\ -\frac{1}{3}\Delta\chi S H^2 + w'_2 H^2 S T^2 - w'_3 H^2 T^2. \end{aligned} \tag{2.38}$$

Minimizing F_T with respect to S yields

$$\frac{\partial F_T}{\partial S} = A'_Q S - w'_1 T^2 - \frac{1}{3}\Delta\chi H^2 + w'_2 H^2 T^2 = 0 \tag{2.39}$$

then

$$S = \frac{\frac{1}{3}\Delta\chi H^2 + w'_1 T^2 - w'_2 H^2 T^2}{A'_Q}. \tag{2.40}$$

Minimizing F_T with respect to T gives

$$\frac{\partial F_T}{\partial T} = A'_T T + 4u'_T T^3 - 2w'_1 ST + 2w'_2 H^2 ST - 2w'_3 H^2 T = 0 \tag{2.41}$$

then

$$T^2 = \frac{2w'_1 S - 2w'_2 H^2 S + 2w'_3 H^2 - A'_T}{4u'_T}. \tag{2.42}$$

Substituting Eq. 2.42 into Eq. 2.40 and solving for S gives,

$$S = \frac{\frac{4}{3}u'_T \Delta\chi H^2 + 2w'_1 w'_3 H^2 - 2w'_2 w'_3 H^4 + w'_2 A'_T H^2 - w'_1 A'_T}{4A'_Q u'_T + 4w'_1 w'_2 H^2 - 2w'^2_2 H^4 - 2w'^2_1}. \tag{2.43}$$

Figure 2.8 shows that $CM^{-1} \propto H^2$ at low fields at temperatures near the clearing point. This suggests that higher order coupling constants, which would cause deviations from linearity in the above relation, are small compared to terms proportional to A'_Q. Now, it is reasonable to assume that the $4A'_Q u'_T$ term is large compared to the $(4w'_1 w'_2 H^2 - 2w'^2_2 H^4 - 2w'^2_1)$ term, so we can express S as a power series in H

$$\begin{aligned} S = (&-4w'_1 u'_T A'_Q A'_T - 2w'^3_1 A'_T + \frac{16}{3}u'^2_T \Delta\chi A'_Q H^2 + 8w'_1 w'_3 u'_T A'_Q H^2 \\ &+4w'_2 u'_T A'_Q A'_T H^2 + \frac{8}{3}w'^2_1 u'_T \Delta\chi H^2 + 6w'^2_1 w'_2 A'_T H^2 + 4w'^3_1 w'_3 H^2 \\ &-8w'_2 w'_3 u'_T A'_Q H^4 - 10w'^2_1 w'_2 w'_3 H^4 - 6w'_1 w'^2_2 A'_T H^4 - \frac{16}{3}w'_1 w'_2 u'_T \Delta\chi H^4 \\ &+12w'_1 w'^2_2 w'_3 H^6 + \frac{8}{3}w'^2_2 u'_T \Delta\chi H^6 + 2w'^3_2 A'_T H^6 - 4w'^3_2 w'_3 H^8) \times (4u'_T A'_Q)^{-2}. \end{aligned} \tag{2.44}$$

Equation 2.45 has two terms that are not dependent on H. These terms represent nematic ordering in the T phase induced by coupling between the nematic and tetrahedratic order parameters (the $w'_1 ST^2$ term in Eq. 2.32). Nematic ordering in the T phase would be manifested by a "smearing out" of the $N_T - T$ transition and residual birefringence at temperatures above the clearing point with no fields present. Optical microscopy between crossed polarizers, dynamic light scattering measurements [3],

and MB measurements indicates that the $N_T - T$ transition is sharp, with no evidence of nematic ordering in the T phase. Therefore, the w_1' coupling term must be very small, and terms containing w_1' may be excluded from this calculation.

Now, we may put Eq. 2.45 into Eq. 2.32 to get a value for Q_{ij} at minimum S

$$\begin{aligned} Q_{ij} = \sqrt{\frac{3}{2}}[\frac{16}{3}u_T'^2\Delta\chi A_Q'(H_iH_j - \frac{1}{3}H^2) + 4w_2'u_T'A_Q'A_T'(H_iH_j - \frac{1}{3}H^2) \\ -8w_2'w_3'u_T'A_Q'H^2(H_iH_j - \frac{1}{3}H^2) + \frac{8}{3}w_2'^2u_T'\Delta\chi H^4(H_iH_j - \frac{1}{3}H^2) \\ +2w_2'^3A_T'H^4(H_iH_j - \frac{1}{3}H^2) - 4w_2'^3w_3'H^6(H_iH_j - \frac{1}{3}H^2)] \times (4u_T'A_Q')^{-2}. \end{aligned} \tag{2.45}$$

Then using

$$\epsilon_{ij} = \bar{\epsilon}\delta ij + (2\Delta\epsilon/3)Q_{ij}, \tag{2.46}$$

where $\Delta\epsilon$ is the saturated dielectric anisotropy in the N_T phase and $\bar{\epsilon} = 1/3(2\epsilon_\perp + \epsilon_\parallel)$, we can solve for the birefringence using the same techniques used with the LdG model for calamitics . With H set in the $\hat{z}$-direction the birefringence is

$$\begin{aligned} \Delta n = \sqrt{\epsilon_{zz}} - \sqrt{\epsilon_{xx}} = \\ \frac{\Delta\epsilon}{\sqrt{6\bar{\epsilon}}}(\frac{16}{3}u_T'^2\Delta\chi A_Q'H^2 + 4w_2'u_T'A_Q'A_T'H^2 - 8w_2'w_3'u_T'A_Q'H^4 \\ +\frac{8}{3}w_2'^2u_T'\Delta\chi H^6 + 2w_2'^3A_T'H^6 - 4w_2'^3w_3'H^8) \times (4u_T'A_Q')^{-2}. \end{aligned} \tag{2.47}$$

Δn may be expressed as a power series in H such that

$$\Delta n = (CM)H^2 + (CM_2)H^4 + (CM_3)H^6 + (CM_4)H^8 \cdots, \tag{2.48}$$

where

$$\begin{aligned} CM &= \frac{\Delta\epsilon}{\sqrt{6\bar{\epsilon}}}\left(\frac{\frac{16}{3}u_T'^2\Delta\chi A_Q' + 4w_2'u_T'A_Q'A_T'}{(4u_T'A_Q')^2}\right) \\ &= \frac{\Delta\epsilon}{\sqrt{6\bar{\epsilon}}}\left(\frac{\frac{1}{3}u_T'\Delta\chi + \frac{1}{4}w_2'a_T'(T - T_T^*)}{u_T'a_Q'(T - T_Q^*)}\right), \end{aligned} \tag{2.49}$$

$$CM_2 = \frac{\Delta\epsilon}{2\sqrt{6\bar{\epsilon}}}\left(\frac{-w_2' w_3'}{u_T' A_Q'}\right), \tag{2.50}$$

$$CM_3 = \frac{\Delta\epsilon}{8\sqrt{6\bar{\epsilon}}}\left(\frac{\frac{4}{3}w_2'^2 u_T' \Delta\chi + w_2'^3 A_T'}{(u_T' A_Q')^2}\right), \tag{2.51}$$

and

$$CM_4 = \frac{\Delta\epsilon}{4\sqrt{6\bar{\epsilon}}}\left(\frac{-w_2'^3 w_3'}{(u_T' A_Q')^2}\right). \tag{2.52}$$

MB IN THE I PHASE

In the I phase both T and S are expected to be zero, so only lowest order terms in each were kept. Then the free energy in the I phase may be expressed in terms of scalar order parameters as

$$\begin{aligned} F_I = F_0 + \frac{1}{2}A_Q' S^2 + \frac{1}{2}A_T' T^2 - w_1' S T^2 - \frac{\bar{\chi}}{2}H^2 \\ -\frac{1}{3}\Delta\chi S H^2 + w_2' H^2 S T^2 - w_3' H^2 T^2, \end{aligned} \tag{2.53}$$

where F_0 is the free energy in the I phase and all other variables were defined in the previous section.

Minimizing F_I with respect to S gives

$$\frac{\partial F_I}{\partial S} = A_Q' S - w_1' T^2 - \frac{1}{3}\Delta\chi H^2 + w_2' H^2 T^2 = 0, \tag{2.54}$$

then

$$S = \frac{\frac{1}{3}\Delta\chi H^2 + w_1' T^2 - w_2' H^2 T^2}{A_Q'}. \tag{2.55}$$

Minimizing F_I with respect to T gives

$$\frac{\partial F_I}{\partial T} = A_T' T - 2w_1' S T + 2w_2' H^2 S T - 2w_3' H^2 T = 0, \tag{2.56}$$

which gives

$$T = 0. \tag{2.57}$$

Then S reduces to the simple solution similar to that seen in calamitics

$$S = \frac{\frac{1}{3}\Delta\chi H^2}{A'_Q}. \tag{2.58}$$

Solving for Δn in the same manner as above gives

$$\Delta n = \sqrt{\epsilon_{zz}} - \sqrt{\epsilon_{xx}} = \frac{\Delta\epsilon}{\sqrt{6\bar{\epsilon}}}\left(\frac{\Delta\chi H^2}{A'_Q}\right). \tag{2.59}$$

The plots in Appendix B show that Δn becomes relatively proportional to H^2 at temperatures greater than $\sim 10^\circ$ above the clearing point in ClPbis10BB and ClPbis10BBs. The lower temperature plots of $\Delta n(H)$ ($T - T_{CP} < 10$°C) could be well fit with Eq. 2.48, while the higher temperature plots ($T - T_{CP} > 10$°C) was well fit by Eq. 2.59. A representative set of data with fits is shown in Fig. 2.14. For temperatures near the clearing point Eq. 2.48, up to eighth order in H, was fit to the experimental data. The CM coefficient was experimentally fixed using the $\Delta n(H)$ data shown in Appendix B. To do this, a straight line was fit to the low field regions at each temperature, where $\Delta n \propto H^2$. The slope of the straight line gave CM for each temperature. CM_2, CM_3, and CM_4 were then allowed to vary as adjustable parameters. At higher temperatures, Eq. 2.59 was fit to the data with one adjustable parameter. These fits show that LdG theory including T ordering can model the experimentally observed behavior. The use of the experimental values for CM is a consistency check, which helps to validate this model. However, the higher order CM coefficients are quite complicated and are not completely independent of each other, so any values determined from the fit parameters are essentially meaningless.

The LdG model developed above for bent-core LCs shows that CM^{-1} should have two different temperature dependent regions. This can best be seen by dividing the CM^{-1} coefficients by $T - T_Q^*$. In this case, Eq. 2.59 shows that the high temperature

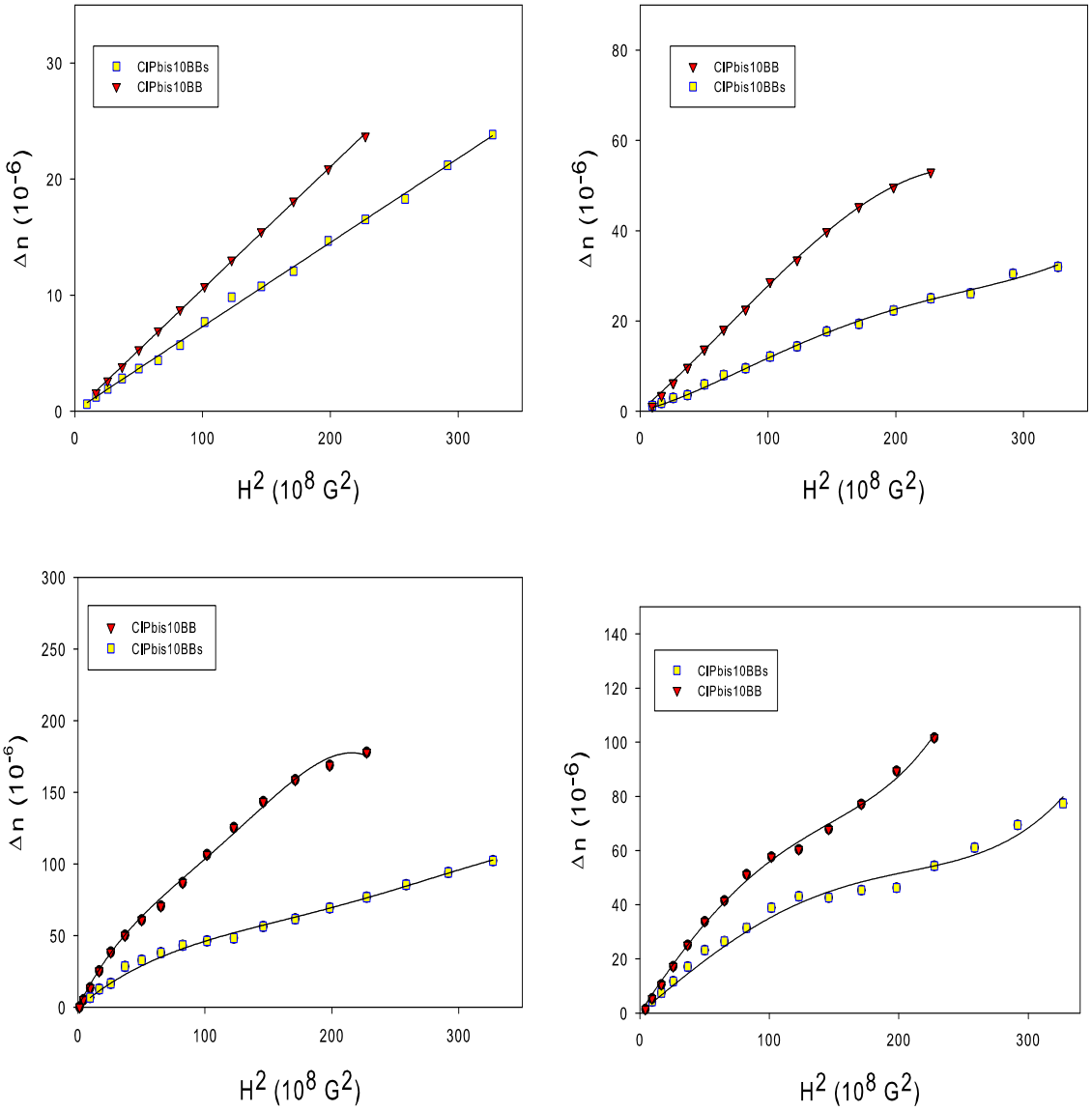

Figure 2.14: Representative plots of Δn as a function of H^2 on cooling from the isotropic phase. ClPbis10BB is denoted by the red triangles. Clockwise from the upper left ClPbis10BB is plotted at 18.1, 6.1, 2.1, and 0.6°C above its clearing point (76.9°C), respectively. ClPbis10BBs is denoted by the yellow squares. Clockwise from the upper left ClPbis10BBs is plotted at 14.8, 8.8, 1.3, and 0.8°C above its clearing point (90.2°C), respectively. The solid lines are fits of Eq. 2.48 or Eq. 2.59 to the data.

data (in the I phase) should be constant in CM^{-1} as the temperature changes. While the low temperature data (in the T phase) has a slighty more complicated temperature dependence, found from Eq. 2.48. Indeed, this is what is seen in Figs. 2.15 and 2.16, in which $CM^{-1}/T - T_Q^*$ was plotted as a function of temperature. At high temperatures CM^{-1} is constant, while at low temperatures the data was well fit with Eq. 2.48 in the form $CM^{-1} = (A + B[T - T_T^*])^{-1}$, where A, B, and T_T^* were allowed to vary. For ClPbis10BB, T_T^* was determined to be $\sim$ 80°C, or about 3.5°C above the clearing point, by a least square fit. For ClPbis10BBs, T_T^* was determined to be $\sim$ 92.3°C, or about 2°C above the clearing point, by a least square fit.

One can use Eq. 2.48 and Eq. 2.59 to find the temperature that the curves in Figs. 2.15 and 2.16 should intersect, which is

$$T_{intersect} = T_T^* + \frac{8u_T'\Delta\chi}{3a_T'w_2'}. \tag{2.60}$$

This equation has to many unknown parameters to yield any useful information, but it helps to clearly show that the intersection of the fits in Figs. 2.15 and 2.16 is not the transition temperature, as one might think.

In conclusion, we have observed that Δn for ClPbis10BB and ClPbis10BBs does not obey the standard H^2 dependence in the T phase and that CM^{-1} does not follow the temperature dependence predicted by LdG theory for calamitics in the T phase. However, I have shown that both of these things may be understood if the LdG theory takes into account tetrahedratic order and the presence of a T-I transition. Thoughts and ideas concerning future work are discussed in chapter 6.

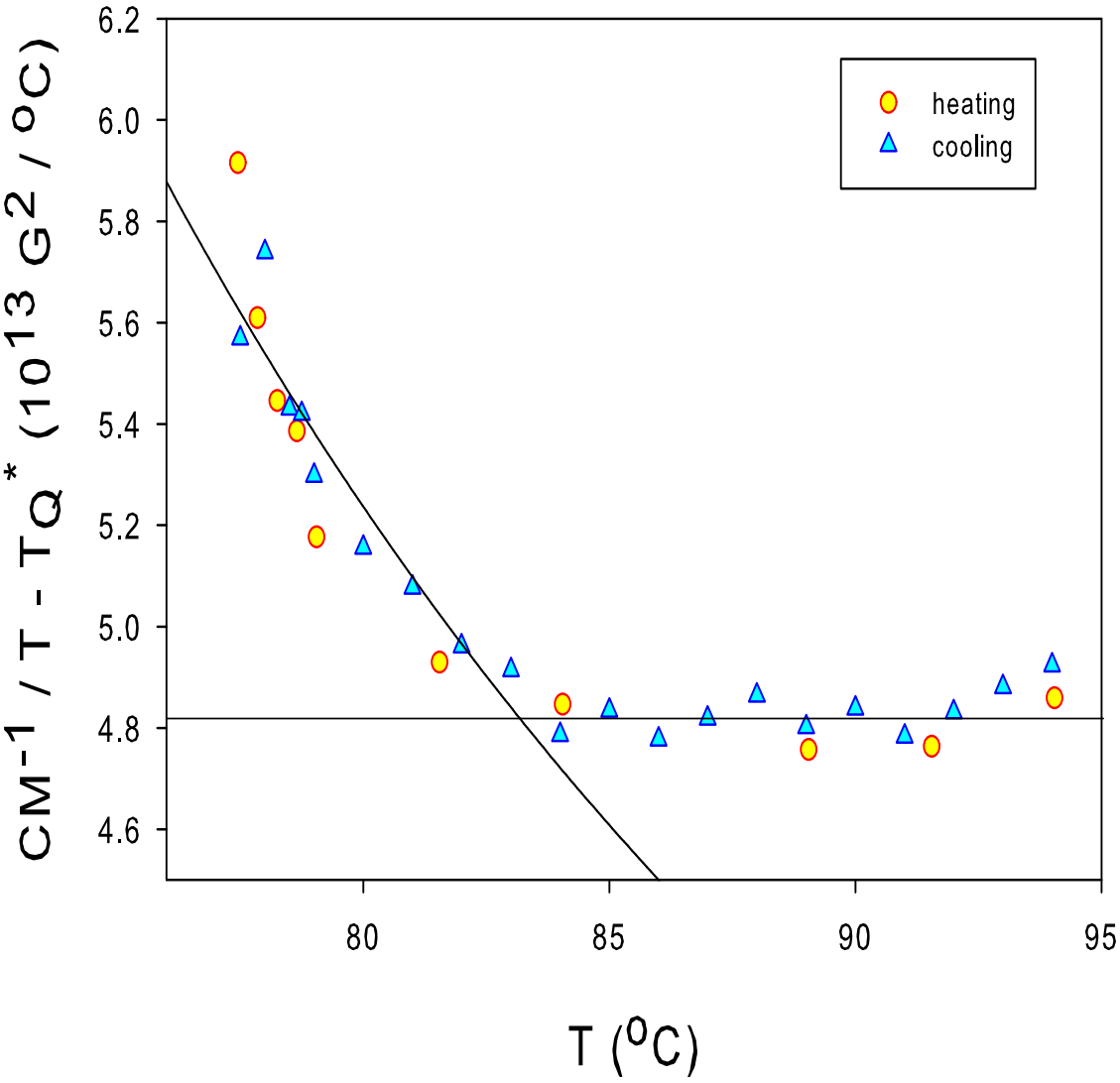

Figure 2.15: CM^{-1} / $T - T_Q^*$ v. T for ClPbis10BB, which clearly illustrates the two different temperature dependent regions, i.e. the T and I phases. The solid lines represent a fit of Eq. 2.48 to the data in the T phase and a fit of Eq. 2.59 to the data in the I phase. Here $T_Q^* \sim 76.4$°C. The error bars are about the size of the data symbols.

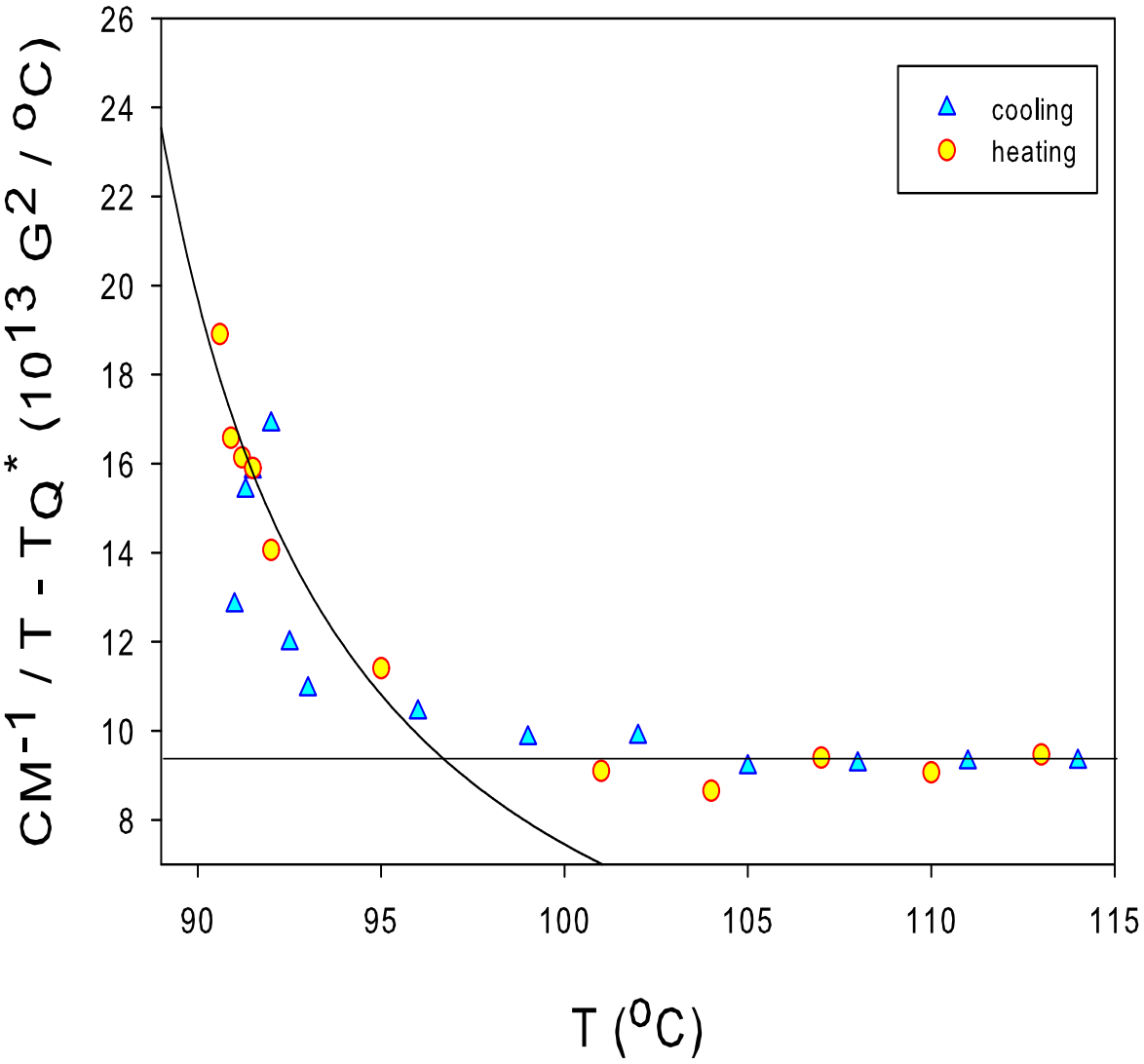

Figure 2.16: CM^{-1} / $T - T_Q^*$ v. T for ClPbis10BBs, which clearly illustrates the two different temperature dependent regions, i.e. the T and I phases. The solid lines represent a fit of Eq. 2.48 to the data in the T phase and a fit of Eq. 2.59 to the data in the I phase. Here $T_Q^* \sim 90.0°$C. The error bars are about the size of the data symbols.

BIBLIOGRAPHY

[1] T. C. Lubensky and L. Radzihovsky. *Phys. Rev. E*, 66:031704–1–27, 2002.

[2] www.magnet.fsu.edu.

[3] S. Stojadinovic. *Light Scattering Studies of Dynamics of Bent-Core Liquid Crystals*. PhD thesis, Kent State University, 2005.

[4] P. G. de Gennes and J. Prost. *The Physics of Liquid Crystals*. Oxford Science Publications, 1993.

[5] T. W. Stinson and J. D. Litster. *Phys. Rev. Lett.*, 25:503, 1970.

[6] T. W. Stinson, J. D. Litster, and N. A. Clark. *J. Phys. (Paris), Colloq.*, 33:C1–69, 1972.

[7] B. Chu, C. S. Bak, and F. L. Lin. *Phys. Rev. Lett.*, 28:1111, 1972.

[8] H. Zink and W. H. De Jeu. *Mol. Cryst. Liq. Cryst.*, 124:287, 1985.

[9] K. Muta, H. Takezoe, A. Fukuda, and E. Kuze. *Jap. J. Appl. Phys.*, 18:2073, 1979.

[10] H. J. Coles. *Mol. Cryst. Liq. Cryst. (Lett.)*, 49:67, 1978.

[11] A. Drozd-Rzoska, S. J. Rzoska, and J. Ziolo. *Liq. Cryst.*, 21(2):273, 1996.

[12] A. Drozd-Rzoska. *Phys. Rev. E*, 59(5):5556, 1999.

[13] H. J. Coles and C. Strazielle. *Mol. Cryst. Liq. Cryst.*, 55:237, 1979.

[14] K. Muta, H. Takezoe, A. Fukuda, and E. Kuze. *Jap. J. Appl. Phys.*, 20(3):503, 1981.

[15] A. Sinha, T. A. Prasada Rao, and R. Dabrowski. *Mol. Cryst. Liq. Cryst.*, 369:1, 2001.

[16] J. Philip and T. A. Prasada Rao. *Phys. Rev. A*, 46(4):2163, 1992.

[17] R. Usha T. A. Prasada Rao. *J. Phys. Soc. Jpn.*, 64(10):4029, 1995.

[18] D. Wiant, S. Stojadinovic, K. Neupane, S. Sharma, K. Fodor-Csorba, A. Jakli, J. T. Gleeson, and S. Sprunt. *Phys. Rev. E*, 73:030703(R), 2006.

[19] N. Blachnik, H. Kneppe, and F. Schneider. *Liq. Cryst.*, 27:1219, 2000.

[20] E. van der Linden, S. Geiger, and D. Bedeaux. *Physica A*, 156:130, 1989.

[21] A. D. Buckingham and J. A. Pople. *Proc. Phys. Soc.*, 69:1133, 1956.

[22] A. Peterlin and H. A. Stuart. *Z. Phys.*, 112:1, 1939.

CHAPTER 3

DYNAMIC LIGHT SCATTERING

Dynamic light scattering (DLS) measurements were made on ClPbis10BB and ClPbis10BBs in the T and I phases in S. Sprunt's lab by Neupane *et al.* [1] on samples that I provided. These measurements give independent evidence of a T-I transition and additional support for the use of tetrahedratic order in the explanation of the behavior observed in the MB experiment. First, I will give a brief description of the DLS technique and then a discussion of the DLS results as they pertain to the T-I transition (for a complete discussion of DLS theory and technique see [2]).

3.1 THEORETICAL BACKGROUND

When incident light interacts with matter the electric field of the light produces an oscillating polarization in the molecules of the said matter. The molecules then emit radiation in all directions in a process known as scattering. The properties of scattered light are dependent on the dielectric constant of the material. In a nematic liquid crystal thermal fluctuations of the nematic order parameter produce changes in the dielectric constant, which produce scattering that can be measured and used to probe properties of the liquid crystal.

The intensity of scattered light has been shown to be proportional to the magnitude of nematic order parameter fluctuations, $< \delta Q_{ij}(t) > \propto < I(t) >$, where δQ_{ij} is the fluctuating part of the nematic order parameter ($<>$ denotes a time average). The incident and scattered angles of the light with respect to the sample and the

polarization of the incident and scattered light can provide information about the ordering of the system. I will refer to these parameters as the geometry of the DLS experiment. The geometry of the situation is usually described in terms of a scattering vector $\vec{q} = \vec{k_f} - \vec{k_i}$, where $\vec{k_f}$ is the wave vector of the scattered light and $\vec{k_i}$ is the wave vector of the incident light. The scattering vector describes the momentum transfer to the sample from the incident light. The polarization is determined in relation to the scattering plane, which is the plane made by $\vec{k_f}$ and $\vec{k_i}$. Although, in this case we are looking at optically isotropic systems, or systems lacking long range order, so the geometry of the set-up reveals little additional information about the systems.

The order parameter fluctuations are generally expressed in terms of a normalized time correlation function using the intensity of the scattered light [2]

$$g^2(\tau) = \frac{< I(0)I(\tau) >}{< I(0) >^2} + 1, \tag{3.1}$$

where $I(0)$ is the scattered intensity at time $t = 0$ and $I(\tau)$ is the scattered intensity at time $t = \tau$. The relaxation rate of the time correlation function, i.e. the fluctuations, can be described in terms of a Landau-de Gennes free energy and a viscosity by the Landau-Khalatnikov relation [2]

$$-\eta \frac{\partial}{\partial t} \delta S = \frac{\partial F}{\partial \delta S}, \tag{3.2}$$

where η is a weakly temperature dependent viscosity that accounts for dissipation of nematic order fluctuations in an isotropic phase, δS describes a small thermal fluctuation in the nematic order parameter, and F is a Landau free energy.

3.1.1 DLS BY UNIAXIAL CALAMITIC LIQUID CRYSTALS

In the classic example of a uniaxial nematic calamitic LC the Landau free energy in the N phase is

$$F = \frac{A}{2}Q_{ij}Q_{ji} - \frac{B}{3}Q_{ij}Q_{jk}Q_{ki} + \frac{C}{4}(Q_{ij}Q_{ji})^2 + \cdots, \tag{3.3}$$

where $Q_{ij} = \frac{1}{2}S(3n_in_j - \delta_{ij})$, $A = a(T - T^*_{NI})$, T^*_{NI} is the supercooling limit at the N-I transition, and the other coefficients can be treated as constants (as they show only a weak temperature dependence). Summing over the indices and rewriting Eq. 3.3 in terms of the scalar order parameter S gives

$$F_N = \frac{3A}{4}S^2 - \frac{B}{4}S^3 + \frac{9C}{16}S^4 + \cdots. \tag{3.4}$$

In the I phase, $S = 0$ in the absence of an external orienting field. So the free energy in the I phase may be written in terms of nematic fluctuations. The changes in free energy due to the fluctuations are small, such that the free energy may be well described by only the lowest order terms in S as,

$$F_I = F_0 + \frac{3A}{4}\delta S^2, \tag{3.5}$$

with F_0 being the free energy of the isotropic phase. Using Eq. 3.5, one may integrate Eq. 3.2 to find δS in terms of viscosity

$$\delta S = e^{-\Gamma t} + CONSTANT, \tag{3.6}$$

where η_I is the viscosity in the isotropic phase and $\Gamma = 3A/2\eta_I = 3a(T - T^*_{NI})/2\eta_I$ is the relaxation rate.

This theory may also be applied to systems that have tetrahedratic ordering, using the arguments developed in chapter 2.

3.1.2 DLS BY BENT-CORE LIQUID CRYSTALS

THE T PHASE

In the tetrahedratic phase the nematic order parameter $S = 0$, so the free energy may be written in terms of the T order parameter and nematic fluctuations as

$$F_T = \frac{1}{2}A'_T T^2 + u'_T T^4 + \frac{1}{2}A'_Q \delta S^2 - w'_1 \delta S T^2. \tag{3.7}$$

Now, light is scattered in the T phase due to fluctuations in the nematic order parameter only, because the third rank T order parameter does not couple to the second rank dielectric tensor. So, we want to look at nematic fluctuations about $S = 0$ at a minimum T. However, before we do this we need to remember that the S-T coupling was shown to be very weak in chapter 2, i.e. w'_1 coefficient was shown to be very small compared to the other terms in the free energy expression. So, in this case the free energy reduces to

$$F_T = \frac{1}{2}A'_T T^2 + u'_T T^4 + \frac{1}{2}A'_Q \delta S^2. \tag{3.8}$$

Here it can be seen that free energy in the T phase due to fluctuations in S, takes a functional form similar to that of the uniaxial calamitic described above. (Later in this section, I will show that the DLS experimental results support the neglect of the w'_1 from the free energy.)

Now, taking the derivative of Eq. 3.8 with respect to δS gives

$$\frac{\partial F_T}{\partial \delta S} = A'_Q \delta S. \tag{3.9}$$

Putting Eq. 3.9 into Eq. 3.2, then integrating and solving for δS yields

$$\delta S = e^{-\Gamma_T t} + CONSTANT, \tag{3.10}$$

where

$$\Gamma_T = \frac{A'_Q}{\eta_T} = \frac{a'_Q}{\eta_T}(T - T^*_Q), \tag{3.11}$$

with η_T being the viscosity that governs dissipation of the nematic fluctuations in the T phase.

THE I PHASE

In the isotropic phase both S and T will go to zero. The free energy due to fluctuations about $S = 0$ and T=0 is

$$F_I = F_0 + \frac{1}{2}A'_Q\delta S^2 + \frac{1}{2}A'_T\delta T^2. \tag{3.12}$$

Again, the w'_1 term is negligible and light is scattered only by fluctuations in the nematic order parameter. So, taking the derivative of Eq. 3.12 with respect to δS gives

$$\frac{\partial F_I}{\partial \delta S} = A'_Q\delta S. \tag{3.13}$$

Putting this value in Eq. 3.2 and integrating to solve for δS gives

$$\delta S = e^{-\Gamma_I t} + CONSTANT, \tag{3.14}$$

where

$$\Gamma_I = \frac{A'_Q}{\eta_I} = \frac{a'_Q}{\eta_I}(T - T^*_Q), \tag{3.15}$$

with η_I being the viscosity in the isotropic phase. Comparing Eqs. 3.11 and 3.15 it can be seen that a change in orientational viscosity will occur at T-I transition, which should lead to a change in the slope of the relaxation rate at this point.

3.2 DLS EXPERIMENT

3.2.1 SAMPLE PREPARATION

For the DLS measurements, 50 μm planar treated sandwich type cells [3] were loaded with ClPbis10BB and ClPbis10BBs in the following manner; the cell was placed on a hot plate situated inside a laminar flow hood. Liquid crystal was placed on the ledge of the cell, which was then heated to $\sim$5°C above the clearing point of the sample and allowed to fill via capillarity.

3.2.2 DLS SET-UP

These samples were then placed in Sprunt's DLS set-up with the incident polarization oriented vertical to a horizontal scattering plane. The relaxation rate's dependence on the scattering vector was tested in the T and I phase for both materials. The relaxation rate of ClPbis10BB was measured over a range $q = (1 - 9) \times 10^4$ cm^{-1} at 5°C above T_{TI} (in the I phase) and 0.8°C above T_{N_TT} (in the T phase), and it showed no dependence on the scattering vector in either case. The relaxation rate of ClPbis10BBs was measured over a similar range of scattering vectors at 3°C above T_{N_TT} (in the I phase) and 0.3°C above T_{N_TT} (in the T phase). Again, the relaxation rate showed no dependence on the scattering vector in either phase. The relaxation rates of the materials were measured over a range of temperatures in the T and I phases at a scattering vector $q = 76000$ cm^{-1}, which corresponds to an incident angle of 0° and a scattering angle of 45°.

3.3 RESULTS AND DISCUSSION

Figures 3.1 and 3.2 are typical examples of normalized correlation functions fit with single exponentials for ClPbis10BB and ClPbis10BBs, respectively. Figures 3.3

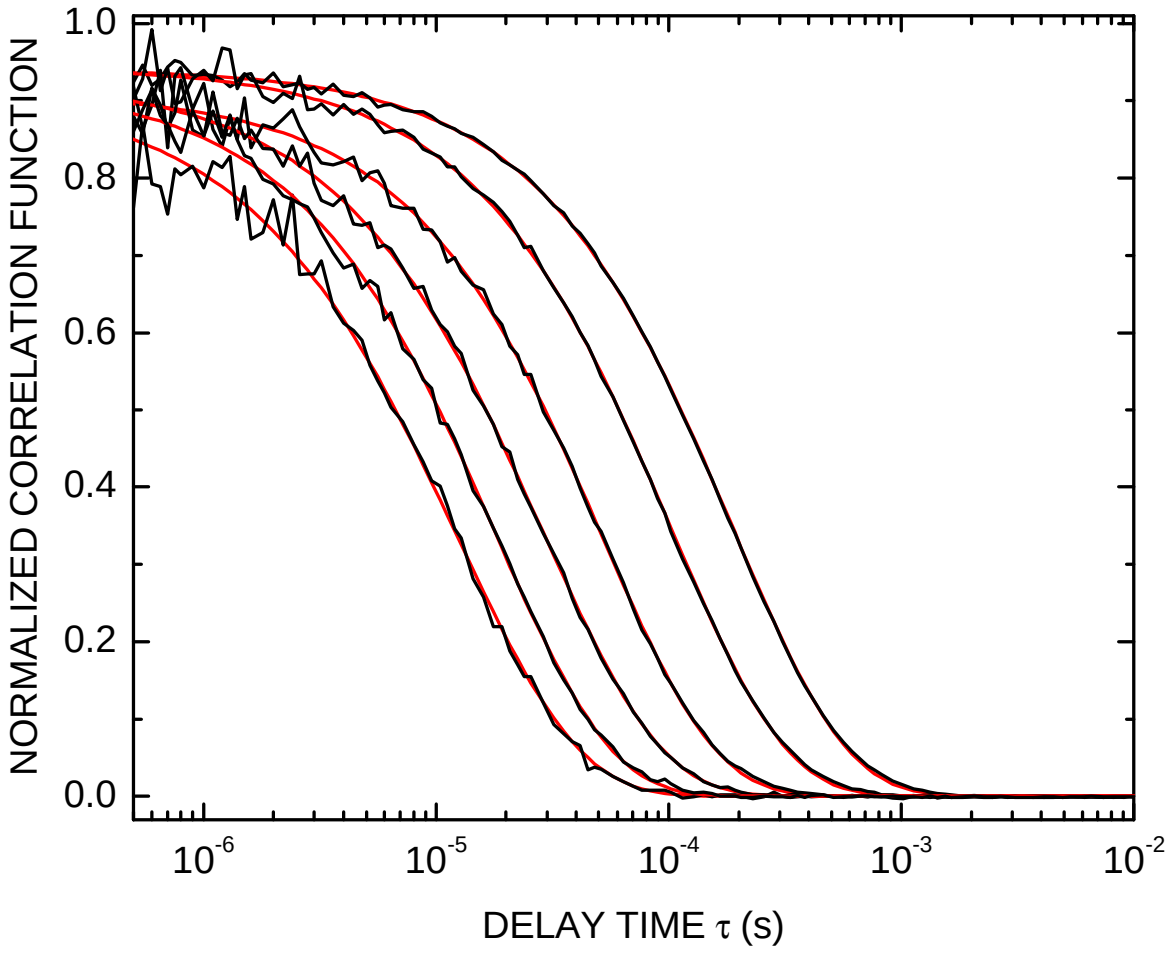

Figure 3.1: Typical correlation function for ClPbis10BB in the T and I phases at temperatures of 82.76, 80.85, 79.34, 77.82, 76.81 and 76.21°C, from left to right, respectively. Plot prepared by K. Neupane, *unpublished*.

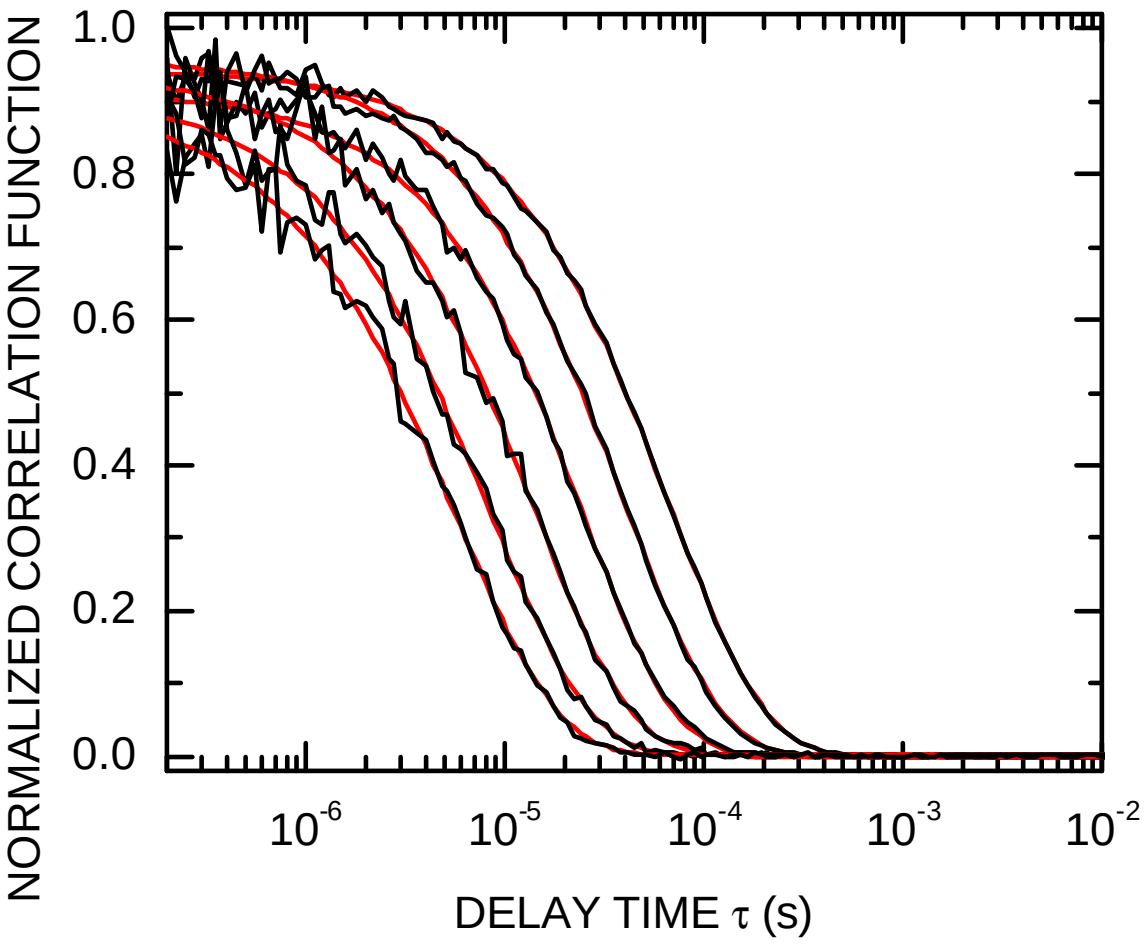

Figure 3.2: Typical correlation functions for ClPbis10BBs in the T and I phases at temperatures of 94.55, 93.23, 92.04, 91.02, 90.32 and 89.87°C, from left to right, respectively. Plot prepared by K. Neupane, *unpublished*.

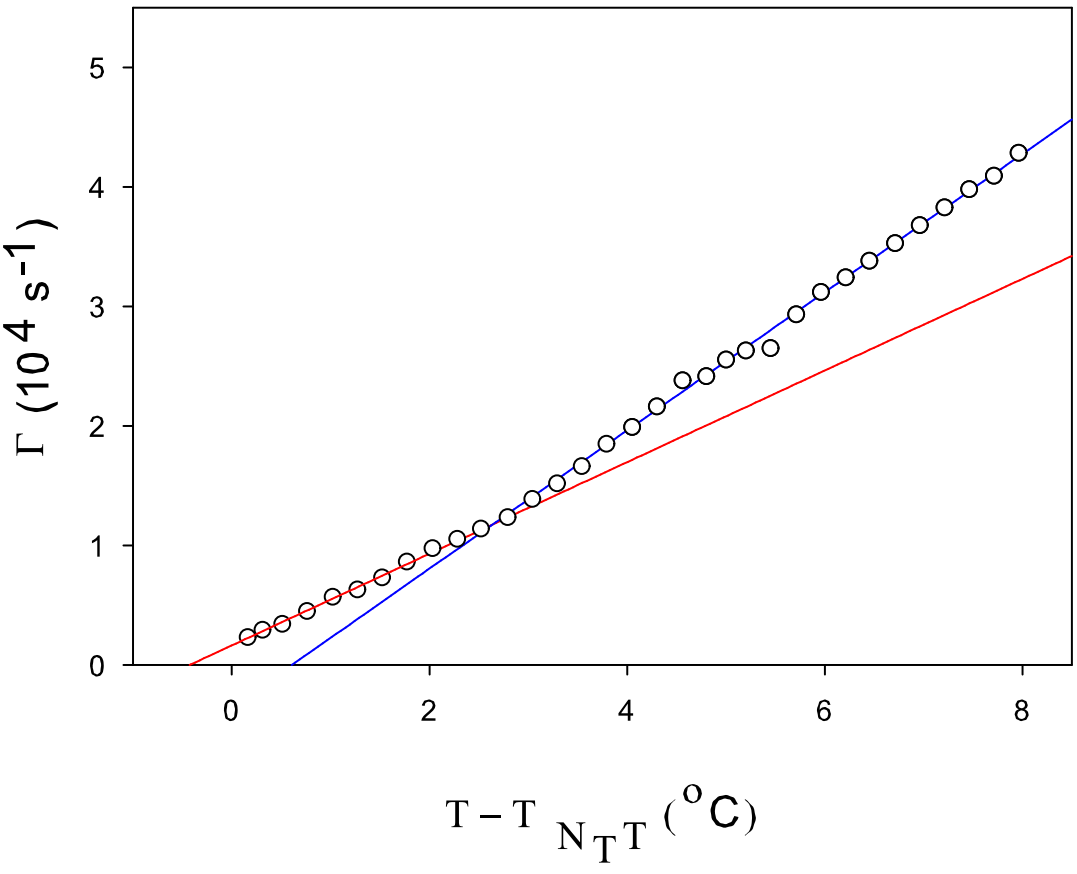

Figure 3.3: The relaxation rate as function of temperature for ClPbis10BB. The red line represents a linear fit to the region just above the N_T-T transition. The blue line represents a linear fit to the region above the T-I transition. There is a change is slope at ~ 3°C above the N_T-T transition [1].

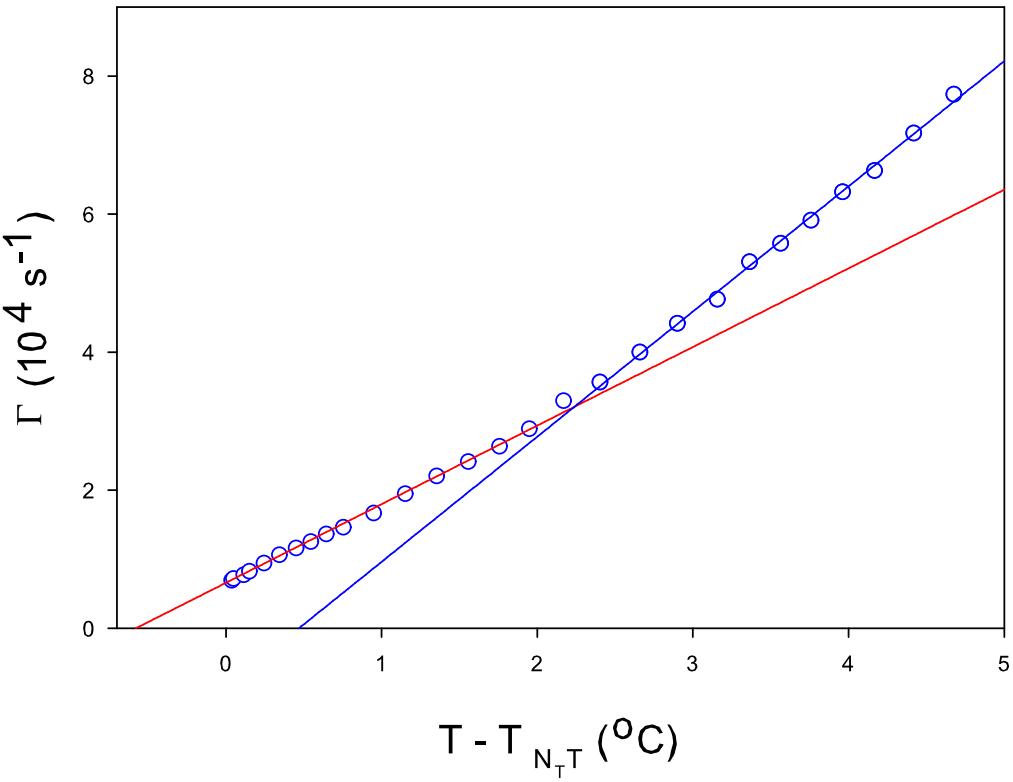

Figure 3.4: The relaxation rates as functions of temperature for ClPbis10BBs. The red line represents a linear fit to the region just above the N_T-T transition. The blue line represents a linear fit to the region above the T-I transition. There is a change in slope at ~ 2°C above the N_T-T transition [1].

and 3.4 show plots of relaxation rate v. temperature for ClPbis10BB and ClPbis10BBs. The plot of relaxation rate v. temperature for ClPbis10BB shows an increase in slope about 3°C above the N_T-T transition. Similarly, ClPbis10BBs shows an increase in the slope of its relaxation rate v. temperature plot $\sim$ 2°C above the N_T-T transition. Thus, a change in slope of the relaxation rate v. temperature, which was predicted to occur at the T-I transition by Eqs. 3.11 and 3.15 is clearly evident in both bent-core LCs. These results indicate a T-I transition in the vicinity of the T_T^*s found by MB in chapter 2. The combined DLS and MB results and analysis strongly indicate that a T-I transition is occurring in both these materials. (Note, the orientational viscosity should show a temperature dependence within a given phase. However, the temperature dependence of the viscosity cannot account for a sharp change in slope of the relaxation rate. See Appendix D for a complete discussion.)

These results, along with those presented in Fig. 3.5, help to validate the predictions of tetrahedratic model for DLS, as well as the exclusion of the w_1' term from the free energy. Figures 3.1 and 3.2 show that the correlation functions for ClPbis10BB and ClPbis10BBs, which are proportional to δS, can be well fit with a single exponential. The exponential dependence is what is predicted by a model that has a lowest order term that is quadratic in δS, which strongly suggests that the w_1' term is not needed in the free energy model. For if w_1' was of a comparable magnitude to the other coefficients, the lowest order term in S would be the first order w_1' term. And if this were true, Eq. 3.2 would predict a linear relaxation for the correlation function, which was not observed.

The inverse scattering amplitude in the T and I can be theoretically described,

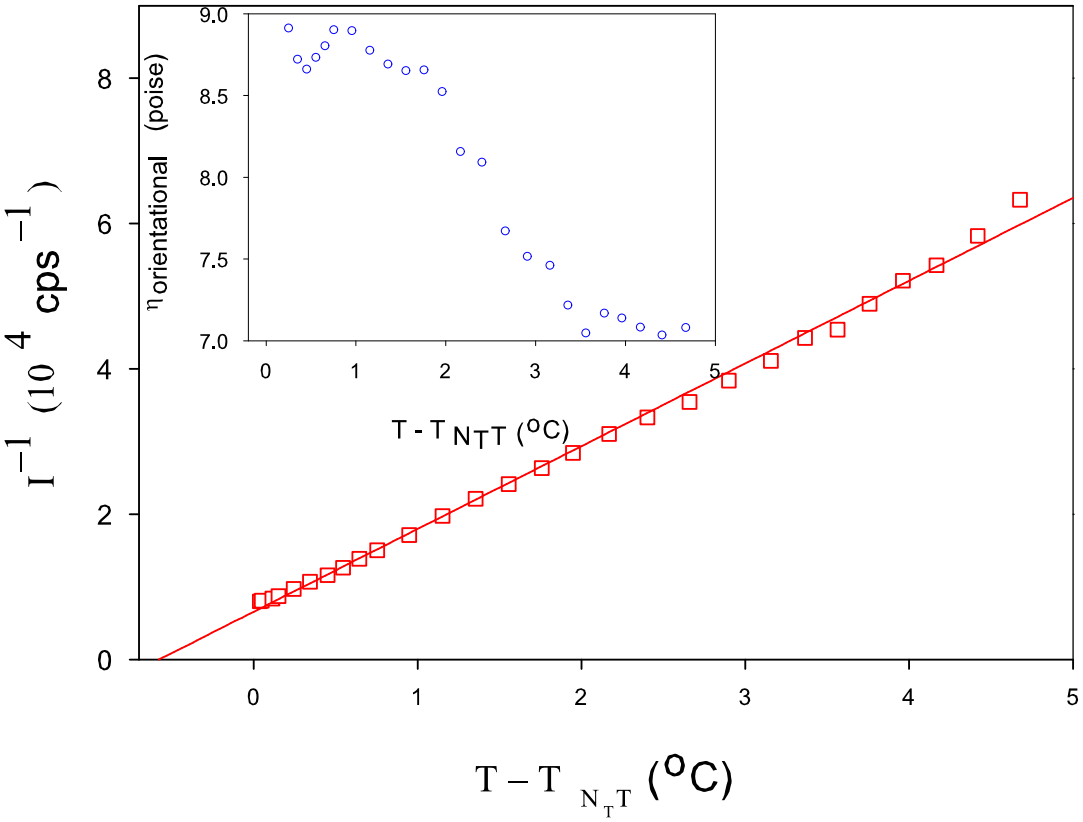

Figure 3.5: I^{-1} as a function of temperature for ClPbis10BBs. The red line represents a linear fit the data, which is relatively constant over the range, which includes the bend in the relaxation rate data. The inset shows the orientational viscosity for ClPbis10BBs as a function of temperature. The viscosity appears to be relatively constant in the region just above the clearing point and then shows a transition region $\sim 2°$C above the clearing point giving way to another constant region [1].

for the free energies above, using the equipartition theorem as [4]

$$I^{-1} \propto < \delta S^2 > = \frac{1}{k_B T} A'_Q. \tag{3.16}$$

Figure 3.5 shows that inverse scattering amplitude is proportional to temperature for ClPbis10BBs, with no abrupt changes in slope. This shows the δS^2 term in the free energy is indeed that dominate term, or that there is no strong S-T coupling, which reinforces the decision to exclude the w'_1 term.

Also, Eqs. 3.11, 3.15, and 3.16 show that the orientational viscosity is proportional to $(I\Gamma)^{-1}$. Sprunt *et al.* plotted $(I\Gamma)^{-1}$ as a function of temperature for ClPbis10BBs [1], and showed that the viscosity was relatively constant just above the clearing point, and then showed a sharp decrease at the same temperature where the change in slope of the relaxation rate occurred, followed by a constant viscosity at higher temperatures (see inset to Fig. 3.5). This supports the notion that a T-I transition, which was predicted to lead to a change in slope of the relaxation rate v. temperature due to a change in orientational viscosity, is indeed what is occurring in these two bent-core LCs.

It is a very difficult task to determine how changes in molecular shape and size, coupled with a change in number density, at the T-I transition affect the viscosity governing the relaxation of nematic fluctuations in bent-core systems with tetrahedratic order. The relaxation of nematic fluctuations in the T phase is a complex process that consists of changes in orientation of the nematic-tetrahedratic complexes and changes in the shape of the mesogenic units, i.e. relaxation from the stretched nematic-tetrahedratic complexes to a tetrahedrons (see Figs. 2.12 and 2.13). In the I phase, the active mesogenic units consist of single bent-core molecules that in theory should have a more anisotropic shape than the clustered complexes present in the T

phase. Although a quantitative formulation of the viscosity in the T phase is beyond the scope of this work, a general argument can be made that the relaxation process in the T phase, which consists of rotations and translations of multiple clusters of molecules, is more complex undertaking than the relaxation in the I phase. And subsequently, the phase with the more complex process should take longer to relax to equilibrium, i.e. should have a higher viscosity.

Another interesting result of this measurement is that the relaxation rate of ClPbis10BB is markedly slower (about one-half) than that of ClPbis10BBs, which would seem to imply that ClPbis10BBs has a lower viscosity than the ClPbis10BB. The two molecules have similar size and structures, which makes it difficult to argue that steric concerns account for the difference in viscosity between the two molecules. It is possible that some molecular forces that have not been considered yet could account for the difference in viscosity. Further work is needed to clarify this question.

Finally, preliminary measurements on the flow viscosity above the clearing point in ClPbis10BB show a viscosity that is much larger than in calamitics, as well as a sharp change in the magnitude of the viscosity at the same temperature as the change in the orientational viscosity observed by DLS [5]. This further bolsters the arguments for a T-I phase transition in these materials, and provides stimulation for theoretical comparisons between the origins of the two different viscosities.

BIBLIOGRAPHY

[1] D. Wiant, K. Neupane, S. Sharma, A. Jakli, J. T. Gleeson, and S. Sprunt. *submitted Phys. Rev. Lett.*, 2006.

[2] S. Stojadinovic. *Light Scattering Studies of Dynamics of Bent-Core Liquid Crystals.* PhD thesis, Kent State University, 2005.

[3] E.H.C. Co, Tokyo, Japan.

[4] P. G. de Gennes. *Mol. Cryst. Liq. Cryst.*, 12:193, 1971.

[5] E. Dorjgotov, K. Fodor-Csorba, J. T. Gleeson, S. Sprunt, and A. Jakli. *to be submitted to Phys. Rev. E*, 2007.

CHAPTER 4

DENSITY CHANGE AT A PHASE TRANSITION

4.1 BACKGROUND

4.1.1 THEORETICAL

Liquid Crystal phases are characterized by a certain molecular order, which changes at a phase transition. In a first order transition this change in molecular order should be accompanied by an abrupt change in density at a well defined transition temperature. A well planned and executed density measurement through a transition can give information about pretransitional ordering, or the strength of a transition, as well as information about the difference in molecular order between the two phases (e.g. a transition between a SmA phase, with 2-D ordering, and an I phase will have a greater density jump than a transition between a N phase, with 1-D ordering, and an I phase). The inclusion of a density dependent parameter in the phenomenological LdG model and Maier-Saupe molecular mean field theory for the N-I transition in uniaxial calamitic LCs has greatly improved the quantitative agreement between these theories and experiments, particularly $T_{NI} - T^*_{NI}$ (see [1] and Refs. within).

Measurements of density changes in bent-core LCs has two possible purposes: first, a jump in density above the clearing point would provide evidence of a T-I transition, and second, the inclusion of a density dependence in the LdG theory with tetrahedratic ordering might improve agreement between theory and experiment. However, in this work I focused mainly on measuring the size of the density jump at the clearing point and on using density changes to look for evidence of a T-I transition.

The theoretical implications of the size of the density changes at the transitions will be left for a later time. In the remainder of this chapter, I will show how density is incorporated into LdG model for uniaxial calamitics following the work of Mukherjee *et al.* [2] (that was later revised in Ref. [1]), then I will discuss current commercial methods to measure density and compare them to the technique used in this chapter, and finally I will discuss the experimental measurements made on the bent-core LCs.

DENSITY DEPENDENT LdG THEORY FOR UNIAXIAL CALAMITIC LCS

The free energy may be expressed in terms of the scalar nematic order parameter, S, as

$$F = F_0 + \frac{a}{2}(T - T^*_{NI})S^2 - \frac{B'}{3}S^3 + \frac{C}{4}S^4 + \frac{\lambda}{2}(\rho - \rho_0)^2 S^2, \tag{4.1}$$

where F_0 is the density dependent free energy in the isotropic phase, T^*_{NI} is the supercooling limit of the I phase, ρ is the density, ρ_0 is the equilibrium density without the order parameter-density coupling, λ and C are positive coupling constants, and $B' = B_0[1 + \alpha(T - T_{NI})]$ with B_0 and α positive constants. The N-I transition is analyzed by requiring that F must be a minimum with respect to S in equilibrium, and that the free energies of the N and I phases must be equal at the transition.

Minimizing F with respect to S gives

$$\frac{\partial F}{\partial S} = a(T - T^*_{NI})S - B'S^2 + CS^3 + \lambda(\rho - \rho_0)^2 S = 0. \tag{4.2}$$

Equations 4.1 and 4.2 can be rewritten as

$$F - F_0 = \frac{S^2}{2}\left[a(T - T^*_{NI}) - \frac{2B'}{3}S + \frac{C}{2}S^2 + \lambda(\rho - \rho_0)\right] = 0 \tag{4.3}$$

and

$$\frac{\partial F}{\partial S} = S\left[a(T - T^*_{NI}) - B'S + CS^2 + \lambda(\rho - \rho_0)^2\right] = 0. \tag{4.4}$$

At T_{NI}, the terms in square brackets in Eqs. 4.3 and 4.4 must equal zero. Using this fact one can then solve for S_{NI},

$$S_{NI} = \frac{2B'}{3C}. \tag{4.5}$$

This value of S_{NI} may be substituted into Eq. 4.2 with B' evaluated at $T = T_{NI}$ to see how the density term modifies the transition temperature

$$T_{NI} = T^*_{NI} + \frac{2B'^2}{9aC} - \frac{\lambda}{a}(\rho^t_N - \rho^t_I)^2, \tag{4.6}$$

where ρ^t_N and ρ^t_I are the nematic and isotropic densities at T_{NI}, respectively. (Note, at the transition B' reduces to the more conventional B_0. The temperature dependence in B' was included to bring the theory into agreement with experimentally observed values of $\frac{dS}{dT}|_{T_{NI}}$.) The addition of a density dependent term into the LdG model of a uniaxial calamitic has greatly improved the quantitative agreement between experiment and theory. It is possible that a density dependent term will improve the quantitative predictions of the LdG type model describing tetrahedratic order in bent-core systems. Therefore, it might prove beneficial to attempt to measure the density dependence of the N_T, T, and I phases so that in the future those trying to improve the current theory describing transitions in bent-core LCs will have these values readily available to them.

4.1.2 EXPERIMENTAL

Most recently reported density measurements are made using a commercial Anton Paar digital precision density system. This system has several different variations, but all work on the same basic principle. A V-shaped glass tube is filled with the sample in question. Vibrations are then induced in the glass tube by means of an excited magnet attached to the tip of the V. The glass tube acts as a tuning fork,

vibrating at its natural frequency, with a period whose square is a linear function of the density of the material [3].

The Anton Paar technique is easy to use and offers a reported resolution of $\pm 1.5 \times 10^{-6}$ g/cm^3 [3] under ideal operating conditions. However, there are some disadvantages to this system that made it impossible for us to use this technique with the bent-core materials. First, and most important, the Anton Paar systems require a minimum of 1 mL of sample to make a measurement. At the time of this work less than a gram of each of the bent-core LCs existed, so it was not feasible to use over 1 mL to make this measurement. Also, the temperature operating range of the set-up was 0-90°C, which is at the edge of the region of interest for ClPbis10BB and below the clearing point for ClPbis10BBs. Finally, and less problematic than the previous issues, are that this apparatus must be calibrated over the investigated temperature region, which introduces uncertainty, and temperature gradients caused by the difficulty associated with uniformly heating a large and irregularly shaped object.

We developed a simple solution to the first two problems mentioned above. Rectangular microcapillaries were filled with μL's of sample, and then volume changes were measured as a function of temperature at a constant pressure using high resolution micrographs of the meniscus of the sample. The change in density is related to the volume change by the following relation

$$\frac{|\Delta\rho|}{\rho} = \frac{|\Delta V|}{V_0}, \tag{4.7}$$

where $\Delta\rho = \rho - \rho_0$ and $\Delta V = V - V_0$ with ρ_0 and V_0 being the density and volume at the clearing point, respectively.

This technique allowed for the measurement of density changes at high temperatures using extremely small amounts of the sample material. However, the problems

with temperature control seen in the commercial set-up remained a problem with this technique. The temperature gradients are particularly troubling because they make it difficult to isolate the density changes due to the phase transition. In a first order transition there should be an abrupt transition at a certain temperature and a corresponding change in the density. But in practice heat gradients and sample impurities can extend a transition over a temperature range and "smear" out the transition. When this happens the phase transition occurs at different temperatures in different regions of the sample, and as each section of the sample changes phase a small change in volume (density) occurs, so that there are in essence several "partial" transitions at temperatures around the true transition temperature rather than one large change in volume at a well defined transition temperature. This smearing effect can make it hard to study pretransitional ordering using this method, as well as to calculate the exact volume change due to the transition, i.e. the end points of the transition. This method allows for extremely accurate measurements of volume change, but it introduces difficulties in determining the exact overall volume of the sample. In the following sections I will discuss the sample preparation, the experimental set-up and procedures, and finally the results.

4.2 EXPERIMENT

4.2.1 SAMPLE PREPARATION

The liquid crystals were loaded into 40 mm long rectangular glass capillaries with inner dimensions of either 1 mm $\times$ 0.1 mm or 0.5 mm $\times$ 0.05 mm. Before filling the glass was treated with a silane solution, used to create a homeotropic surface alignment, in order to prevent wetting of the glass (the liquid crystal "sticking" to

the glass) during filling. The first step of the silane treatment was a thorough cleaning of the glass. The glass was soaked in a isopropanol bath overnight, then the inside was flushed with deionized water ten times. After the flushing, the glass was baked in an oven at 150°C for 2 hrs. to dry the inside of the glass. Next, the glass was soaked in a mixture of 0.1% n-Octadecyltriethoxysilane (purchased from TCI America) in isopropanol for 30 minutes. Then the glass was baked for 3 hrs. at 150°C. Finally, the capillary was sealed at one end by melting the glass over a small flame produced by a Weller Portasol soldering tool.

The capillaries were filled in a vacuum using the following process. A Fisher Scientific hot plate was placed inside the vacuum chamber. Two glass slides were placed ∼2 mm apart in the middle of the hot plate. (The glass had been wiped, with acetone then wiped and soaked in isopropanol, and finally rinsed with deionized water before use.) The LC, in a solid state, was placed in a small pile on one slide and the capillary was placed with its open end on the slide with the LC and the rest of its body on the other slide (see Fig. 4.1). The gap between the slides was left to prevent the liquid crystal from being drawn down the outside of the capillary during filling. Then the vacuum chamber was sealed and evacuated to ∼400 milliTorr for 30 minutes. The temperature of the hotplate was slowly raised until the LC melted, then the sample was allowed to fill via capillarity. Once the tube was filled to about 3 cm the open end of the capillary was removed from the pool of LC and the air was slowly allowed to enter the vacuum chamber forcing the liquid crystal to the bottom of the capillary while forcing out air bubbles. Only one end of the capillary was sealed so that the pressure would remain constant as the volume of the LC changed.

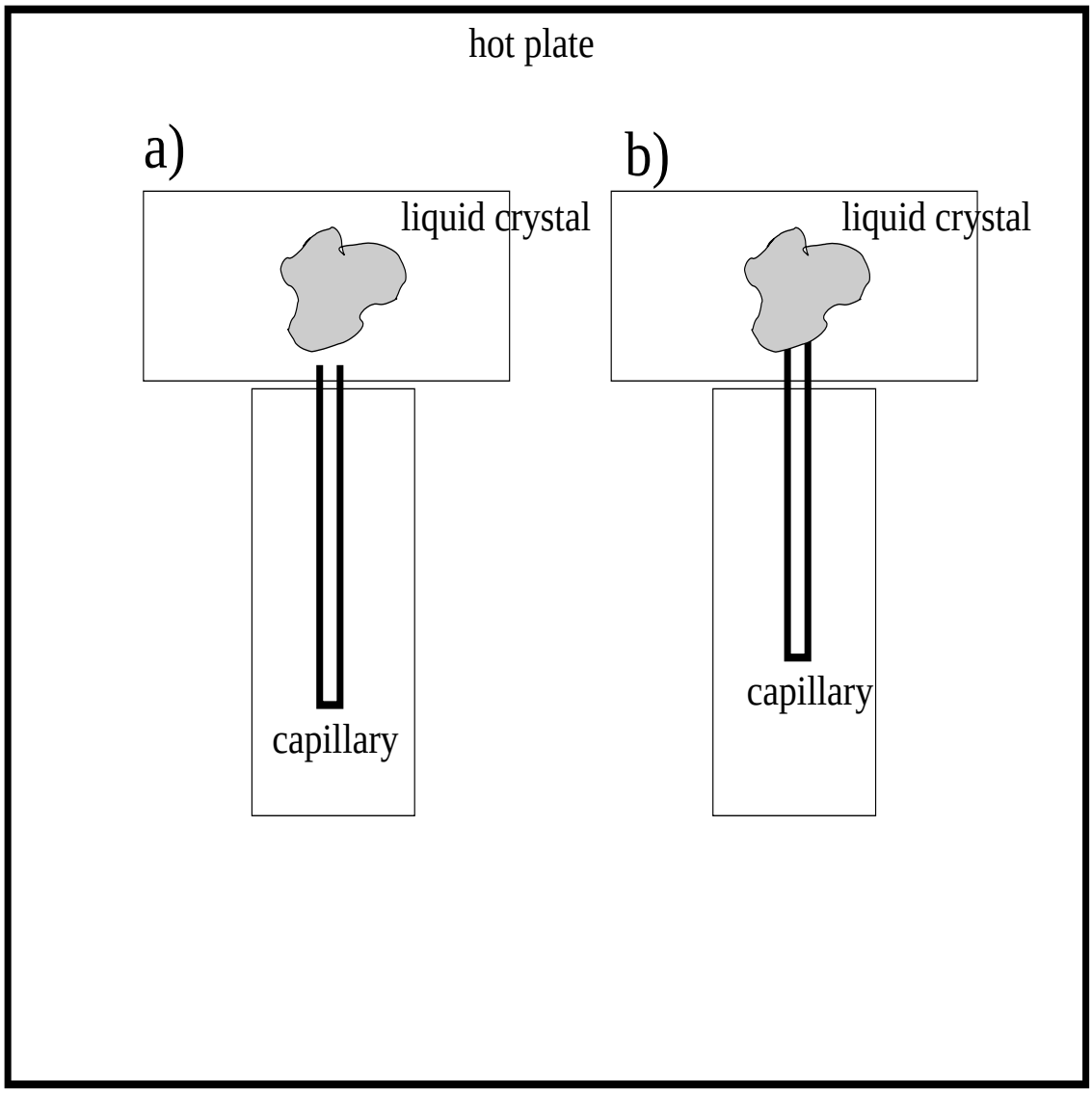

Figure 4.1: A schematic model of the filling of a sample cell. The entire set-up was housed inside a vacuum chamber. a) The capillary is not touching the LC while the vacuum chamber is evacuated. b) The capillary is moved into the LC for filling, when the chamber is evacuated.

4.2.2 EXPERIMENTAL SET-UP

To make the measurements the sample was placed in a Instec HS-1 hot stage, which had been modified to use with a microscope in reflection mode. A solid copper plate was painted white then inserted into the bottom of the hot stage with heat sink grease used between the copper plate and the base of the hot stage. The sample rested on the copper plate. It was covered by an aluminum jacket with a 2 mm diameter circular hole over the meniscus (see Fig. 4.2 for a schematic representation of the set-up). The hot stage was surrounded by a teflon cover, whose edges were surrounded by styrofoam insulation. The sample was imaged with an Olympus BH-2 microscope in reflection mode using a 10X objective. This lens had a numerical aperture (NA) of 0.3, which gives a diffraction limit for visible light of $\sim$1 μm using the Airy function, $r_{airy} = 0.61\lambda/NA$. A Canon EOS digital Rebel camera was used to capture images of the sample with a size of 2048$\times$3072 pixels. Calibration using a stage micrometer found that each pixel represented $\sim$0.3 μm using the 10X objective, which is near the diffraction limit and will provide very good resolution with the given objective.

Phase transitions were found by observing changes in the texture of the material as the temperature was slowly varied. After the clearing point was determined the sample was allowed to crystallize, then heated until the crystal melted, then cooled in to the nematic phase about a degree below the clearing point. The sample was allowed to sit in the nematic phase for 30 minutes, then the temperature was ramped up at a rate of 0.1°C / min. to about 10°C above the clearing point, with a picture of the meniscus being taken every minute. Once this scan was finished the sample was allowed to sit at the final temperature in the isotropic phase for 30 minutes, then the process was repeated with the sample being cooled at 0.1°C / min.. This process was

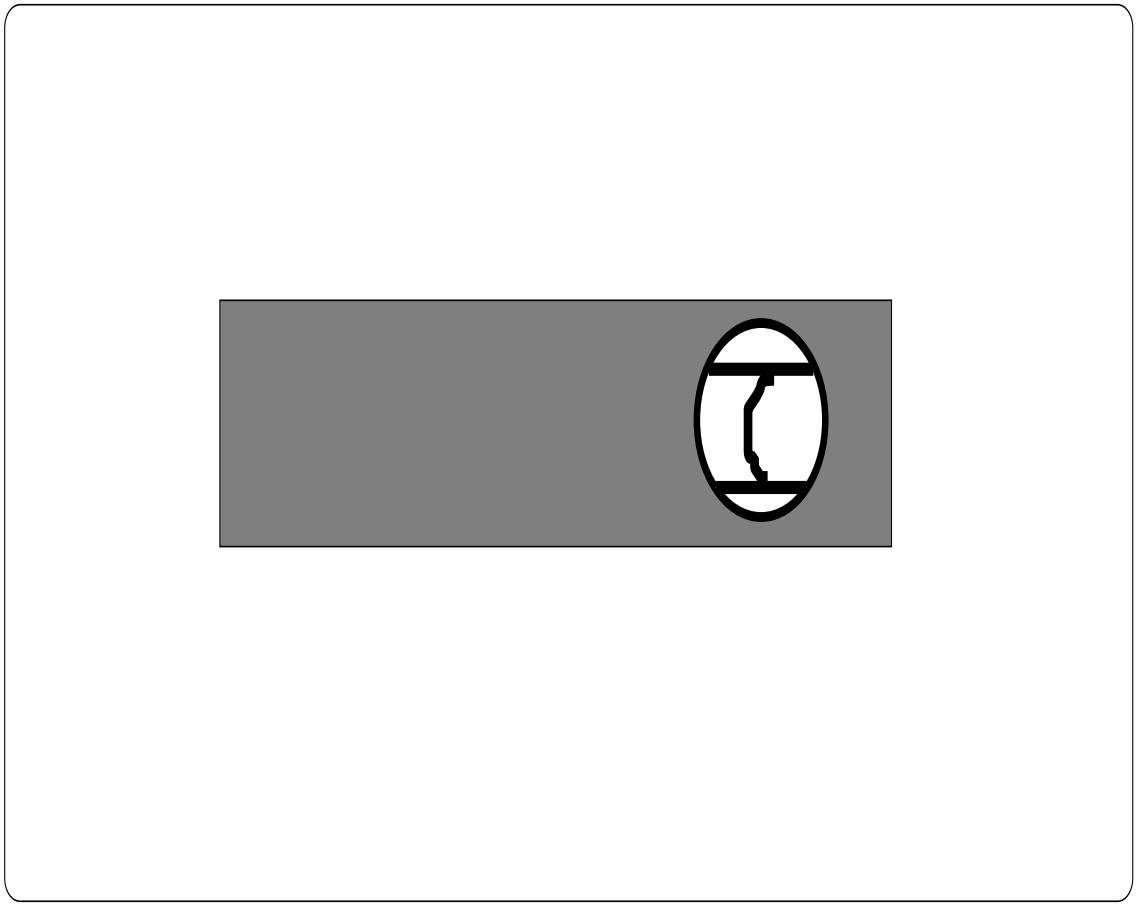

Figure 4.2: A schematic model of the sample resting on the white copper plate, covered by the aluminum jacket. The meniscus can be seen through the hole in the aluminum jacket. Drawing is not to scale.

fully automated using the Instec controller to ramp the temperature and a Canon utility to take the pictures and save them to a computer via remote control. The camera was placed in manual mode with the white balance set for Tungsten light, the ISO = 100, the $T_\nu = 1/30$, and the size at large/fine.

The images were digitally analyzed in a multi-step process. First, the 24-bit RGB image was read into the Matrox Inspector 3.1 image analysis program. The image was changed to a grayscale 32-bit float, and then to an 8-bit unsigned grayscale image. The contrast of each picture was increased by a uniform amount using a histogram equalization function in Matrox (it is important to note that this process was reversible, i.e. it did not alter the content of the picture). Next, the enhanced images were saved and then read into a custom edge finder written in the Matlab language (see Appendix E). The edge finder was used to determine the area between the bottom of the meniscus and the bottom edge of the picture. The change in this area is proportional to the change in volume of the LC as the temperature is changed.

The change in position of the meniscus could be measured extremely accurately using digital imaging and analysis, however some uncertainty was introduced from the experimental set-up. A small region at each edge of the meniscus was left outside of the width of the picture ($< 5\%$ in total). Although great care was taken to avoid temperature gradients, they no doubt existed over a 4 cm long sample. The alignment of the sample in the field of view of the camera could also affect the results. It was assumed in the analysis that the meniscus was moving vertically in the image, if it was misaligned and moving at a slight angle, that would alter the results. The uncertainty due to the temperature was not taken into account in the presentation of the results. However, any temperature gradients could move the transitions to higher

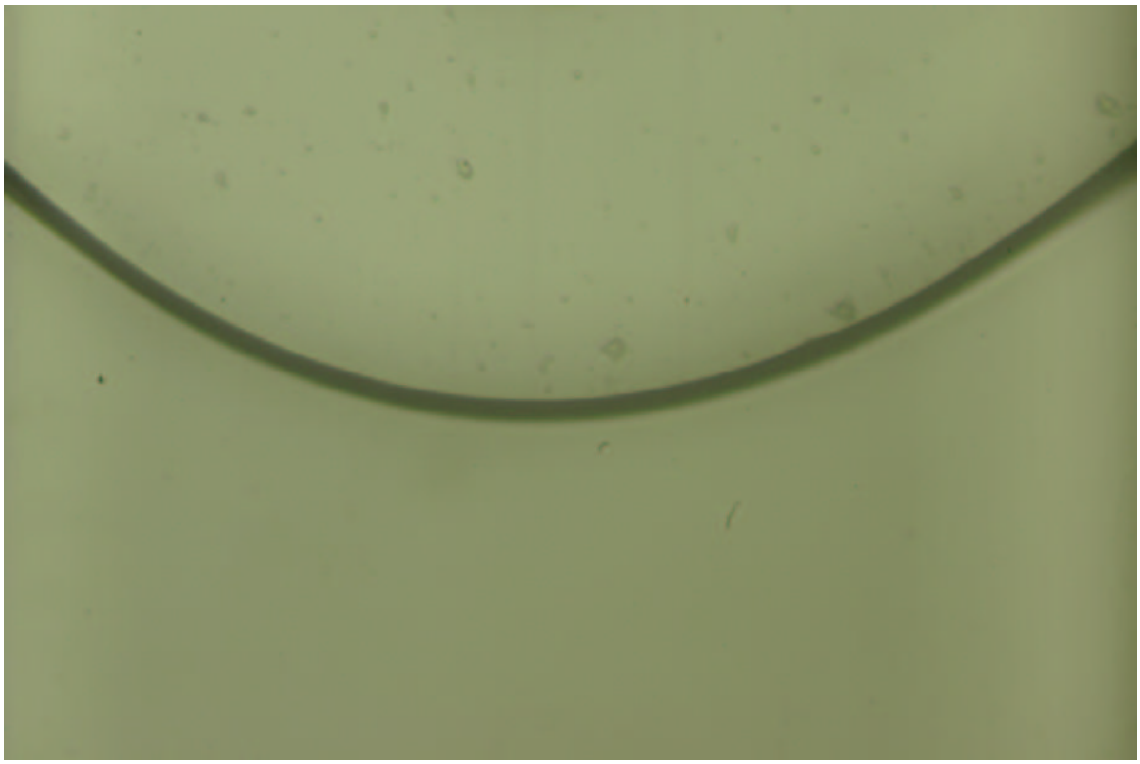

Figure 4.3: An example of a micrograph of the meniscus. As the temperature is increased the meniscus will move from bottom to top in the picture.

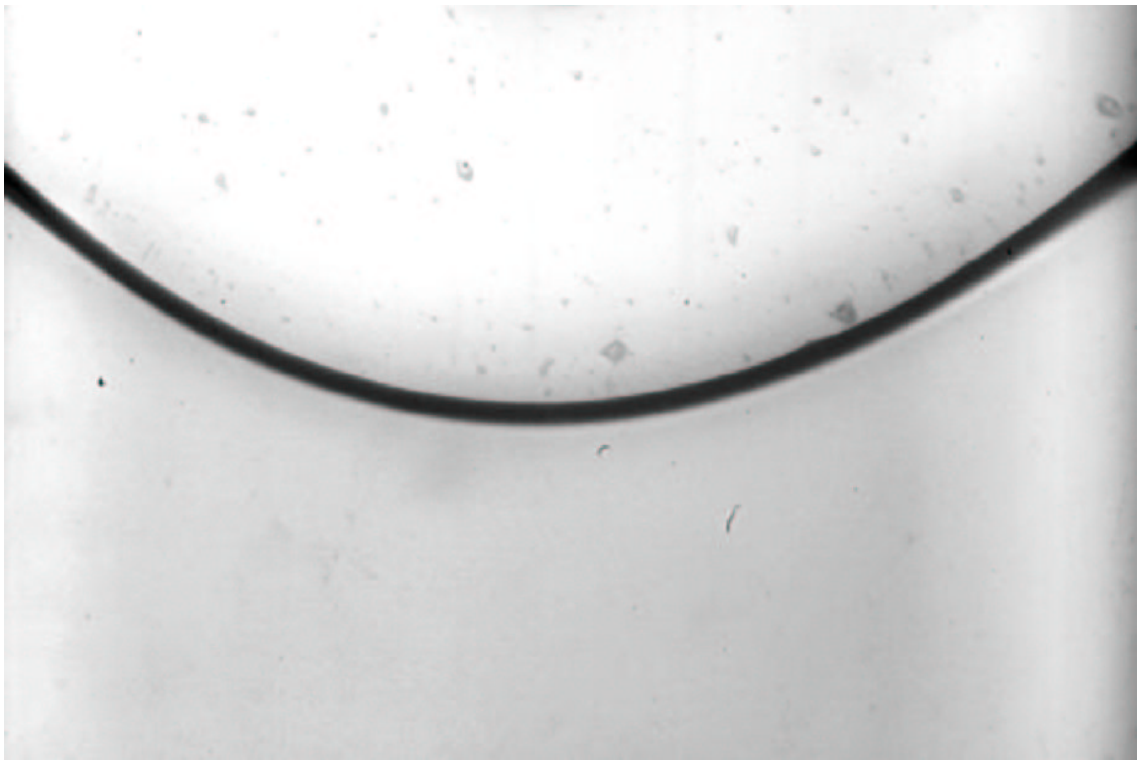

Figure 4.4: An example of the enhanced grayscale image after editing in the Matrox Inspector program.

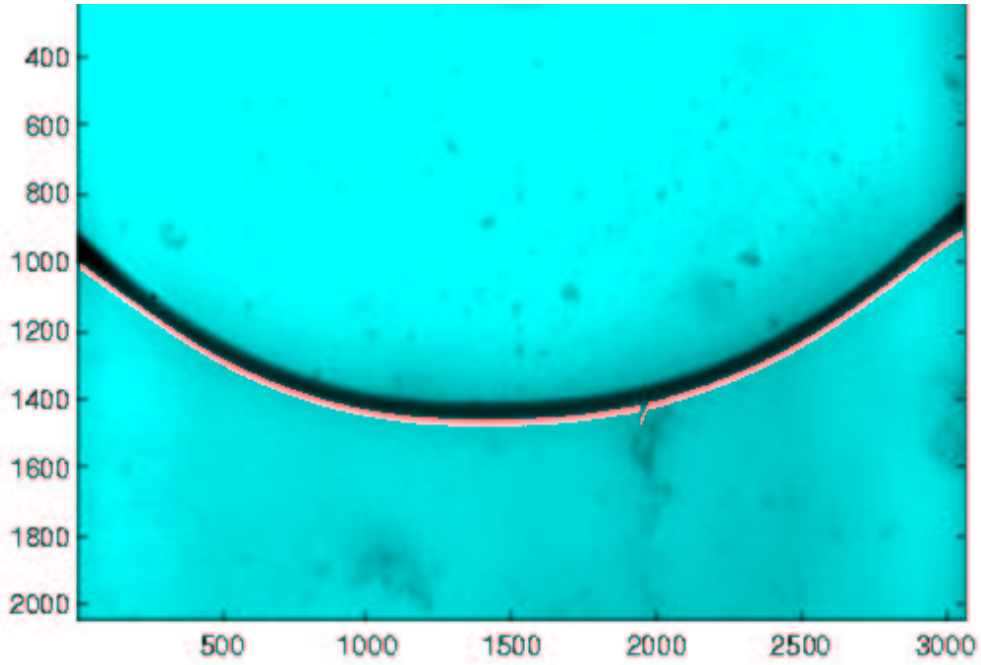

Figure 4.5: An example of edge detected by the Matlab edge finder. The grayscale image was changed to color to outline the edge. The green and blue channels were equally weighted, while the red channel was used to display the edge.

or lower temperatures, or smear out the transitions somewhat. The uncertainty shown in the results was due to two main factors. The largest contribution came from the uncertainty in measuring the total volume of the sample in the capillary, which was about 3%. Measuring the volume of the capillary was difficult because the sealed end of the capillary had an irregular shape that only allowed the height of the sample to be determined to ∼1 mm. Some uncertainty also came from the edges of the pictures. I estimated that the misalignment and the missing edges of the meniscus would affect a maximum region of about 50 columns and 500 rows at each edge of the image, which gave an uncertainty of ∼1% per point. The typical uncertainty for each point was ∼4%.

The set-up was tested in several ways. First, the thermal expansion coefficient was determined for a 29±1 mm column of n-tetradecane in a 1 mm × 0.1 mm capillary. The temperature was raised in 1°C intervals every 10 minutes from 24°C to 30°C, with a picture being taken at every temperature. The thermal expansion coefficient in this region was found to be $0.00085 \pm 0.00005 \mathrm{K}^{-1}$, which is in good agreement with the literature value of $0.0009 \mathrm{K}^{-1}$ [4]. Tetradecane was chosen to calibrate the set-up because it has a documented thermal expansion coefficient near room temperature, and a low vapor pressure in this temperature region, i.e. evaporation will not be noticeable over the course of the experiment. Next, the N-I transition was measured for the common calamitic LC 5CB. A 1 mm × 0.1 mm capillary about 40 mm long was filled to 35±2mm with 5CB in the manner described above. The temperature was changed in 0.25°C intervals every 10 minutes with a picture taken at each temperature. The change in volume of 5CB as a function of temperature is shown in Fig. 4.6. The change in volume at the N-I transition for 5CB in terms of reduced volume was

found to be 0.0022 ± 0.0003, which is in good agreement with published values of 0.0021 ± 0.0001 [5]. The experimental value was found by summing the values of the points above the baseline thermal expansion at the N-I transition. This figure also shows that the thermal expansion of 5CB is relatively constant in both the N and I phases, and larger in the N phase than in the I phase. These results are in good agreement with those reported in Ref. [3]. Finally, ClPbis10BB was heated to 95°C to melt the crystal, then cooled to 89°C and allowed to sit for 14 hours with a picture being taken every 5 minutes. After the initial temperature equilibriation the meniscus did not change position over the 14 hours. This confirms that no evaporation was occurring over this time, and that no evaporation would occur over the course of the experiments (∼4 hours).

4.3 RESULTS AND DISCUSSION

A 1 mm × 0.1 mm capillary approximately 40 mm long was filled with ClPbis10BB to a height of 24 ± 1 mm in the manner described above. The sample was heated to 95°C to melt the crystal, then cooled to 75°C ($T_{N_TT} \cong 76.4$°C) then ramped up and down at a rate of 0.1°C / min. in the manner described above. Figure 4.7 shows the results of several heating and cooling scans on ClPbis10BB. The density change at the N_T-T transition is found by summing the points above the baseline thermal expansion using the average of the scans on heating and cooling. The reduced volume at the N_T-T transition is $6.4 \pm 0.5 \times 10^{-4}$ on heating and $5.5 \pm 0.4 \times 10^{-4}$ on cooling. There was a small hysteresis present upon cooling as the transition occurred at $T_{N_TT} = 76.4$°C on heating and at $T_{N_TT} = 76.2$°C on cooling. The volume change in ClPbis10BB is ∼4 times smaller than that found in a calamitic liquid crystal, such as 5CB, which agrees with the MB and DLS results that show the N_T-T transition to be much more

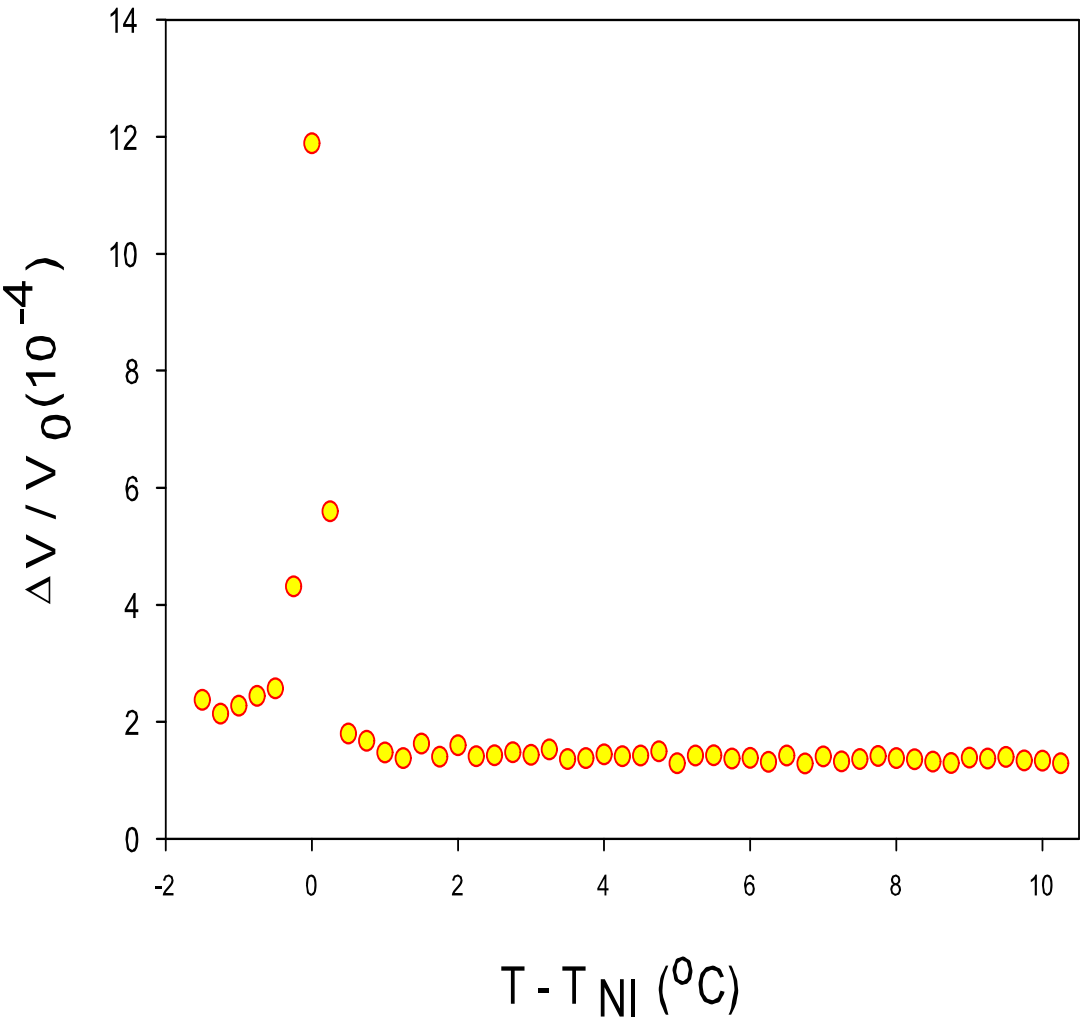

Figure 4.6: The change in volume for 5CB as it was heated through the clearing point. The N-I transition occurred at 34.7°C.

weakly first order than the N-I transition in calamitics.

Looking past the N_T-T transition there is no clear change in volume associated with the T-I transition. There are small peaks, on the order of the uncertainty, present at $\sim$ 3.5°C above the N_T-T transition in the heating and cooling scans. These peaks could not be clearly resolved with averaging, or any modifications to the experimental procedure or set-up. Although this experiment did not have the resolution to identify the T-I transition it can be used to place an upper limit on the size of the density change at the transition. The reduced volume change at the transition can be no larger than 1.6×10^{-4}, or about 25% of the N_T-T transition. The small volume change observed at the T-I transition in this experiment suggests that the transition, which was predicted to be first order [6], must be a weak first order transition. Impurities and temperature gradients in the sample, would make it difficult to isolate this transition using the method employed here.

A smaller capillary, 0.5 mm $\times$ 0.05 mm, was used with the ClPbis10BBs. This was done because the larger cell could not be filled via capillarity with this material. This could be due to a reduction in surface tension between the LC and glass due to the silane treatment. Regardless, the cell was approximately 40 mm in length and was filled with a 27 ± 1 mm column of ClPbis10BBs. This sample was heated to 95°C to melt the crystal, then cooled in to the N_T phase at 90°C where the scans were began in the manner described above. The reduced volume at the N_T-T transition was $9 \pm 2 \times 10^{-4}$ on heating and cooling (the uncertainty was larger in this measurement because of the difficulty in discerning beginning and ending points of the transition peak). The volume change in ClPbis10BBs is nearly twice as large as the one observed in ClPbis10BB, but still less than half of that observed in 5CB.

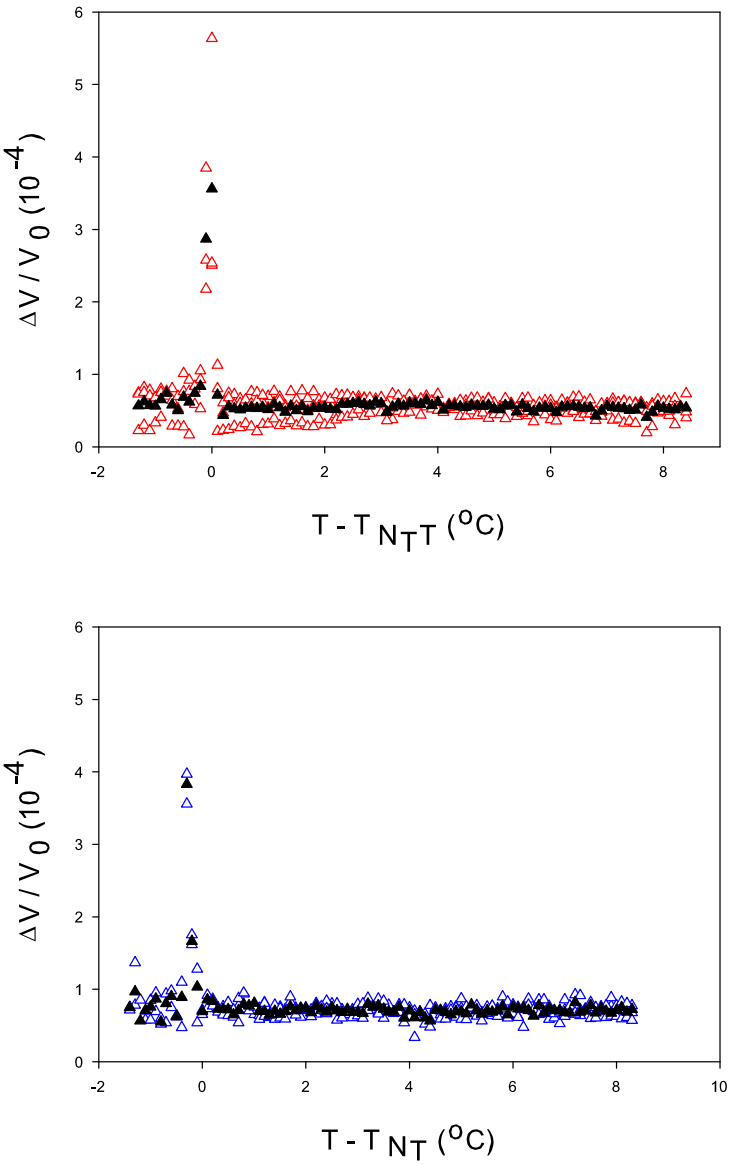

Figure 4.7: The change in volume for ClPbis10BB as a function of temperature. The empty triangles represent the data from three separate scans. The solid triangles represent the average of these scans. (top) The volume change on heating. The transition temperature on heating was found to be 76.4°C. (bottom) The volume change on cooling. The transition temperature on cooling was found to be 76.2°C.

The maximum reduced volume change possible at the T-I transition is very near the volume change due to thermal expansion, and is bounded at $\Delta V/V = 1.6 \times 10^{-4}$, similar to ClPbis10BB.

In this section the volume change at the N_T-T transition was shown to be 25 - 50% of that seen in calamitics such as 5CB at the N-I transition and an upper bound was placed on the volume change at the T-I transition. Although this method has limited resolution in its current embodiment, it is a valuable tool to gain information about liquid crystals when only a minimal amount of material is present.

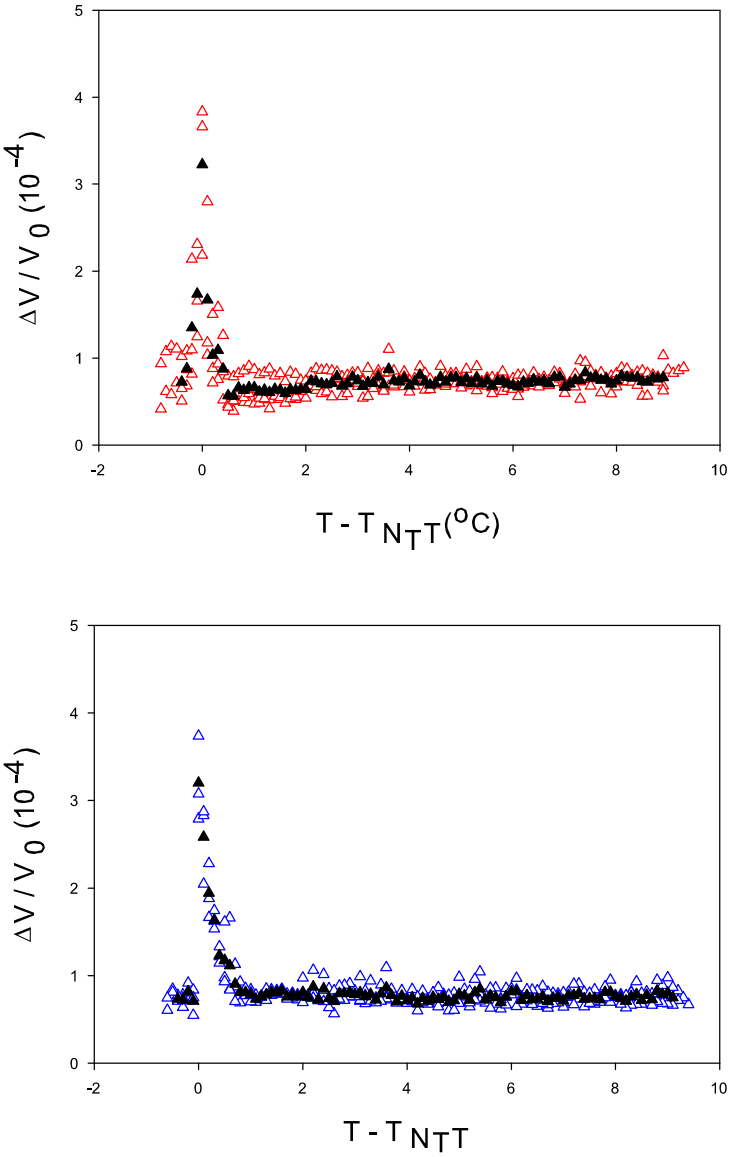

Figure 4.8: The change in volume for ClPbis10BBs as a function of temperature. The empty triangles represent the data from three separate scans. The solid triangles represent the average of these scans. (top) The volume change on heating. The transition temperature on heating was found to be 91.0°C. (bottom) The volume change on cooling. The transition temperature on cooling was found to be 90.9°C.

BIBLIOGRAPHY

[1] J. Zhang, Y. Zheng, and R. Tao. *Inter. J. Mod. Phs. B*, 16:4105, 2002.

[2] P. K. Mukherjee, T. R. Bose, D. Ghose, and M. Saha. *Phys. Rev. E*, 51:5745, 1995.

[3] D. A. Dunmar and W. H. Miller. *J. Phys. (Paris), Colloq.*, 40:C3–141, 1979.

[4] Lide. *Handbook of Chemistry and Physics.* CRC Press, 1998.

[5] G.A. Oweimreen, A.K. Shihab, K. Halhouli, and S.F. Sikander. *Mol. Cryst. Liq. Cryst.*, 138:327, 1986.

[6] L. Radzihovsky and T. C. Lubensky. *Europhys. Lett.*, 54:206, 2001.

CHAPTER 5

ELECTROHYDRODYNAMIC CONVECTION

5.1 BACKGROUND

Repetitive spatio-temporal structures, or patterns, are present in every aspect of life with an incredible diversity of size and structure. The stripes and spots that cover the coats of animals, the layout of cities, even the distribution of stars and galaxies within the universe are all examples of patterns. The incredible prevalence of patterns compels us to search for the underlying mechanisms that govern the formation of different types of patterns. The study of pattern formation in non-linear, dissipative systems driven out of thermodynamic equilibrium by an external stress is an old and very challenging field of physics that still has many unanswered questions. In some instances, this endeavor amounts to the solving of systems of non-linear partial differential equations, which is nearly impossible to do analytically except for a few specific cases. The difficulty in solving these equations makes the performance of very precise experiments on these systems a valuable tool for developing phenomenological theories and approximations to describe pattern formation mechanisms.

Rayleigh-Bernard convection (RBC) and Taylor Vortex Flow (TVF) are two examples of fluid dynamical systems that have been frequently studied with regard to pattern formation in systems with isotropic components (see [1] and Refs. within), while electrohydrodynamic convection (EHC) in nematic LCs has become a paradigm for pattern formation in anisotropic systems because of its large aspect ratio and easily manipulated control parameters.

In RBC, a fluid is confined between two parallel plates and is heated from below. The heating produces a temperature gradient between the plates. Below a certain critical value of the temperature difference (ΔT_c) heat is transported by conduction, above ΔT_c fluid starts to flow and convection rolls form. The control parameter for this experiment is given by the Rayleigh number

$$R_a = \frac{g\alpha\Delta T d^3}{\nu\kappa}, \tag{5.1}$$

where g is the acceleration due to gravity, α is the thermal expansion coefficient, d is the space between the plates, ν is kinematic viscosity, and κ is the thermal diffusivity. Generally, in an experimental situation ΔT is varied with the other parameters held constant. Many different patterns are possible depending on the conditions of the system, including straight rolls, hexagons, squares, and spirals (see [1] and Refs. within).

In TVF, a fluid is confined between two concentric cylinders with one or both cylinders rotating. The simplest case is when the inner cylinder is rotating and the outer cylinder is held fixed. Here, the dimensionless control parameter is the Taylor number

$$T = \frac{2r_i^2 d^3}{(r_i + r_o)(\Omega/\nu)^2}, \tag{5.2}$$

where r_i is the inner cylinder radius, r_o is the outer cylinder radius, d= $r_o - r_i$, Ω is the rotation rate of the inner cylinder, and ν is the kinematic viscosity. However, the stress applied to the system is often described by the Reynolds number

$$R = \frac{(r_o + r_i)r_i\Omega}{\nu}, \tag{5.3}$$

which is linear in Ω, the parameter that is generally controlled in experiments. Below a critical Reynolds number (R_c) the flow is smooth and axially uniform, above R_c

pairs of counter rotating rolls form along the axis of the cylinder.

The most widely studied theoretical model of EHC in calamitic nematic LCs is the standard model (SM), which explains pattern formation in LCs by the Carr-Helfrich mechanism [2, 3]. The original mechanism proposed by Helfrich gives a detailed treatment of EHC in one dimension [4]. This model was later extended to three dimensions [5, 6], it is this three dimensional model that I will refer to as the SM. The SM was later extended to explain experimental observations not predicted by the Carr-Helfrich mechanism. This extended model is known as the weak electrolyte model (WEM) [7]. In the remainder of this section, I will demonstrate the formation of the SM by deriving the one-dimensional model of Helfrich (which can be extended to three dimensions without loss of generality) and then show how it can be extended to the WEM following the explanation used by Dennin [1].

5.2 THE STANDARD MODEL

5.2.1 THEORETICAL BACKGROUND FOR THE STANDARD MODEL

Electrohydrodynamic convection in liquid crystals is generally studied with a calamitic nematic liquid crystal sandwiched between two parallel glass plates coated with a transparent conducting medium (usually indium tin oxide). The plates are separated by an inert spacer (usually mylar) to a distance d between 5 μm - 100 μm. The plates are treated to produce a specific alignment of the director either parallel (planar) or perpendicular (homoetropic) at the plates, which causes a bulk alignment of the liquid crystal due to energetic concerns (this will be discussed in more detail later). The nematic LC possess several properties that are relevant to EHC, namely its anisotropic material parameters, its elastic properties, and its viscosity tensor. The

nature of these properties needs to be reviewed before looking at the Carr-Helfrich model.

The dielectric constant ϵ, the magnetic susceptibility χ, and the electric conductivity σ are all anisotropic properties of the uniaxial nematic LC, which are important to EHC. These properties can be represented by the second-rank tensor

$$b_{ij} = b_{\perp}\delta_{ij} + b_a n_i n_j \tag{5.4}$$

where δ_{ij} represents the Kronecker delta, $b_a = b_{||} - b_{\perp}$ (with $b_{||}$ and $b_{\perp}$ being the values of the parameter parallel and perpendicular to the director, respectively), and n_i represents a component of the director. In this uniaxial case the anisotropic tensor has one component parallel to the director and two equal components perpendicular to the director. In most literature discussing EHC the signs of the dielectric and conductivity anisotropies are written in the compact notation (sign of ϵ_a, sign of σ_a). And the liquid crystal is then referred to as being $(++)$, $(+-)$, $(-+)$, or $(--)$.

THE MOLECULAR FIELD

There are three basic types of elastic deformations that occur in LCs, they are the splay, twist, and bend. Examples of these deformations can be seen in Fig. 5.1. The elastic behavior of a liquid crystal is best understood by looking at the free energy density of the material F. The contribution of the elastic deformations F_d to F is given by

$$F_d = \frac{1}{2}[K_{11}(\nabla\cdot\mathbf{n})^{\mathbf{2}} + K_{22}[\mathbf{n}\cdot(\nabla\times\mathbf{n})]^2 + K_{33}[\mathbf{n}\times(\nabla\times\mathbf{n})]^2] \tag{5.5}$$

where K_{11}, K_{22}, and K_{33} are known as the Frank elastic constants for the splay, twist, and bend, respectively [8]. The total free energy density may also contain interactions

with external magnetic and electric fields, at a constant temperature

$$F_m = -\int \mathbf{M}\cdot d\mathbf{H} = -\frac{1}{2}\chi_\perp H^2 - \frac{1}{2}\chi_a(\mathbf{n}\cdot\mathbf{H})^2 \tag{5.6}$$

and

$$F_e = -\int \mathbf{D}\cdot d\mathbf{E} = -\frac{1}{2}\epsilon_\perp\epsilon_0 E^2 - \frac{1}{2}\epsilon_a\epsilon_0(\mathbf{n}\cdot\mathbf{E})^2 \tag{5.7}$$

respectively. Here ϵ_0 is the permittivity. The terms in F_m and F_e that are independent of $\mathbf{n}$ are constant and therefore are generally not included in free energy calculations.

In equilibrium the free energy $\mathcal{F} = \int F d^3\mathbf{x}$ in the bulk must be minimized with respect to variations in $\mathbf{n}$ subject to the constraint $\mathbf{n}^2 = 1$. This extremum can be found using the Euler-Lagrange equations with Lagrange multipliers

$$\frac{\delta F}{\delta n_i} = \partial_j\left[\frac{\partial F}{\partial(\partial_j n_i)}\right] - \frac{\partial F}{\partial n_i} = -\lambda(\mathbf{x})n_i \tag{5.8}$$

where δ represents a functional derivative, $\partial_j = \partial/\partial j$, and $\lambda(\mathbf{x})$ is a Lagrange multiplier. Note the Einstein summation convention is used for all repeated indices. For notational purposes it is helpful to define the molecular field $\mathbf{h}$ [2], such that

$$h_i = \partial_j\left[\frac{\partial F}{\partial(\partial_j n_i)}\right] - \frac{\partial F}{\partial n_i}. \tag{5.9}$$

The equilibrium condition may then be written as $[h_i + \lambda(\mathbf{x})n_i] = 0$. For this statement to be true $\mathbf{n}$ and $\mathbf{h}$ must be parallel, and since the cross product of two parallel vectors must be zero, a required, but not complete, condition for equilibrium, independent of the Lagrange multiplier is

$$\mathbf{n}\times\mathbf{h} = 0. \tag{5.10}$$

The notation $\mathbf{h}_d$, $\mathbf{h}_m$, and $\mathbf{h}_e$ will be used to denote the contributions to the molecular field from the corresponding elastic, magnetic, and electric parts of the free energy density.

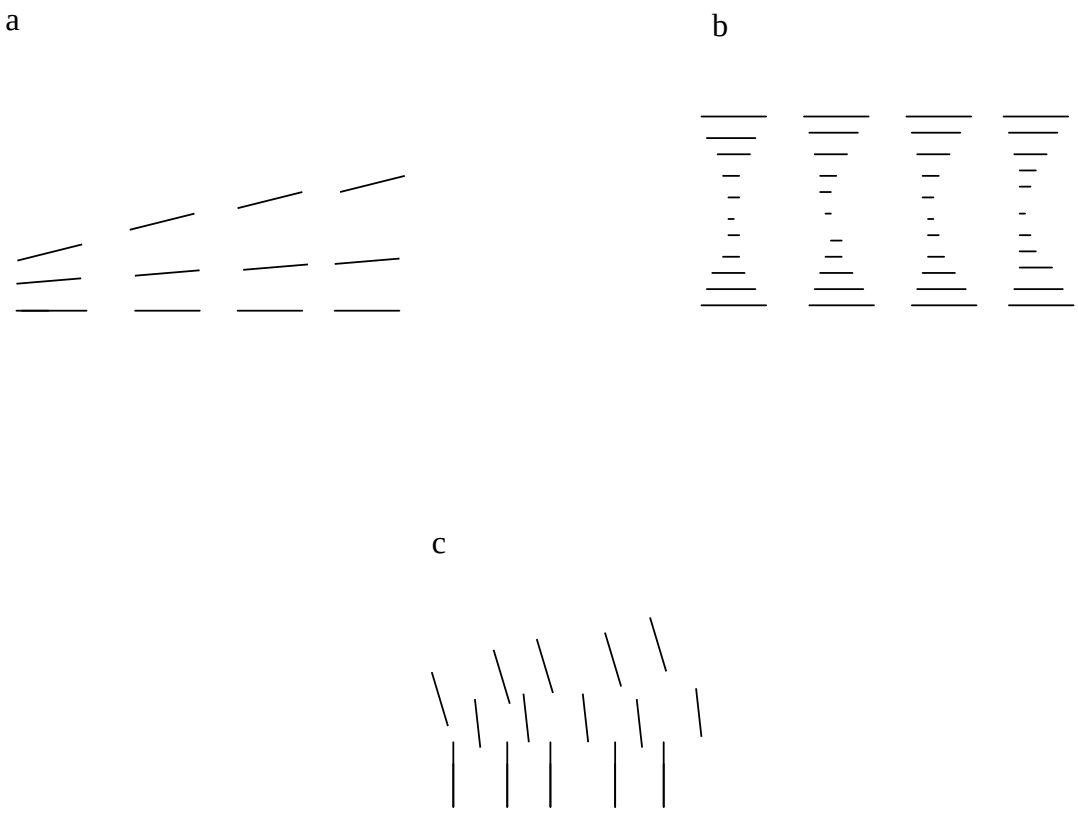

Figure 5.1: A schematic representation of the three basic elastic deformations. The thin lines represent the portion of the molecular director that is in the plane of the page. (a) Example of a pure splay deformation. (b) Example of a pure twist deformation. (c) Example of a pure bend deformation.

When discussing EHC it is beneficial to discuss director distortions in terms of torques, rather than free energies. The torque per unit volume $\mathbf{\Gamma}$ of the nematic system may be described in terms of the molecular field as

$$\mathbf{\Gamma} = \mathbf{n} \times \mathbf{h}. \tag{5.11}$$

This can be shown generally be using variational calculus, but the easiest way to see this principle is to look at an example, such as the case of a nematic LC at equilibrium in a uniform magnetic field, with no other external stresses. The torque due to a magnetic field when $\mathbf{M}$ and $\mathbf{H}$ are at an arbitrary angle to one and other is

$$\mathbf{\Gamma_m} = \mathbf{M} \times \mathbf{H} = \chi_a(\mathbf{n} \cdot \mathbf{H})\mathbf{n} \times \mathbf{H} \tag{5.12}$$

where $\mathbf{M} = \chi_\perp \mathbf{H} + \chi_a(\mathbf{n} \cdot \mathbf{H})\mathbf{n}$ is the magnetization of the LC. Putting Eq. 5.6 into Eq. 5.9 yields

$$\mathbf{h_m} = \chi_a(\mathbf{n} \cdot \mathbf{H})\mathbf{H}. \tag{5.13}$$

In this case Eq. 5.10 has a component from the elastic deformation and the magnetic field

$$\mathbf{n} \times \mathbf{h_d} + \mathbf{n} \times \mathbf{h_m} = 0. \tag{5.14}$$

Inserting the value of $\mathbf{h_m}$ from Eq. 5.13 into Eq. 5.14 gives

$$\mathbf{n} \times \mathbf{h_d} + \chi_a(\mathbf{n} \cdot \mathbf{H})\mathbf{n} \times \mathbf{H} = 0. \tag{5.15}$$

or

$$\mathbf{n} \times \mathbf{h_d} = -\mathbf{\Gamma_m}. \tag{5.16}$$

From this it can be seen that the torques in the system must sum to zero for the system to be in equilibrium. This is also the principle that is used to achieve alignment in

the sandwich type cells used to study EHC. By fixing the LC at the plates an elastic torque is created which causes the molecules in bulk to orient in a preferred direction of minimum energy.

NEMATODYNAMICS

The Navier-Stokes equation describes the motion of the nematic fluid

$$\rho(\partial_t v_i + (\mathbf{v}\cdot\nabla)v_i) = \partial_j t_{ji} + f_i \tag{5.17}$$

where ρ is the density, v_i are the components of the velocity, f_i are body forces, and t_{ji} are the elements of the stress tensor. The stress tensor contains a contribution from the hydrostatic pressure, a stress component connected with the free energy, and a viscous component σ_{ij} [2]. In EHC calculations the first two terms are neglected and the viscous component is usually written in terms of the Leslie coefficients α_i [9]

$$\begin{aligned}\sigma_{ij} = \alpha_1[n_i n_j n_l n_k A_{kl}] + \alpha_2[n_i N_j] \\ +\alpha_3[n_j N_i] + \alpha_4[A_{ij}] \\ +\alpha_5[n_i n_k A_{kj}] + \alpha_6[n_j n_k A_{ki}]\end{aligned} \tag{5.18}$$

where $A_{ij} = \frac{1}{2}(\partial_i v_j + \partial_j v_i)$ and $\mathbf{N} = \partial\mathbf{n}/\partial t + (\mathbf{v}\cdot\nabla)\mathbf{n} - \omega\times\mathbf{n}$, with $\omega = \frac{1}{2}\nabla\times\mathbf{v}$. There are actually only five independent α_i because of the Onsager relation, which can be used to eliminate one of the variables: $\alpha_6 - \alpha_5 = \alpha_2 + \alpha_3$.

The viscous stresses exert a torque Γ_ν on the director field given by [10]

$$\Gamma_i^\nu = \sigma_{jk} - \sigma_{kj} \tag{5.19}$$

or in terms of vectors

$$\mathbf{\Gamma}_\nu = -\mathbf{n}\times(\gamma_1\mathbf{N} + \gamma_2\mathbf{n}\cdot A). \tag{5.20}$$

where $\gamma_1 = \alpha_3 - \alpha_2$ and $\gamma_2 = \alpha_6 - \alpha_5 = \alpha_2 + \alpha_3$. (Remember that A is a second-rank tensor.) Looking at Eqs. 5.11 and 5.20 one can see that the total torque can be written as

$$\mathbf{\Gamma} = \mathbf{n} \times [\mathbf{h} - (\gamma_1 \mathbf{N} + \gamma_2 \mathbf{n} \cdot A)]. \tag{5.21}$$

5.2.2 THE CARR-HELFRICH MECHANISM

Now we are ready to examine the Carr-Helfrich mechanism. The original one-dimensional case of Helfrich [4] was formulated for a nematic LC with enough ionic impurities to provide a non-zero conductivity σ, a positive σ_a, a negative to slightly positive ϵ_a, and an initial planar orientation. The electric field is applied in the direction perpendicular to the plates. In practice an *ac* electric field is used to avoid electrode effects, but here we will use a dc field as it somewhat simplifies the explanation and it very clearly carries over to the case of low frequency applied *ac* fields with the same basic mechanism describing both situations.

The usual set up for an experiment involving the Carr-Helfrich mechanism is shown in Fig. 5.2. The direction perpendicular to the two conducting plates is the z-axis, the x-axis is set in the direction of the initial director alignment (the rubbing direction of planar treated cell plates), and the y-axis is perpendicular to the other two axes. The angle ϕ represents the orientation of the director with respect to $\hat{\mathbf{x}}$, in the $x - z$ plane. The applied electric field $\mathbf{E}$ is in the z-direction.

The SM predicts two distinct frequency dependent EHC regimes for the case of an applied *ac* electric field, $\mathbf{E} = (\sqrt{2}V/d)\cos(\omega t)\hat{\mathbf{z}}$, where V is the voltage applied across the cell plates and ω is the frequency of the applied voltage. The regimes are separated in frequency by a point known as the cutoff frequency. The conduction regime exists at frequencies lower than the cutoff frequency. In the conduction regime

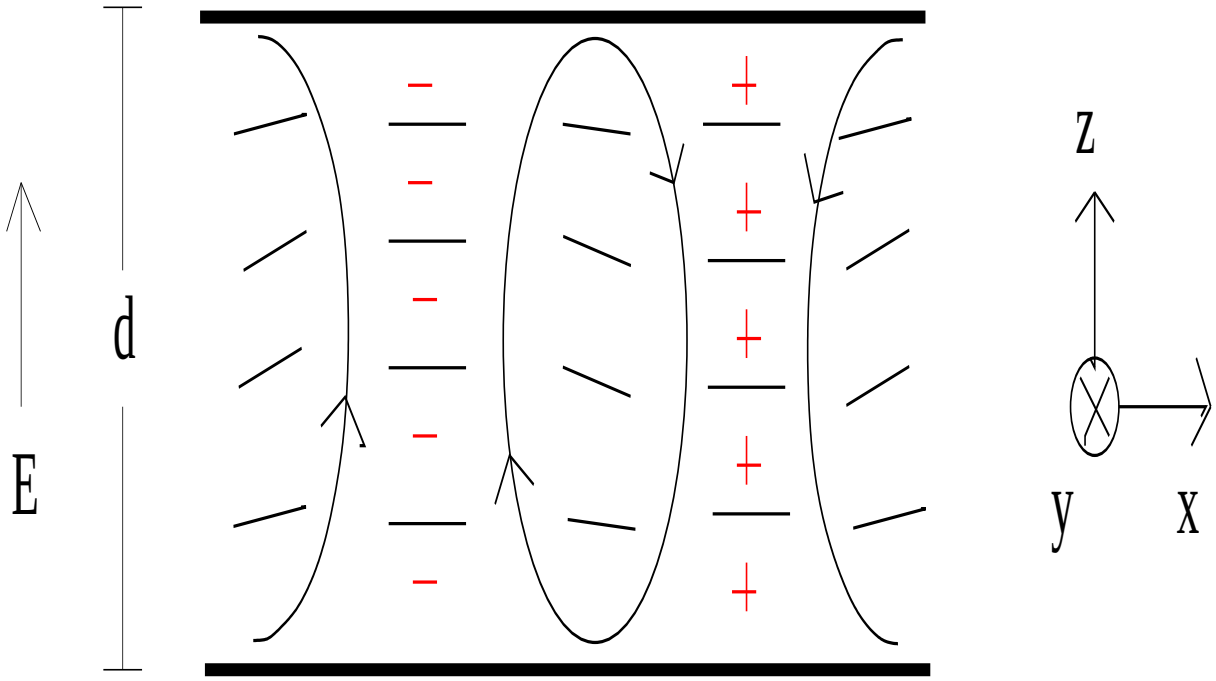

Figure 5.2: An example of EHC for a $(-+)$ material in a planar alignment in the conduction regime. The rotation of the molecules in the x-z plane is represented by the black lines. The flow is represented by the arrows. The space charge distribution is represented by the red symbols.

the ionic impurities follow the applied field, and the director orientation and the flow are essentially time independent. The SM predicts that the instability of this regime will spontaneously produce stationary roll patterns with wavelength $\lambda \approx d$ whose wave vector is parallel (normal rolls) to the director below a cut-off frequency called the Lifshitz point, and at an angle (oblique rolls) to the director above the Lifshitz point.

Above the cutoff frequency is the dielectric regime. Here the director and the flow velocity oscillate at the frequency of the applied field ω, but the charge density of the ionic impurities along $\hat{\mathbf{x}}$ is essentially constant in time. The SM calls for stationary roll patterns with orientation similar to that of the conduction regime, but with $\lambda < d$ in the dielectric regime. The cutoff frequency is related to the charge relaxation time $\tau_q = \epsilon_0 \epsilon_a / \sigma_\perp$ and the director relaxation time $\tau_d = \gamma_1 d^2 / \pi^2 (K_{11} + K_{33})$ [5]. The conduction regime corresponds roughly to the conditions $\omega \tau_d \gg 1$ and $\tau_d \gg \tau_q$. Now I will present the description of the Carr-Helfrich mechanism for the conduction regime, the Carr-Helfrich mechanism also explains the dielectric regime when extended to cover time-dependent behavior [11].

The relevant equations used to derive the SM are the Navier-Stokes (Eq. 5.17), with the body force $f_i = \rho_e E_i$; the conservation of angular momentum, illustrated by the balance of torques (Eq. 5.21); the incompressibility of the nematic LC

$$\nabla \cdot \mathbf{v} = 0, \tag{5.22}$$

the equations of electrostatics

$$\nabla \cdot \epsilon_0 \epsilon \mathbf{E} = \rho_e, \tag{5.23}$$

$$\nabla \times \mathbf{E} = 0,$$

and charge conservation

$$\nabla \cdot \mathbf{j} + \partial_t \rho_e = 0 \tag{5.24}$$

where ρ_e is the charge density of ionic impurities, ϵ is the dielectric tensor, ϵ_0 is the dielectric constant in vacuum, and $\mathbf{j} = \sigma \mathbf{E} + \rho_e \mathbf{v}$ is the electric current.

In the one-dimensional case considered by Helfrich [4] the director has planar alignment and is confined to the $x - z$ plane. The displacement of the director is in $\hat{\mathbf{z}}$ and is considered to be small, such that $\cos\phi \approx 1$ and $\sin\phi \approx \phi$. The local director orientation is described by $\mathbf{n}$=[1,0,ϕ] (note that in the one-dimensional case all position dependent variables, e.g. ϕ, are only dependent on x). A uniform dc electric field is applied in the z-direction. (See Fig. 5.2.) Although Helfrich [4] addressed the situation where $\epsilon_a \leq 0$, I will simplify the situation by following the convention used by Dennin [1] and setting $\epsilon_a = 0$. This choice eliminates the dielectric torques from the situation, but leaves the qualitative features of the instability virtually unchanged.

In this case the electric field produces a current in the x-direction given by $I_x = \sigma_a E_z \phi$, which leads to an x-dependent charge density due to the separation of positive and negative ions. The localized accumulation of positive, or negative, charge generates an electric field in $\hat{\mathbf{x}}$, E_x, which produces an opposing current in $\hat{\mathbf{x}}$, $I_x = \sigma_{||} E_x$. Applying Eq. 5.24 to the situation that is not varying in time gives the relation between the currents in the x direction

$$\sigma_{||} \partial_x E_x = -\sigma_a E_z \partial_x \phi. \tag{5.25}$$

Now, using this relation and Eq. 5.23 the space charge density due to E_z can be found by looking at the field E_x generated by this space charge density

$$\rho_e = \epsilon_0 \epsilon \partial_x E_x = -\epsilon_0 \epsilon \frac{\sigma_a}{\sigma_{||}} E_z \partial_x \phi. \tag{5.26}$$

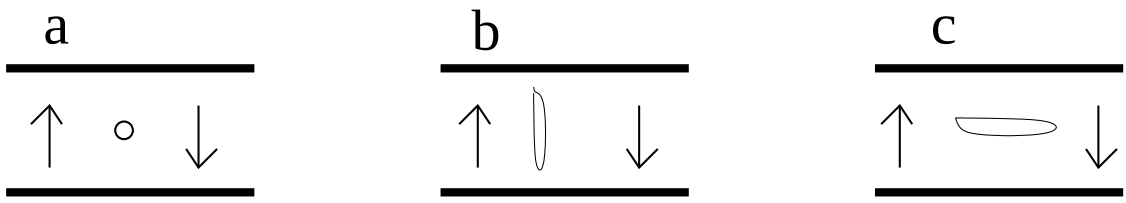

Figure 5.3: Three geometries of director and fluid velocity for which the viscosity reduces to the form for an isotropic fluid, $\eta\nabla^2\mathbf{v}$. The arrows represent the direction of the velocity. (a) The director is perpendicular to the plane of the paper, $\eta = \alpha_4/2$. (b) The director is vertical, $\eta = (\alpha_4 + \alpha_3 + \alpha_6)/2$. (c) The director is horizontal, $\eta = (\alpha_4 + \alpha_5 - \alpha_2)/2$.

This gives the body force on the fluid that appears in Eq. 5.17, $E_z\rho_e$.

The resulting flow and director orientation in this situation allows the viscous contribution to Eq. 5.17 to be reduced to the form for an isotropic fluid $\eta\nabla^2\mathbf{v}$, where η is a combination of the Leslie coefficients $\eta = (\alpha_4 + \alpha_5 - \alpha_2)/2$. (See Fig.5.3 for a description of the flow.) For a constant flow, assuming that the viscous term in Eq. 5.17 is much larger than the $(\mathbf{v}\cdot\nabla)\mathbf{v}$ term, Eq. 5.17 reduces to

$$\eta\partial_x^2 v_z + E_z\rho_e = 0 \tag{5.27}$$

or

$$\eta\partial_x^2 v_z = E_z^2\epsilon_0\epsilon\frac{\sigma_a}{\sigma_{||}}\partial_x\phi. \tag{5.28}$$

Considering only a single Fourier mode with wavenumber q, $\partial_x^2 v_z = iq\partial_x v_z$. Then Eq. 5.28 can be written as

$$iq\eta\partial_x v_z = E_z^2\epsilon_0\epsilon\frac{\sigma_a}{\sigma_{||}}\partial_x\phi. \tag{5.29}$$

The viscous torque due to the flow in the z-direction can be found from Eq. 5.20 to be $\mathbf{\Gamma}_\nu = \alpha_2\partial_x v_z\hat{\mathbf{y}}$, keeping only the lowest order ϕ terms. For LCs used in EHC α_2 is

negative, therefore the viscous contribution to the torque is always destabilizing (see Fig. 5.4). The viscous torque is opposed by the elastic torque, which can be found using Eqs. 5.9 and 5.11 to be $\mathbf{\Gamma_d} = -K_{33}\partial_x^2\phi\hat{\mathbf{y}}$ (again assuming that $\epsilon_a = 0$, which removes the electrical contribution to the elastic torque, and keeping only lowest order ϕ terms). As the applied electric field is increased (i.e. the flow velocity is increased) a critical field E_c will be reached such that the total torque will be zero and a situation of dynamic equilibrium is created. At the critical field the viscous and elastic torques are related such that

$$K_{33}\partial_x^2\phi = \alpha_2\partial_x v_z. \tag{5.30}$$

Replacing $\partial_x v_z$ in Eq. 5.30 with Eq. 5.29 and using $\partial_x^2\phi = iq\partial_x\phi$ one can solve for E_c

$$E_c^2 = -\frac{K_{33}\sigma_{\|}\eta q_c^2}{\alpha_2\epsilon_0\epsilon\sigma_a} \tag{5.31}$$

where q_c is the critical wave number. Experiments and detailed linear stability analysis suggest that $q_c \approx \pi/d$ [1,12]. Using this relation and expressing the critical field in terms of a critical potential

$$V_c^2 = E_c^2 d^2 = -\frac{\pi^2 K_{33}\sigma_{\|}\eta}{\alpha_2\epsilon_0\epsilon\sigma_a}. \tag{5.32}$$

Although this simple model does not give a good quantitative prediction for EHC it accurately illustrates the essential physical features of the Carr-Helfrich mechanism. This model shows that anisotropic conductivity and director fluctuations are needed to create a charge density in order for EHC to occur. Also, because of the observed d dependence of the critical field, V^2 is the preferred control parameter. Even when the full equations of motion are used in three-dimensions the basic structure of the mechanism remains nearly the same as it is here.

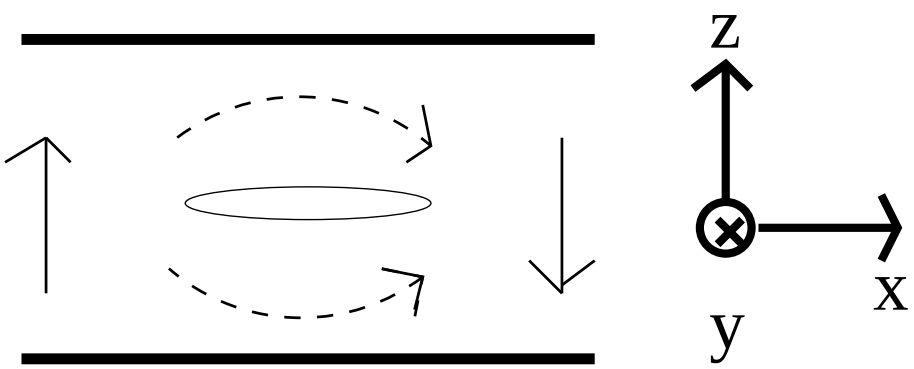

Figure 5.4: The director is parallel to the shear and perpendicular to the direction of the velocity. The solid arrow represents the direction of the velocity. The dashed arrow represents the initial direction of motion of the director, where the to line is for positive α_2 and the bottom line is for negative α_2.

The model described above, also, did not deal with applied *ac* fields. The frequency of the field has a significant impact on the type of pattern expressed by the LC and needs to be considered. Frequency often separates different EHC regimes that might possess very different properties, for example the conduction and dielectric regimes mentioned earlier. In the lower frequency conduction regime, V_c shows a strong frequency dependence and does not vary with d. In the dielectric regime, V_c shows a relatively weaker frequency dependence, $V_c \propto \omega^{1/2}$, a dependence on d.

5.2.3 THE WEAK ELECTROLYTE MODEL

The SM predicts that only stationary roll patterns will occur in $(-+)$ uniaxial nematic LCs. However, patterns of traveling rolls, called a Hopf bifurcation, have been seen in $(-+)$ uniaxial nematic LCs as well (see [10] and Refs. within). The WEM [7] is an extension of the SM, which has been shown to quantitatively describe Hopf bifurcations in several materials [13–15]. In the SM the conductivity was assumed

to be frequency independent, and electric fields and currents were related by Ohm's Law, subsequently no combination of variables predicted traveling rolls. In the WEM a dissociation-recombination reaction for the positive and negative ions is considered, which when taken into account allows for a non-zero Hopf frequency to occur at the onset of EHC under certain conditions. (See [1] and Refs. within for a complete description of the WEM.)

The SM and WEM have also been extended to describe EHC in situations not originally considered by Helfrich [10, 12]. The SM has been used to describe roll patterns for a material with an initial homeotropic alignment (the long axes are oriented perpendicular to the cell plates) and $(+-)$ anisotropies. Here, after a Freedericksz transition has been induced, the situation reduces to a one similar to that of a $(-+)$ material with an initial planar alignment. As mentioned earlier the SM predicts EHC for a $(++)$ planar system where ϵ_a is very small $(\epsilon_a/\epsilon_\perp < 0.06)$ [12], it also can be used to predict EHC in a homeotropic aligned $(--)$ system with a small ϵ_a $(\epsilon_a/\epsilon_\perp > -0.1)$ [12]. Also, a weakly non-linear analysis of the WEM [16] has been shown to explain the origin of sets of traveling oblique rolls, or spatiotemporal chaos.

5.3 ELECTROHYDRODYNAMIC CONVECTION IN A BENT-CORE LIQUID CRYSTAL

5.3.1 INTRODUCTION

There exist several examples of experimentally observed EHC patterns that do not fit into any extension of the SM or WEM [12]. Two examples of such systems are the wide stripe, or prewavy, domains (PW) and non-standard parallel stripes (PS). The PS has been observed in several $(--)$ calamitic materials with planar

orientation [17, 18]. The PS consists of patterns of oblique rolls whose wavevector runs roughly perpendicular to $\hat{\mathbf{x}}$ with wavelengths on the order of d. The direction of the rolls in the PS regime clearly distinguishes it from SM type behavior.

The PW instability has been observed in both planar and homeotropic alignments and in several different combinations of anisotropies [19–30]. The PW pattern consists of alternating dark and bright rolls. The wavevector for the PW pattern is parallel to $\hat{\mathbf{x}}$, with a wavelength $\lambda \sim 4d$–$8d$. The PW instability is best viewed between crossed polarizers, which suggests a periodic modulation of the director in the xy-plane. The long wavelength and the director modulation in the xy-plane distinguish the PW from the SM.

As I mentioned earlier bent-core liquid crystals have been the subject of a great deal of research in the last few years, even developing into a separate sub-field of liquid crystal research, but still little work has been done on EHC in bent-core nematics. In the following sections I will detail the characteristics of two cases of non-SM EHC, the PW and the PS, along with a frequency region void of EHC, in a bent-core nematic LC. First, I will discuss the experimental set-up and methods used in this study. Then I will present the measured physical parameters of the bent-core LC that are relevant for EHC. Finally, I will give the characterization of the EHC instabilities in order of their appearance with increasing driving frequency.

5.3.2 EXPERIMENTAL SET-UP AND DETERMINATION OF THE MATERIAL PARAMETERS

The experiments were performed on the bent-core liquid crystal 4-chloro-1,3-phenylene bis4-[4'-(9-decenyloxy)benzoyloxy]benzoate (ClPbis10BB) [31] synthesized

at the Hungarian Institute for Solid State Physics and Optics. ClPbis10BB exhibits a monotropic nematic phase upon cooling. The phase sequence on cooling is $I \rightarrow 80°\text{C} \rightarrow T \rightarrow 77°\text{C} \rightarrow N_T \rightarrow 53°\text{C} \rightarrow SmC \rightarrow 48°\text{C} \rightarrow Cr$. This compound, with no added impurities, was placed in commercially obtained sandwich type cells [32] with d of 10 μm to 50 μm. (The addition of impurities would not only change σ, but could also change such things as transition temperatures, critical voltages, and cut-off frequencies. Therefore, it is beneficial to first attempt to understand the behavior of a relatively pure sample of a new material, then to add impurities in a controlled manner and monitor there effect, if one so chooses.) The spacing of the cell plates was measured to less than a micron using a spectrometer to analyze interference peaks. The cells were filled by placing ClPbis10BB in its crystal state on the ledge of the cell, then heating the cell to $\sim$5°C above its clearing point using a hot plate. Once, in the isotropic phase the liquid crystal entered the cell via capillarity. This process was carried out inside a laminar flow hood to avoid contamination of the sample. The surfaces of the cells were coated with transparent electrodes (indium tin oxide). The area of the conducting regions ranged from 100 mm^2 on the 10 μm cell to 50 mm^2 on the 50 μm cell. Cells for all EHC and splay Freedericksz transition measurements were treated for planar alignment unless otherwise noted.

All optical measurements were made using either a Zeiss Axiovert or a Nikon Optiphot polarizing microscope and a Panasonic CCD camera with a frame grabber. For these measurements the temperature was stabilized to $\pm$0.1°C using an Instec HS-1 hot stage. An *ac*-voltage was sustained across the plates of the cell by means of a Hewlett Packard 33120A function generator and a Krohn-Hite DCA-10 amplifier. The magnitude of the potential difference was monitored using a Hewlett-Packard

$T_{N_TT} - T(^\circ\text{C})$	$\epsilon_\perp$	$\epsilon_\parallel$	K_{11}(N)	K_{33}(N)
7.1	6.85	5.20	2.23 x 10^{-12}	2.37 x 10^{-12}

$\sigma_\perp$(1/Ohm·m)	$\sigma_\parallel$(1/Ohm·m)	χ_a(SI)	γ_1(Pa·s)
1.58 x 10^{-7}	1.57 x 10^{-7}	1.76 x 10^{-7}	2.67

Table 5.1: Material properties of ClPbis10BB. The electric transport properties were measured at a probe frequency of 1 kHz.

34401A digital multimeter in *ac*-voltage mode. This potential subjected the liquid crystal to an applied electric field $\mathbf{E} = (\sqrt{2}V/d)\cos(\omega t)\hat{\mathbf{z}}$.

In order to examine the EHC instabilities in ClPbis10BB, the physical parameters relevant to EHC were measured. I measured the dielectric constants ϵ and the conductivities σ. While the splay K_{11} and bend K_{33} elastic constants, the anisotropy of the diamagnetic susceptibility χ_a, and the rotational viscosity γ_1 were measured by J. T. Gleeson [33]. The results of these measurements are presented in Table 5.1.

The determination of the clearing point was the first measurement made on each sample. The clearing point was found within $\pm 0.1^\circ$C by melting the sample, then cooling the sample below the clearing point, and then slowly heating the sample until it became black between crossed polarizers (it became optically isotropic). Many of the other measurements made on the sample involved the use of magnetic field induced Freedericksz transitions in various geometries. I will describe the theory behind Freedericksz transitions, and then discuss the material parameter measurements.

FREEDERICKSZ TRANSITIONS

The critical field H_c, or the field at which the molecules begin to reorient in the direction of the field, can be derived for the different geometries using free energy considerations. I will follow the arguments of Ref. [3] in doing this. Consider the

general situation where the LC is confined between two parallel plates that are separated by a distance d in the z-direction (the bottom plate is located at $z = 0$ and the top plate is at $z = d$). The initial director orientation can be either planar or homeotropic. Now starting from an initially unperturbed state, with the director in the $\mathbf{n_0}$ direction, when a magnetic field $\mathbf{H}$ is applied perpendicular to $\mathbf{n_0}$ the director is a deflected such that

$$\mathbf{n} = \mathbf{n_0} + \delta\mathbf{n}(\mathbf{r}) \tag{5.33}$$

where $\delta\mathbf{n}(\mathbf{r})$ is normal to $\mathbf{n_0}$ and parallel to $\mathbf{H}$. The distortion $\delta\mathbf{n}(\mathbf{r})$ will only depend on z. Then the distortion energy, given in Eq. 5.5, reduces to

$$F_d = \frac{1}{2}K_i(\frac{\partial\delta\mathbf{n}}{\partial z})^2 \tag{5.34}$$

where $i = 1$ for an induced splay, $i = 2$ for an induced twist, and $i = 3$ for an induced bend. The magnetic contribution to the free energy, from Eq. 5.6, is

$$F_m = -\frac{1}{2}\chi_a H^2 \delta\mathbf{n}^2. \tag{5.35}$$

Assuming strong anchoring at the boundaries, $\delta\mathbf{n}(\mathbf{r})$ must go to zero at $z = 0$ and $z = d$. Then $\delta\mathbf{n}(\mathbf{r})$ can be expanded in a Fourier series

$$\delta\mathbf{n} = \sum_q \delta n_q \sin(qz) \tag{5.36}$$
$$q = \nu\frac{\pi}{d}$$

where ν is a positive integer. Putting this into the free energy and integrating over the thickness gives (per cm^2 of the slab of liquid crystal)

$$\mathcal{F} = \frac{d}{4}\sum_q \delta\mathbf{n_q}^2(K_i q^2 - \chi_a H^2). \tag{5.37}$$

For the unperturbed state to be stable, the change in free energy $\mathcal{F}$ must be positive for all values of δn_q, that is

$$K_i q^2 > \chi_a H^2. \tag{5.38}$$

The smallest value of q is $q = \pi/d$, which gives a threshold field of

$$H_{c,i} = \frac{\pi}{d}(\frac{K_i}{\chi_a})^{1/2}. \tag{5.39}$$

MATERIAL PARAMETERS

Two sets of measurements of electrical transport properties were made by monitoring the capacitance C and conductance g of planar-aligned samples as they underwent the magnetic field induced Freedericksz transition. The first set was made by J. T. Gleeson using an auto-balancing Andeen Hagerling 2500A capacitance bridge with a probe frequency of 1 kHz. The capacitance and loss of a $d = 55.1\mu$m thick sample with a 50 mm^2 electrically active area were measured as the magnetic field was swept from 0 to 13.5 kG. The sample was held in a homemade copper oven whose temperature was controlled to ± 0.1°C by a Lake Shore 331 temperature controller using a platinum RTD to monitor the temperature. The oven was placed between the pole faces of an electromagnet with the normal to the cell faces perpendicular to the pole faces of the magnet. A PC using a custom program written in the Yorick language was used to record the capacitance and control the temperature and magnetic field. At this thickness we were able to reach approximately 6-7 times the Freedericksz threshold field H_c. At $H = 0$ the perpendicular components, $\epsilon_\perp$ and $\sigma_\perp$, could be directly calculated from the measured capacitance and loss by means of the simple electrodynamics equations

$$C_\perp = \frac{\epsilon_\perp \epsilon_0 A}{d} \tag{5.40}$$

and

$$\frac{1}{g_\perp} = \frac{d}{\sigma_\perp A} \tag{5.41}$$

where A is the active conductive area on the cell plates. Then from data at $H >> H_c$ we could accurately extrapolate to infinite field, and thus obtain the parallel components, $\epsilon_\parallel$ and $\sigma_\parallel$, using formulas analogous to those above. An example of such data is shown in Fig. 5.5. (The oscillations in the conductance plot in Fig. 5.5 are caused by temperature oscillations. The temperature was stable to about 6 mK in this experiment, which led to small (less than 0.4%) oscillations in g. The only reason these are visible is because g only changes by around 1% over the entire range of magnetic field.) Then the value of H_c can be used to determine χ_a (dimensionless cgs volume susceptibility) from Eq. 5.39 once the Frank elastic constants are determined. A numerical fit of the $C(H)$ curve just above onset can be used to find the ratio K_{33}/K_{11} [34].

The second measurement used a Quadtech 1920 frequency scanning LCR meter to obtain the conductance and dielectric constants. For this measurement a $d = 25\mu$m cell with a 25 mm^2 conducting area was used. This sample was placed in a homemade copper oven whose temperature was controlled to $\pm 0.1^\circ$C by a Lake Shore 331 temperature controller using a platinum RTD to monitor the temperature. The oven was place between the pole faces of an electromagnet with the normal to the cell faces normal to the pole faces of the magnet. At this thickness the magnetic field could only be raised to 2-3 H_c (13.5 kG), which did not allow for an accurate extrapolation to infinite field. Therefore, these measurements could not give precise quantitative values for the parallel components of ϵ and σ, but they could provide information about the signs of ϵ_a and σ_a as a function of frequency. As I discussed in the previous

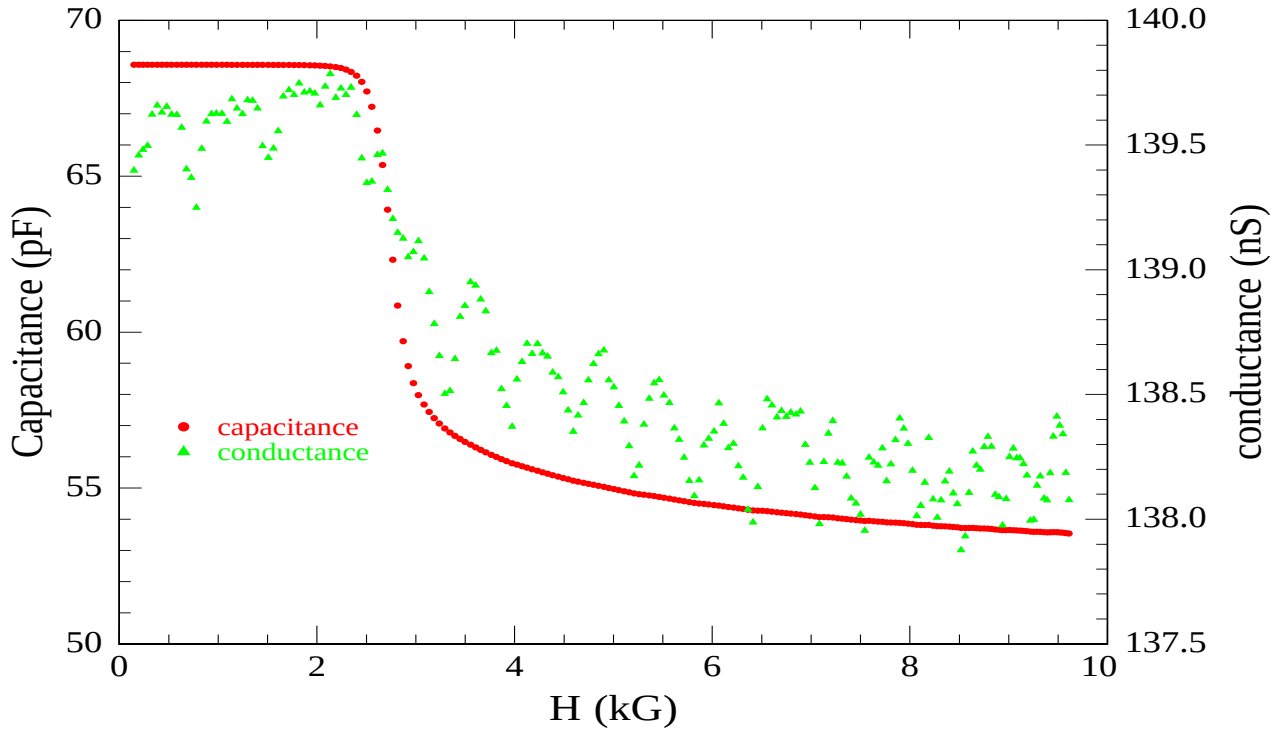

Figure 5.5: Example of the variation of the measured capacitance and conductance with magnetic field, at a temperature of 70°C.

section, the signs of the dielectric and conductivity anisotropies play an important role in determining the type of mechanism that is driving pattern formation. For example, the SM mechanism only is applicable in a planar alignment with $(-+)$ - $(0,+)$ anisotropies. So, knowing the signs of the anisotropies provides valuable information about what sorts of mechanisms might be present in a given situation.

The LCR meter was used to measure ϵ and σ at temperatures of 70°C, 75°C, and 77°C at frequencies from 1 Hz to 100 kHz in zero field and 13.5 kG. The sampling was done on a logarithmic scale over the entire frequency range. The LCR meter was controlled by a custom program in the Labview language. ϵ_a was found to be negative at all temperatures and frequencies. However, σ_a showed a strong frequency dependence, and it exhibited some unique features not usually seen in calamitics. The conductivity anisotropy was negative below $\sim$ 1.5 kHz, then positive between about 1.5 kHz and 8 kHz, and then negative again at frequencies above $\sim$ 8 kHz (see Fig. 5.6). The location of the frequencies where the sign inversions of σ_a occur show a marked temperature dependence, with both sign inversion frequencies shifting toward higher f as the temperature is increased. The lower sign inversion frequency falls into the range $1500 - 1900$ Hz, the upper sign inversion occurs between $8100 - 11000$ Hz. This temperature dependence of the inversion frequency is shown in Fig. 5.11. Measurements on the $d = 55.1\mu$m sample using the capacitance bridge at 1 kHz confirm this behavior. In the $d = 55.1\mu$m sample, the relative conductivity anisotropy, $\sigma_a/\sigma_\perp$, was found to be $\sim$0.09 in magnitude and positive at temperatures well below the clearing point. At about 3 degrees below the clearing point the conductivity anisotropy became negative, which corresponds to the lower frequency sign inversion seen in the 25μm sample.

The double sign inversion of σ_a can likely be attributed to a dielectric relaxation process occurring in the specified frequency range. The dielectric loss has a frequency dependent contribution to the conductivity, which has a maximum at the relaxation frequency f_r and decays when moving to either higher or lower f. The loss due to the relaxation in the parallel component can raise $\sigma_{||}$ enough to induce the change from $\sigma_a < 0$ to $\sigma_a > 0$ and back near f_r. The relaxation in the parallel component should be accompanied by a reduction of $\epsilon_{||}$. And indeed, the capacitance of the cell with the magnetic field on showed a slight decrease as frequencies were increased, while no significant frequency dependence was found in the field off case (i.e. for $\epsilon_\perp$ and $\sigma_\perp$). Dielectric relaxation frequencies of nematics are generally in the MHz range (see [35] and references therein). An f_r at about 4kHz (as shown in Fig. 5.6) is quite unusual. The rare cases in which nematics are known to exhibit relaxation in the kHz range are, however, characterized by a (single) sign inversion of ϵ_a, and they show no change in the sign of σ_a, i.e. they exhibit a different behavior than the ClPbis10BB.

The director relaxation time [10]

$$\tau_d = \gamma_1 d^2 / K_{11} \pi^2 \tag{5.42}$$

was obtained by using the capacitance bridge to monitor changes in capacitance as the magnetic field is raised above the critical field. For this measurement the 55.1 μm cell was placed in a homemade copper oven controlled by a Lake Shore 331 temperature controller using a platinum RTD, which was placed between the pole faces of an electromagnet with the normal to the cell plates normal to the pole faces of the magnet. Although backflow is expected in this geometry, its presence does not affect the time constant [36]. The experiment was fully automated and controlled by a custom program in the Yorick language. The relaxation time combined with the

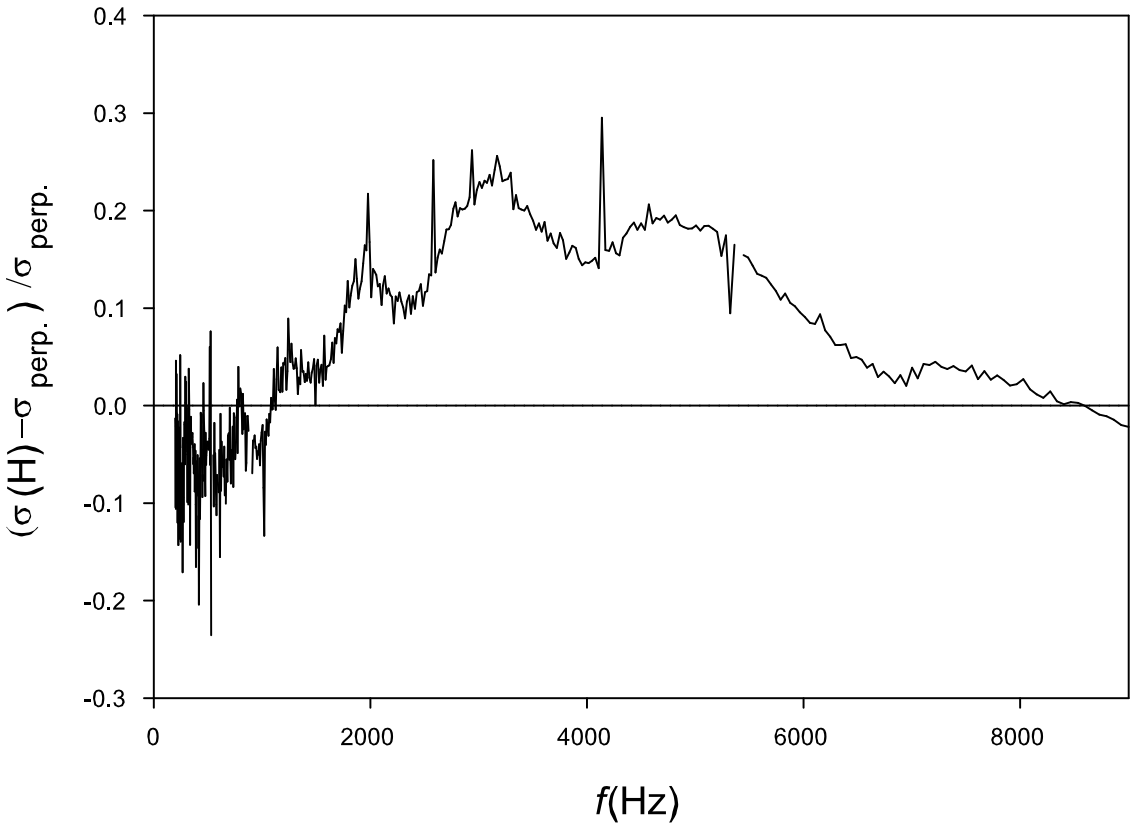

Figure 5.6: This figure shows $\frac{\sigma(H)-\sigma_\perp}{\sigma_\perp}$, where $\sigma(H)$ is the (nearly) parallel component measured in the Freedericksz state with $H = 10.9$ kG, which is well above the Freederickz field, calculated to be 4.8 kG. σ_a is negative from 1 Hz to roughly 1500 Hz, positive for 1500 $\rightarrow$ 8100 Hz, and then negative again up to the end of the measurement at 100 kHz. These measurements were made on the 25 μm sample at 70°C.

measured elastic constants yielded γ_1.

Finally, the critical potential difference for the electric field induced bend Freedericksz transition was found by J.T. Gleeson by monitoring the light transmitted through a homeotropically aligned sample $d = 50\mu$m housed in a Mettler FP90 hot stage, which controlled the temperature to $\pm 0.1°$C, placed between crossed Glan-Thompson polarizers. The laser light was provided by a polarized 4.5 mW intensity stabilized Spectra Physics laser at $\lambda = 632.8$ nm. The light was detected by a Thor Labs PDA-55 photovoltaic detector, which fed the signal to a Hewlett-Packard 34401A digital multimeter in *dc*-voltage mode. This experiment was also controlled by custom program in the Yorick language. This situation is analogous to the magnetic induced Freederickz transition. The same derivation applies if $\chi_a H^2$ is replaced by $\epsilon_a E^2/4\pi$. This measurement yields the ratio K_{33}/ϵ_a in cgs units.

The elastic properties of ClPbis10BB appear to be similar, i.e. the same order of magnitude, to those of rod-like calamitic LCs (see [3] and references therein). However, $\gamma_1 = 2.67$ Pa·s was found to be more than thirty times larger than that of typical rod-like nematics such as MBBA [37] and 5CB [38,39]. Also, $\chi_a = 1.76 \times 10^{-7}$ (in SI units) is about an order of magnitude smaller than that of calamitics (see [3] and references therein). This is probably due either to the tetrahedratic order in the N_T phase, which induces a conformation of the molecules into stretched tetrahedral structures, which in turn limits the ability of the molecules to align their long axes with the magnetic field; or to a twisting of the molecules, which leaves the benzene rings of the molecule in different planes and acts to lower the magnetic susceptibility anisotropy of the molecule.

5.3.3 THE PARALLEL STRIPE INSTABILITY

ClPbis10BB exhibits four different EHC regimes as the driving frequency is changed. These four regimes are defined using Fig. 5.7, which shows threshold voltages, V_{th}, for the sample at 75°C. All V_{th} values referred to were found by slowly raising the voltage then waiting 15 minutes at each interval to see if a pattern became visible through crossed polarizers using a 5X objective. A pattern was considered to be present when stripes where clearly defined in any part of the field of view of the microscope. This process was then repeated with the voltage being lowered. V_{th} was recorded as the voltage at which the pattern was no longer present at any point in the field of view. Raising and lowering the voltage produced thresholds that were in agreement with each other. Therefore, the thresholds presented are applicable to the lowering and raising voltage situations.

The PS instability is the primary bifurcation as the voltage is increased at frequencies of $1 - 24$ Hz (see Fig. 5.8a). From $25 - 27$ Hz a coexistence of the PS and the perpendicular wide stripes (PW2, to be described below) could be seen (see Fig. 5.8b). At frequencies above 28Hz, PS was no longer present. The PS consists of many localized clusters of roll patterns with wavelength slightly less than d, which went from parallel to slightly oblique with regard to the initial director orientation. The best contrast was achieved between crossed polarizers. ClPbis10BB is $(--)$ in the PS region, and is optically similar to patterns seen by Kochowska *et al.* [17] in $(--)$ calamitic liquid crystals.

The threshold curve for PS is shown as a function of frequency at three different temperatures in Fig. 5.9a. The frequency dependence of V_{th} remains linear at each of the different temperatures, exhibiting only a slight change in slope as the temperature

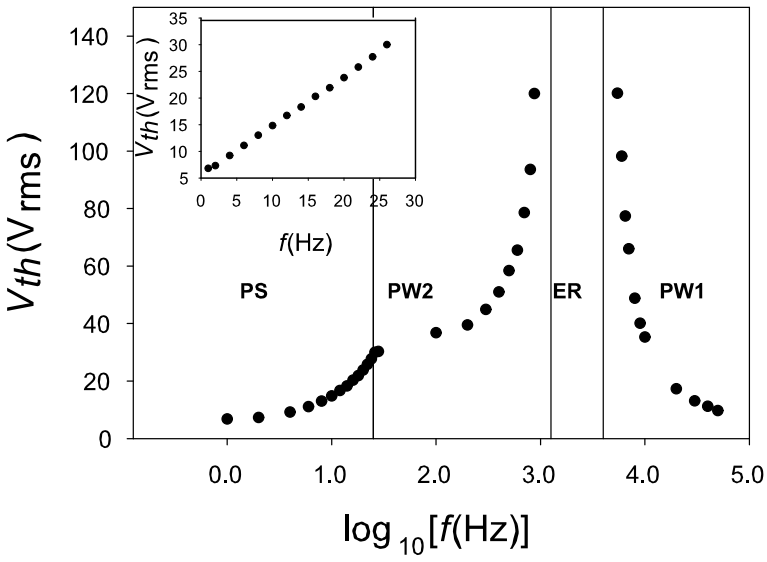

Figure 5.7: Threshold curve for a 15μm sample at 75°C in the V-$log(f)$ plane. Below 28 Hz PS is observed. From $28-1000$ Hz a wide stripe pattern (PW2) is seen. The region from $1000-5000$ Hz does not show any EHC (ER). Above 5000 Hz another wide stripe pattern (PW1) is observed. Regions are separated by solid lines. Inset shows PS threshold versus frequency to better demonstrate the linearity of the threshold curve in this region.

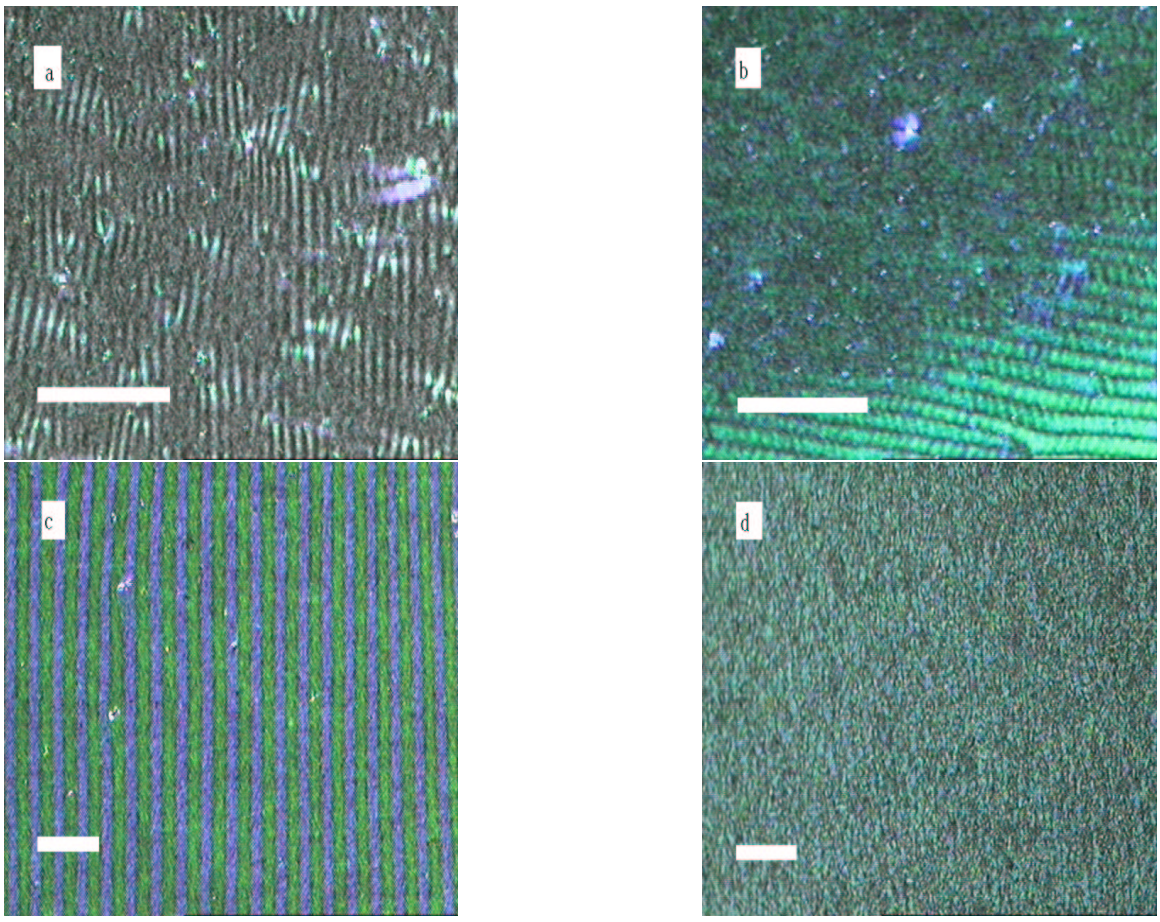

Figure 5.8: (a) PS at 12 Hz and 28 V_{rms}. (b) PS and PW2 coexisting at 26 Hz and 32 V_{rms}. (c) PW2 at 200 Hz and 48 V_{rms}. (d) Turbulent state at 5 Hz and 32 V_{rms}, which is well above threshold at this frequency. Images were taken with a 15μm sample at 75°C between crossed polarizers that were rotated $\sim 15°$ with respect to the vertical direction in the picture. Length scale represents 100 μm in each picture. In 'a' and 'b' the rubbing direction of the cell plates is in the vertical direction in the picture. In 'c' and 'd' the rubbing direction is in the horizontal direction in the picture.

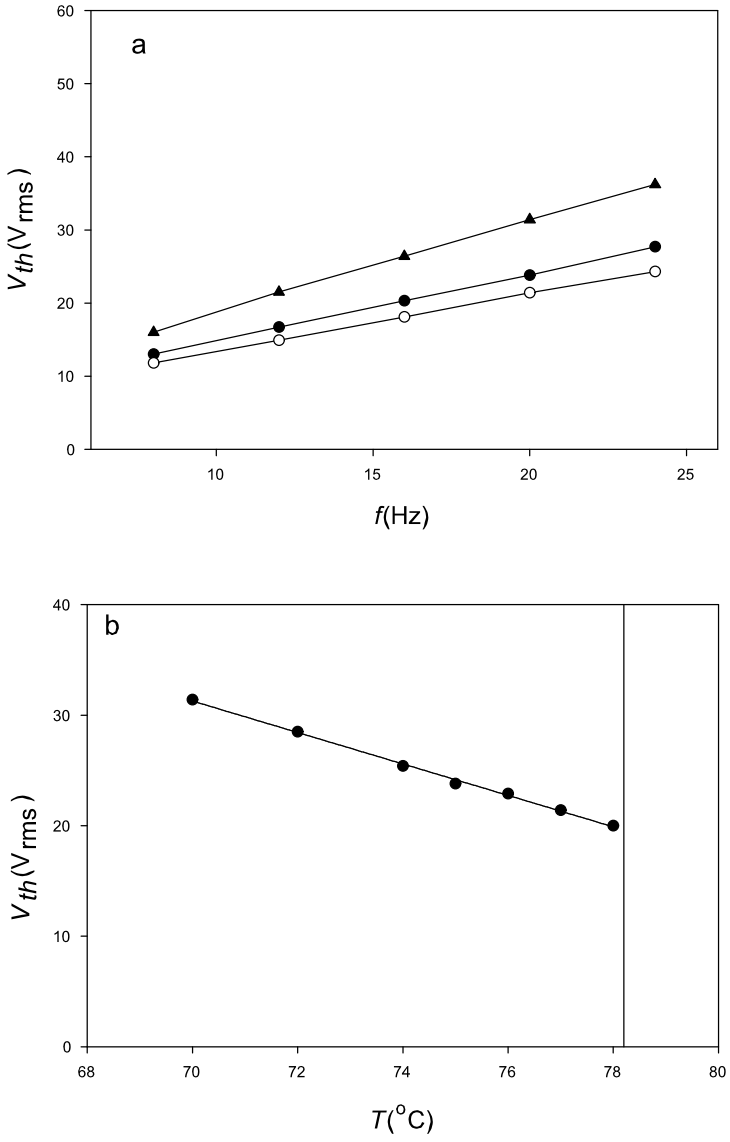

Figure 5.9: (a) V_{th} versus frequency in the PS regime. Solid triangles, solid circles, and open circles represent data at 70°C, 75°C, and 77°C, respectively. (b) Temperature dependence of V_{th} at 20Hz in the PS regime. The clearing point is at 78.2°C and is represented by the solid black line. Both measurements were made on a 15μm sample.

is changed. Figure 5.9b shows that V_{th} decreases monotonically as the clearing point is approached.

The small wavelength, poor contrast, and tendency to form in small localized clumps made it difficult to observe flow patterns in PS by means of a dust particle, or any other impurity. Although flow was not directly observed in this region, the formation of a pattern in an electric field and a transition to a turbulent state (Fig. 5.8d) at voltages well above the PS threshold provide convincing evidence that this pattern was due to EHC and not a static pattern forming mechanism.

CONCLUSIONS

As stated above it appears that PS is not formed by a mechanism explained by the SM or WEM. The SM and WEM explain anisotropically driven mechanisms, which are expected to show a divergence of V_{th} as the clearing point is approached because the voltage needed to establish these instabilities is inversely proportional to the anisotropy of the system, which becomes very small as T approaching the clearing point. The monotonic decrease of V_{th} through the clearing point for the PS suggests that an isotropic mechanism (one not dependent on ϵ_a and σ_a) is responsible for this instability.

Another possibility is that the PS is caused by the flexoelectric effect. The flexoelectric effect in non-calamitic (i.e. not able to be approximated as a rod) nematics was first considered theoretically in 1969 by R.B Meyer [40]. In this effect a director deformation produces an electric polarization, and alternatively an applied field induces a director deformation. (Only splay and bend deformations can result in macroscopic polarization, with flexoelectric coupling constants e_1 and e_3, respectively.) A molecular statistical approach for calculating the flexoelectric coefficients

was subsequently developed by Helfrich [41]. This approach predicts that the coefficient e_3 for bent-core molecules is proportional to the kink angle, which is defined as $\beta = 180° - \psi$, where ψ is the opening angle between the molecular arms. For rod-shape molecules $\psi \sim 180°$, and $\beta < 1°$, however for ClPbis10BB $\psi \sim 120°$, i.e. $\beta \sim 60°$. In conventional rod-shaped nematics, the flexoelectric coefficients are typically 10^{-11} - 10^{-12}C/m; Helfrich's model suggests that BCN nematics may have coefficients 50 times greater than rod-like molecules. This prediction is far exceeded in practice as recent measurements of e_3 for ClPbis10BB have found it to be nearly 1000 times larger than found in calamitics ($e_3 \sim 60$ nC/m for ClPbis10BB compared to ~40 pC/m for 5CB) [42].

The extremely large flexoelectric coefficients for ClPbis10BB make it a strong possibility that a mechanism driven by the flexoelectric effect is creating the PS. The flexoelectric effect has been reported to produce two kinds of patterns composed of parallel stripes with the wavelength on the order of d in calamitic liquid crystals; one at low frequencies [18, 43–47] and another at high frequencies [18]. The high frequency longitudinal rolls observed by Blinov, *et al* [18] were not related to flexoelectricity at the time of their discovery, but it was later proposed in Ref. [47] that the reported pattern might be a result of the flexoelectric effect. This high frequency flexoelectric pattern consists of randomly oriented longitudinal domains, and was observed in a calamitic $(--)$ material. These domains had periods less than d, which were independent of temperature. V_{th} for these patterns showed a linear frequency dependence and was proportional to the cell thickness, i.e. had a field threshold.

The PS was oriented into small domains that went from parallel to oblique with λ slightly less than d. PS showed a weak temperature dependence and V_{th} for PS

exhibited a linear frequency dependence. It was proposed in Ref. [47] that the high frequency flexoelectric regime in $(--)$ materials is analogous to the dielectric regime in $(-+)$ materials, i.e. it is an anisotropic mode. It was stated previously that the threshold voltage of an anisotropic mode generally shows a divergence as T_{NI} is approached. However, this is not always the case. Certain materials that exhibit instabilities explained by the SM, such as Phase 5 (Merck), do not show a divergence in V_{th} at the clearing point. This apparent discrepancy is believed to be related to the nature of the nematic to optically isotropic transition. A divergence is in fact only expected for weakly first order transitions, where the anisotropies go to zero almost continuously. If the anisotropies show only a weak temperature dependence then fall to zero suddenly at the clearing point, a divergence might not be present. ClPbis10BB exhibits a fairly large jump of ϵ_a near T_{N_TT} at 1 kHz. Thus, a lack of divergence of V_{th} near T_{N_TT} could in theory be possible. If this were the case, PS might be explained by an anisotropic high frequency flexoelectric effect, and might actually be explained by the SM if the flexoelectric effect could be incorporated into it.

5.3.4 THE EMPTY REGION

Next, I will discuss the region that appears to be void of any EHC. Figure 5.7 shows that the region between the two wide stripe domains appears to be void of any EHC (ER). The potential difference was increased up to 130 V_{rms} ($\mathbf{E}$=12.3V/μm $\hat{\mathbf{z}}$) in this region, which was nearly large enough to cause dielectric breakdown in the sample, yet no EHC was appeared. In Fig. 5.10 the reciprocals of $V_{th}(f)$ for both the regions neighboring the ER (PW1 at higher and PW2 at lower frequencies) were plotted as a function of frequency. Each set of points could be well fitted with a

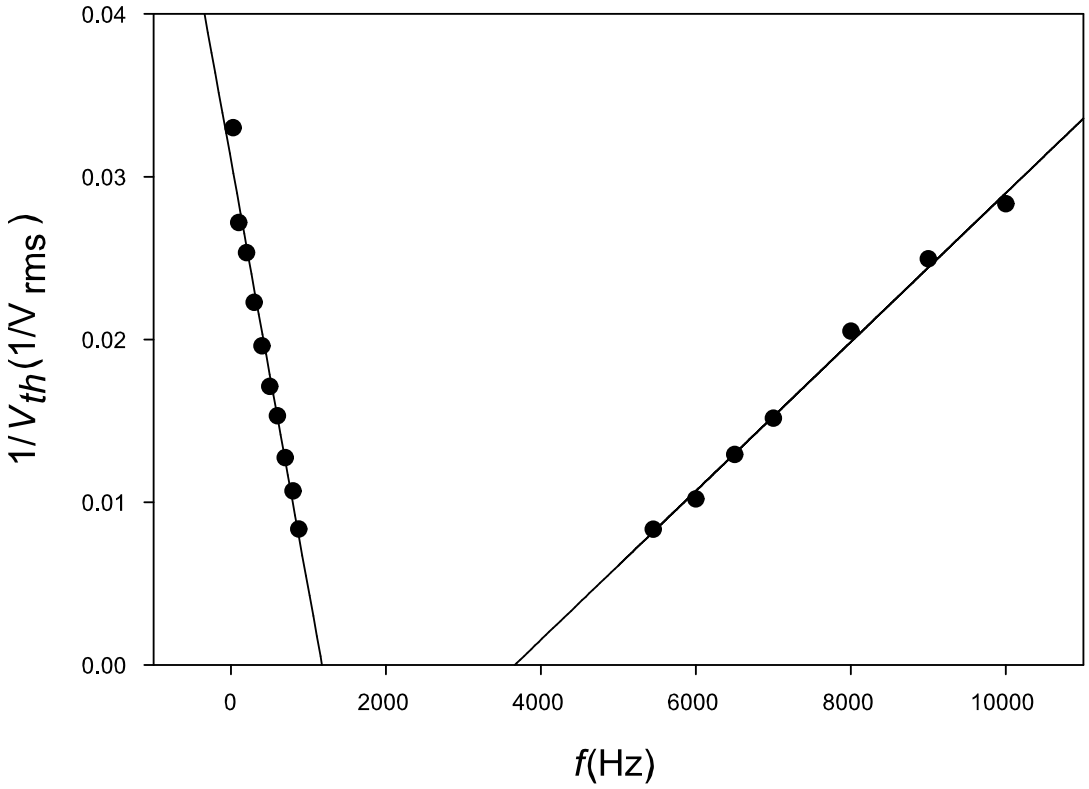

Figure 5.10: The linear fits (solid lines) to $1/V_{th}(f)$ for PW2 (at low f) and PW1 (at high f) at 75°C for a 10 μm sample indicate that an ER exists even as $V_{th}(f) \rightarrow \infty$.

straight line. Assuming that the linearity of $1/V_{th}(f)$ survives even at higher voltages, the lines were extrapolated to zero. The intersections enclose a band of frequency, which suggests that the increase of the V_{th} on both sides of ER is not simply due to a divergence at a single frequency, rather it points to an absence of EHC at all voltages. Figure 5.11 shows that the PW1 region extends towards lower frequencies as the temperature is increased, i.e. the width of ER is reduced, but even within 0.5°C of the clearing point the inverse of $V_{th}(f)$ still indicated an ER of finite width.

The ER in ClPbis10BB is an extremely interesting peculiarity. The material has an initial planar alignment, is $(-+)$ through most of the ER, and has a non-zero conductivity; i.e. it fits all the criteria for SM type EHC to be present. To the best of my knowledge there has not been another case in which no EHC was observed, in a region with suitable conditions for EHC to occur. The cause of the ER is still unclear at this time. I speculate that competition between the PW1 and the PW2 might be inhibiting pattern formation in this region, but this is merely a guess that needs to be looked into further in the future.

5.3.5 THE PREWAVY INSTABILITIES

I will call the two wide stripe domains that border the ER the prewavy1 (PW1) and the prewavy2 (PW2). The PW1 is the regime that occurs at frequencies higher than the ER, while the PW2 occurs at frequencies lower than the ER. The two instabilities are so named because PW1 shows nearly identical characteristics to the prewavy mode described earlier [25, 26], and PW2 is visually indistinguishable from PW1 under a polarizing microscope, but is clearly separated from PW1 by the ER and by differing threshold behavior. I will discuss the differences between the two PW regimes, followed by their similarities.

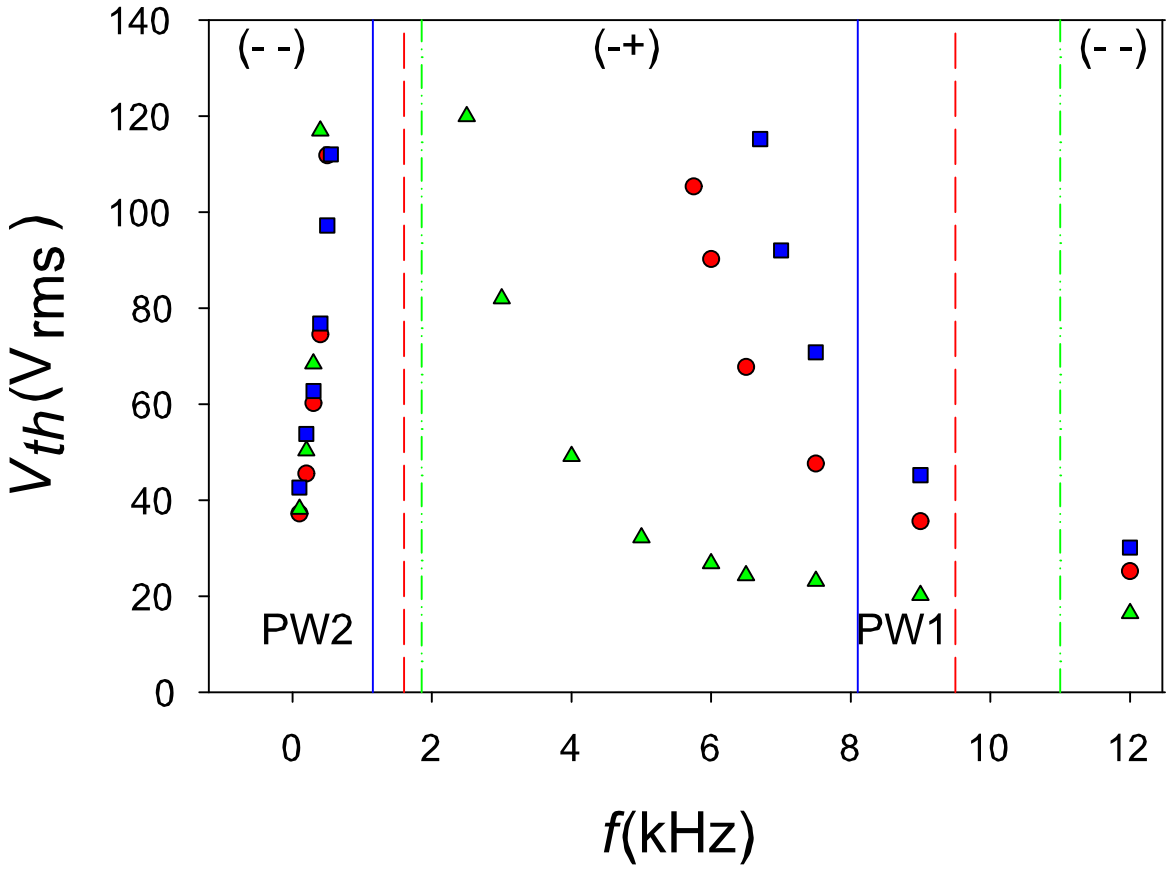

Figure 5.11: Frequency dependence of the threshold voltages for PW1 and PW2. Squares, circles and triangles represent V_{th} at 70°C, 75°C, and 77°C, respectively. The solid, dashed, and dashed-dotted lines mark the frequencies where the sign of σ_a changes at 70°C, 75°C, and 77°C, respectively. These measurements were made on a 25μm cell. $V_{th}(T)$ for PW1 shows a strong temperature dependence, while $V_{th}(T)$ for PW2 shows only a slight temperature dependence compared to PW1.

Apart from being separated by the ER, PW1 and PW2 also exhibit several differences in their threshold behavior. First, the threshold curve for PW2 shows a much stronger frequency dependence then does the curve for PW1. Figure 5.12 shows that $V_{th}(T)$ for PW1 monotonically decreases as the temperature is raised towards the clearing point, while $V_{th}(T)$ for PW2 increases in the vicinity of T_{N_TT}. $V_{th}(f)$ for PW2 diverges near the frequency were a change in the sign of the conductivity anisotropy occurs, without ever diverging at a frequency greater than the sign inversion frequency of σ_a (see Fig. 5.11). In contrast, $V_{th}(f)$ for PW1 appears not to be affected by the change in the sign of σ_a that occurs at higher frequencies. The location of the higher sign inversion frequency of σ_a and the threshold for PW1 both show a strong temperature dependence, while the lower frequency sign inversion and the PW2 threshold seem to be much less affected by temperature changes.

Now, on to the similarities between the two PW regimes. Both PW regimes show nearly identical dynamic properties, which are markedly slower than those of most EHC instabilities seen in calamitic LCs. Both regions form patterns on the order of hours, or days, versus the minutes it takes for PS at low frequencies or for SM type patterns in other materials. Both PW1 and PW2 share many properties in common with the previously mentioned prewavy pattern. Both are only visible between crossed polarizers, indicating that director modulation occurs in the xy-plane. Both have rolls that are perpendicular to the initial director orientation and have $\lambda \sim 3d - 4d$. Both patterns develop disclinations, which evolve into "wavy" patterns [48] at voltages much greater than the threshold. (Which were also viewed through crossed polarizers, see Fig. 5.13.)

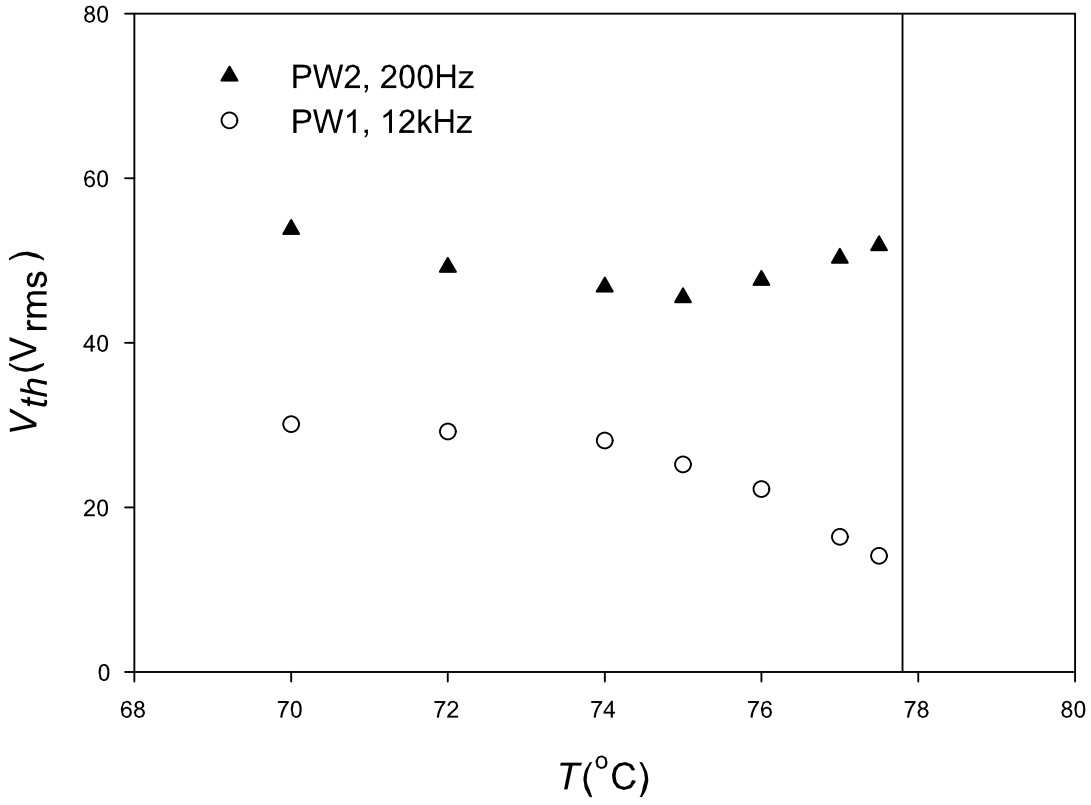

Figure 5.12: Temperature dependence of threshold voltages for the prewavy regimes. Solid triangles represent $V_{th}(T)$ for PW2 at 200 Hz, open circles represent $V_{th}(T)$ for PW1 at 12000 Hz. The clearing point is at 77.8°C. Both measurements were made on a 25μm sample.

DIRECTOR MODULATION IN THE PW REGIMES

All optical measurements on the EHC instabilities in ClPbis10BB were made between crossed polarizers. This configuration provided the best contrast in all instances. These patterns were also visible under nearly parallel polarizers with reduced contrast, but with one polarizer removed the pattern can not be clearly optically discerned. The darker broad stripes in the prewavy patterns are produced by regions in which the director is roughly parallel, or perpendicular, to the polarizer. In this configuration the incoming light will be polarized parallel to one optic axis of the liquid crystal and will experience no phase shift, i.e. the light will be perpendicular to the analyzer and will not pass through it. The brighter broad stripes are produced by regions where the director is at an angle to the polarizer, here one component of the incoming light will experience a phase lag due to the birefringence of the liquid crystal. This will leave the initially linearly polarized light elliptically polarized, and thus able to pass through the analyzer.

When the sample is rotated between crossed polarizers by 90° the directions parallel and perpendicular to the polarizer interchange, which will leave the intensities unchanged by this operation. Thus, the pattern has a 90° periodicity with respect to rotation. If the sample is rotated 45°, with respect to its initial position, the director for the darker stripes will be at an angle of 45° to the polarizer, which produces the greatest possible passage of light. As a result the darkest regions become the brightest, which means that the pattern is inverted from its initial state. This behavior shows that the director modulations are in the xy-plane for the broad stripes [20, 25]. The black lines between the broad stripes, most easily seen in Fig. 5.16, do not change color or intensity under rotation of the polarizers, which suggests that the director

displacement is purely in the z-direction in the narrow black stripes.

The voltage and frequency dependence of these director modulations were measured by rotating the sample between crossed polarizers. Initially, the sample was positioned so that the x-axis was aligned with a polarizer. Then the sample was rotated in one direction until the optical intensity was minimized for the stripes that were initially bright, i.e. until the director of those stripes was aligned with the polarizer. This point was determined visually by starting from the initial position and rotating the sample until the initially bright stripes appeared dark. This was repeated five separate times and then the average of those measurements was used to determine the angle of the director displacement. This was then repeated with the sample being rotated in the opposite direction. To make the measurement the sample was placed in the Instec hot stage, which was fixed to the rotation stage of the Nikon microscope. The voltage was changed in 1-5 V intervals at a rate of $dV/dt \sim 0.001$ V/s with the frequency fixed at either 100 Hz or 20 kHz. After each voltage interval was reached the pattern was allowed to relax for one hour. Then the angle ϕ the sample had to be rotated through to make the initially bright stripes dark was recorded. This procedure was then repeated with the voltage being quickly varied, i.e. the final voltage was reached in ~ 1 s. These measurements were then repeated with the frequency being varied at a fixed voltage. The amplitude of director modulations showed no frequency dependence in the observed region in either case. The images obtained by rotations in opposite directions were inverted, which indicates that the director modulation is symmetric with respect to the initial director orientation ($\hat{\mathbf{x}}$).

Below the threshold voltage $\phi(V) = 0$. For $V > V_{th}$, ϕ exhibits a supercritical pitchfork bifurcation. Figure 5.14 shows that $\phi(V)$ saturates at a value of about 23°

for the slowly varied pattern and about 18° for the quickly varied pattern, in both cases saturation occurs at voltages well above V_{th}. At 100 Hz (PW2), the director has a behavior similar to that of the 20 kHz (PW1) case (with respect to the shape and the saturation values of the $\phi(V)$ curve), though over a different voltage range. The amplitude of the azimuthal director modulation obtained by slowly varying a parameter can be well fit by the formula

$$\phi(\varepsilon) = \phi_0 \sqrt{\frac{V^2 - V_{th}^2}{V_{th}^2}} \tag{5.43}$$

for voltages slightly above V_{th}, where $\varepsilon = \frac{V^2 - V_{th}^2}{V_{th}^2}$. These findings are in agreement with the prewavy behavior described in Ref. [25]. Also, the value of $\phi(\varepsilon)$ seems to be dependent on the way in which the point in the $V - f$ space was reached (slowly or quickly varying the voltage). However, the angular modulations of the states found after quickly and slowly varying the voltage tend to converge to an intermediate value over a period greater than 24 hours. This suggests that one stable history dependent state would emerge given enough time.

WAVELENGTHS OF THE PW PATTERNS

The wavelength was measured at different points in the frequency-voltage plane in four different ways. The points could be reached quasi-statically by holding one parameter fixed and varying the other slowly ($dV/dt \sim 0.001$ V/s or $df/dt \sim 1$ Hz/s), rates of change increased to faster than about 0.005 V/s or 10 Hz/s would produce different patterns compared to the case when the parameters where changed more slowly. The pattern was allowed to relax for one hour after the point was reached. A video camera and a frame grabber were then used to capture a pnm image of the pattern using a 10X objective. The camera was oriented so that the rolls were vertical

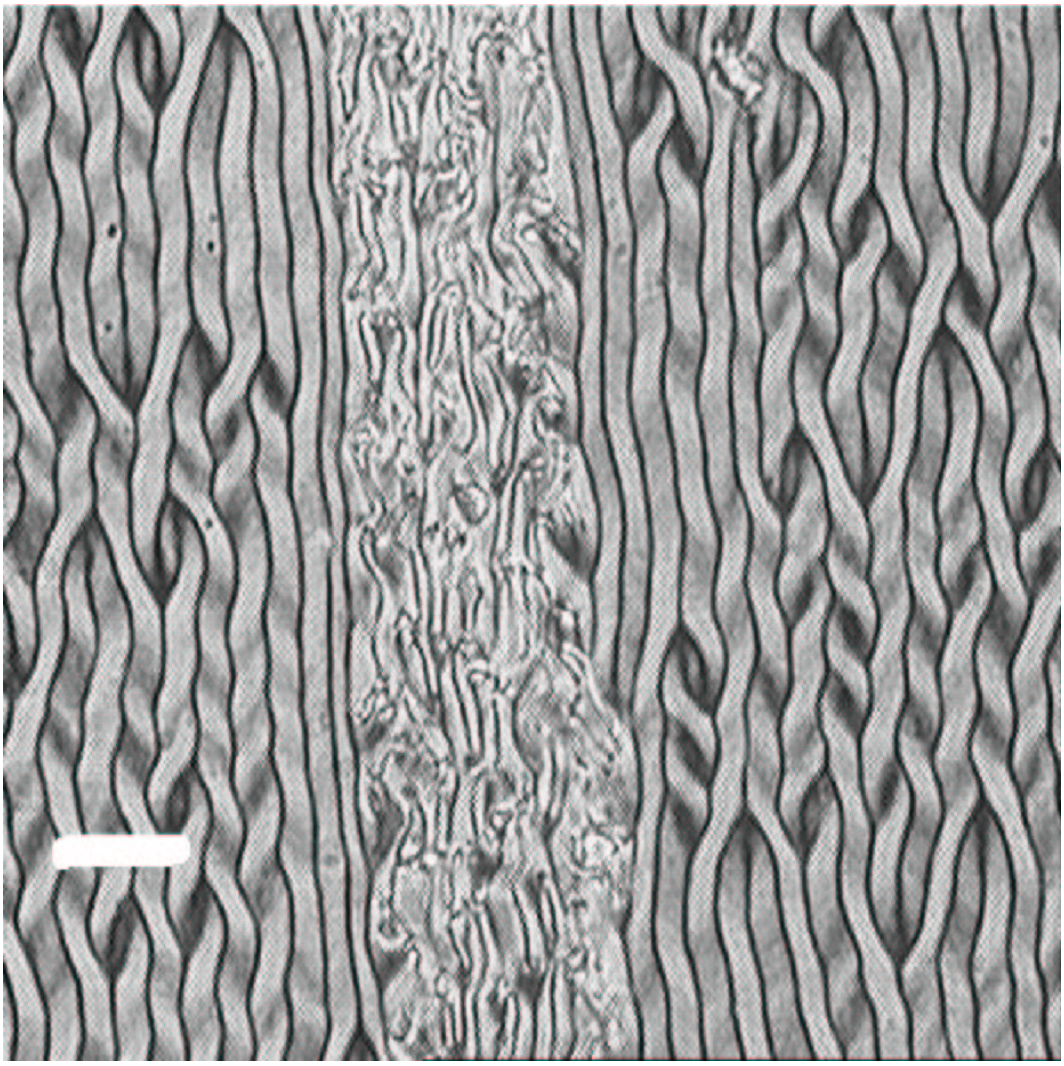

Figure 5.13: Example of the wavy pattern, which is seen in the center region of the image, at 30 kHz and 55 V_{rms}. Image taken with a 10μm at 70°C between crossed polarizers that were rotated $\sim 15°$ with respect to the vertical direction in the picture. The rubbing direction of the cell plates is in the horizontal direction of the picture, the length scale represents 100μm.

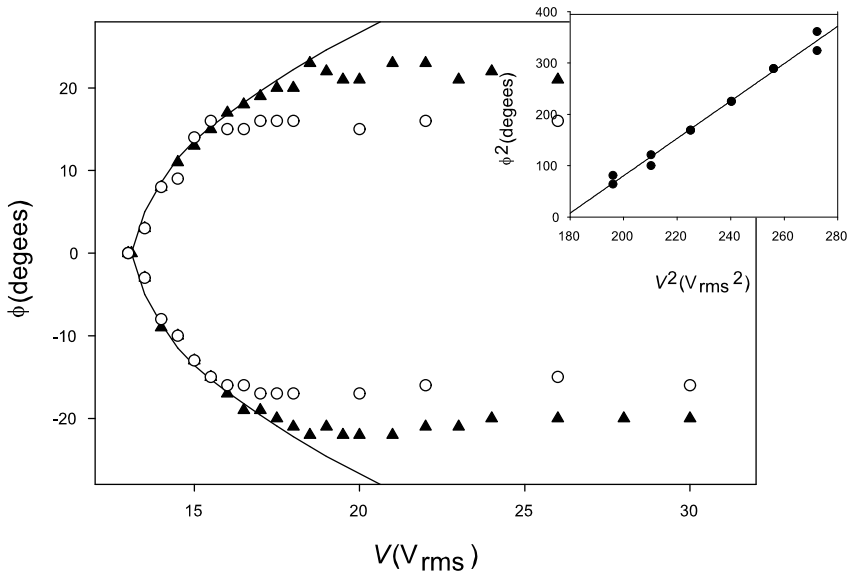

Figure 5.14: Maxima of the azimuthal director modulation measured at 20 kHz and 70°C. The solid triangles and the open circles show the director angle found by slowly varying and by quickly varying the voltage, respectively. The solid line shows the fit to Eq. (5.43) with $\phi_0 = 22.4°$ for the case where the voltage was slowly varied. The inset shows that the goodness of the fit can be better demonstrated by manipulating Eq. (5.43) to the form $\phi^2 = (\phi_0/V_{th})^2 V^2 - {\phi_0}^2$, which more clearly shows the linear relation between ϕ^2 and V^2. Again, this was done for the case where the voltage was slowly varied. The fact that the ϕ values saturated at higher voltages made it difficult to discern the point where the quadratic behavior ended, so there is an amount of uncertainty introduced into the fit of the straight line depending on how many data points are used.

in the captured image (as in Fig. 5.8c). Then one color channel of the recorded RGB image was selected. The fast Fourier transform (FFT) of each row in the image was taken and recorded. Then the average of the FFTs of the rows was determined and used to determine the wavelength of the pattern. (See Appendix F for Yorick code.)

The wavelength was determined using the following logic: A 1-D periodic function in real-space may be expressed as a Fourier series

$$F(x) = \sum_n a_n e^{i2\pi x n/\lambda}, \tag{5.44}$$

where n is a summation index, a is a constant, and λ is the wavelength of the function. If we take the Fourier transform of $F(x)$ we can relate λ to k such that

$$F(k) \propto \int e^{i2\pi x n/\lambda} e^{-ikx} dx = \delta(k - 2\pi n/\lambda). \tag{5.45}$$

So, this shows us that if we take the Fourier transform of a 1-D periodic function we should see a series of delta functions at equal intervals in k-space, that is a peak for each n value.

Now, the average of the FFTs of the rows, from above, essentially gives us a 1-D FFT of a periodic function, which is a series of peaks in k-space. By plotting k vs. n for the FFT peaks, and then fitting a straight line to this plot, we get an average value for k/n (the space between the peaks in k-space). This value can then be used to solve for λ,

$$\lambda = \frac{2\pi}{\bar{k}}, \tag{5.46}$$

where $\bar{k}$ = slope $k(n)$. (Note the Yorick FFT function drops the factor of 2π, so in this case $\lambda = 1/(\bar{k})$. The wavelength is in k-space, so we need to switch from k-space back to real space to get λ in a useful form. This is done using the equation

$$k = 2 f_c N, \tag{5.47}$$

to relate k and x. Here $f_c = 1/2\Delta$ is the Nyquist critical frequency with Δ being the interval between samples (which is one pixel in this case) and N is the number of points sampled. (The size of a pixel was measured by taking micrographs of a stage micrometer at each magnification.) The wavelength could be calculated to an accuracy of better than one pixel using this method.

Slowly varying the voltage with f fixed, or slowly varying the frequency with V fixed, to reach a point in V-f space produced patterns with similar wavelengths. Quickly changing the voltage at constant f, or the frequency at constant V, (reaching the final value in $\sim$1 s) produced the same wavelengths. However, the wavelengths found by quickly changing a parameter were different from the wavelengths found after the slowly changing a parameters.

Figure 5.15 shows that PW1 and PW2 exhibit similar qualitative behavior in regards to how the wavelength varies with ε and f. Quickly varying one parameter produced a pattern with a shorter wavelength and many more dislocations, of both the types shown in Fig. 5.16, than a pattern produced by slowly varying a parameter. Also, after a period of 48 hours it was found that PW1 and PW2 patterns with dislocations, created by quickly varying the voltage, would relax to dislocation free patterns with a slightly longer wavelength (than what was found after one hour). Likewise, patterns formed by slowly varying the voltage would relax to a dislocation free pattern with a slightly shorter wavelength (than what was found after one hour), i.e. the wavelengths of the quickly varied and slowly varied patterns converge to an intermediate value after a certain time. This seems to show that λ and ϕ are coupled, and that at least two quasi-stable history dependent states can exist for at least 24 hours until the wavelengths and director modulations of the two states converge to

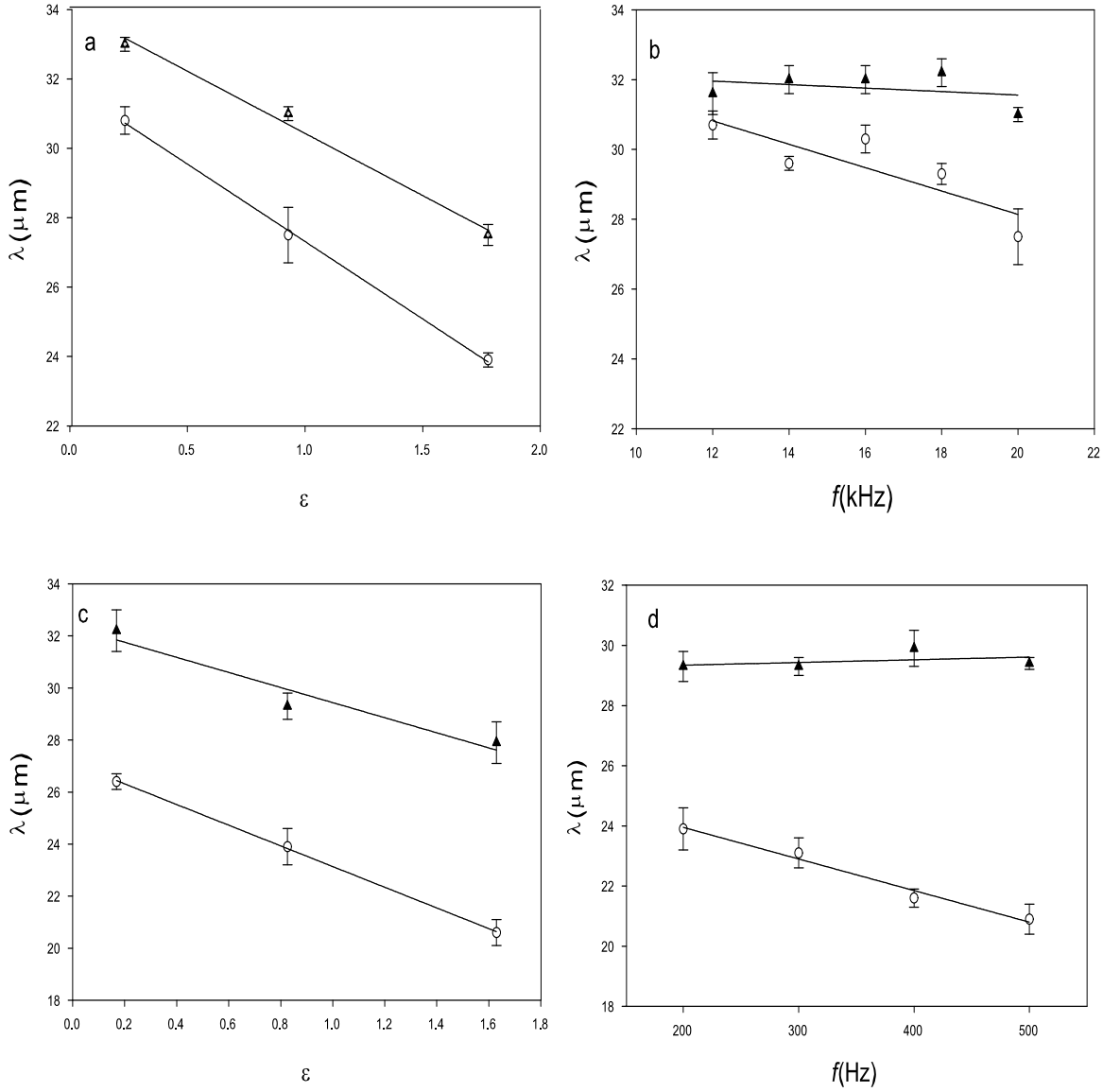

Figure 5.15: (a)Wavelength as a function of ε at 20 kHz for PW1. (b)Wavelength as a function of frequency at 25 V_{rms} for PW1. (c) Wavelength as a function of ε at 200 Hz for PW2. (d) Wavelength as a function of frequency at 25 V_{rms} for PW2. In all charts the solid triangles and the open circles represent the pattern achieved by slowly varying and by quickly varying the voltage, respectively. All measurements were made on a 10μm sample at 70°C.

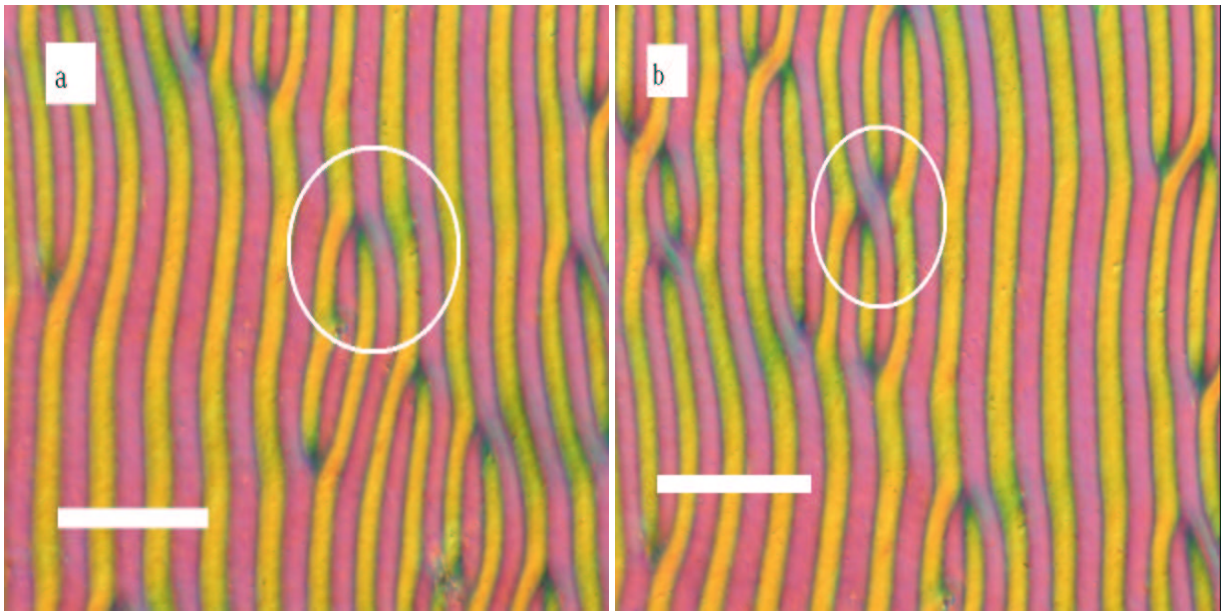

Figure 5.16: Examples of the two main types of dislocations which form in the prewavy regions. (a) The stripes appear to split apart. (b) The stripes appear to cross over, or twist around each other. Both images taken at 20 kHz after quickly moving from 0 V_{rms} to 30 V_{rms} with a 10μm sample at 70°C between crossed polarizers that were rotated $\sim$ 15° with respect to the vertical direction in the picture. The rubbing direction of the cell plates is in the horizontal direction in the pictures, the length scales represent 100μm.

form one stable state with intermediate λ and ϕ values.

THE KNITTING INSTABILITY

Another interesting pattern, which we termed the "knitting" instability (Fig. 5.17), was produced by abruptly raising the voltage from one of the prewavy states. The knitting stability had a wavelength up to two times as long as that of the PW states. After several hours the knitting instability would relax to a stripe pattern with dislocations, and would proceed to behave as the quickly varied state mentioned above. Several different types of long wavelength instabilities have been observed in other materials during system relaxation from an initial state to a final state after a change of a control parameter; e.g. the Eckhaus, the zigzag, and the skewed varicose instabilities [49]. The knitting instability has a great deal in common with these other long wavelength relaxation mechanisms and is believed to represent a new long wavelength relaxation mechanism, which has not been previously observed.

For example the Eckhaus instability, which has been widely studied (see [50] and Refs. within), is an important mechanism for pattern selection that can lead to substantial changes in wavelength (or wavenumber). Under certain conditions, a change in parameter can drive the wavenumber of a periodic pattern so far from its critical value that the pattern cannot go unstable through slow spatial modulations, but must relax through the nucleation of roll pairs to return to its critical wavenumber [50]. Relaxation by means of creation of roll pairs is accomplished through the Eckhaus instability, which allows for smooth dislocation motion that leads to the nucleation of roll pairs. Similarly, the knitting instability appears after an abrupt change in control parameter as an unstable long wavelength state. The knitting instability allows for drastic changes in wavenumber through the creation of new stripe pairs.

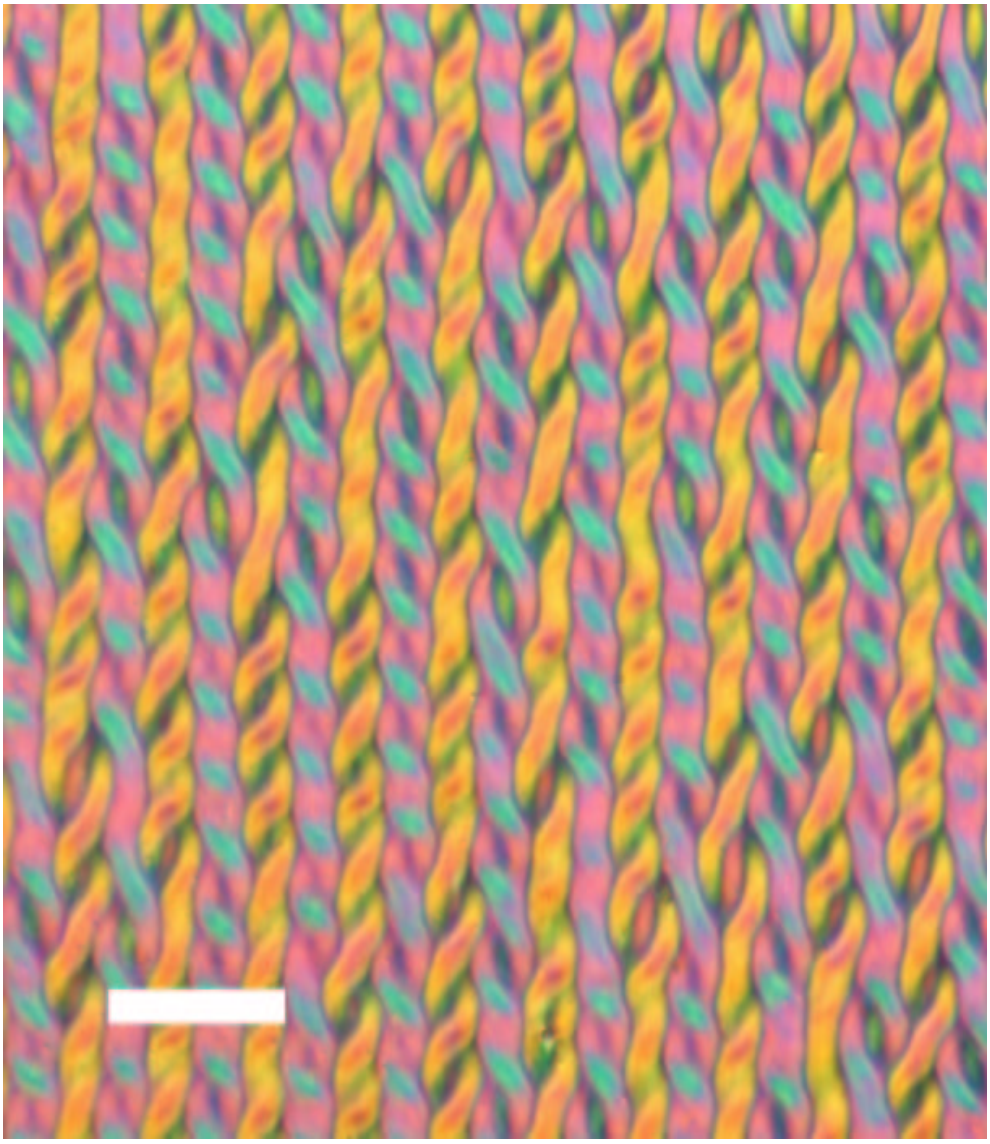

Figure 5.17: The "knitting" instability at 40 kHz and 35 V_{rms}. It is produced by abruptly raising the voltage from one of the prewavy states. Image taken with a 10μm sample at 70°C between crossed polarizers that were rotated $\sim 15°$ with respect to the vertical direction in the picture. The rubbing direction of the cell plates is in the horizontal direction in the picture, the length scale represents 100μm.

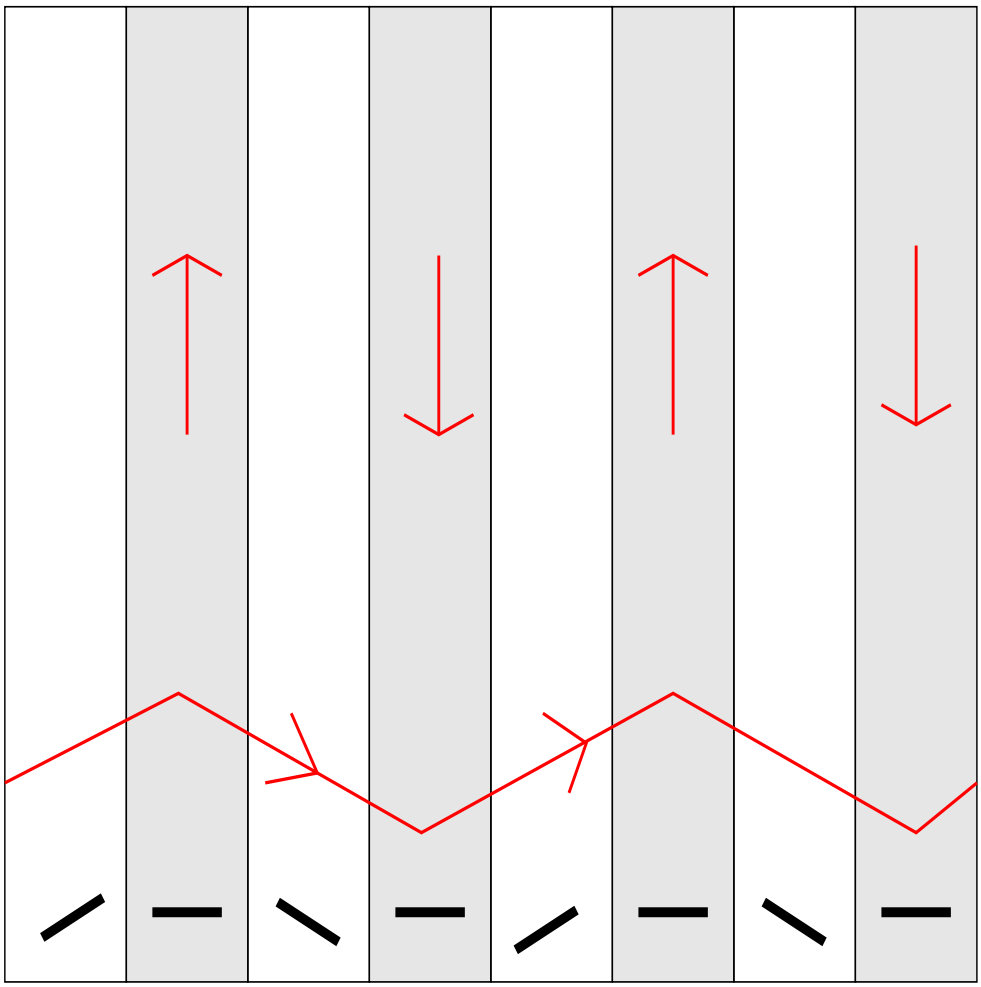

Figure 5.18: This is a proposed schematic representation of the flow in the PW regimes. The dark lines near the bottom of the figure represent the director orientation. The arrows represent the two distinct flow patterns. One pattern has motion parallel to the stripes, while the other pattern has motion perpendicular to the stripes in a "zig-zag" type motion. The stripes with horizontal director positioning are dark, the stripes with rotated directors are bright, and the solid black lines represent the black lines between the stripes where the director is out of plane.

FLOW IN THE PW REGIMES

The PW regimes had wider stripes and a larger scale than the PS region, which made it possible to observe flow via dust particles. The velocity of the flow was very slow, taking up to several hours to move across the field of view (about 500μm) in some cases. Pictures were taken in five minute intervals and then viewed to track the motion of the dust particles. Two distinct flow patterns were observed. The "zig-zag" flow [26] along the director was the most frequently observed scenario, while dust particles were also observed to move parallel to the stripes (see Fig. 5.18). The two different flow patterns were probably due to the location of the dust particle in the z-direction, i.e. there were different layers (planes) of flow patterns perpendicular to the z-axis.

CONCLUSIONS

It was shown in the previous section that the characteristics of the PW1 instability correspond to those of the prewavy pattern [26], except for the frequency dependence of the thresholds. The optical appearance and the dynamical behavior of PW2 was found to be almost identical to those of PW1. One interpretation of the situation, based on the differences in the temperature and frequency dependencies of the threshold voltages is that PW1 and PW2 are of different origins. PW2 exhibits a divergent $V_{th}(f)$ at a frequency that is always in the $(--)$ region of the material, and is near to the frequency where the sign of σ_a changes. Also, PW2 always has an increase in $V_{th}(T)$ as the clearing point is approached. These features are strong evidence that PW2 may be caused by an anisotropic mechanism. An anisotropic mechanism, such as the SM, is driven by the anisotropy of the system, and thus is dependent

on the values of ϵ_a and σ_a. A pattern formed by an anisotropic mechanism should show a dependence on the signs of the anisotropies, i.e. a change in behavior such as a divergence in V_{th}, at a change in sign of σ_a. Also, such a system should have a divergence of V_{th} as the clearing point is approached because the voltage needed to drive the mechanism is inversely proportional to the anisotropy of the system, which becomes very small as T approaches the clearing point. Both of which are shown by PW2.

On the contrary, PW1 seems to be unrelated to the sign inversion of σ_a and shows a monotonic decrease of $V_{th}(T)$ through the clearing point. These observations seem to indicate that PW1 does not depend on the anisotropy of σ_a, or that it is caused by an isotropic mechanism. This behavior is not without precedent, as there have been several reports of LC EHC systems, other than the prewavy, that appear to be driven by an isotropic mechanism called the isotropic electrolyte model (see [26] and Refs. within). However PW1 shows different λ and threshold values than these cases, and cannot be described by the isotropic electrolyte model.

Unfortunately no rigorous theoretical treatment of the isotropic EHC modes has been developed at this time which could give an account of the mechanism of the prewavy pattern. Nor has the influence of a frequency dependent ϵ_a and σ_a been fully analyzed within the framework of SM, which could answer how the observed dielectric relaxation is related to the current situation. The few reports of EHC associated with dielectric relaxation [35, 51] concern substances applicable for dual frequency addressing , i.e. exhibiting a sign inversion of ϵ_a at increasing f, but having $\sigma_a > 0$ at all frequencies, which are not relevant to this case. So, although this material is fully characterized, there are many unanswered questions at this point.

BIBLIOGRAPHY

[1] M. Dennin. *A Study in Pattern Formation: Electroconvection in Nematic Liquid Crystals.* PhD thesis, University of California at Santa Barbara, 1995.

[2] W. J. A. Goossens. *Advances in Liquid Crystals*, volume 3. edited by G. H. Brown. Academic Press, 1995.

[3] P. G. de Gennes and J. Prost. *The Physics of Liquid Crystals.* Oxford Science Publications, 1993.

[4] W. Helfrich. *J. Chem. Phys.*, 51:4062, 1969.

[5] E. Bodenschatz, W. Zimmermann, and L. Kramer. *J. Phys. (Paris)*, 49:1875, 1988.

[6] L. Kramer, E. Bodenschatz W. Pesch, W. Thom, and W. Zimmermann. *Liq. Cryst.*, 5:699, 1989.

[7] M. Treiber and L. Kramer. *Mol. Cryst. Liq. Cryst.*, 261:311, 1995.

[8] F. C. Frank. *Discuss. Faraday Soc.*, 25:19, 1958.

[9] F. M. Leslie. *Q. J. Mech. Appl. Math.*, 19:357, 1966.

[10] A. Buka and L. Kramer. *Pattern Formation in Liquid Crystals.* Springer-Verlag, 1996.

[11] E. Dubois Violette, P. G. de Gennes, and O. Parodi. *J. Phys. (Paris)*, 32:305, 1971.

[12] A. Buka, N. Eber, and W. Pesch. *El. Liq. Cryst. Commun., <http://www.e-lc.org/docs/2005_07_12_04_29_54>*, 2005.

[13] M. Dennin, M. Treiber, L. Kramer, G. Ahlers, and D. Cannell. *Phys. Rev. Lett.*, 76:319, 1996.

[14] M. Treiber. PhD thesis, University of Bayreauth, 1996.

[15] M. Treiber, N. Eber, A. Buka, and L. Kramer. *J. Phys. II*, 7:649, 1997.

[16] M. Treiber and L. Kramer. *Phys. Rev. E*, 58:1973, 1998.

[17] E. Kochowska, S. Nemeth, G. Pelzl, and A. Buka. *Phys. Rev. E*, 70:011711, 2004. El. Liq. Cryst. Commun., <http://www.e-lc.org/docs/2004_01_23_11_12_27>.

[18] L. M. Blinov, M. I. Barnik, V. T. Lazareva, and A. N. Trufanov. *J. Phys. (Paris), Colloq.*, C3:C3–263, 1979.

[19] P. Petrescu and M. Giurgea. *Phys. Lett. A*, 59:41, 1976.

[20] L. Nasta, A. Lupu, and M. Giurgea. *Mol. Cryst. Liq. Cryst.*, 71:65, 1981.

[21] A. N. Trufanov, M. I. Barnik, and L. M. Blinov. *JETP*, 51:314, 1980.

[22] S. Kai and K. Hirakawa. *Solid State Commun.*, 18:1573, 1976.

[23] R. Ribotta and G. Durand. *J. Phys. (Paris), Colloq.*, 40:C3–334, 1979.

[24] W. Weissflog, G. Pelzl, H. Kresse, and D. Demus. *Cryst. Res. Technol.*, 23:1259, 1988.

[25] J.-H. Huh, Y. Yusuf, Y. Hidaka, N. Eber, T. Toth-Katona, A. Buka, and S. Kai. *Mol. Cryst. Liq. Cryst.*, 364:111, 2001.

[26] J.-H. Huh, Y. Yusuf, Y. Hidaka, and S. Kai. *Phys. Rev. E*, 66:031705, 2002.

[27] S. Komineas, H. Zhao, and L. Kramer. *Phys. Rev. E*, 67:031701, 2003.

[28] M. I. Barnik, L. M. Blinov, S. A. Pikin, and A. N. Trufanov. *JETP*, 45:396, 1977.

[29] S. A. Pikin and V. G. Chigrinov. *JETP*, 51:123, 1980.

[30] W. Weissflog, S. Sokolowski, H. Dehne, B. Das, S. Grande, M. Schroder, A. Eremin, S. Diele, G. Pelzl, and H. Kresse. *Liq. Cryst.*, 31:923, 2004.

[31] K. Fodor-Csorba, A. Vajda, G. Galli, A. Jakli, D. Demus, S. Holly, and E. Gacs-Baitz. *Macromol. Chem. Phys.*, 203:1556, 2002.

[32] E.H.C. Co, Tokyo, Japan.

[33] D. Wiant, J. T. Gleeson, N. Eber, K. Fodor-Csorba, A. Jakli, and T. Toth-Katona. *Phys. Rev. E*, 72:041712, 2005.

[34] Hp. Schad, B. Scheuble, and J. Nehring. *J. Chem. Phys.*, 71:5140, 1979.

[35] W. H. De Jeu, C. J. Gerritsma, and W. J. A. Goosens. *Phys. Lett.*, 39A:355, 1972.

[36] F. Brochard. *Mol. Cryst. Liq. Cryst.*, 23:51, 1973.

[37] H. Kneppe, F. Schneider, and N. K. Sharma. *J. Chem. Phys.*, 77:3203, 1982.

[38] K. Skarp, S. T. Lagerwall, and B. Stebler. *Mol. Cryst. Liq. Cryst.*, 60:215, 1980.

[39] M. Cui and J. R. Kelly. *Mol. Cryst. Liq. Cryst.*, 331:1909, 1999.

[40] R. B. Meyer. *Phys. Rev. Lett.*, 22:918, 1969.

[41] W. Helfrich. *Z. Naturforsch*, 26A:833, 1971.

[42] J. Harden, B. Mbanga, N. Eber, K. Fodor-Csorba, S. Sprunt, J. T. Gleeson, and A. Jakli. *submitted Phys. Rev. Lett.*, 2006.

[43] M. I. Barnik, L. M. Blinov, B. A. Umansky, and A. N. Trufanov. *J. Phys. (Paris)*, 39:417, 1978.

[44] L. M. Blinov. *J. Phys. (Paris), Colloq.*, 40:C3–247, 1979.

[45] Y. Bobylev, V. G. Chigrinov, and S. Pikin. *J. Phys. (Paris), Colloq.*, 40:C3–331, 1979.

[46] M. Goscianski and L. Leger. *J. Phys. (Paris), Colloq.*, C1:C1–231, 1975.

[47] N. V. Madhusudana and V. A. Raghunathan. *Liquid Crystals*, 5:1789, 1989.

[48] J.-H. Huh, Y. Hidaka, A. Rossberg, and S. Kai. *Phys. Rev. E*, 61:2769, 2000.

[49] S. Kai, Y. Adachi, and S. Nasuno. *Spatio-Temporal Patterns.* edited by P. Cladis and Palffy-Muhoray. Addison-Wesley Publishing Company, 1995.

[50] M. Lowe and J. P. Gollub. *Phys. Rev. Lett.*, 55:2575, 1985.

[51] V. G. Chigrinov, A. Sparavigna, and A. Strigazzi. *Phys. Rev. E*, 53:4918, 1996.

CHAPTER 6

CONCLUSIONS

The structures of bent-core LCs are fundamentally different from that of the more common calamitic liquid crystals. The shape of the bent-core molecules allows for arrangements and organization in these materials that are not possible in calamitics. The interactions between the bent-core molecules gives us the B phases, as well as the exotic fluid phases described in the introduction. These molecules also provide us with new platforms to study and test current ideas about such things as N-I transitions and the flexoelectric effect, which occur in bent-core systems with features different from calamitics. Bent-core liquid crystals present an excellent chance to further theoretical and empirical knowledge of liquid crystals through their unique features and the opportunity to look at old situations in a new way.

6.1 MAGNETIC FIELD INDUCED BIREFRINGENCE

The magnetic field induced birefringence was measured for ClPbis10BB and ClPbis10BBs as a function of temperature and magnetic field. These measurements showed that Δn did not follow the standard H^2 dependence predicted by LdG mean field theory for calamitics. I showed that this behavior could be explained by including tetrahedratic ordering in the LdG model. This model predicted a phase transition between two optically isotropic phases, which could be seen by a change in the CM coefficient. This transition was observed and was related to the isotropic-tetrahedratic (I-T) phase change described by Lubensky and Radzihovsky.

Lubensky and Radzihovsky predicted that a clustered nematic phase (N_T) exists below the T phase. A large viscosity, a small magnetic susceptibility anisotropy, and a large flexoelectric effect in the phase below the clearing point (in comparison to calamitics) make it probable that the phase below the clearing point in ClPbis10BB and ClPbis10BBs is indeed a clustered nematic phase, but this should be experimentally verified through x-ray scattering, or a comparable method. The MB experiment is physically challenging to perform, in Appendix G, I present a variation on this experiment which should be easier and more efficient to perform. The experiment in its current form is still useful, and subsequently the set-up for use in high fields has been retooled. The tower has been removed and the oven is suspended from the top of the magnet with all wires coming out the top, in the next iteration of this experiment. Also, the movable mirrors previously mounted on the top plate have been replaced by fixed right angle prism with an external face coated with silver. These changes make the set-up more rigid and easier to align.

6.2 DYNAMIC LIGHT SCATTERING

Dynamic light scattering measurements on ClPbis10BB and ClPbis10Bbs made by Neupane *et al.* show that the relaxation rates of nematic order parameter fluctuations exhibit a sharp change in temperature dependence, driven by a change in viscosity, at the same temperatures where the T_T^*'s were calculated in the magnetic birefringence measurements. I showed that this behavior could be explained by including the tetrahedratic ordering into Landau free energy for the bent-core liquid crystals, and using this free energy in the Landau-Khalatnikov relation.

The results also showed that w_1' is very small, or that the S-T coupling is very weak, which is in good agreement with the MB theory and In this work, I have

shown evidence of a phase transition between two optically isotropic phases, above the clearing point in two bent-core LCs. These transitions may be understood within the framework of the previously predicted tetrahedratic ordering. These measurements provided independent verification of the phase transitions observed in the magnetic birefringence experiment, and further support to the idea that tetrahedratic ordering is present in the liquid phases of these bent-core molecules.

In the future, some theoretical work on the relation between the size, number density, and shape and the viscosity in the T and I phase might prove interesting. Also, an attempt to probe the size of the w_1' term might be helpful. DLS, DNMR, or x-ray scattering might be able to provide information on this question.

6.3 VOLUME CHANGE AT A PHASE TRANSITION

The volume measurements on ClPbis10BB and ClPbis10BBs accomplished two things. First, they introduced a new method to measure volume change with small sample volumes. And second, they found that the volume change at the N_T-T transition in these bent-core materials is significantly smaller than that of calamitics at a N-I transition. Also, these measurements placed on upper bound on the size of the volume change at the T-I transition. The extremely small volume change at the T-I transition suggests that this transition is weakly first order.

In the future refinements on the volume measurement technique, such as longer cell sizes and improvement on temperature stability over the length of the sample, could greatly improve the accuracy and resolution of the measurements. A longer cell, of the same inner dimensions, would lead to a greater volume change at the transition, while better temperature control would lead to sharper transitions (reduce the smearing). To accomplish this a new oven would need to be built, which would

not be difficult, but a new method to fill the capillaries would need to be found. The present method is very time consuming, and I had great difficulties trying to get more than 3-4 cm into a capillary. Also, the programs controlling need to be modified so that the temperature and camera are controlled by the same software and so that the image editing is all done in Matlab. This will save a great deal of time and effort. As for ClPbis10BB and ClPbis10BBs, if larger volumes of materials become available it would be interesting to use more precise dilatometry techniques to determine the exact density change at the T-I transition. Also, the theoretical implications of including a density dependence in the LdG model for systems with tetrahedratic ordering should be considered.

6.4 ELECTROHYDRODYNAMIC CONVECTION

The bent-core liquid crystal ClPbis10BB showed four distinct frequency dependent regions of EHC. The lowest frequency region was the parallel stripe (PS) region. The PS showed strong similarities to the flexoelectric effect observed in $(--)$ calamitics. The gigantic flexoelectric coefficient observed in ClPbis10BB make it very probable that the PS is in fact caused by the this effect, though this needs to be verified.

Following the PS is the prewavy2 regime (PW2). This broad stripe pattern is optically identical to the so called prewavy instability in calamitics, which is believed to be caused by an isotropic mechanism, and to the PW1 pattern observed on the other side of the empty region. Though the threshold behavior of the PW2 seems to discourage these comparisons, as I mentioned earlier, there are several circumstances in which the threshold behavior of an instability may be masked or altered. So, the main questions left to answer are whether the PW1 and PW2 are the same type of instability and what sort of mechanism drives the prewavy instability.

The next region with increasing frequency is the empty region (ER). ClPbis10BB is $(-+)$ in the ER, so a standard model type instability should be present in this region. Standard model EHC in the ER is probably being prevented by some combination of interactions between a dielectric relaxation mechanism, a flexoelectric mechanism, and a broad stripe mechanism, again this needs to be further studied. Also, initial results show that the location and width of the PS regime and the ER, with respect to frequency, tend to vary as the conductivity of the sample is changed. Further experiments that start with very pure samples and alter the conductivity might help to explain ER in ClPbis10BB.

There are many questions left to be answered about EHC in ClPbis10BB and in bent-core liquid crystals in general. Possible lines of further investigation are the purification of ClPbis10BB followed by a pattern of doping to determine the effect of conductivity on each of the instabilities. Three dimensional imaging of the director orientation in an EHC state, using a method such as fluorescent polarizing confocal microscopy, might be helpful to explain the how the dislocations and knitting instability are formed. Also, a more careful examination of the knitting instability to determine how dislocations move along the stripes and interact to form new stripe pairs could be of interest. The characterization of other bent-core materials would be useful to determine if the ER and sign changes of the conductivity are specific to ClPbis10BB. Finally, the theoretical implications of a clustered nematic phase on EHC need to be considered.

APPENDIX A

YORICK CODE TO DRIVE THE KSU MB EXPERIMENT

Yorick is an interpreted programming language that resembles the C programming language, but without explicit variable declarations. More information on Yorick can be found at: **yorick.sourceforge.net/index.php**. The Yorick code used to drive the KSU MB experiment:

```
//goes to temp pauses than records values with getPts
//odd number files are with out field, even numbers with field.


#include "jlib.i"
#include "getPts.i"
func mag Bi(num, temp, interval) //num of temp steps,start temp, temp steps
{
        for(i=1;i¡num;i++)
        {
                J_SetTempCts(temp);
                pause,600000; //10min
                num1 = swrite(format = "%i.dat",j);
                getPts(100,num1);
                pause, 10000; //10sec
                j = j+1;
```

```
                num2 = swrite(format = "%i.dat",j);
                J_SetField(5,1);
                pause, 90000; //1min30sec
                getPts(100,num2);
                j = j+1;
                J_SetField(0, 1);
                temp = temp - interval;
        }
}

func getPts(number,outfile)
{
        outfile = create(outfile);
        for(i=0;i¡number;i++)
        {
                sub1 = J_GetLI(1);
                sub2 = J_GetLI(2);
                subTot = (sub1^2) + (sub2^2);
                midTot = subTot^.5;
                dc = J_GetVoltDC(HPDVM1);
                temp = J_GetTempConductus();
                write, outfile,midTot,dc,temp;
        }
}
```

APPENDIX B

Δn AS A FUNCTION OF MAGNETIC FIELD FOR ClPBis10BB AND ClPBis10BBs

B.1 ClPBis10BB

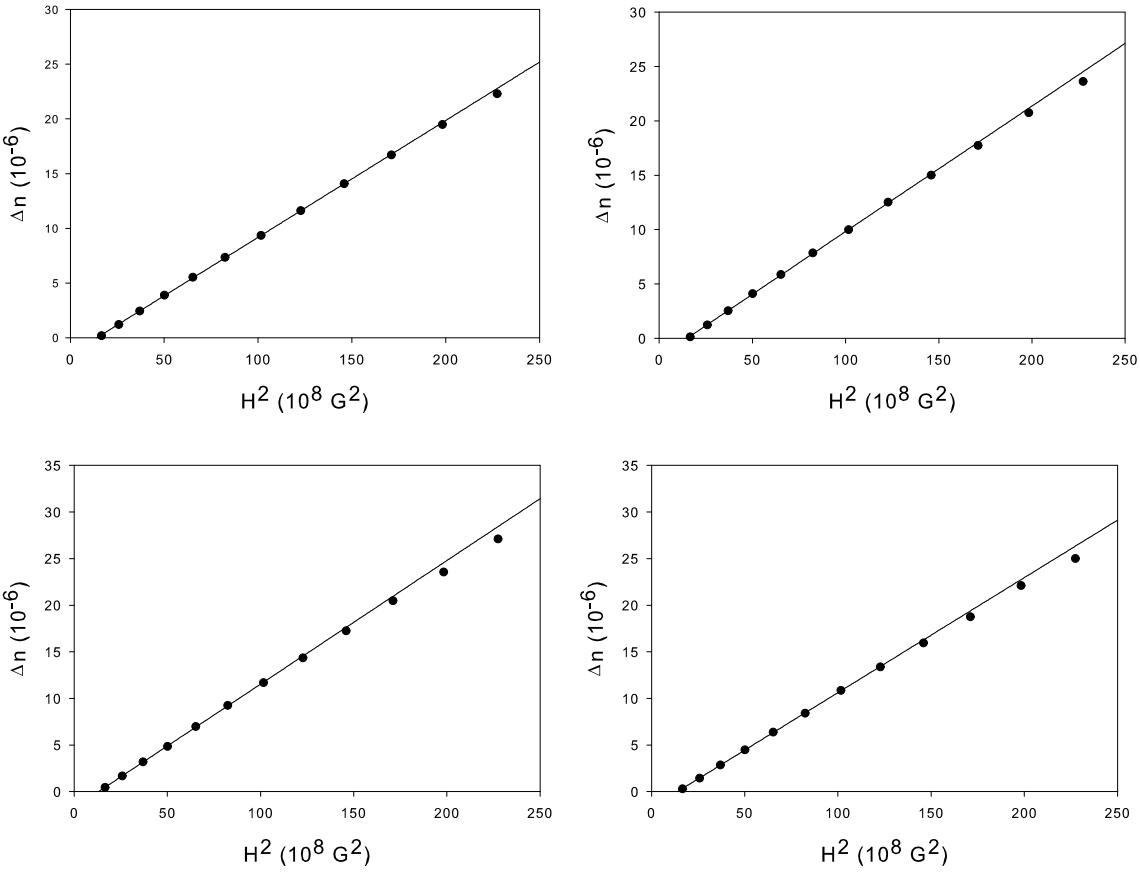

Figure B.1: Induced birefringence as a function of squared magnetic field for ClPBis10BB on cooling from the isotropic. The clearing point on cooling was 76.9°C. The straight line is a linear fit to the low field data points. Clockwise from upper left: $T - T_{N_T T} = 18.1$, 17.1, 16.1, and 15.1°C.

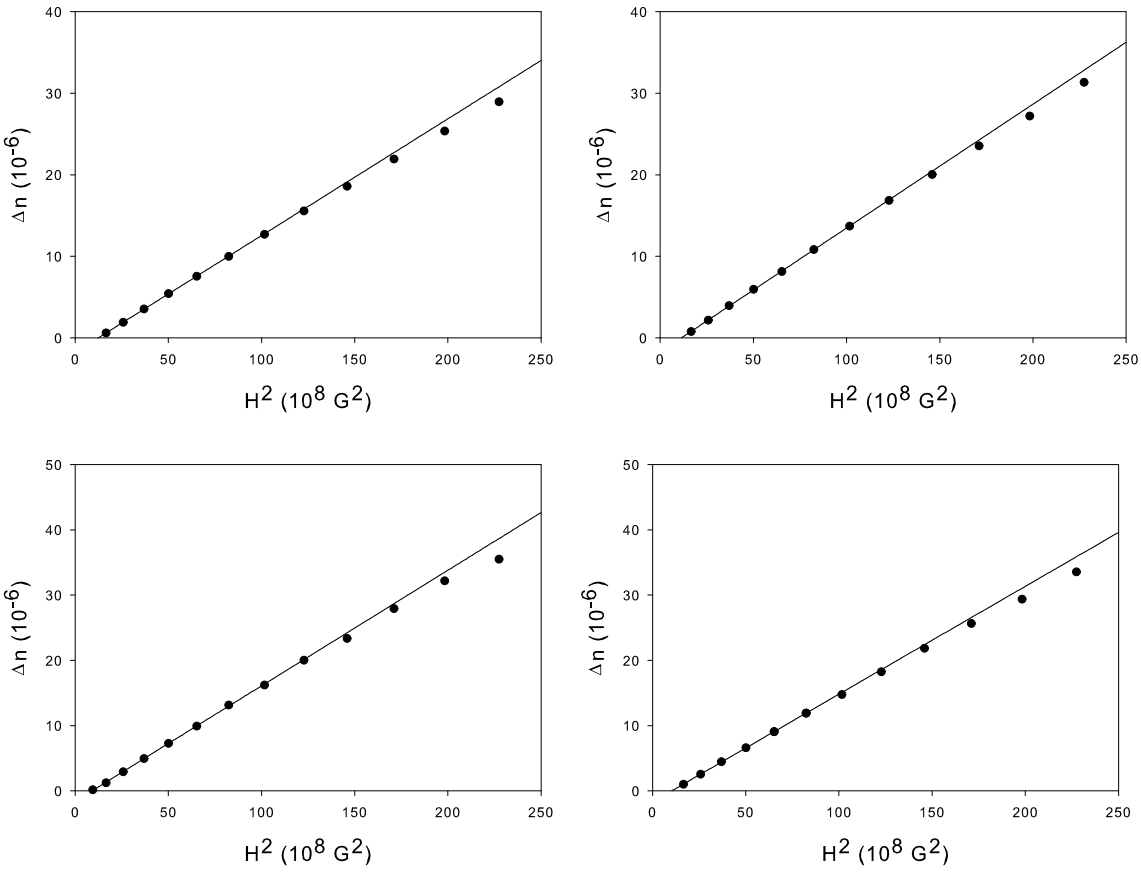

Figure B.2: Induced birefringence as a function of squared magnetic field for ClP-bis10BB on cooling from the isotropic. The clearing point on cooling was 76.9°C. The straight line is a linear fit to the low field data points. Clockwise from upper left: $T - T_{N_T T} = 14.1$, 13.1, 12.1, and 11.1°C.

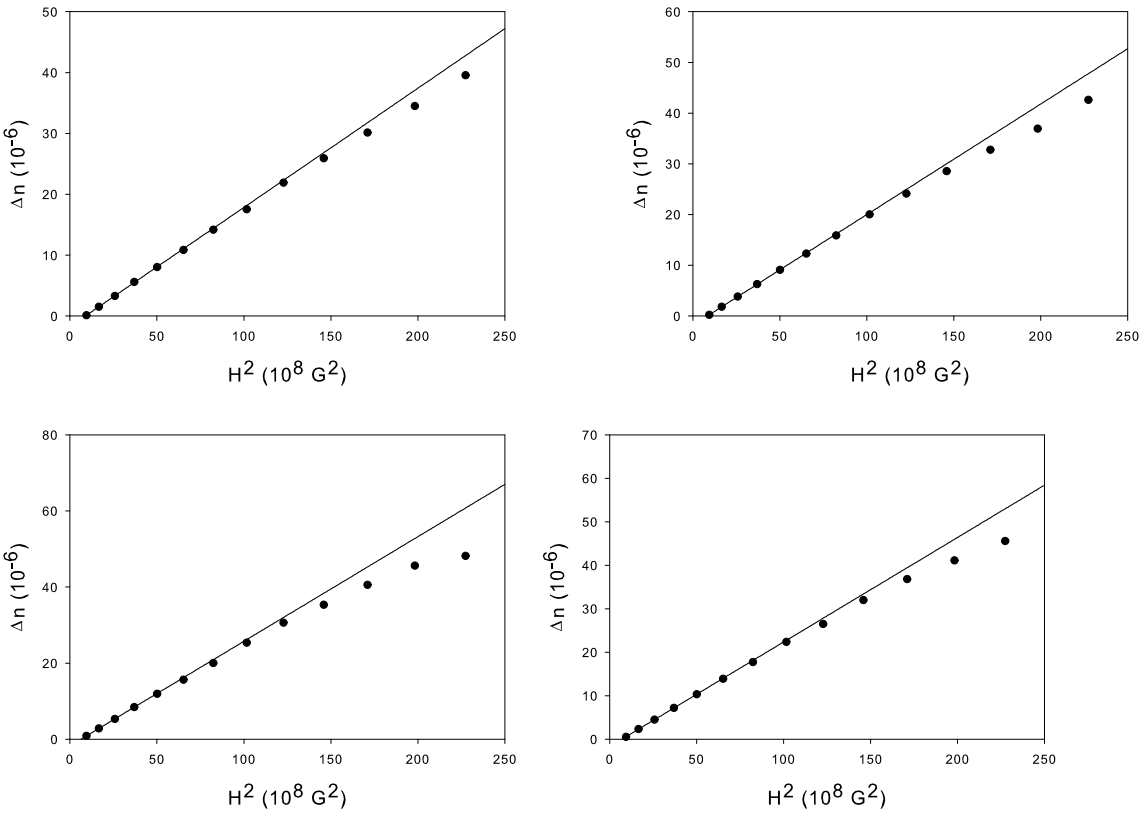

Figure B.3: Induced birefringence as a function of squared magnetic field for ClP-bis10BB on cooling from the isotropic. The clearing point on cooling was 76.9°C. The straight line is a linear fit to the low field data points. Clockwise from upper left: $T - T_{N_T T} = 10.1$, 9.1, 8.1, and 7.1°C.

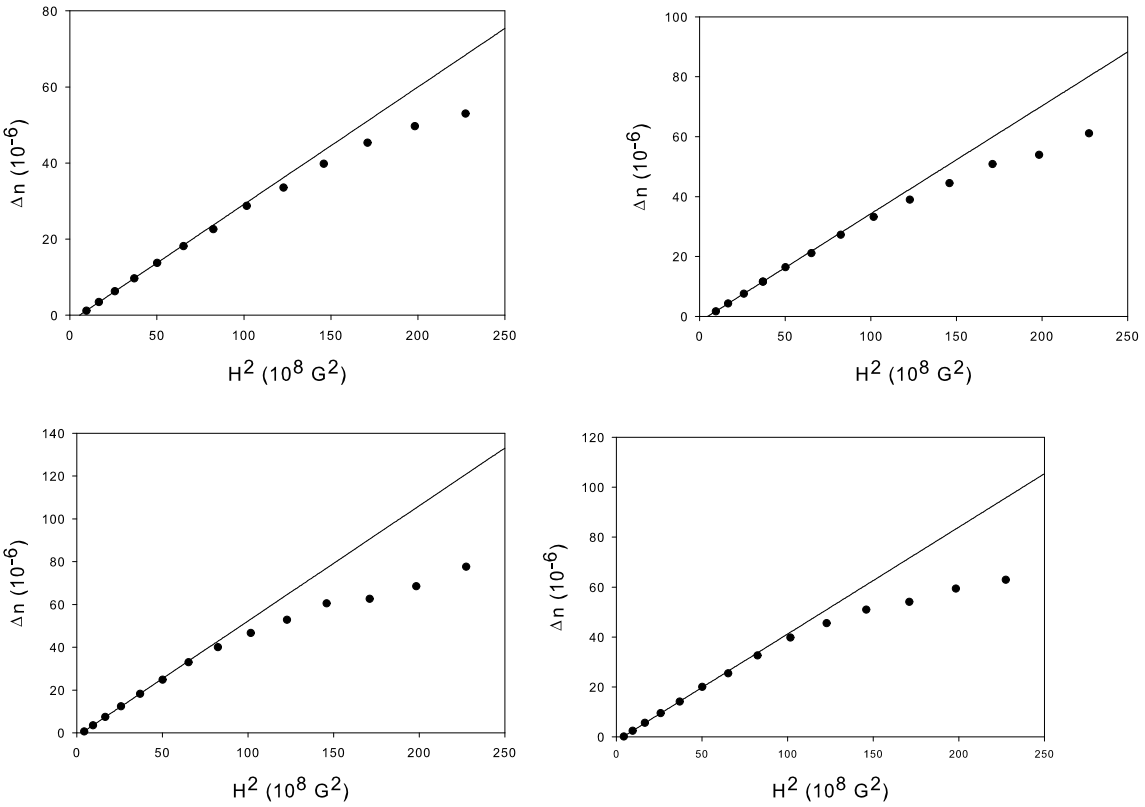

Figure B.4: Induced birefringence as a function of squared magnetic field for ClP-bis10BB on cooling from the isotropic. The clearing point on cooling was 76.9°C. The straight line is a linear fit to the low field data points. Clockwise from upper left: $T - T_{N_T T} = 6.1$, 5.1, 4.1, and 3.1°C.

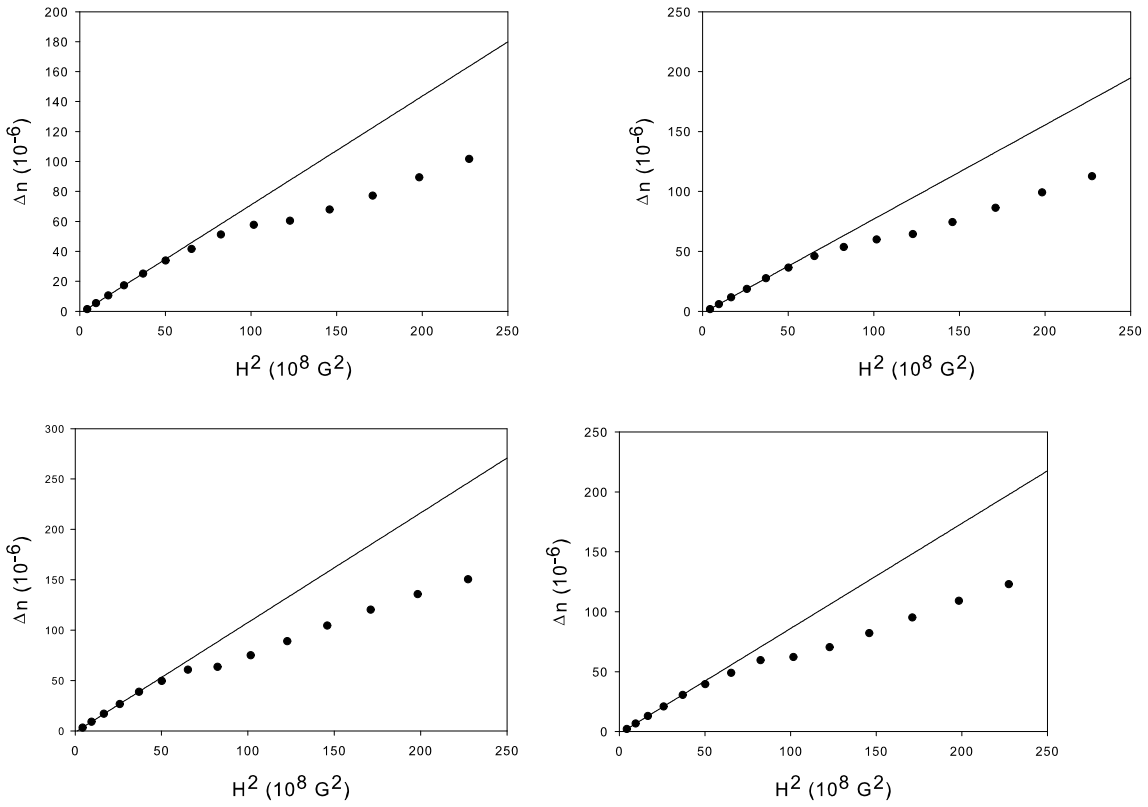

Figure B.5: Induced birefringence as a function of squared magnetic field for ClP-bis10BB on cooling from the isotropic. The clearing point on cooling was 76.9°C. The straight line is a linear fit to the low field data points. Clockwise from upper left: $T - T_{NTT} = 2.1$, 1.85, 1.6, and 1.1°C.

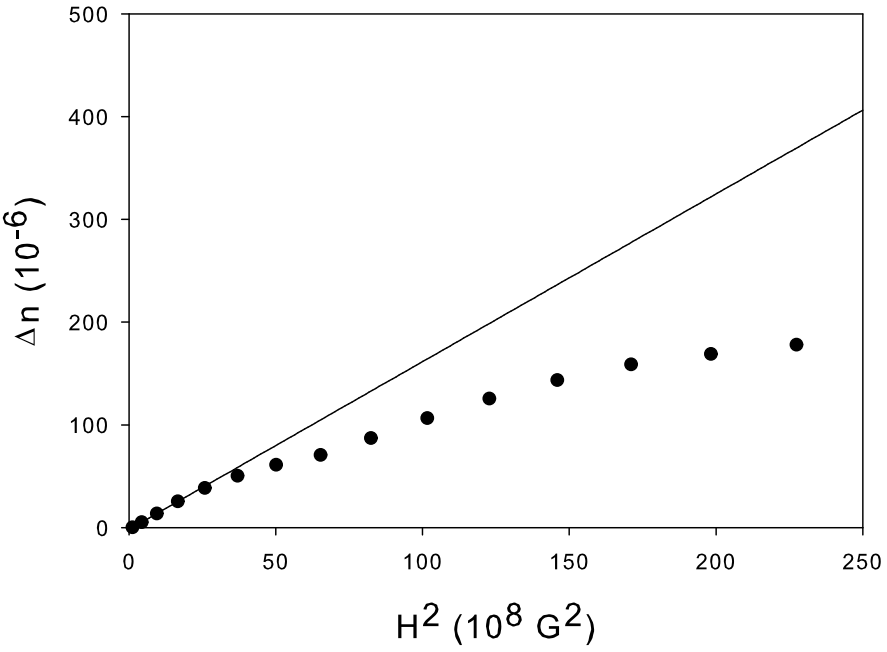

Figure B.6: Induced birefringence as a function of squared magnetic field for ClP-bis10BB on cooling from the isotropic. The clearing point on cooling was 76.9°C. The straight line is a linear fit to the low field data points. In the this figure $T - T_{N_T T}$ =0.6°C.

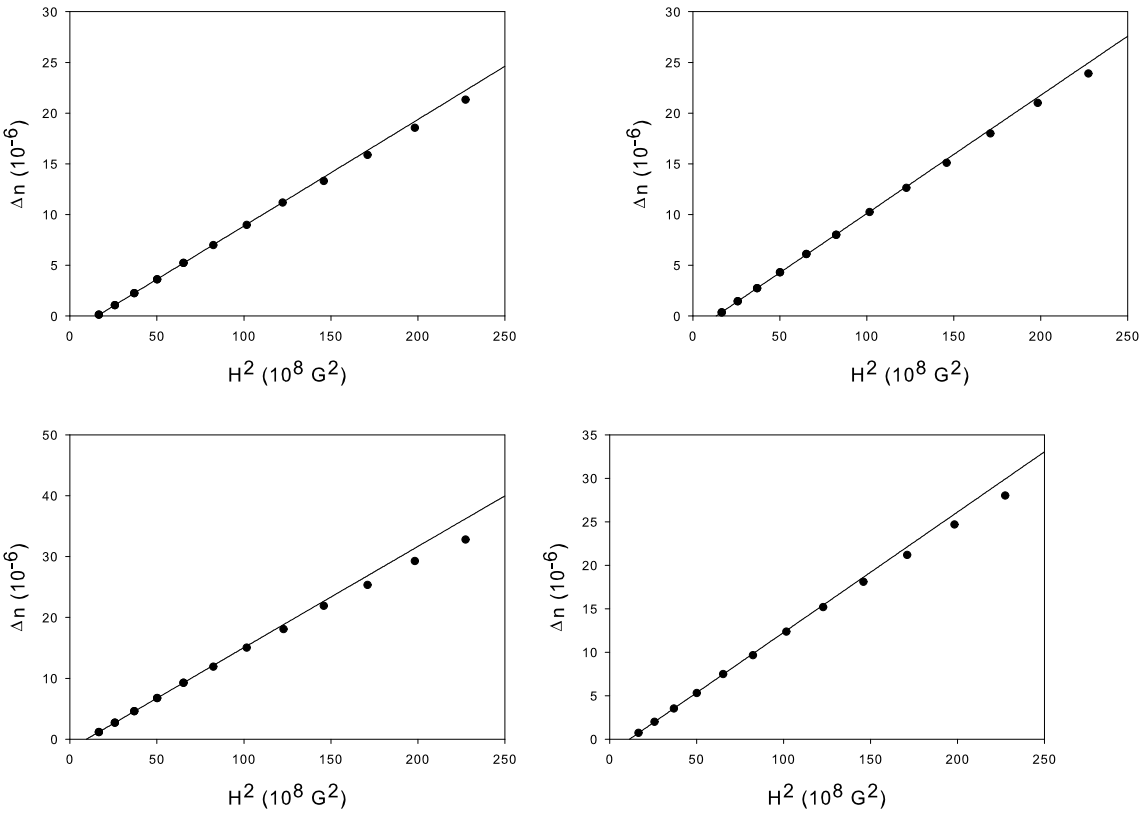

Figure B.7: Induced birefringence as a function of squared magnetic field for ClP-bis10BB on heating from the N_T phase. The clearing point on heating was 77.0°C. The straight line is a linear fit to the low field data points. Clockwise from upper left: $T - T_{N_T T} = 19$, 17, 14.5, and 12°C.

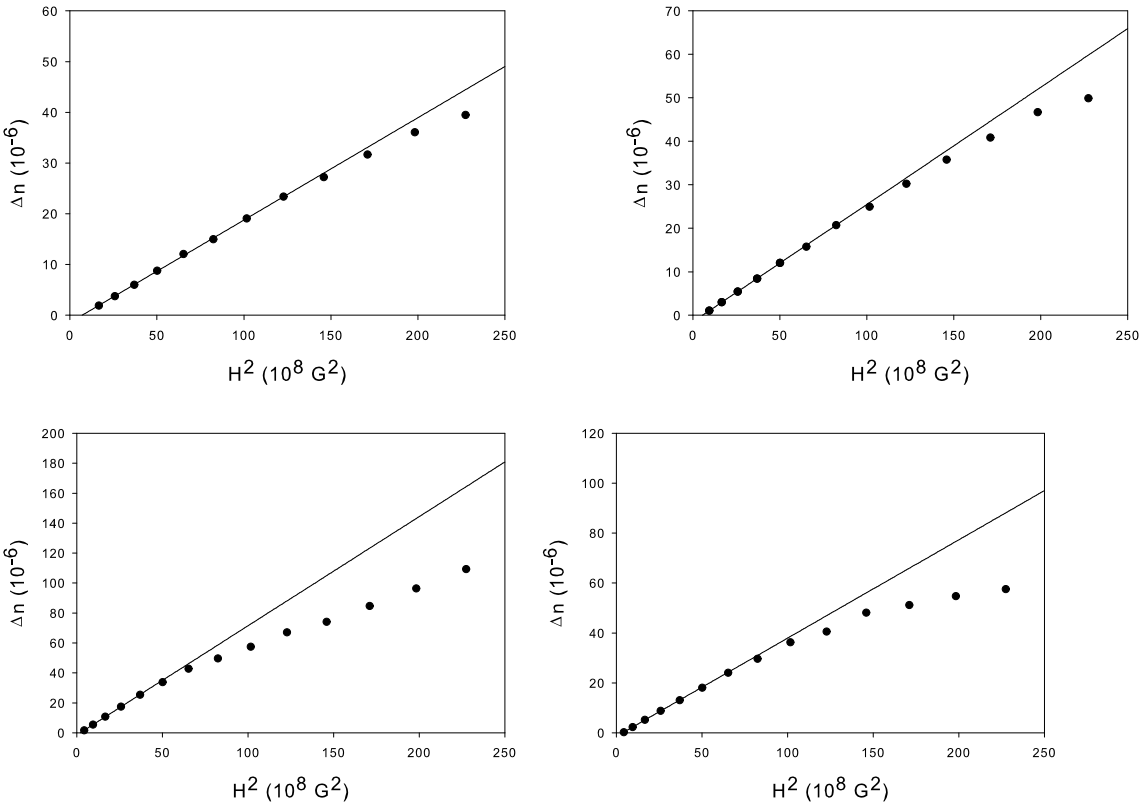

Figure B.8: Induced birefringence as a function of squared magnetic field for ClP-bis10BB on heating from the N_T phase. The clearing point on heating was 77.0°C. The straight line is a linear fit to the low field data points. Clockwise from upper left: $T - T_{N_T T} = 9.5$, 7, 4.5, and 2°C.

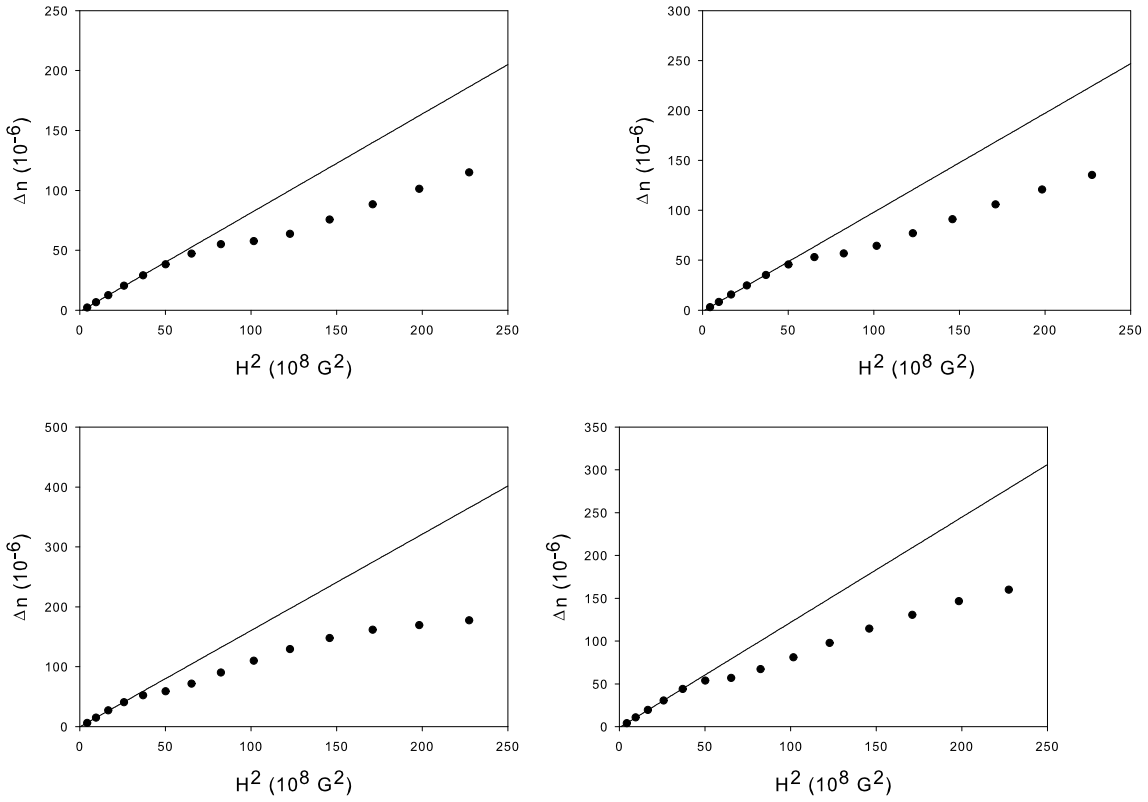

Figure B.9: Induced birefringence as a function of squared magnetic field for ClP-bis10BB on heating from the N_T phase. The clearing point on heating was 77.0°C. The straight line is a linear fit to the low field data points. Clockwise from upper left: $T - T_{N_T T} = 1.6$, 1.2, 0.8, and 0.4°C.

B.2 ClPBis10BBs

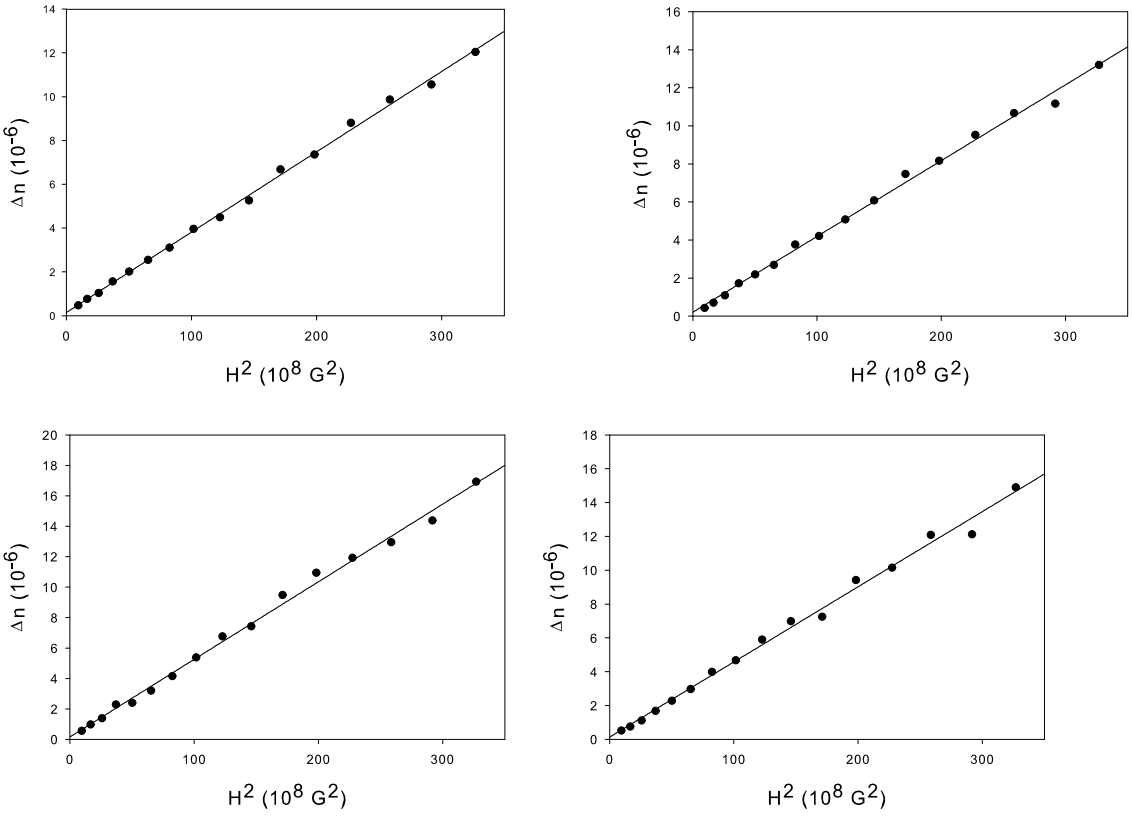

Figure B.10: Induced birefringence as a function of squared magnetic field for ClPbis10BBs on cooling from the isotropic. The clearing point on cooling was 90.2°C. The straight line is a linear fit to the low field data points. Clockwise from upper left: $T - T_{NTT} = 29.8$, 26.8, 23.8, and 20.8°C.

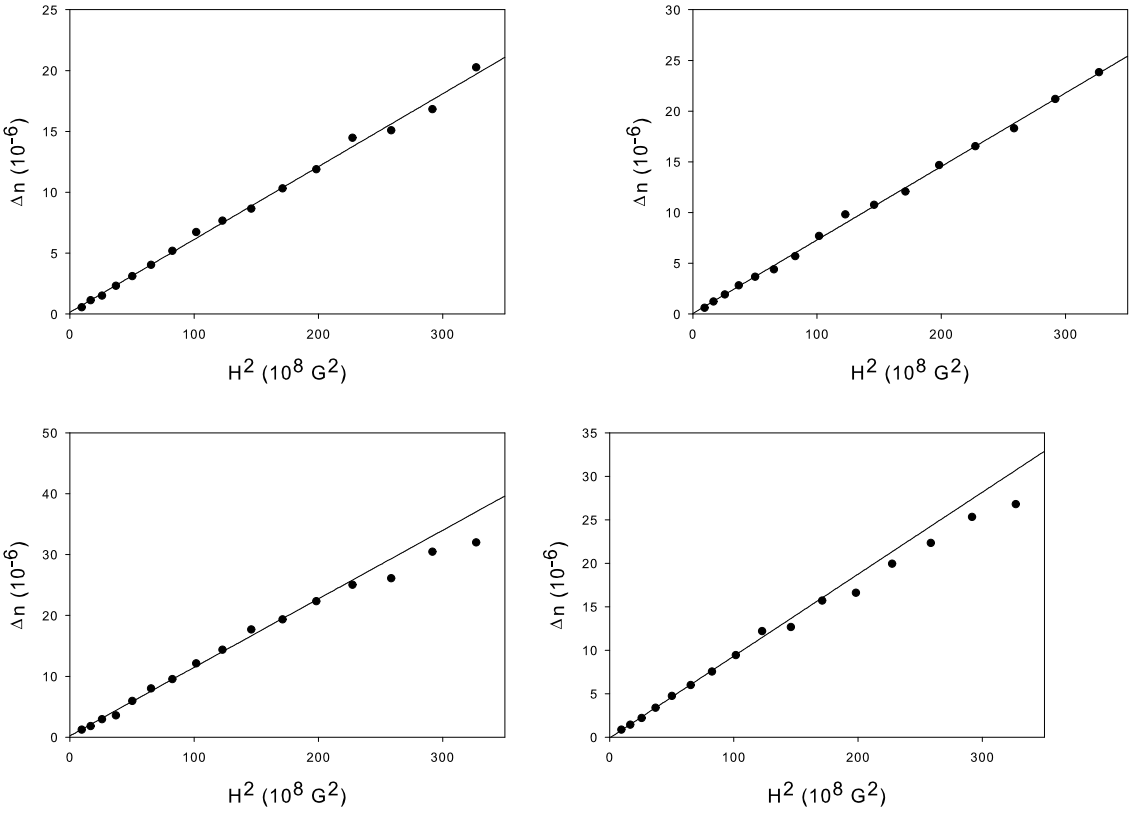

Figure B.11: Induced birefringence as a function of squared magnetic field for ClP-bis10BBs on cooling from the isotropic. The clearing point on cooling was 90.2°C. The straight line is a linear fit to the low field data points. Clockwise from upper left: $T - T_{N_T T} = 17.8$, 14.8, 11.8, and 8.8°C.

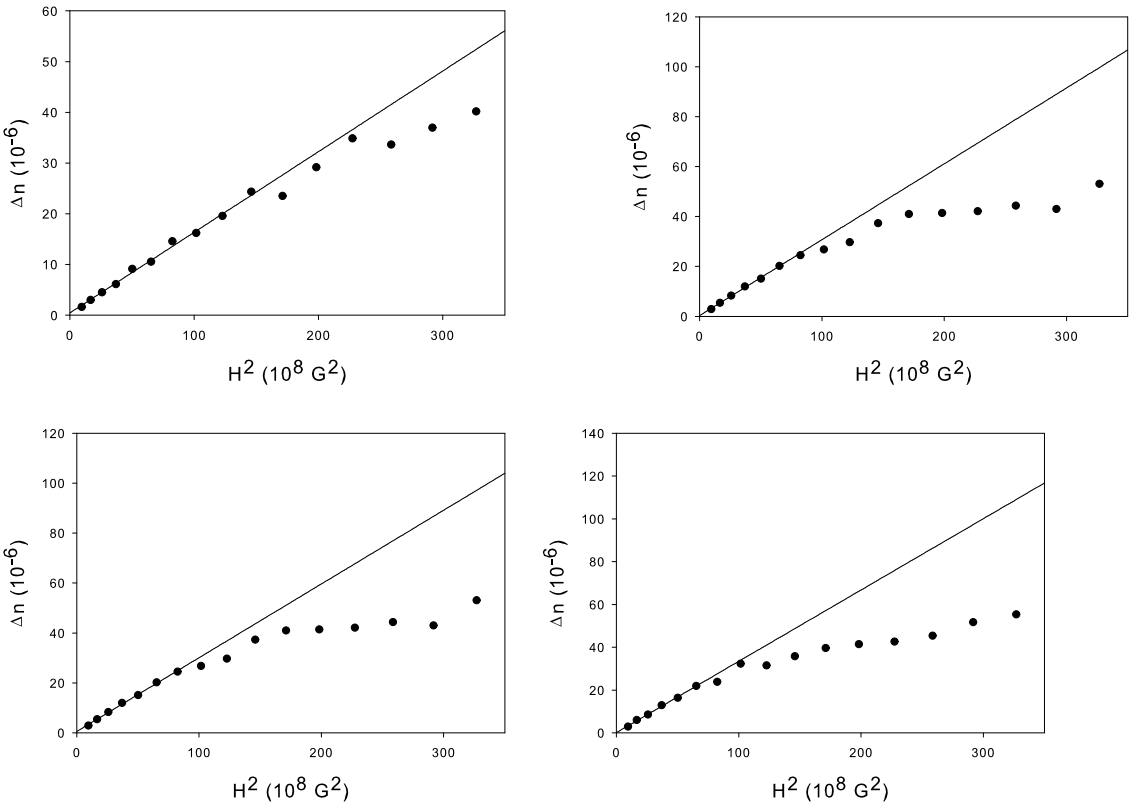

Figure B.12: Induced birefringence as a function of squared magnetic field for ClP-bis10BBs on cooling from the isotropic. The clearing point on cooling was 90.2°C. The straight line is a linear fit to the low field data points. Clockwise from upper left: $T - T_{N_T T} = 5.8$, 2.8, 2.3, and 1.8°C.

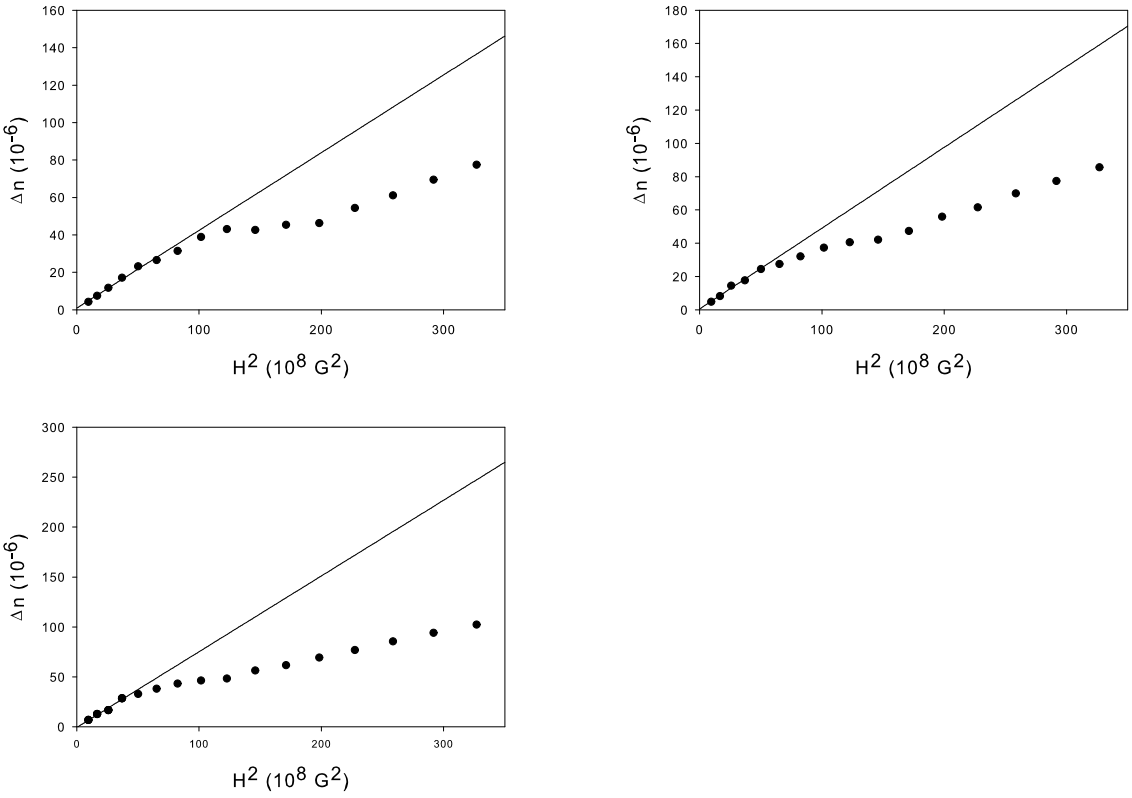

Figure B.13: Induced birefringence as a function of squared magnetic field for ClP-bis10BBs on cooling from the isotropic. The clearing point on cooling was 90.2°C. The straight line is a linear fit to the low field data points. Clockwise from upper left: $T - T_{N_T T} = 1.3$, 1.1, and 0.8°C.

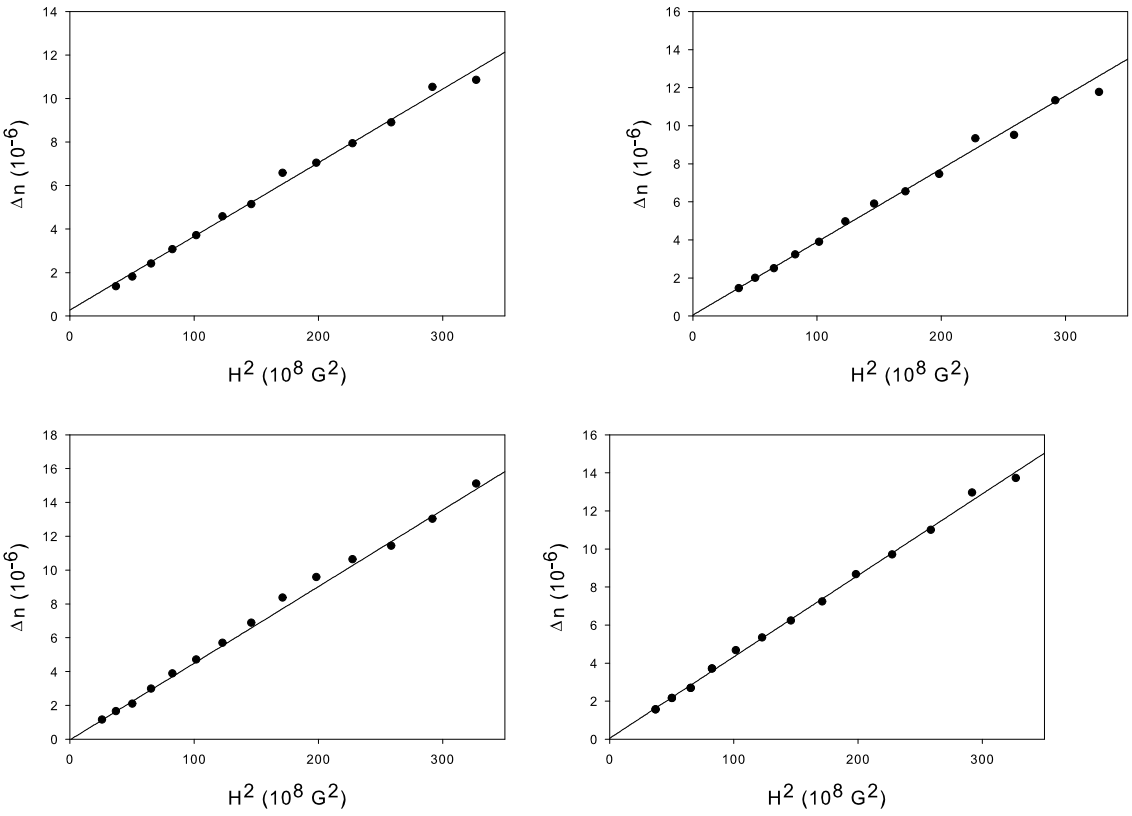

Figure B.14: Induced birefringence as a function of squared magnetic field for ClP-bis10BBs on heating from the N_T phase. The clearing point on heating was 90.3°C. The straight line is a linear fit to the low field data points. Clockwise from upper left: $T - T_{N_T T} = 31.7$, 28.7, 25.7, and 22.7°C.

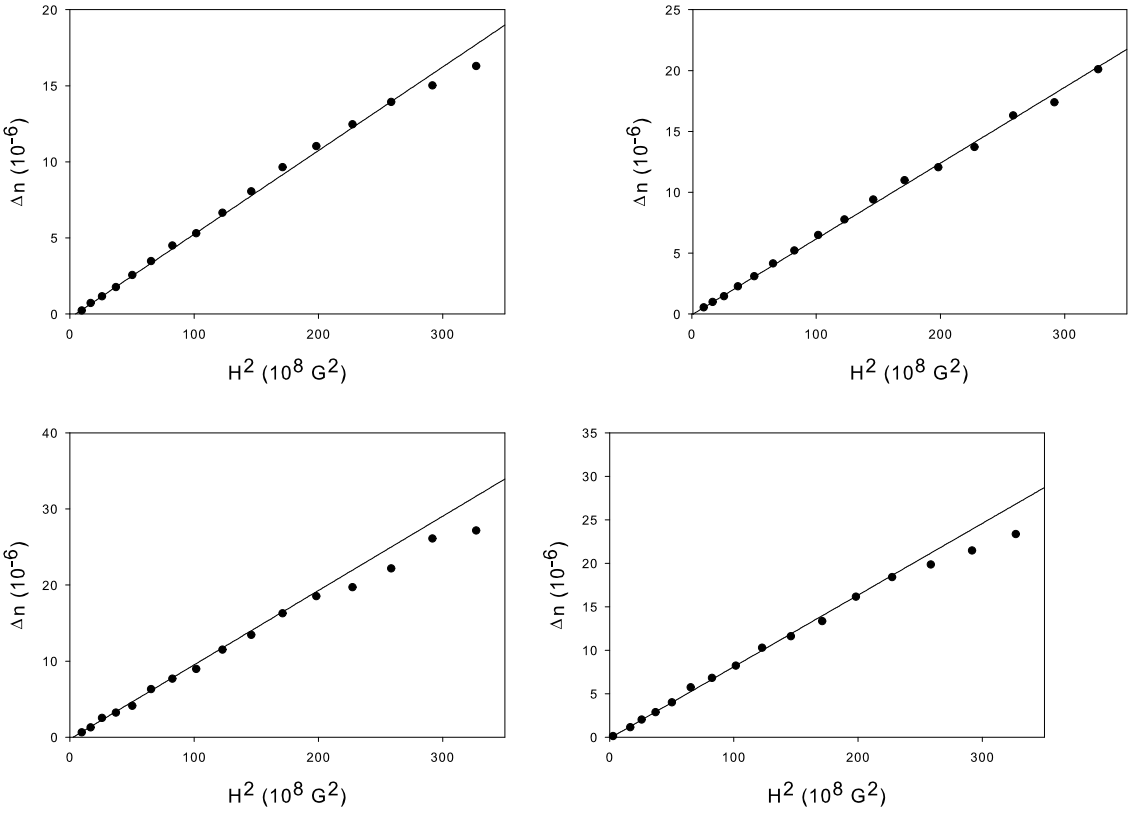

Figure B.15: Induced birefringence as a function of squared magnetic field for ClP-bis10BBs on heating from the N_T phase. The clearing point on heating was 90.3°C. The straight line is a linear fit to the low field data points. Clockwise from upper left: $T - T_{N_T T} = 19.7$, 16.7, 13.7, and 10.7°C.

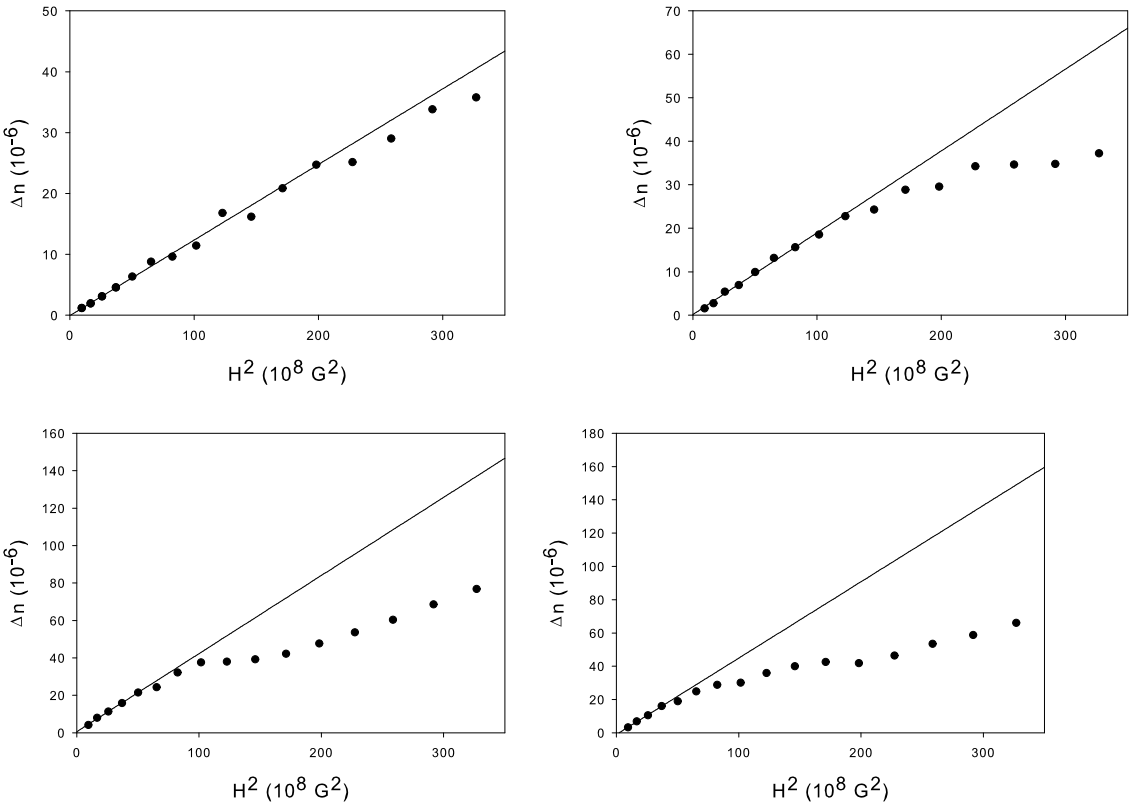

Figure B.16: Induced birefringence as a function of squared magnetic field for ClP-bis10BBs on heating from the N_T phase. The clearing point on heating was 90.3°C. The straight line is a linear fit to the low field data points. Clockwise from upper left: $T - T_{N_T T} = 7.7$, 4.7, 1.7, and 1.2°C.

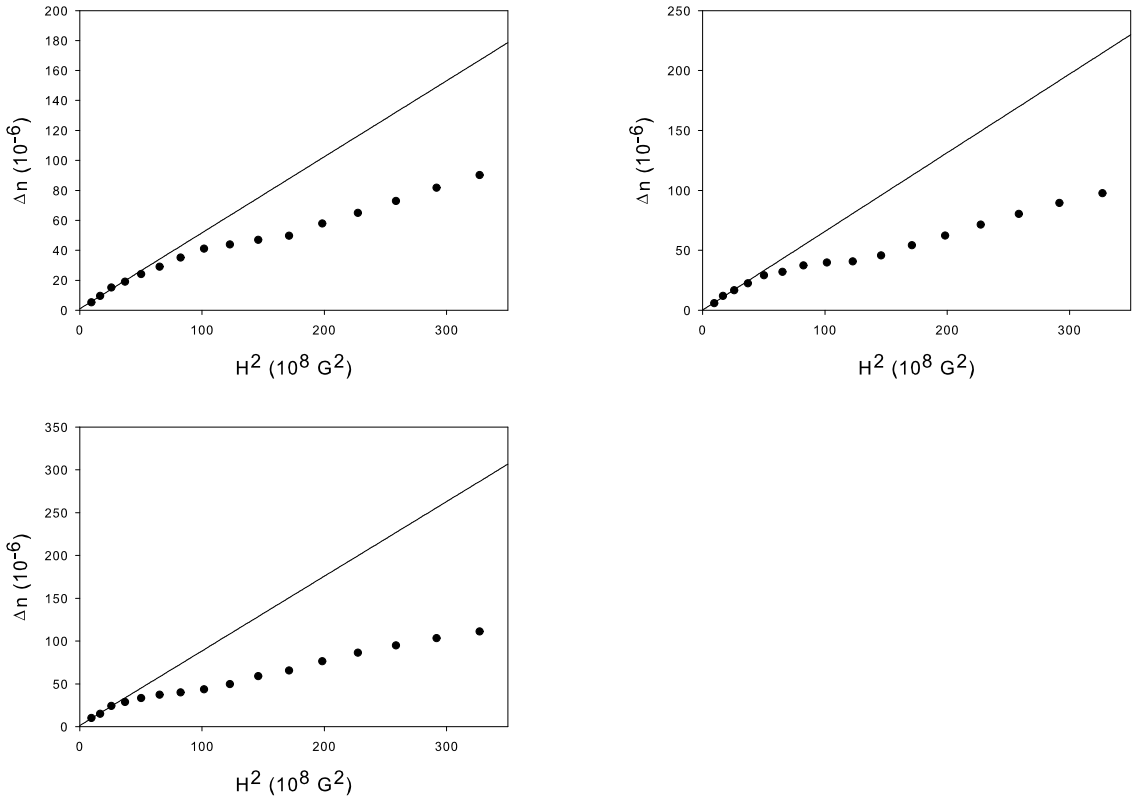

Figure B.17: Induced birefringence as a function of squared magnetic field for ClP-bis10BBs on heating from the N_T phase. The clearing point on heating was 90.3°C. The straight line is a linear fit to the low field data points. Clockwise from upper left: $T - T_{N_T T} = 0.9$, 0.6, and 0.3°C.

APPENDIX C

ALTERNATIVE MODELS TO EXPLAIN MB IN BENT-CORE LIQUID CRYSTALS

C.1 INCLUDING HIGHER ORDER TERMS IN LDG THEORY FOR CALAMITICS

In chapter 2, the free energy for a uniaxial calamitic liquid crystal in a magnetic field was expressed to lowest order in the nematic order parameter S as

$$F = \frac{3A}{4}S^2 - \frac{1}{3}\Delta\chi H^2 S. \tag{C.1}$$

In a large magnetic field it is possible that higher order terms in the free energy might become important. Therefore, the free energy to S^2 and H^4 is

$$F = \frac{3A}{4}S^2 - \frac{1}{3}\Delta\chi H^2 S - v_1 H^2 S^2 - v_2 2H^4 S, \tag{C.2}$$

where the v terms are higher order coupling coefficients and $A = a(T - T^*_{NI})$. Minimizing Eq. C.2 with respect to S gives

$$\frac{\partial F}{\partial S} = \frac{3}{2}AS - \frac{1}{3}\Delta\chi H^2 - 2v_1 H^2 S - v_2 H^4 = 0. \tag{C.3}$$

Solving for S gives,

$$S = \frac{\frac{\Delta\chi}{3}H^2 + v_2 H^4}{\frac{3}{2}A - 2v_1 H^2}. \tag{C.4}$$

Assuming that $v_1 H^2$ is small compared to $3A/2$, S can be written in the form,

$$S = \frac{6A\Delta\chi H^2 + 6Av_2 H^4 + 8\Delta\chi v_1 H^4 + 8v_1 v_1 H^6}{9A^2}. \tag{C.5}$$

Now one can define Q_{ij} using Eq. C.5 as,

$$Q_{ij} = \frac{1}{9A^2}[6A\Delta\chi(3H_iH_j - H^2\delta_{ij}) + 6Av_2H^2(3H_iH_j - H^2\delta_{ij}) \\ +8\Delta\chi v_1H^2(3H_iH_j - H^2\delta_{ij}) + 8v_1v_2H^4(3H_iH_j - H^2\delta_{ij})]. \tag{C.6}$$

Then defining H to be in the z-direction and using the relation between ϵ and Q_{ij}, $\epsilon_{ij} = \bar{\epsilon}\delta_{ij} + \frac{2\Delta\epsilon}{3}Q_{ij}$, to solve for Δn gives

$$\Delta n = \sqrt{\epsilon_{zz}} - \sqrt{\epsilon_{xx}} = \frac{\Delta\epsilon}{27A^2\sqrt{\bar{\epsilon}}}\left(18A\Delta\chi H^2 + 18Av_2H^4 + 24\Delta\chi v_1H^4 + 24\Delta\chi v_1v_2H^6\right). \tag{C.7}$$

This equation may be expressed as a power series in H, similar to the one used to represent tetrahedratic model in chapter 2,

$$\Delta n = (CM_1')H^2 + (CM_2')H^4 - (CM_3')H^6, \tag{C.8}$$

where the primes are used to differentiate these CM coefficients from those appearing in chapter 2. Here,

$$CM_1' = \frac{\Delta\epsilon}{27A^2\sqrt{\bar{\epsilon}}}(18A\Delta\chi), \tag{C.9}$$

$$CM_2' = \frac{\Delta\epsilon}{27A^2\sqrt{\bar{\epsilon}}}(18Av_2 + 24\Delta\chi v_1), \tag{C.10}$$

$$CM_3' = \frac{\Delta\epsilon}{27A^2\sqrt{\bar{\epsilon}}}(24v_1v_2). \tag{C.11}$$

C.1.1 MAGNITUDE OF THE INDUCED NEMATIC ORDER PARAMETER IN THE T AND I PHASES

Equation C.8 is of the same form as Eq. 2.46, and subsequently provides comparable fits to the data with a large number of unknown parameters and negative fit parameters. However, a simple estimate of the size of S in the isotropic phase using

LdG theory and the data for ClPbis10BB in chapter 2 shows that S is very small in the I phase. Using

$$S = \frac{2\Delta\chi}{9a(T - T^*_{NI})}H^2, \tag{C.12}$$

with $\Delta\chi = 3.0 \pm 0.6 \times 10^{-8}(cgs)$, $a = 5 \pm 1 \times 10^4$ erg cm$^{-3\circ}$C^{-1}, and $H = 20$ kG gives a value of

$$S = 0.005 \pm 0.002(T - T^*_{NI})^{-1}. \tag{C.13}$$

Even near the clearing point S will be very small, therefore higher order S terms in the LdG free energy should not have a strong influence on the on the behavior of the system and without these terms this model fails to describe the experimentally observed behavior. Also, Eq. C.9 predicts that $CM^{-1} \propto (T - T^*_{NI})$, which clearly does not agree with experimental observations. A change in slope of CM^{-1} v. T for ClPbis10BB and ClPbis10BBs is evident in the MB data. The DLS experiment, which measures properties in a manner unrelated to that used in MB, shows a change in observed behavior in the same temperature region. These two independent observations make a strong case that the effect seen in MB (DLS) is not some peculiarity due to the specific type of measurement technique, but is evidence of a phase transition that can only be explained by including tetrahedratic ordering in the theory.

C.2 FAN AND STEPHEN THEORY INCORPORATING NEMATIC FLUCTUATIONS

Fan and Stephen have incorporated nematic fluctuations into the static LdG theory and developed a new equation to explain the temperature dependence of the CM coefficient [1]

$$CM^{-1} \propto a\left(\frac{T - T^*}{T^*}\right)\left[1 + \frac{7c\nu_0 T^{*1/2}}{2\pi^2 a^2 \xi_0^3 (T - T^*)^{1/2}} - \frac{7b^2\nu_0 T^{*3/2}}{4\pi^2 a^3 \xi_0^3 (T - T^*)^{3/2}}\right] \tag{C.14}$$

$$= P_1 \left(\frac{T - T^*}{T^*}\right) \left[1 + \frac{P_2}{(T - T^*)^{1/2}} - \frac{P_3}{(T - T^*)^{3/2}}\right],$$

where a, b, and c are the dimensionless Landau coefficients, ν_0 is the molecular volume, and ξ_0 is the coherence length at 0 K. These coefficients are not well known and are lumped together into P_1, P_2, and P_3 in the second equation which is generally used to produce numerical fits to data.

This model can account for the slight bend in the CM^{-1} v. temperature near the N-I transition seen in some calamitics, most notably in MBBA in Stinson and Litster's early work [2]. However, this model cannot explain the curvature observed in the CM^{-1} v. temperature plots of the bent-core liquid crystals. For ClPbis10BB, a fit of this model to the data yielded a nonsensical negative P_2 coefficient, which by definition must be positive. A fit of the Fan-Stephen model to the ClPbis10BBs data could not handle the observed kink in the data, as evidenced by a plot of the ln of the CM residua v. the ln of the reduced temperature, which produced residua two orders of magnitude larger than those observed by Blanchik *et al.* [1]. So the Fan-Stephen model is clearly not able to explain the experimentally observed temperature dependence of the CM coefficient of bent-core liquid crystals.

A more convincing case against the applicability of the Fan-Stephen model to this situation can be made by looking at the field dependence of Δn. At a constant temperature Fan-Stephen theory predicts a linear relation between H and Δn, and thus cannot explain the highly non linear behavior observed in the experiments.

C.3 SATURATION

The low values estimated, above, for S in a 20 kG field make it very unlikely that any saturation effects are present in the MB measurements. However, for completeness I will present a more thorough argument ruling out saturation. A complete alignment, or saturation, of the molecules with the magnetic field will produce a plateau in $\Delta n(H)$. The MB experiments where carried out in some of the largest fields ever used with liquid crystals for this type of measurement, so it is possible that saturation effects will be present. Saturation effects for a uniaxial liquid crystal in a magnetic field were derived using a Maier-Saupe molecular theory in Refs. [3–5]. I will follow presentation of this model developed by Sprunt using the proceeding references.

The average polarizability per particle may be defined as

$$\langle \alpha_{ij} \rangle = \bar{\alpha} + \Delta\alpha \langle n_i n_j - \frac{1}{3}\delta_{ij} \rangle = \bar{\alpha} + \langle \Delta\alpha_{ij} \rangle, \tag{C.15}$$

where $\bar{\alpha}$ is the average polarizability in the isotropic phase, $\Delta\alpha$ is the maximum polarization anisotropy, n is a component of the director, and i is a component of the average particle dipole moment and

j is a component of the applied field at the particle. Using the Lorentz-Lorenz relation the average polarizability per particle may be recast as

$$\langle \alpha_{ij} \rangle = \frac{3}{4\pi N} \left(\frac{\epsilon_{ij} - 1}{\epsilon_{ij} + 2} \right), \tag{C.16}$$

where N is the number of particles per unit volume and ϵ is the dielectric permittivity. Using the relation $n_{ij} = \sqrt{\epsilon_{ij}}$, Eq. C.16 may be written as

$$\langle \alpha_{ij} \rangle = \frac{3}{4\pi N} \left(\frac{n_{ij}^2 - 1}{n_{ij}^2 + 2} \right), \tag{C.17}$$

then

$$\langle \alpha_{zz} \rangle = \frac{3}{4\pi N} \left(\frac{n_{\|}^2 - 1}{n_{\|}^2 + 2} \right) = \bar{\alpha} + \langle \Delta\alpha_{zz} \rangle, \tag{C.18}$$

and

$$\langle \alpha_{xx} \rangle = \frac{3}{4\pi N} \left(\frac{n_{\perp}^2 - 1}{n_{\perp}^2 + 2} \right) = \bar{\alpha} + \langle \Delta\alpha_{xx} \rangle. \tag{C.19}$$

Solving Eqs. C.18 and C.19 for $n_{\|}$ and $n_{\perp}$ to lowest order in $\Delta\alpha$ gives

$$\begin{aligned} n_{\|} - n_{\perp} &= \frac{2\pi N}{9} \frac{(n_0^2 + 2)^2}{n_0} (\langle \Delta\alpha_{zz} \rangle - \langle \Delta\alpha_{xx} \rangle) \\ &= \frac{2\pi N}{9} \frac{(n_0^2 + 2)^2}{n_0} \Delta\alpha \langle n_z - n_x \rangle \\ &= \frac{2\pi N}{9} \frac{(n_0^2 + 2)^2}{n_0} \Delta\alpha \langle cos^2\theta - sin^2\theta cos^2\phi \rangle, \end{aligned} \tag{C.20}$$

where the definition $\mathbf{n} = (\cos\phi \sin\theta, \sin\phi \sin\theta, \cos\theta)$ was used.

For non-interacting particles the energy in a magnetic field is given by

$$U = U_0 - \frac{1}{2} H_i \chi_{ij} H_j, \tag{C.21}$$

where $\chi_{ij} = \bar{\chi} + \Delta\chi(n_i n_j - \frac{1}{3}\delta_{ij})$ is the magnetic susceptibility anisotropy. Then with H chosen to be in the z-direction Eq. C.21 may be written as

$$U = U_0 - \frac{1}{2}(\bar{\chi} - \frac{1}{3}\Delta\chi) H^2 - frac12 \Delta\chi H^2 cos\theta. \tag{C.22}$$

The first two terms in Eq. C.22 are constant and can be neglected in the calculation of the average in Eq. C.21, then

$$\langle \cos^2\theta - \sin^2\theta \cos^2\phi \rangle = \frac{\int_{-1}^{1} d(\cos\theta) \int_0^{2\pi} d\phi (\cos^2\theta - \sin^2\theta \cos^2\phi) e^{\Delta\chi H^2 \cos^2\theta / 2k_B T}}{\int_{-1}^{1} d(\cos\theta) \int_0^{2\pi} d\phi e^{\Delta\chi H^2 \cos^2\theta / 2k_B T}}. \tag{C.23}$$

Carrying out the integral over ϕ gives

$$\langle \cos^2\theta - \sin^2\theta\cos^2\phi \rangle = \frac{\int_0^1 d(\cos\theta)(\frac{3}{2}\cos^2\theta - \frac{1}{2})e^{\Delta\chi H^2\cos^2\theta/2k_BT}}{\int_0^1 d(\cos\theta)e^{\Delta\chi H^2\cos^2\theta/2k_BT}}. \tag{C.24}$$

Putting this integral into Eq. C.21 gives

$$n_{\|} - n_{\perp} = \frac{2\pi N}{9}\frac{(n_0^2+2)^2}{n_0}\Delta\alpha\frac{\int_0^1 d(\cos\theta)(\frac{3}{2}\cos^2\theta - \frac{1}{2})e^{\Delta\chi H^2\cos^2\theta/2k_BT}}{\int_0^1 d(\cos\theta)e^{\Delta\chi H^2\cos^2\theta/2k_BT}}. \tag{C.25}$$

Lumping constants together this equation may be written in the simplified form

$$n_{\|} - n_{\perp} = A\frac{\int_0^1 d(\cos\theta)(\frac{3}{2}\cos^2\theta - \frac{1}{2})e^{BH^2\cos^2\theta}}{\int_0^1 d(\cos\theta)e^{BH^2\cos^2\theta}}. \tag{C.26}$$

This equation can be solved numerically for varying values of A and B to determine the best fit to a data set.

Equation C.26 was fit to a representative set of data for ClPbis10BB and ClPbis10BBs using a custom written Matlab program which minimized χ^2 with respect to A and B. The results of these fits are shown in Figs C.1 and C.2. The adjustable parameter A should be fixed for all temperatures, while B can vary with temperature. Here, both adjustable parameters were allowed to vary for all the plots to produce a best fit. Even with this concession, saturation effects cannot explain the experimentally observed behavior near the transition temperature. At high temperatures, where the energy due to the magnetic field is small compared to the entropy k_BT term, Eq. C.26 can be made to fit the data (i.e. nearly linear) by assuming a very small B value. But if the A and $B(T)$ values found here were used for the lower temperature data the fit produced is even worse than that pictured in the Figs. C.1 and C.2.

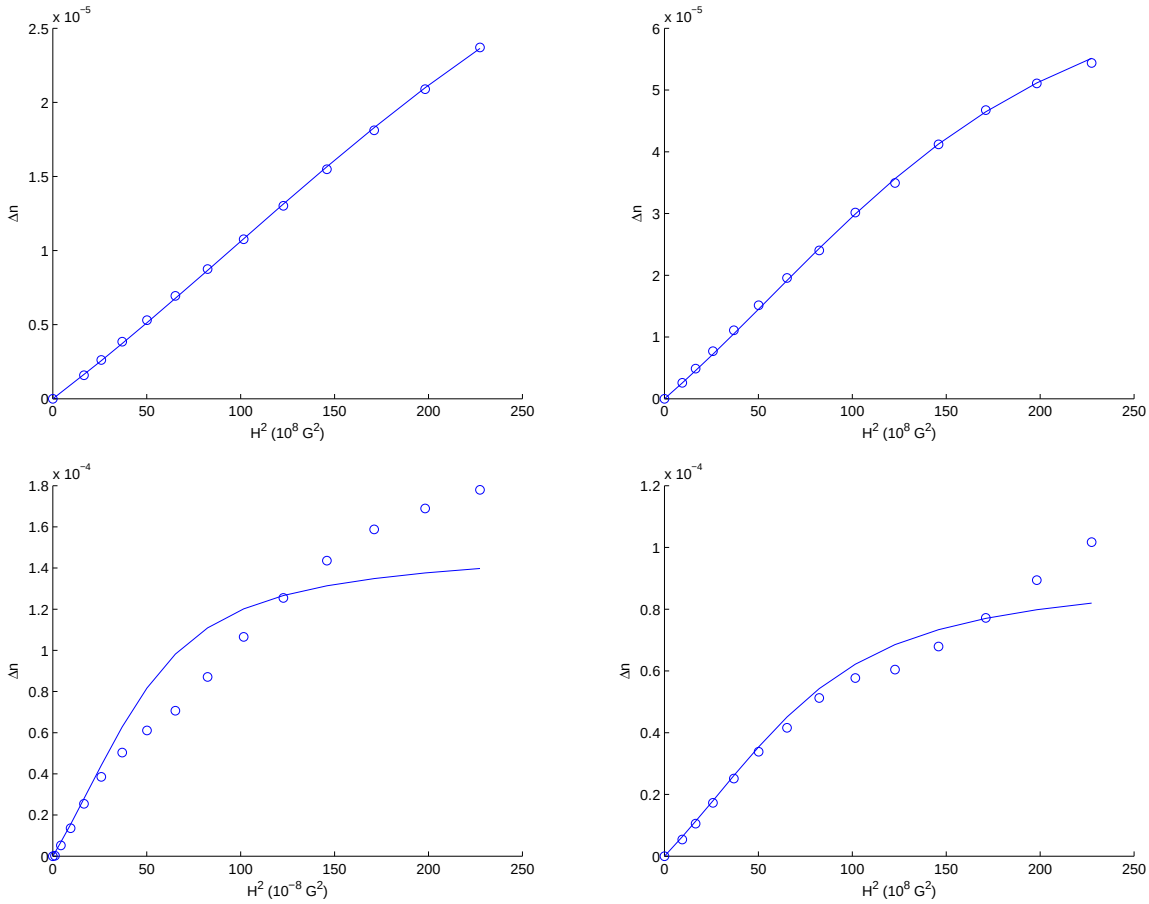

Figure C.1: A fit to $\Delta n(H^2)$ using the equation to describe saturation, for ClPbis10BB on cooling from the higher temperature isotropic phase. The circles represent the experimental data, while the solid line represents the fit to the data. Clockwise from the upper left ClPbis10BB is plotted at 18.1, 6.1, 2.1, and 0.6°C above its clearing point (76.9°C), respectively.

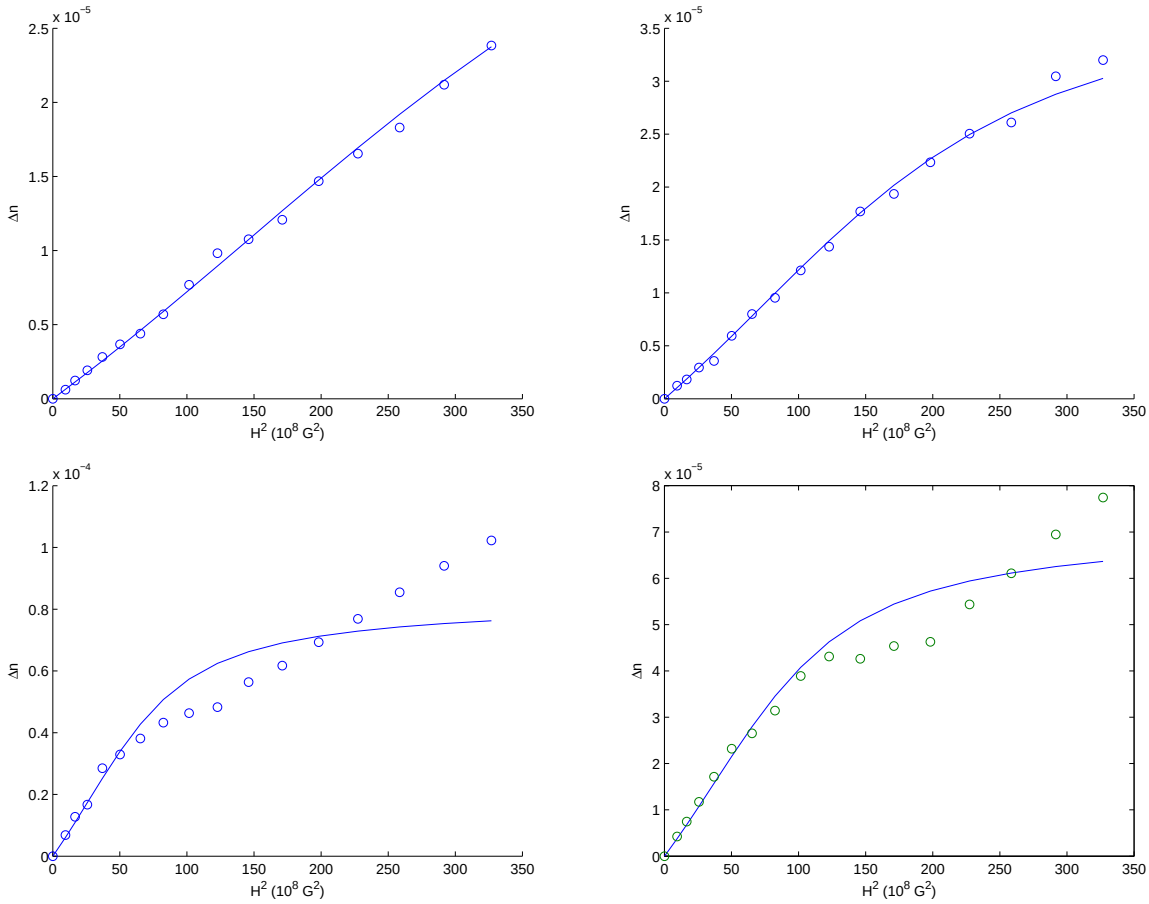

Figure C.2: A fit to $\Delta n(H^2)$ using the equation to describe saturation, for ClPbis10BBs on cooling from the higher temperature isotropic phase. The circles represent the experimental data, while the solid line represents the fit to the data. Clockwise from the upper left ClPbis10BBs is plotted at 14.8, 8.8, 1.3, and 0.8°C above its clearing point (90.2°C), respectively.

BIBLIOGRAPHY

[1] N. Blachnik, H. Kneppe, and F. Schneider. *Liq. Cryst.*, 27:1219, 2000.

[2] T. W. Stinson and J. D. Litster. *Phys. Rev. Lett.*, 25:503, 1970.

[3] E. van der Linden, S. Geiger, and D. Bedeaux. *Physica A*, 156:130, 1989.

[4] A. D. Buckingham and J. A. Pople. *Proc. Phys. Soc.*, 69:1133, 1956.

[5] A. Peterlin and H. A. Stuart. *Z. Phys.*, 112:1, 1939.

APPENDIX D

FITTING THE DLS DATA WITH A CALAMITIC MODEL USING A TEMPERATURE DEPENDENT ORIENTATIONAL VISCOSITY

The temperature dependence of the orientational viscosity in the I phase of calamitic LCs has been shown to obey an Arrhenius type temperature dependence [1,2]

$$\nu = \nu_0 e^{E_\nu / K_B T}, \tag{D.1}$$

where ν_0 is a constant, K_B is the Boltzmann constant, and E_ν is the activation energy. Equation D.1 can be inserted into the equation describing the relaxation rate derived in chapter 3 to get

$$\Gamma = \frac{a}{\nu}(T - T^*_{CL}) = \frac{a}{\nu_0} e^{-E_\nu / K_B T}(T - T^*_{CL}). \tag{D.2}$$

Equation D.2 can be rewritten in the following form

$$\Gamma = A(T - B)e^{-CT}, \tag{D.3}$$

where A, B, and C are adjustable fit parameters. This equation was fit to the relaxation rates for ClPbis10BB and ClPbis10BBs assuming that no transition is present above the clearing point, and that the change in the slope of the relaxation rate v. temperature is due to a temperature dependence of the orientational viscosity within a single optically isotropic phase. These fits are shown in Figs. D.2 and D.1.

Equation D.2 clearly does not model the experimental behavior as well as the two straight line fits predicted by the theory that considers T ordering (shown in Figs. 3.3

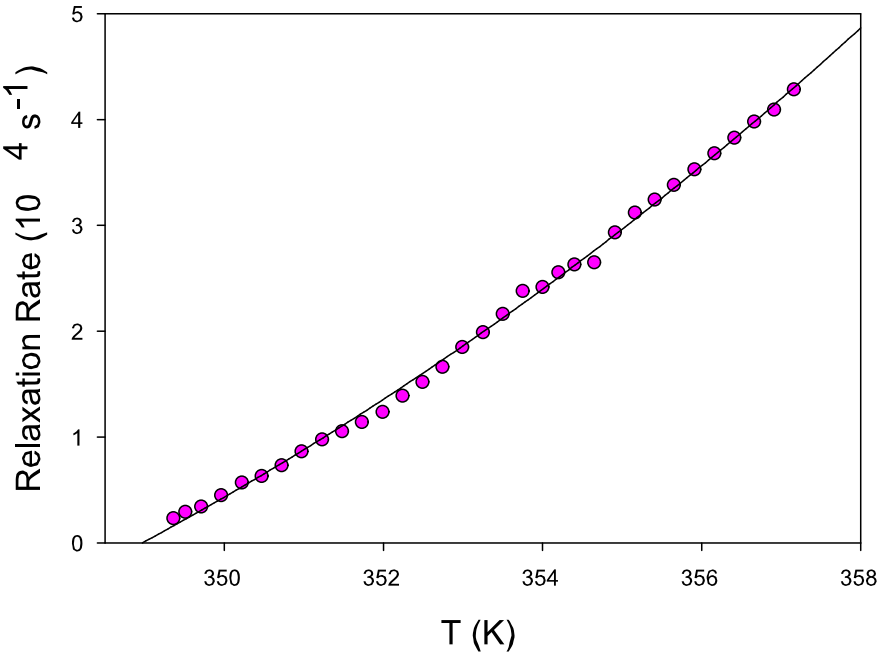

Figure D.1: Relaxation rate as a function of temperature for ClPbis10BB. The solid line represents a least square fit of Eq. D.3 to the data. $T_{CL} = 349.2$ K

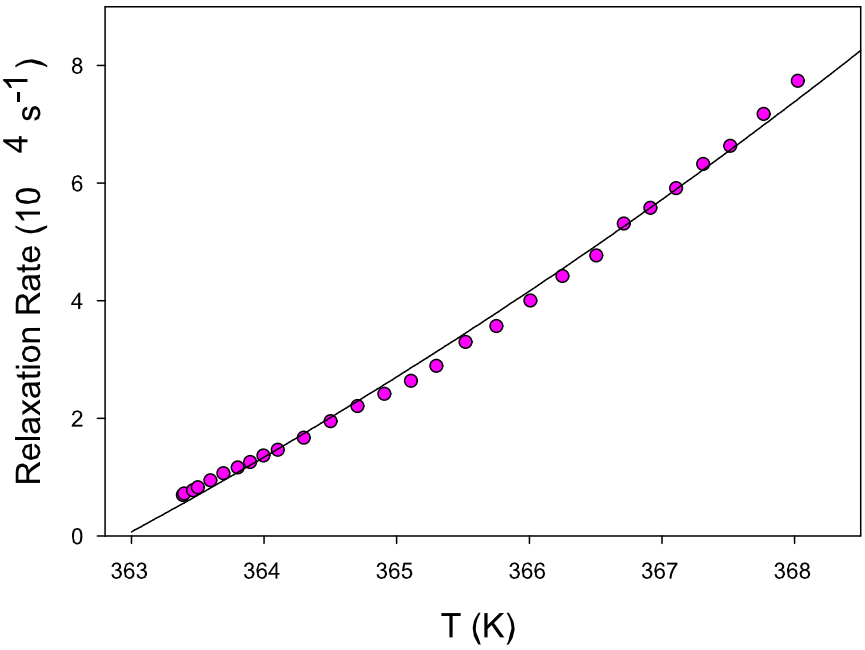

Figure D.2: Relaxation rate as a function of temperature for ClPbis10BBs. The solid line represents a least square fit of Eq. D.3 to the data. $T_{CL} = 363.1$ K

and 3.4). This is most evident in Fig. D.2, where Eq. D.2 is completely unable to account for the sharp bend in the relaxation rate $\sim 2^{\circ}$ above the clearing point.

Also, it is not unusual for a LC to show $\Gamma \propto T$ within a phase, i.e. for the orientational viscosity to show a weak temperature dependence. The relaxation rate has been shown to be proportional to temperature up to 12°C above the clearing point in 7CB [3]. Ueno *et al.* have shown that $\Gamma \propto T$ for 7°C above T_{NI}, until this gives way to an Arrhenius type dependence [2] in 6CB. Stojadinovic has shown that $\Gamma \propto T$ up to 6°C above the clearing point [4] in several different bent-core LCs. Therefore, it is reasonable to assume that we are observing a phases in ClPbis10BB and ClPbis10BBs, in which the orientational viscosity is only weakly temperature dependent.

In summary, a linear relation between Γ and temperature with a sharp transition to a different linear relation between Γ and temperature was observed in ClPbis10BB and ClPbis10BBs. This behavior has not been observed in calamitics (to the best of my knowledge) and cannot be explained by assuming that the temperature dependence of the orientational viscosity within a single phase is causing the change is slope of Γ.

BIBLIOGRAPHY

[1] T. W. Stinson, J. D. Litster, and N. A. Clark. *J. Phys. (Paris), Colloq.*, 33:C1–69, 1972.

[2] T. Ueno, K. Sakai, and K. Takagi. *Phys. Rev. E*, 54:6457, 1996.

[3] S. Takagi and H. Tanaka. *Phys. Rev. Lett.*, 93:257802, 2004.

[4] S. Stojadinovic. *Light Scattering Studies of Dynamics of Bent-Core Liquid Crystals.* PhD thesis, Kent State University, 2005.

APPENDIX E

MATLAB CODE FOR THE EDGEFINDER

The Matlab code used to determine the area below the mensicus in each picture and write the area of each picture to a file and then to write the difference in area between neighboring pictures to a file:

```
function getEdge2(start, finish)
howBig = finsish- start;
areaholder = zeros(howBig, 1);
fid = open('filename.txt','wt');
for k = start:finish
        x = ['C:\Documents and Settings\david\F493sat97\'int2str(k)'.tif'];
        area = getAreaModified(x);
        y = k - (start - 1);
        areaHolder(y) = area;
        fprintf(fid, '%i %f\n',k,area);
end
fclose(fid);
getDiff(areaHolder);
end
```

```
function totArea = getAreaModified(fileName)
        meniscus = imread(fileName);
        howBig = size(meniscus);
        height = howBig(1);
        width = howBig(2);
        height2 = height - 0; %starting height of edge finder
        row = height2;
        column = 1;
        temp = 0;
        subTot = 0;
        number = 0;
        tot = 0;
        area = 0;
        totArea = 0;
        pixVal = 0;
        pixMax = getThreshLow(filename);
        column = column+10; %left offset
        while column ≤ (width-10) %right offset
            pixVal = meniscus(row,column);
            if pixVal ≤ pixMax
                if row ≥ 70
                    subTot = mean(meniscus((row -69):row,column));
                else
```

```
                    subTot = mean(meniscus(1:row,column));
                end

                if subTot≤ pixMax
                    area = area + (height - row);
                    subTot = 0;
                    row = height2;
                    column = column + 1;
                else
                    subTot = 0;
                    row = row - 1;
                end
            else
                if row > 1
                    row = row -1;
                else
                    column = column + 1;
                    row = height2;
                    area = area + height;
                end
            end
        end
totArea = area;
end
```

```
function threshlow = getThreshLow(fileName)
        meniscus = imread(fileName);
        howBig = size(meniscus);
        height = howBig(1);
        width = howBig(2);
        height2 = height - 0; %starting height of edge finder
        row = height2;
        column = 1;
        temp = 0;
        subTot = 0;
        number = 0;
        tot = 0;
        area = 0;
        totArea = 0;
        pixVal = 0;
        pixMaxSub = mean(meniscus(height-50:height,800:width-2000));
        pixMax = mean(pixMaxSub) - 210;
        column = column+10; %left offset
        colStart = column;
        while column ≤ (width-10) %right offset
                pixVal = meniscus(row,column);
                if pixVal ≤ pixMax
                        if row ≥ 70
```

```
                    subTot = mean(meniscus((row -69):row,column));
                else
                    subTot = mean(meniscus(1:row,column));
                end

                if subTot≤ pixMax
                    subTot = 0;
                    row = height2;
                    column = column + 1;
                else
                    subTot = 0;
                    row = row - 1;
                end
            else
                if row > 1
                    row = row -1;
                else
                    pixMax = pixMax + 1;
                    row = height2;
                    column = colStart;
                end
            end
        end
threshLow = pixMax;
```

```
end


function getDiff(areas)
fid = open('filename.txt','wt');
howBig = size(areas);
length = howBig(1);
areaDiff = zeros(length, 1);
for k = 1:(length - 1)
        areaDiff(k) = areas(k + 1) - areas(k);
end
fprintf(fid, '%i\n', areaDiff);
fclose(fid);
end
```

APPENDIX F

YORICK CODE TO DETERMINE WAVELENGTH

The Yorick code used to determine the wavelength of the PW images using the FFT function:

```
//This takes pnm file as input, then returns the average of the sums of the
// fast fourier transforms of each row of data for the intensity of one of the
// colors. Set for use with a file that is 480rowsX640cols. Also remember
// to specify directory of file, or go to file directory w/
// cd, "directory" to use.


#include "pnm.i"
#include "fft.i"
func get Trans(filename)
{
        f= pnm_read(filename);
        s = (numberof(f))/3;
        color = array(0.0,s);
        for(i=1;i<s+1;i++)
        {
                color(i) = f((i*3)-1);//by -1, -2 can change which color
        }
```

```
        row = array(0.0,640);
        tot = array(0.0,512);
        i=1;
        while(i<480)
        {
                for(j=1;j<640;j++)
                {
                   row(j) = color((i*640)+j);
                }
                y = row(1:512);
                k = avg(y)//new code
                junk = y - k; //new code
                x = fft(junk,1);//newcode
                //x = fft(y,1);
                rex = x.re;
                imx = x.im;
                part = (rex^2)+(imx^2);
                part = part^.5;
                tot = tot + part;
                i++;
        }
        tot = tot/639;
        return tot;
}
```

APPENDIX G

MAGNETIC FIELD INDUCED CAPACITIVE ANISOTROPY

The MB experiment is a very precise way to probe pretransitional behavior in LCs. However, the experiment has certain technical difficulties, which are magnified in a large vertical bore magnet. Optical alignment and orientation is a major concern, especially inside the magnet. The restriction of having all the components completely non-magnetic makes the use of standard optical mounts impossible, which dictates that all mounting components have to be home-made. The process is tedious and would best be avoided. This might happen if we were able to directly measure the magnetic field induced change in capacitance, without the use of an optical probe.

In chapter 2, I showed that the dielectric anisotropy could be written as a function of the nematic order parameter

$$\epsilon_{ij} = \bar{\epsilon}\delta_{ij} + \frac{2\Delta\epsilon}{3}Q_{ij}, \tag{G.1}$$

where $\Delta\epsilon$ is the saturated anisotropy and $\bar{\epsilon} = \frac{1}{3}(2\epsilon_\perp + \epsilon_\parallel)$ is the isotropic dielectric constant. It was also shown that for a calamitic LC in a magnetic field the nematic order parameter that gave a minimum free energy could be written as

$$Q_{ij} = \frac{\Delta\chi}{9A}(3H_iH_j - H^2\delta_{ij}). \tag{G.2}$$

Using this value for the minimum Q_{ij}, Eq. G.1, and the simple electrodynamics equation for a parallel plate capacitor

$$C_{ij} = \frac{A}{4\pi d}\epsilon_{ij} \tag{G.3}$$

where A is conducting area of the plates and d is the separation of the plates, the magnetic field induced capacitance may be calculated. For a field in the z direction the capacitive anisotropy will yield a relation between C and H^2 similar to the effect seen in the MB experiment

$$C_{zz} = \frac{A}{4\pi d}\epsilon_{zz} = \frac{A}{4\pi d}[\bar{\epsilon} + \frac{4\Delta\epsilon\Delta\chi H^2}{27a(T-T^*)}] \tag{G.4}$$

$$C_{xx} = \frac{A}{4\pi d}\epsilon_{xx} = \frac{A}{4\pi d}[\bar{\epsilon} - \frac{2\Delta\epsilon\Delta\chi H^2}{27a(T-T^*)}] \tag{G.5}$$

$$C_{zz} - C_{xx} = \frac{A\Delta\epsilon\Delta\chi}{18\pi da(T-T^*)}H^2. \tag{G.6}$$

This method can determine $T_{NI} - T^*$ and the leading Landau coefficient via a more direct measurement than MB and with much less effort. However, there are some drawbacks to this method. The most significant being the small value for the induced capacitance anisotropy. For example, taking typical values for 5CB of $a =$ 1.3 erg / cm^3, A = 1 cm^2, d = 5×10^{-4} cm, $\Delta\chi = 1.8 \times 10^{-7}$, $\Delta\epsilon = 10$, $H = 100$ kG, and $\Delta T = 1$°C (one degree above T^*) the induced capacitive anisotropy is about 0.5 cm in cgs units. In the more common SI unit of the Farad, $\Delta C \sim 5 \times 10^{-13}$ F. In order to measure ΔC one needs better than picoFarad resolution in their capacitance measurement and a very large magnetic field. Another drawback to this method is that the sample must be rotated by 90° in the magnetic field to detect the parallel and perpendicular components of the capacitance, while in the MB method no mechanical movement is needed.

All of the fore mentioned obstacles can be readily overcome in practice. The NHMFL provides magnets with fields up to 310 kG with large enough bores to rotate a sample. Andeen Hagerling auto-balancing capacitance bridges offer resolution on the order of 0.0001 pF for a properly shielded and configured set-up. A well designed and

constructed sample holder can provide adequate temperature stability and shielding, along with rotational freedom within the magnet.

This method may also be used with bent-core LCs if the appropriate free energy is chosen to evaluate the results. From chapter 2, the minimum Q_{ij} at temperatures above T_{N_TT} is described by

$$\begin{aligned} Q_{ij} = \sqrt{\frac{3}{2}}[\frac{16}{3}u_T'^2\Delta\chi A_Q'(H_iH_j - \frac{1}{3}H^2) + 4w_2'u_T'A_Q'A_T'(H_iH_j - \frac{1}{3}H^2) \\ -8w_2'w_3'u_T'A_Q'H^2(H_iH_j - \frac{1}{3}H^2) + \frac{8}{3}w_2'^2u_T'\Delta\chi H^4(H_iH_j - \frac{1}{3}H^2) \\ +2w_2'^3A_T'H^4(H_iH_j - \frac{1}{3}H^2) - 4w_2'^3w_3'H^6(H_iH_j - \frac{1}{3}H^2)] \times (4u_T'A_Q')^{-2}. \end{aligned} \tag{G.7}$$

Using Eqs. G.1 and G.3 and assuming the magnetic field is in the z-direction, the capacitive anisotropy for a bent-core LC can be written as (again using the fact that w_1' is negligible)

$$\begin{aligned} C_{zz} - C_{xx} = \frac{A\Delta\epsilon}{48\pi d u_T'^2A_Q'^2}\sqrt{\frac{3}{2}}(\frac{8}{3}u_T'^2\Delta\chi A_Q'H^2 + 2w_2'u_T'A_Q'A_T'H^2 \\ -4w_2'w_3'u_T'A_Q'H^4 + \frac{4}{3}w_2'^2u_T'\Delta\chi H^6 + w_2'^3A_T'H^6 - 2w_2'^3w_3'H^8) \end{aligned} \tag{G.8}$$

Bent-core liquid crystals typically have significantly smaller $\Delta\epsilon$ values than the calamitic example (5CB) used above, so some experimental work will need to be done to determine if this method can detect capacitive anisotropy changes in bent-core materials.